

**MODELLING OF TURBULENT  
CROSS-FLOW MICROFILTRATION  
OF  
PARTICULATE SUSPENSIONS**

**Visvanathan Lingamurthi Pillay**

**MSc Eng (Natal)**



Submitted in partial fulfilment of  
the requirements for the degree of

**Doctor of Philosophy**

in the

Department of Chemical Engineering  
University of Natal, Durban.

December 1991

## *Declaration*

---

I hereby declare that this dissertation is my own work, unless stated to the contrary in the text, and that it has not been submitted for a degree to any other University or Institution.



---

V L Pillay

December 1991

## *Acknowledgements*

---

I wish to express my sincere gratitude to the following people, for their contributions towards this dissertation :

- (i) My colleagues in the Department of Chemical Engineering, for their various assistances, stimulating discussions and the creation of a relaxed working atmosphere
- (ii) Messrs N Clarence, K Jack, B Mungan and O Msomi, of the Department of Chemical Engineering Workshop, for their assistance in constructing the experimental apparatus
- (iii) Mr Allen Stretton of High Tech Water NV, London, for his assistance in procuring literature
- (iv) Mrs N Kissoon, for her assistance in typing this dissertation
- (v) The Secretaries of the Pollution Research Group, Mrs N Kissoon and Mrs M Thotharam, for accepting my general rantings, ravings and disturbances to their schedules stoically
- (vi) Professor V G Jenson, for his valuable insight and input into the project
- (vii) The Durban Corporation, for granting me the Pollution Research Scholarship
- (viii) The Water Research Commission, for sponsoring the project
- (ix) The Computing Centre for Water Research, for the use of their computer facilities
- (x) Professor J D Raal, the supervisor of the project, for his invaluable input, guidance and encouragement, and also for accepting my offer to wash his car for a week in return for an acceptable supervisor's report (only joking - I only had to wash his car for two days)
- (xi) Professor Chris Buckley, the head of the Pollution Research Group and co-supervisor of this project, for the invaluable input in terms of discussions, assistance, guidance and encouragement. Indeed, it can be said that Professor Buckley was the one most responsible for putting me back on my feet (he was late with a grant payment, and the bank repossessed my car)
- (xii) My friends, for their general encouragement. In particular, mention must be made of Mr H P Gopal, without whose encouragement and assistance this dissertation would have been finished in half the time
- (xiii) Finally, my extreme gratitude must be expressed to my parents, for their encouragement and assistance during this study

This dissertation is  
dedicated to  
my  
Parents

## *Summary*

---

In cross-flow microfiltration (CFMF), the suspension is pumped tangentially over the filtration medium. Clear liquid permeates the filtration medium and is recovered as the *permeate*, while the solids accumulate at the filtration barrier to form a fouling layer, or *cake*. The cake, constituting an increase in hydraulic resistance, decreases the permeate flux. However, the tangential suspension flow tends to limit the growth of the cake. Thus, after an initial rapid increase in cake thickness, cake growth ceases, and the cake thickness becomes limited to some steady-state value. Correspondingly, after an initial rapid decrease, the permeate flux levels off and either attains a steady-state, or exhibits a slow, long-term decline with time.

Design and optimisation of CFMF systems necessitates a knowledge of the factors that govern CFMF behaviour. More specifically, it is necessary to know the effects that the operating variables, system variables and suspension properties have on the permeate flux. Although various models have been proposed for CFMF, there still exists a lack of knowledge of the basic mechanisms that determine CFMF behaviour, especially for systems operated under turbulent flow conditions.

This study constitutes a contribution towards the understanding and the modelling of the turbulent CFMF of particulate suspensions. The primary objective was to model the steady-state cake thickness and permeate flux in terms of the operating variables, equipment variables and suspension properties. The secondary objective was to investigate the influence that the cake characteristics have on the system behaviour. These objectives were accomplished as described below.

In the experimental study, the characteristic flux-time curve, effects of inlet velocity, bulk concentration and pressure on flux, and system responses to step-changes in operating conditions were obtained for a limestone suspension cross-flow filtered in a 25 mm woven hose tube. Inlet velocities investigated ranged from 0.85 m/s to 1.98 m/s, bulk concentrations from 10.0 g/l to 77.6 g/l, and pressures from 100 kPa to 300 kPa. The steady-state flux was found to be a function of all the operating variables studied, over the ranges investigated. However, it was also found that the flux is not uniquely determined by the operating conditions, but can exhibit a dependence on the operating path taken to reach the operating point.

A qualitative model of the mechanisms that determine cake growth and limit was then developed, based on an analysis of the likely particle transport processes in the system. The observations from the experimental study were utilised to infer the controlling processes. Three significant particle transport processes were identified – convection of particles towards the cake, shearing of particles off the cake and into the adjacent suspension layer, and diffusion from this layer

back to the bulk suspension. This back diffusion is effected by shear induced hydrodynamic diffusion, entrainment by turbulent bursts, and entrainment by turbulent eddies. The limiting or steady-state cake thickness is controlled by the convection-diffusion processes.

The qualitative model was then formulated into a mathematical model of the steady-state. The appropriate steady-state equations were identified. Functions required for the solution of the equations were then formulated from current fluid and particle dynamics technology and correlations. Four model parameters result, and these were subsequently quantified by computational experiments and a regression technique. An iterative, nested finite difference solution procedure was developed, permitting the prediction of the steady-state flux, cake thickness and concentration profile, for specified operating and system variables.

Predicted steady-state fluxes exhibit a notably good correspondence with experimental observations, and on average are within 10 % of experimentally observed values. The model also predicts a unique concentration profile, indicating that cake growth and limit is most probably controlled by a thin, distinct, concentrated suspension layer adjacent to the cake.

There are however significant limitations to the model. Firstly, the model is only applicable to systems where the limiting cake thickness is convection-diffusion controlled. Secondly, the inclusion of a shear induced hydrodynamic diffusivity in the model restricts its applicability to particulate suspensions that do not exhibit significant non-Newtonian characteristics. Further, the model parameters cannot be easily quantified from either current knowledge or simple laboratory tests, thereby limiting the predictive ability of the model.

Observations in the experimental study indicated that some system behaviours, i.e. the long-term flux decline and dependence of flux on the operating path, were seemingly determined by the characteristics of the cake. Accordingly, the nature of the cake and its influence on system behaviour was investigated. Three phenomena contributing to changes in the cake characteristics were addressed, viz. hydraulic compression, the preferential deposition effect and the fines infiltration effect. The mechanisms of these processes are discussed, together with their individual effects on the cake characteristics. Mechanisms proposed for the preferential deposition effect and fines infiltration effect are partially based on the qualitative model of cake growth and limit. The individual effects were then combined to indicate the net effect on cake characteristics during the cake growth period as well as during the slow decline in flux period. This was then applied to explain the seemingly anomalous behaviours observed in the experimental study.

# *Table of Contents*

---

## SUMMARY

List of Figures .....	vii
-----------------------	-----

List of Tables .....	xii
----------------------	-----

Nomenclature .....	xiii
--------------------	------

## Chapter 1 INTRODUCTION

1.1 BACKGROUND .....	1-1
1.2 OBJECTIVES .....	1-4
1.3 APPROACH AND THESIS ORGANISATION .....	1-4

## Chapter 2 EXPERIMENTAL STUDY

2.1 INTRODUCTION .....	2-1
2.2 EXPERIMENTAL SYSTEM .....	2-1
2.2.1 Apparatus .....	2-1
2.2.2 Instrumentation .....	2-3
2.2.3 CFMF Tubes .....	2-3
2.2.4 Suspension .....	2-4

<b>2.3</b>	<b>EXPERIMENTAL PROCEDURE .....</b>	<b>2-4</b>
2.3.1	Feed Preparation .....	2-4
2.3.2	Start-up Procedure .....	2-4
2.3.3	Measurement Techniques .....	2-5
<b>2.4</b>	<b>PROCESSING OF PRIMARY MEASUREMENTS AND ERROR ANALYSIS .....</b>	<b>2-6</b>
2.4.1	Primary Measurements .....	2-6
2.4.2	Calculation of Permeate Flux and Superficial Inlet Velocity .....	2-7
2.4.2.1	Permeate flux .....	2-7
2.4.2.2	Superficial Inlet Velocity .....	2-7
2.4.3	Error Analysis .....	2-7
2.4.3.1	Uncertainty in Permeate Flux .....	2-7
2.4.3.2	Uncertainty in Superficial Inlet Velocity .....	2-7
2.4.3.3	Errors in Flux-Time Curves .....	2-8
2.4.3.4	Errors in Flux vs Operating Variables Curves .....	2-9
2.4.3.5	Repeatability .....	2-9
<b>2.5</b>	<b>RESULTS .....</b>	<b>2-10</b>
2.5.1	Flux-Time Behaviour .....	2-10
2.5.2	Effects of Operating Variables on Flux .....	2-15
2.5.2.1	Effect of Superficial Inlet Velocity on Flux .....	2-15
2.5.2.2	Effect of Bulk Concentration on Flux .....	2-17
2.5.2.3	Effect of Pressure on Flux .....	2-20
2.5.3	Operational Path Dependence of Flux-time Behaviour .....	2-23
2.5.3.1	Dependence of Flux-Time Behaviour on Path to Reach Operating Velocity .....	2-23
2.5.3.2	Dependence of Flux-Time Behaviour on Path to Reach Operating Concentration .....	2-25
2.5.3.3	Dependence of Flux-Time Behaviour on Path to Reach Operating Pressure .....	2-27

2.6	SUMMARY OF EXPERIMENTAL STUDY .....	2-30
<b><u>Chapter 3      QUALITATIVE MODEL OF STEADY-STATE CONDITION</u></b>		
3.1	INTRODUCTION .....	3-1
3.1.1	A Note on <i>State</i> and <i>Measured</i> Variables .....	3-1
3.2	STATEMENT OF PROBLEM AND LITERATURE REVIEW .....	3-3
3.2.1	Force Balance Models .....	3-4
3.2.1.1	Inertial Lift (Lateral Migration) Models .....	3-4
3.2.1.2	Critical Drag or Critical Shear Models .....	3-6
3.2.2	Enhanced Back Diffusion Models .....	3-11
3.2.2.1	Shear Enhanced Back-Diffusion .....	3-11
3.2.2.2	Turbulent Back Diffusion .....	3-13
3.2.3	Axial Convection Models .....	3-18
3.2.4	Scour/Erosion Models .....	3-21
3.3	MODELLING APPROACH .....	3-24
3.4	FLUID DYNAMICS OF TURBULENT FLOW IN A POROUS TUBE .....	3-25
3.4.1	General Description of Turbulence .....	3-25
3.4.2	Turbulent Flows in Non-Porous Tubes .....	3-26
3.4.3	Fluid Dynamics in Porous Tubes .....	3-33
3.4.4	Effect of Particles on Fluid Dynamics .....	3-35
3.4.5	Summary of Fluid Dynamics .....	3-35
3.5	FLUID PARTICLE INTERACTIONS AND PARTICLE DYNAMICS .....	3-36
3.5.1	Particle Motion in a Turbulent Flow Field .....	3-36
3.5.2	Particle Motion in a Viscous Flow Field .....	3-36
3.5.3	Summary of Particle Dynamics .....	3-42
3.6	MODEL DEVELOPMENT .....	3-43

3.7	PARTICLE TRANSPORT MECHANISMS .....	3-47
3.8	QUALITATIVE MODEL FOR THE GROWTH AND LIMIT OF THE CAKE .....	3-56
3.9	DISCUSSION .....	3-58

## Chapter 4 INVESTIGATIONS INTO CHANGES IN CAKE STRUCTURE AND CHARACTERISTICS

4.1	INTRODUCTION .....	4-1
4.2	HYDRAULIC COMPRESSION EFFECT .....	4-2
4.2.1	Radial Variation in Permeability .....	4-5
4.2.2	Radial Variation in Critical Shear Stress .....	4-6
4.2.3	Summary of Hydraulic Compression Effect .....	4-7
4.3	PREFERENTIAL DEPOSITION EFFECT .....	4-8
4.4	FINES INFILTRATION EFFECT .....	4-15
4.5	NET EFFECT ON CAKE STRUCTURE AND CHARACTERISTICS .....	4-23
4.6	APPLICATIONS .....	4-26
4.6.1	Long-term Flux Decline .....	4-26
4.6.2	Irreversibility of Cake .....	4-26
4.6.3	Cake Growth in Period II .....	4-27
4.7	SUMMARY OF CHANGES IN CAKE STRUCTURE AND CHARACTERISTICS .....	4-27

## Chapter 5 MATHEMATICAL MODEL OF THE STEADY-STATE

5.1	INTRODUCTION .....	5-1
5.1.1	A Reminder on <i>State</i> and <i>Measured Variables</i> , and the <i>Wall</i> .....	5-2

		5-2
5.2	THE STEADY-STATE EQUATIONS .....	5-2
5.2.1	Continuity Equation .....	5-2
5.2.2	Hydraulic Resistance Equation .....	5-7
5.2.3	Summary of Steady-State Equations .....	5-9
		5-10
5.3	APPLICABILITY OF CURRENT FLUID AND PARTICLE DYNAMICS TECHNOLOGY TO CFMF .....	5-10
5.3.1	Applicability of Correlations Developed for Non-porous Tubes to CFMF .....	5-10
5.3.2	Applicability of Correlations Developed for Radially-Invariant Viscosity Systems to CFMF .....	5-15
5.3.3	Summary of Applicability of Current Technology .....	5-15
		5-15
5.4	FORMULATION OF MODEL PARAMETERS .....	5-15
5.4.1	Particle Diffusivity Distribution - $D_p$ .....	5-16
5.4.1.1	Particle Diffusivity due to Turbulent Bursts and Eddies .....	5-16
5.4.1.2	Shear Induced Hydrodynamic Diffusivity .....	5-26
5.4.1.3	Effective Particle Diffusivity .....	5-29
5.4.2	Radial fluid velocity distribution - $V$ .....	5-29
5.4.3	Boundary Concentrations - $C_{in}$ and $C_{out}$ .....	5-33
5.4.4	Cake Permeability - $K$ .....	5-33
5.4.5	Concentration Boundary Layer Thickness - $(b)$ .....	5-34
5.4.6	Miscellaneous .....	5-37
5.4.7	Summary of Model .....	5-40
5.4.7.1	Steady-State Equations .....	5-40
5.4.7.2	Model functions .....	5-40
5.4.7.3	Model parameters .....	5-40
		5-40
5.5	NUMERICAL SOLUTION PROCEDURE .....	5-40

5.6	QUANTIFICATION OF MODEL PARAMETERS .....	5-46
5.6.1	Introduction .....	5-46
5.6.2	Diffusivity Parameters ( $n$ , $S_c$ , $K_{sh}$ ) .....	5-46
5.6.3	Boundary Layer Parameter ( $K_b$ ) .....	5-52
5.6.4	Summary of Model Parameters .....	5-53
5.7	RESULTS AND DISCUSSION .....	5-54
5.7.1	Comparison Between Model Prediction and Experimental Observations .....	5-54
5.7.2	Characteristics of Typical Solutions .....	5-59
5.7.3	Sensitivity to Parameters .....	5-64
5.7.4	Are the Parameter Values Realistic ? .....	5-66
5.7.4.1	Boundary Layer Constant - $K_b$ .....	5-66
5.7.4.2	Turbulence Attenuation Parameter - $n$ .....	5-66
5.7.4.3	Shear Diffusivity Parameter - $K_{sh}$ .....	5-67
5.7.4.4	Inverse Particle Schmidt Number - $S_c$ .....	5-67
5.8	EVALUATION OF MODEL .....	5-68
<u>Chapter 6</u>	<u>CONCLUSION AND RECOMMENDATIONS</u> .....	6-1
<u>References</u> .....		Ref-1
<u>Appendix 1</u>	<u>SUSPENSION PROPERTIES</u> .....	A1-1
<u>Appendix 2</u>	<u>RESULTS OF EXPERIMENTAL STUDY</u> .....	A2-1

## *List of Figures*

---

<b>Chapter 1</b>		
Figure 1.1	Description of CFMF Process	1-1
Figure 1.2	Typical Flux-Time Curves for Cross-Flow and Dead-end Filtration	1-2
Figure 1.3	Differentiation Amongst Cross-Flow Processes	1-2
Figure 1.4	Overview of Thesis Organisation	1-6
<b>Chapter 2</b>		
Figure 2.1	Experimental Apparatus	2-2
Figure 2.2	Typical Uncertainties in Measured Flux Values	2-8
Figure 2.3	Typical Repeatabilities in Flux measurements	2-9
Figure 2.4	Typical Flux-Time Curve	2-10
Figure 2.5	Typical Flux-Time Curve (log-log scale)	2-11
Figure 2.6	Flux-Time Curve Obtained on Switching Feed Stream to Water	2-12
Figure 2.7	Expected Cake Thickness Profile	2-13
Figure 2.8	Typical Flux Gradient Profile	2-14
Figure 2.9	Effect of Inlet Velocity on Flux-Time Behaviour	2-15
Figure 2.10	Effect of Inlet Velocity on Flux-Time Behaviour (log-log scale)	2-16
Figure 2.11	Effect of Inlet Velocity on Steady-State Flux	2-16
Figure 2.12	Effect of Bulk Concentration on Flux-Time Behaviour	2-18
Figure 2.13	Effect of Bulk Concentration on Flux-Time Behaviour (log-log scale)	2-18
Figure 2.14	Effect of Bulk Concentration on Steady-State Flux	2-19
Figure 2.15	Effect of Bulk Concentration on Steady-State Flux (concentration in log scale)	2-19
Figure 2.16	Effect of Pressure on Flux-Time Behaviour	2-21

Figure 2.17	Effect of Pressure on Flux-Time Behaviour (log-log scale)	2-21
Figure 2.18	Effect of Pressure on Steady-State Flux	2-22
Figure 2.19	System Responses to Step-Increases in Velocity	2-24
Figure 2.20	System Responses to Step-Decreases in Velocity	2-25
Figure 2.21	System Responses to Step-Decreases in Bulk Concentration	2-26
Figure 2.22	System Responses to Step-Increases in Bulk Concentration	2-27
Figure 2.23	System Responses to Step-Decreases in Pressure	2-28
Figure 2.24	System Responses to Step-Increases in Pressure	2-29
Figure 2.25	Extrapolation to Ascertain Flux Immediately After Step-Increase in Pressure	2-30

### Chapter 3

Figure 3.1	Inertial Lift Model	3-5
Figure 3.2	Critical Drag Force Model	3-6
Figure 3.3	Trend for Effect of Inlet Velocity on Steady-State Flux, as Predicted by Rautenbach and Schocks' Model	3-9
Figure 3.4	Trend for Effect of Concentration on Steady-State Flux, as Predicted by Rautenbach and Schocks' Model	3-10
Figure 3.5	Trend for Effect of Inlet Velocity on Steady-State Flux, as Predicted by Hunt's Model	3-16
Figure 3.6	Trend for Effect of Concentration on Steady-State Flux, as Predicted by Hunt's Model	3-17
Figure 3.7	Trend for Effect of Pressure on Steady-State Flux, as Predicted by Hunt's Model	3-17
Figure 3.8	Simple Axial Convection Model	3-19
Figure 3.9	Axial Convection with Shear-Induced Back Diffusion	3-20
Figure 3.10	Sub-Regions in a Turbulent Flow Field	3-27
Figure 3.11	Universal Velocity Profile for Turbulent Flow	3-28
Figure 3.12	Dimensional Turbulent Velocity Profile	3-29
Figure 3.13	Radial Distribution of Prandtl's Mixing Length	3-30
Figure 3.14	Radial Distribution of Eddy Diffusivity of Momentum	3-31
Figure 3.15	The Turbulent Burst Phenomenon	3-32
Figure 3.16	Typical Radial Velocity Profile	3-33

Figure 3.17	Effect of Radial Flow on Axial Velocity Profile	3-34
Figure 3.18	Lift Force Created by Updraft Under a Burst	3-38
Figure 3.19	Expected Fluid Flow Patterns at Cake Surface	3-41
Figure 3.20	Expected Flux Decline Curves if Critical Shear/Drag Model Applies	3-44
Figure 3.21	Expected Concentration Profiles in Systems With and Without Back Diffusion	3-48
Figure 3.22	Hypothetical Zones in CFMF Tube	3-50
Figure 3.23	Differences Between Cake and Precake Particles	3-50
Figure 3.24	Forces Acting on Cake Surface Particle	3-51
Figure 3.25	Stable and Unstable Cake Surface Particles	3-52
Figure 3.26	Particle Exchange Processes Between Cake Surface and Precake	3-53
Figure 3.27	Particle Exchange Processes Between Precake and Suspension Zone	3-54

#### Chapter 4

Figure 4.1	Idealised Representation of Cumulative Drag Forces Through Cake	4-3
Figure 4.2	Pressure and Voidage Profiles Resulting from Hydraulic Compression of the Cake	4-4
Figure 4.3	Change in Solids Compressive Pressure Profiles as Cake Grows	4-5
Figure 4.4	Permeability Profiles Resulting from Hydraulic Compression of Cake	4-6
Figure 4.5	Critical Shear Stress Profile Resulting from Hydraulic Compression of the Cake	4-7
Figure 4.6	Particles of Different Sizes at Cake Surface	4-9
Figure 4.7	Control Volumes Near Cake Surface	4-9
Figure 4.8	Particle Transport Processes Between Control Volumes	4-10
Figure 4.9	Effect of Preferential Particle Deposition on Cake Characteristics During the Cake Growth Period	4-13
Figure 4.10	Effect of Preferential Particle Deposition on Cake Surface Characteristics After the Steady-State	4-14
Figure 4.11	Geometric Limitation of Infiltrating Particles	4-15

Figure 4.12	Expected Flux Decline Curves if Fines Saturate Entire Cake Volume	4-17
Figure 4.13	Possible Trends for Flux Decline Curves if Fines Saturate Only the Surface Layers of the Cake	4-18
Figure 4.14	Expected Cake Thickness Profiles for a Step-Decrease in Velocity	4-20
Figure 4.15	Expected Cake Cross-Sections if Fines Saturate Only the Surface Layers of the Cake	4-21
Figure 4.16	Effect of Fines Infiltration on Characteristics of Cake Surface Layers	4-22
Figure 4.17	Effect of Preferential Particle Deposition on Profiles Resulting from Hydraulic Compression of the Cake	4-23
Figure 4.18	Net Effects of Hydraulic Compression and Preferential Deposition During the Cake Growth Period	4-24
Figure 4.19	Net Effects on Cake Characteristics After the Steady-State	4-25

## Chapter 5

Figure 5.1	Section Through a Cake Formed on a Cylindrical Surface	5-8
Figure 5.2(a)	Effect of Radial Flow on Axial Velocity Profile (whole tube)	5-12
Figure 5.2(b)	Effect of Radial Flow on Axial Velocity Profile (near wall region)	5-13
Figure 5.3	Comparison of Axial Velocity Profiles Obtained at Low Radial Flows with Non-Porous Tube Profiles	5-14
Figure 5.4(a)	Comparison of Eddy Diffusivity Correlations (near wall region)	5-22
Figure 5.4(b)	Comparison of Eddy Diffusivity Correlations (core region)	5-23
Figure 5.5	Effect of Turbulence Attenuation Parameter on Turbulence Attenuation Function	5-25
Figure 5.6	Qualitative Effect of Radial Concentration Profile on Shear Rate at Wall	5-28
Figure 5.7	Fluid Mass Balance Across a Porous Tube	5-30
Figure 5.8	Comparison of Calculated Radial Velocity Profile with that of Kinney and Sparrow	5-31
Figure 5.9	Qualitative Effect of Radial Concentration Profile on Radial Velocity Profile	5-32

Figure 5.10	Concentration Profiles Illustrating Validity of Boundary Layer Analysis	5-34
Figure 5.11	Concentration Profiles Illustrating Validity of Assumed Boundary Layer Thickness	5-36
Figure 5.12	Algorithm I - Overall Iteration Scheme	5-41
Figure 5.13(a)	Algorithm II - Nested Iteration Procedure to Obtain Simultaneous Solutions for Concentration and Diffusivity	5-43
Figure 5.13(b)	Algorithm II (continued)	5-44
Figure 5.14	Two-Dimensional Representation of a Typical Solution Surface	5-48
Figure 5.15	Algorithm III - Algorithm to Generate Solution Surface	5-49
Figure 5.16	Illustration of Realistic and Unrealistic Concentration Profiles	5-50
Figure 5.17	Solution Curves for All Datapoints	5-51
Figure 5.18	Effect of Boundary Layer Parameter on Concentration Profiles	5-52
Figure 5.19	Effect of Boundary Layer Parameter on Predicted Flux	5-53
Figure 5.20	Predicted Effect of Velocity on Steady-State Flux	5-54
Figure 5.21	Predicted Effect of Concentration on Steady-State Flux	5-55
Figure 5.22	Predicted Effect of Pressure on Steady-State Flux	5-55
Figure 5.23	Predicted Effect of Velocity on Steady-State Cake Thickness	5-57
Figure 5.24	Predicted Effect of Concentration on Steady-State Cake Thickness	5-57
Figure 5.25	Predicted Effect of Pressure on Steady-State Cake Thickness	5-58
Figure 5.26	Overall Comparison of Predicted and Experimental Steady-State Fluxes	5-58
Figure 5.27	Typical Predicted Concentration, Radial Velocity and Diffusivity Profiles (across whole boundary layer)	5-60
Figure 5.28	Typical Predicted Concentration, Radial Velocity and Diffusivity Profiles (near cake surface)	5-60
Figure 5.28	Origin of Diffusivity Profile	5-61
Figure 5.29	Indication of Distinct Thickened Suspension Layer next to Cake Surface	6-62
Figure 5.30	Predicted Boundary Layer Thicknesses	5-66

# *List of Tables*

---

<b>Chapter 2</b>		
Table 2.1	Values and Uncertainties in Primary Measurements	2-6
Table 2.2	Normalised Fluxes Before and After Pressure Decreases	2-28
Table 2.3	Summary of Effects of Operating Variables on Steady-State Permeate Flux	2-31
<b>Chapter 3</b>		
Table 3.1	Comparison Between Fluxes Predicted by Rautenbach and Schocks' Model and Experimental Results Obtained in This Study	3-8
Table 3.2	Hunt's Regressed Parameters for a Limestone Suspension	3-15
<b>Chapter 5</b>		
Table 5.1	Summary of Fractional Changes in Operating Variables Along Tube	5-6
Table 5.2	Velocity Combinations investigated to Ascertain Whether Axial Velocity Profiles at Low Radial Flows are Similar to Non-Porous Tube Profiles	5-14
Table 5.3	Correlations for Turbulent Diffusivities	5-19
Table 5.4	Summary of Experimental Dataset	5-47
Table 5.5	Parameter Combinations Used in Model Predictions	5-54
Table 5.6	Typical Model Predictions	5-59
Table 5.7	Typical Sensitivity Analyses	5-64

## Nomenclature

---

$A$	area ( $\text{m}^2$ )
$C$	concentration (volume fraction)
$c$	concentration (mass fraction)
$C_b$	bulk concentration (volume fraction)
$C_b^*$	bulk concentration ( $\text{g}/\ell$ )
$C_\theta$	bulk concentration (mass fraction)
$C_b^*$	bulk concentration in Fane's model ( $\text{mg}/\ell$ ) (equation 3.28)
$C_{crit}$	critical concentration at which suspension consolidates into cake (volume fraction)
$C_D$	drag coefficient for spheres
$C_{eq}$	theoretical equilibrium concentration of precake (volume fraction) (equation 3.51)
$C_{max}$	maximum packing density of particles (volume fraction)
$C_{vf}, \dots, C_{vt}$	control volumes (Chapter 4.3)
$C_w$	concentration at the wall (volume fraction) (equation 3.19)
$C_w^*$	concentration at the wall in Fane's model ( $\text{mg}/\ell$ ) (equation 3.28)
$C_0$	boundary concentration in Hunt's model (mass fraction) (equation 3.26)
$D_p$	particle diffusivity vector ( $\text{m}^2/\text{s}$ ) $(= D_{p,z} \cdot D_{p,y} \cdot D_{p,x})$

$D$	molecular diffusivity ( $\text{m}^2/\text{s}$ )
$\hat{D}$	non-dimensional shear induced diffusivity of spherical particles (equation 3.17)
$\hat{D}^*$	non-dimensional shear induced diffusivity of angular particles (equation 5.36)
$D'$	diffusivity in Hunt's model ( $\text{kg}/\text{ms}$ ) (equation 3.20)
$D_{net}$	net diffusivity of mass in turbulent flow ( $\text{m}^2/\text{s}$ )
$D_p$	particle diffusivity in radial direction ( $\text{m}^2/\text{s}$ ) (simpler annotation for $D_{p,r}$ )
$D_{p,r}$	particle diffusivity in radial direction ( $\text{m}^2/\text{s}$ )
$D_{p,z}$	particle diffusivity in axial direction ( $\text{m}^2/\text{s}$ )
$D_{p,\theta}$	particle diffusivity in azimuthal direction ( $\text{m}^2/\text{s}$ )
$D_{ps}$	particle diffusivity due to shear induced hydrodynamic diffusion ( $\text{m}^2/\text{s}$ )
$D_{pt}$	particle diffusivity due to turbulent bursts and eddies ( $\text{m}^2/\text{s}$ )
$d$	particle diameter (m)
$\bar{d}_p$	mean particle diameter (m)
$E$	modified error function $E(x) = \frac{1}{2} \operatorname{erf} \left( \frac{x}{\sqrt{2}} \right)$ (equation 5.12)
$E_0$	earth stress ratio in cylindrical cakes (lateral stress/radial stress) (equation 4.6)
$F_{ad}$	axial drag force on particle (N) (Figure 3.2)
$F_D$	drag force on particle due to radial fluid flow (N) (Figure 3.1)

$F_d$	drag force on cake particles due to permeate flow (N) (equation 4.2)
$F_f$	friction force on particle (N) (Figure 3.2)
$F_i$	inertial lift force on particle (N) (Figure 3.1)
$F_{pd}$	radial drag force on particle due to permeate flow (N) (Figure 3.2)
$F_r$	resultant force on cake surface particles (N) (Figure 3.24)
$F_s$	solids compressive force (kN) (equation 4.2)
$F_x$	axial force on cake surface particle due to axial shear stress (N) (Figure 3.24)
$F_y$	radial force on cake surface particle due to permeate drag and inter-particle forces (N) (Figure 3.24)
$f$	friction factor in porous tubes (equation 5.14)
$f_m$	Moody friction factor (equation 5.22)
$f_0$	Blausius friction factor for non-porous tubes
$g$	gravity ( $m/s^2$ )
$g'$	equivalent gravity in Scarlett and Treasure's Model (equation 3.33)
$h_4(r)$	function in lift force expression (equation 3.8)
$h_2 \dots h_4$	functions in Scarlett and Treasure's Model (equation 3.33)
$h_5, h_6$	functions in Weissberg's correlation (equation 5.13)
$h_7$	velocity defect function (equation 5.22)
$h_8 \dots h_{10}$	functions in Hsu's correlation (equation 5.27)

$J'$	permeate flux in Hunt's model ( $\text{kg/m}^2\text{h}$ ) (equation 3.25)
$J_{cs}$	permeate flux at cake surface ( $\ell/\text{m}^2\text{h}$ )
$J_w$	permeate flux at tube wall ( $\ell/\text{m}^2\text{h}$ )
$J_0$	permeate flux at tube wall in Hunt's model ( $\text{kg/m}^2\text{h}$ ) (equation 3.25)
$j$	symbolises $j^{\text{th}}$ iteration (Section 5.5)
$K$	cake permeability ( $\text{m}^2$ )
$K'$	permeability constant in Hunt's model (equation 3.25)
$K_1, K_2$	attenuation constants (equations 5.36 and 5.37)
$K_{at}$	turbulence attenuation function (equation 5.30)
$K_{sh}$	shear induced diffusivity parameter $(= K_1 K_2)$ (equation 5.38)
$K_b$	boundary layer parameter (equation 5.49)
$K_e$	erosion coefficient (equation 3.25)
$k_1 \dots k_6$	regression constants (equation 2.3)
$k_7, k_8$	constants in lift force expression (equation 3.8)
$k_9$	constant in Hunt's diffusivity expression (equation 3.20)
$k_{10}$	constant in Hunt's boundary layer expression (equation 3.23)
$k_{11}$	constant in Hunt's friction velocity expression (equation 3.24)
$k_{12}, k_{13}$	regression constants in Hunt's model (equation 3.26)

$k_{14} \dots k_{17}$	regression constants in Fane's model (equation 3.31)
$k_{18}$	permeability constant in Scarlett and Treasure's model (equation 3.34)
$k_m$	mass transfer coefficient (m/s) (equation 3.18)
$L$	length of tube (m)
$t$	Prandtl mixing length
$m$	initial concentration profile parameter (equation 5.58)
$n$	turbulence attenuation parameter (equation 5.32)
$P$	operating pressure (kPa)
$P_L$	liquid hydraulic pressure (kPa)
$P_S$	solids compressive pressure (kPa) (equation 4.1)
$\Delta P$	pressure drop across cake (kPa)
$Q$	suspension flowrate ( $\text{m}^3/\text{s}$ )
$Q_p$	permeate flowrate ( $\text{m}^3/\text{s}$ )
$Q_s$	net solids flowrate in radial direction ( $\text{m}^3/\text{s}$ )
$q_1$	exponent in permeability expression (equation 4.7)
$q_2$	exponent in critical shear stress expression (equation 4.8)
$r$	radial distance from tube centreline (m)
$r^*$	non-dimensional radial distance $(= r / R )$
$r_p$	particle radius (m)
$R$	tube radius (m)
$R_c$	radius of free core (m) $( = R - t_c )$

$s$	correlation parameter in Weissberg's correlation (equation 5.12)
$\mathcal{R}_d$	rate of back-diffusion of particles from precake to suspension zone
$\mathcal{R}_c$	rate of convection of particles into precake from suspension zone
$Re$	Reynolds Number
$RF_1, RF_2$	relaxation factors (Chapter 5.5)
$S_c$	molecular Schmidt Number
$S'_c$	Inverse Particle Schmidt Number $(= D_{pi}/\epsilon)$
$t$	time (seconds)
$t_c$	cake thickness (m)
$t_{co}$	equivalent resistance of tube wall (m) (equation 3.34)
$t_{perm}$	time to collect permeate of volume $V_{perm}$ (s)
$T_1 \dots T_5$	expressions in finite difference analogue of equation 5.3
$U'$	suspension velocity in axial direction (m/s)
$\bar{U}'$	time-averaged axial velocity component in turbulent flows (m/s)
$U^*$	friction velocity (m/s) $(= \sqrt{\tau_w/\rho})$
$U^+$	non-dimensional axial velocity in turbulent flows $(= U'/U^*)$
$U'$	axial component of instantaneous fluctuating velocity in turbulent flows (m/s)
$\overline{U'V'}$	time averaged value of $U'V'$
$\bar{U}_c$	bulk average axial suspension velocity in free core (m/s) $(= Q/(\pi R_c^2))$
$\bar{U}_s$	bulk average superficial axial suspension velocity (m/s) $(= Q/(\pi R^2))$

$\bar{U}_{cr}$	critical deposition velocity for pipe flow of suspensions (m/s) (equation 3.32)
$\bar{U}_p$	mean axial fluid velocity over particle (m/s) (Figure 3.2)
$U_{max}$	maximum axial velocity (velocity at centreline of tube ) (m/s)
$V$	suspension velocity vector (m/s) $(= V + U + W')$
$V'$	radial suspension velocity (m/s) (equals radial fluid velocity when net radial solids velocity is zero)
$V^*$	non-dimensional permeate velocity at tube wall $(= V_w/U^*)$ (equation 5.12)
$V''$	radial component of instantaneous fluctuating velocity in turbulent flows (m/s)
$V(r)$	radial velocity at radius $r$ (m/s)
$V_{cs}$	permeate velocity at cake surface (m/s)
$\bar{V}_{cs}$	length averaged permeate velocity in Zydny and Colton's model (m/s) (equation 3.19)
$V_L$	inertial lift velocity (m/s) (equation 3.8)
$V_w$	permeate velocity at tube wall (m/s)
$V_{perm}$	volume of permeate collected ( $\ell$ )
$V_{sat}$	volume of cake available for saturation by fines (m <sup>3</sup> )
$W'$	suspension velocity in azimuthal direction (m/s)
$w$	distance through cake (m)
$\bar{w}$	depth to which fines saturate cake (m)
$x$	axial distance co-ordinate (in direction of bulk flow) (m)
$y$	distance from wall (m)

$Y^+$	non-dimensional distance from wall, in turbulent flows $(= Y U^+ / \nu )$
$Y^*$	non-dimensional distance from wall $(= Y / R )$
$y$	radial (normal) distance co-ordinate (in direction normal to bulk flow) (m)
$\left( \frac{\partial \delta_{ss}}{\partial t} \right)$	scour rate in Fane's model (equation 3.29)
<hr/>	
$\alpha$	specific cake resistance
$\beta$	cake voidage
$\delta$	concentration boundary layer thickness (m)
$\delta_v$	momentum boundary layer thickness (m)
$\epsilon$	eddy diffusivity of momentum in pure fluids ( $m^2/s$ ) ( also called eddy viscosity)
$\epsilon_M$	eddy diffusivity of mass ( $m^2/s$ )
$\epsilon_H$	eddy diffusivity of heat ( $m^2/s$ )
$\epsilon^*$	eddy diffusivity of momentum (attenuated for concentration effects) ( $m^2/s$ ) (equation 5.30)
$\epsilon'_H$	non-dimensional diffusivity of heat (equation 5.26)
$\langle \epsilon_H \rangle$	average diffusivity of heat over cross section of tube ( $m^2/s$ ) (equation 5.26)
$\epsilon'_{ch}$	non-dimensional diffusivity of heat for core region (equation 5.26)
$\epsilon'_{wh}$	non-dimensional diffusivity of heat for wall region (equation 5.26)
$\gamma$	shear rate ( $s^{-1}$ )

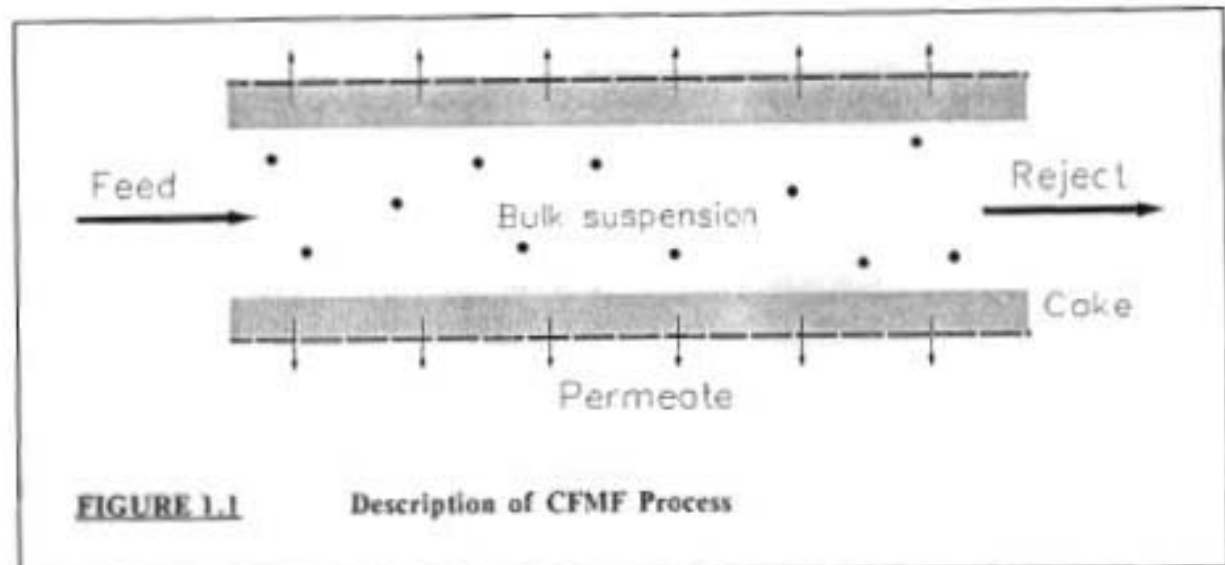
$\dot{\gamma}^*$	shear rate at wall, in systems having a radial concentration profile ( $s^{-1}$ ) (equation 5.37)
$\dot{\gamma}_w$	shear rate at wall ( $s^{-1}$ ) (wall refers to <i>cake surface</i> in the instance of CFMF, and <i>tube wall</i> if pure fluids are being considered)
$\rho_s$	solids density ( $kg/m^3$ )
$\rho_l$	liquid density ( $kg/m^3$ )
$\rho$	suspension density ( $kg/m^3$ )
$\tau$	shear stress (Pa)
$\tau_{crit}$	critical shear stress to destabilise cake surface particles (Pa)
$\tau_w$	shear stress at wall (Pa)
$\tau_t$	turbulent shear stress (Pa)
$\mu$	suspension viscosity (Pa.s)
$\mu_l$	liquid viscosity (Pa.s)
$\mu_t$	turbulent viscosity (Pa.s)
$\nu$	suspension kinematic viscosity
$\nu_l$	liquid kinematic viscosity (Pa.s)
$\nu_t$	turbulent kinematic viscosity ( $m^2/s$ )
$\psi$	friction coefficient (or proportionality constant) in Schock's model (equation 3.9)

# Chapter 1

## INTRODUCTION

### 1.1 BACKGROUND

The technique of cross-flow microfiltration (CFMF) potentially enables the continuous filtration of particulate suspensions. The suspension is pumped into a porous tube (Figure 1.1).



Clear liquid permeates the tube wall, driven by the pressure difference across the wall, and is recovered as the *permeate*. This flow of fluid normal to the wall convects particles to the wall where they accumulate to form a polarised layer, the *cake*. The cake, constituting an increase in the hydraulic resistance, decreases the permeate flux. However, the flow of the bulk suspension tangential to the cake tends to limit its growth, eventually resulting in a cake thickness, and hence permeate flux, that is relatively constant with time - the *steady-state* condition. This can be contrasted to standard *dead-ended* filtration techniques where the cake thickness increases continuously with time, resulting in a permeate flux that decreases continuously and rapidly (Figure 1.2). Permeate production rates obtained in CFMF systems are thus substantially higher than that obtained in equivalent dead-end filtration systems.

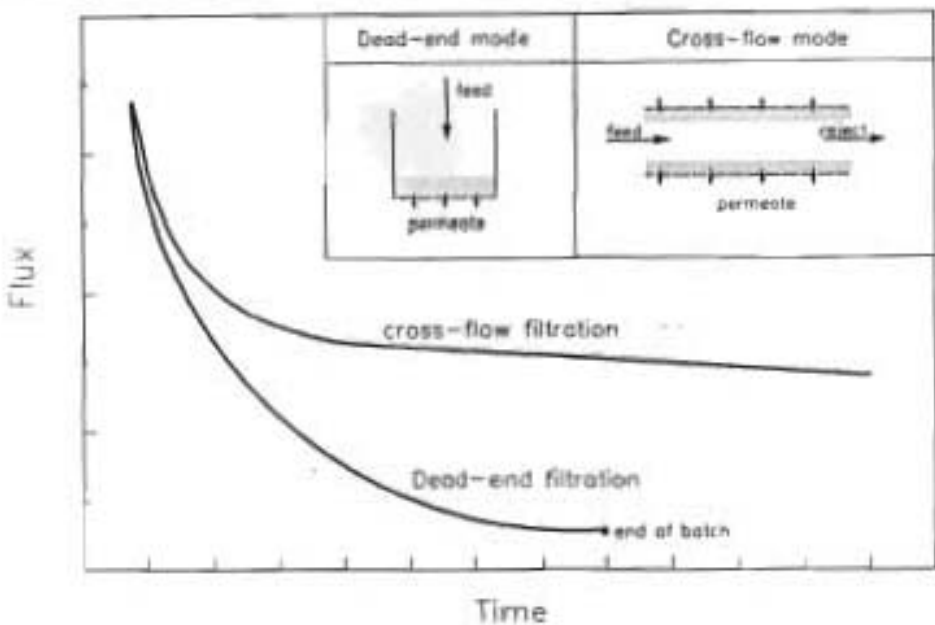


**FIGURE 1.2** Typical Flux-Time Curves for Cross-flow and Dead-end Filtration

The technique of utilising a tangential flow to minimise the growth of the polarised layer is, of course, also used in other membrane separation processes e.g. reverse osmosis (RO), nanofiltration (NF) and ultrafiltration (UF). Differentiation amongst the processes essentially resolve to the size of the rejected species, and in general can be represented by Figure 1.3 [Schneider and Klein (1982)].

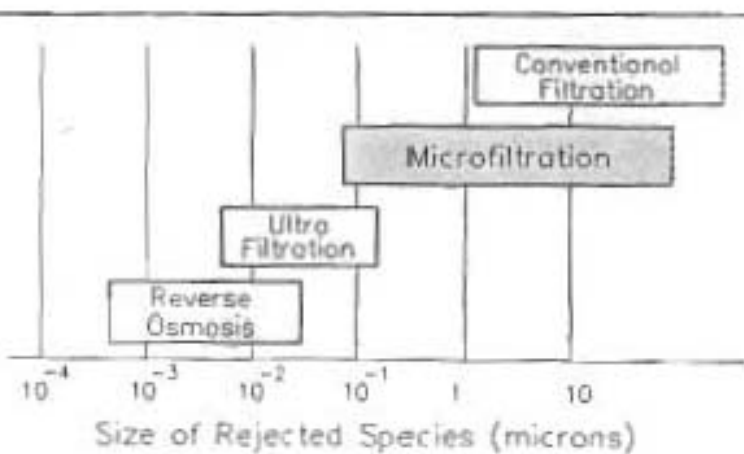


**FIGURE 1.3** Differentiation Amongst Cross-flow Processes

Porous supports utilised in CFMF include stainless steel, ceramic, rigid plastic and woven fibre tubes [Henry (1972), Kraus (1974)]. The major advantage of stainless steel, ceramic and rigid plastic tubes is that they maintain their geometric integrity and can thus be back-flushed. They also enable operation at elevated pressures. Woven fibre tubes can be produced relatively inexpensively in large lengths [Dalheimer et al. (1970), Kraus (1974)]. This potentially extends the economic viability of CFMF to large-scale high-volume applications.

In considering the rigid tubes, the tube wall is usually the filtration barrier, and the formation of a cake is undesirable. In the woven fibre tubes the actual filtration barrier is invariably the cake that forms on the tube wall. The close packing of the cake can enable the retention of particles that are often orders of magnitude smaller than the pores in the tube wall. This system thus affords the advantage that tubes with relatively large pores may be used, enabling easier cleaning and minimising irreversible fouling of the pores [Kraus (1974)].

Applications of CFMF range widely, from the filtration of beer and wine to the recovery of bacterial cultures. Of interest are the current attempts by the Pollution Research Group at the University of Natal to investigate the viability of CFMF for the large scale filtration of water for potable use, as well as the filtration of waste water. If proved viable, this could be of major significance to the water industry and CFMF could replace a substantial fraction of conventional water treatment facilities. The use of CFMF for the provision of potable water is of special significance in the Southern African context. Rapid growth of informal settlements in peri-urban areas has created an almost overnight demand for potable water, a demand that cannot be met in the immediate future by the existing conventional water treatment facilities [Umgeni Water (1990)]. CFMF, being relatively simple in concept, could potentially fulfil a substantial fraction of this demand.

Various models have been proposed to describe CFMF behaviour, and in general attempt to describe the mechanisms responsible for the eventual limiting of cake growth<sup>1</sup>. Most models are restricted to systems operating in the laminar flow regime. Of the models specific to turbulent flow systems, there are discrepancies between model predictions and experimentally observed trends. Further, various contradictions exist between model assumptions and known fluid and particle dynamics. Effectively, there is a distinct lack of knowledge of the fundamental mechanisms that determine particle transport, and hence cake growth and limit, in turbulent CFMF systems.

In most real systems, the permeate flux does not remain constant after the limiting (or *steady-state*) cake thickness has been achieved, but continues to show a slow decline with time. This is generally attributed to changes in the characteristics of the cake. Although some studies have been initiated into the nature of these changes, no major attempt has been made to fully describe the effects that changes in cake characteristics have on the system behaviour.

<sup>1</sup> These will be discussed in a later chapter of this thesis.

This study constitutes a contribution towards an understanding of the basic mechanisms that determine the flux-time behaviour of a CFMF system operated in the turbulent flow regime. The prime intention is to determine the fundamental mechanisms responsible for cake growth and limit in turbulent flow systems, and hence to develop a model of the steady-state condition. The secondary intention is to investigate the nature of changes experienced by the cake and the effects that this has on system behaviour.

## 1.2 OBJECTIVES

The specific objectives of the study are as follows :

- i) To develop a realistic, qualitative model to describe the steady-state condition in turbulent CFMF systems, from current knowledge of fluid and particle dynamics in turbulent flows.
- ii) To investigate the mathematical formulation of this qualitative model, identifying parameters that may, and may not, be quantified from existing knowledge of fluid and particle dynamics and suspension properties.
- iii) To investigate changes experienced by the cake structure, for the system under study, and the effect that these have on system behaviour.

## 1.3 APPROACH AND THESIS ORGANISATION

The starting point in modelling the system is to establish the characteristic behaviour of the system viz. the flux-time behaviour and the effects of operating conditions on flux. Although numerous studies on CFMF behaviour do exist, there are often contradictions in reported trends for the effects of operating conditions on flux, as will be shown in Chapter 2. Further, the global processes responsible for the flux-time behaviour (i.e. cake growth, cake compression, cake ageing, fines infiltration) seemingly differ from system to system. The first task in this study thus resolved to obtaining a consistent dataset of typical CFMF behaviour, prior to attempting to model this behaviour. Accordingly, this thesis deviates from the usual thesis organisation i.e. *Introduction - Literature Survey - Theory - Experimental - Discussion - Conclusions*. Here, the experimental study is presented first, and the subsequent model development is based on these experimental observations. Further, reporting of literature is not confined to a single chapter, but is interspersed throughout the study, where appropriate.

Chapter 2 concerns the experimental study. The characteristic flux-time behaviour and the effects of operating variables on flux are obtained for a limestone suspension, and system responses to step-changes in operating variables are monitored. From this, the controlling processes responsible for the flux-time behaviour (i.e. cake growth and fines infiltration) are confirmed, and the trends that the steady-state flux exhibits with respect to inlet velocity, bulk concentration and pressure are characterised.

In Chapter 3 a qualitative mechanistic model of the steady-state condition is developed. Existing CFMF models are critically reviewed in terms of the experimental observations. An overview of particle transport mechanisms in a turbulent CFMF system is developed, based on current knowledge of fluid and particle dynamics in turbulent flows. This is then consolidated into a qualitative model of the steady-state condition. This qualitative model is translated into a mathematical model of the steady-state in Chapter 5. The reason for the separation of the qualitative and quantitative aspects of the model will be addressed in Chapter 3.

Changes in the cake structure and characteristics, and the effects that this has on system behaviour, forms the topics of Chapter 4. Three phenomena that effect changes in the cake characteristics are addressed - hydraulic compression, fines infiltration and the preferential deposition of smaller particles. The mechanisms by which these occur are discussed, together with their individual and combined effects on the cake characteristics. Mechanisms proposed for fines infiltration and the preferential deposition of smaller particles are based on the qualitative model of particle dynamics developed in Chapter 3. These are then applied to explain various "anomalies" observed in the experimental study.

In Chapter 5 the qualitative model of the steady-state developed in Chapter 3 is formulated into a mathematical model. The appropriate steady-state equations are identified. Model functions required for the solution of the equations are then formulated from existing fluid and particle dynamics technology and correlations. A numerical solution procedure is developed, enabling the prediction of the steady-state cake thickness, permeate flux and concentration profile for specified system and operating variables. Model predictions are then evaluated in terms of experimental observations.

Finally, in Chapter 6, the major findings of this study are summarised, shortcomings of the models are discussed, and suggestions for future research are made.

The overall thesis organisation is depicted pictorially in Figure 1.4. Note that Chapter 4 does not form a part of the mainstream of the thesis.

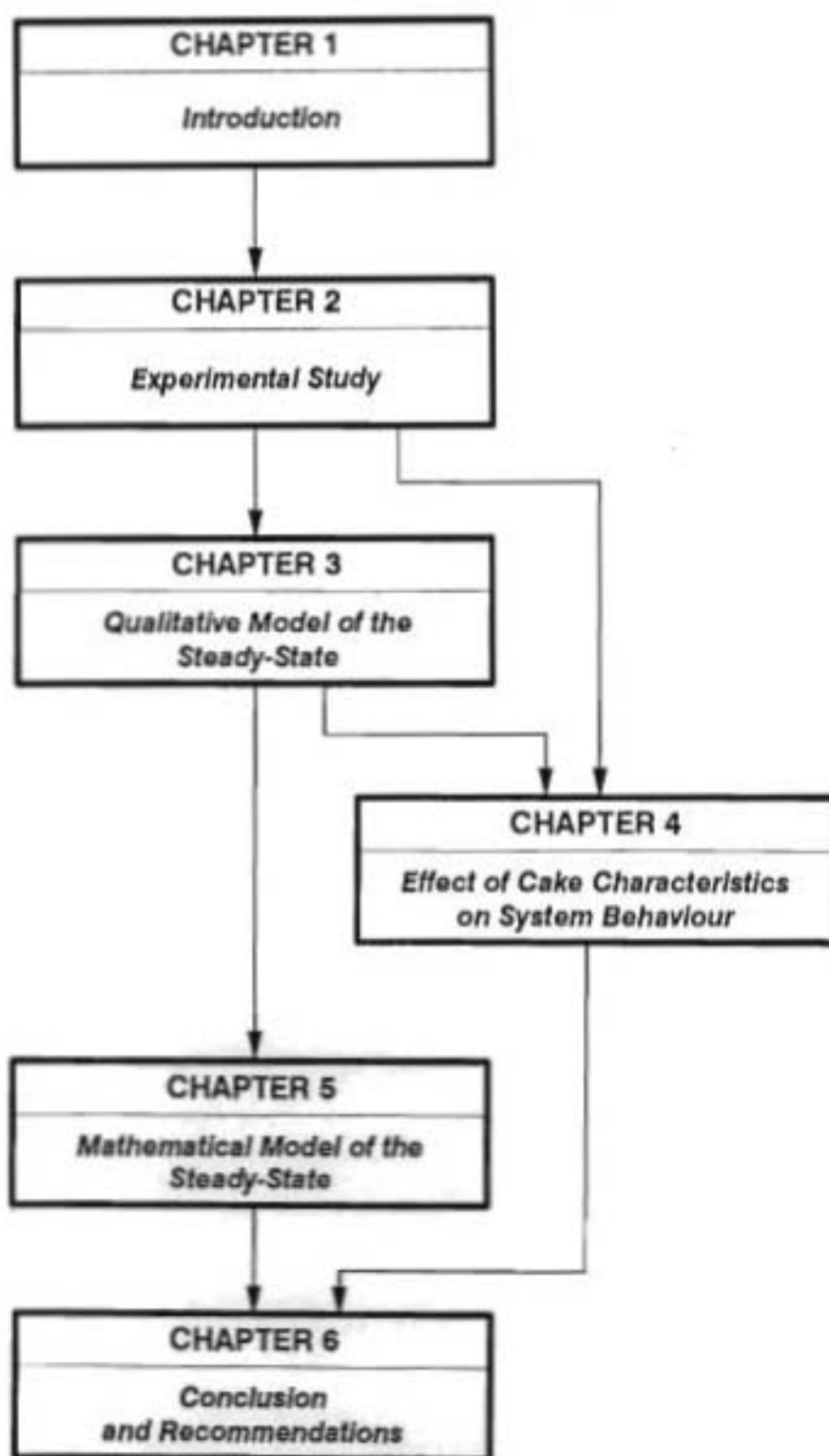


FIGURE 1.4

Overview of Thesis Organisation

## *Chapter 2*

### **EXPERIMENTAL OBSERVATIONS**

---

#### **2.1 INTRODUCTION**

The objectives in this chapter are as follows :-

- 1) To identify the characteristic behaviour of a cross-flow microfiltration (CFMF) system operated in the turbulent flow regime, including flux-time behaviour, effects of operating variables on steady-state flux and the operational path dependence of flux-time behaviour.
- 2) To identify the global processes (e.g. cake growth, compression effects) responsible for the characteristic flux-time behaviour of the system under study.

It is recognised that the effects of operating variables on flux have been widely studied and reported [Saw et al. (1985), Dalheimer et al. (1970), Hunt et al. (1987b), Rautenbach and Schock (1988)], and further that some studies have identified the global processes responsible for characteristic flux-time behaviour [Baker et al. (1985)]. These experiments are repeated in this study in order to ascertain whether previously reported observations are applicable to the system under study, and to obtain an internally consistent dataset for the evaluation of proposed models.

#### **2.2 EXPERIMENTAL SYSTEM**

##### **2.2.1 Apparatus**

A schematic diagram of the experimental CFMF apparatus is presented in Figure 2.1.

Feed from either of two feed tanks is pumped into the CFMF tube by two HYDRACELL® D25 triplex positive displacement pumps driven by a single 15 kW AC motor. The speed of the motor, and hence of the pumping rate, is controlled by a CCL TRIDENT® AC frequency inverter. The sequence of the pump diaphragms are offset by 60° from each other and this, together with the downstream accumulator, results in smooth delivery of pumped fluid. The feed tanks are well stirred and are fitted with heating and cooling coils linked to a temperature controller, enabling constant temperatures to be maintained during experiments.

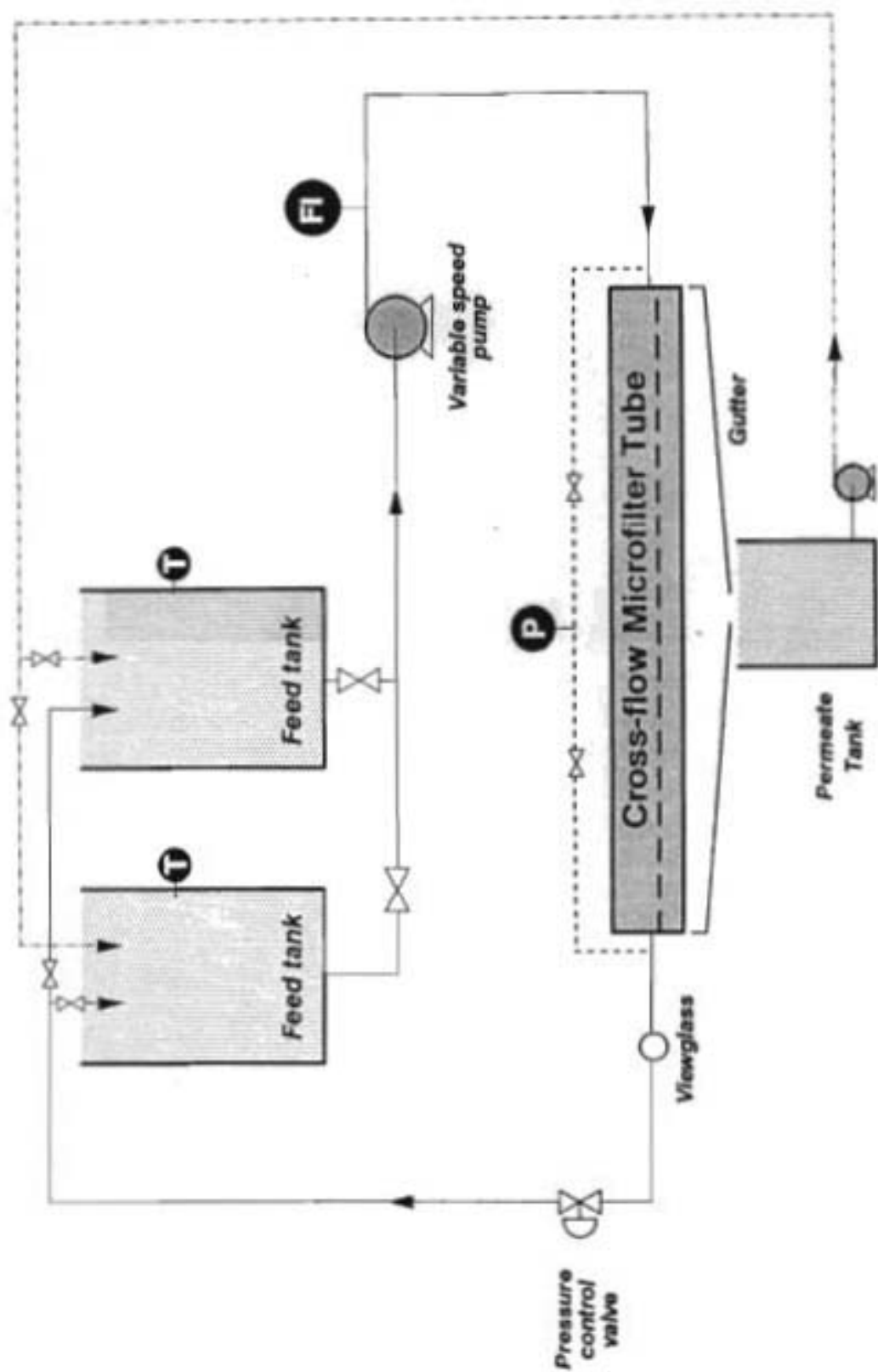


FIGURE 2.1 Schematic Diagram of Experimental Apparatus

FIGURE 2.1

A view glass downstream of the CFMF tube permits observation of the reject stream. Back-pressurisation is accomplished by a Saunders diaphragm valve downstream of the view glass. The reject stream may be returned to either of the feed tanks. Permeate flows down the permeate gutter into a permeate tank from which it is pumped back into the appropriate feed tank by a centrifugal pump controlled by level probes in the permeate tank. The permeate gutter is covered with perspex, reducing evaporation of permeate.

The system operates on a closed recycle basis i.e. all streams are returned to the feed tank, maintaining a constant feed tank volume. Further, the flowrate, pressure and concentration may all be varied independently.

### 2.2.2 Instrumentation

- (a) Flowrate - Feed flowrate is measured by a KROHNE® magnetic induction flowmeter. Empirical calibrations indicated that the flowmeter is accurate to greater than 99 % of actual flow, and is insensitive to feed concentration over the range considered here.
- (b) Pressure - Pressure tappings are positioned at the entrance to, and the exit of, the CFMF tube. These are connected via a single switching valve to a WIKA® pressure sensor. A facility exists to purge the pressure lines with water to remove any solids which may have entered during experiments.
- (c) Concentration - batch samples are obtained from the feed tank and the concentration is then ascertained by a gravimetric method. Although sample valves exist upstream and downstream of the CFMF tube, these were not used during experiments. The reason for this will be addressed in Section 2.5.3.1
- (d) Temperature - The temperature of the feed tank is indicated on the temperature controller. During each experiment the temperatures of the feed, permeate and reject streams were also monitored with a thermometer, to ensure consistency.

### 2.2.3 CFMF Tubes

The tube consists of a single length of woven polyester hose of outside diameter 25,2 mm (under pressure) and length 4,5 m. The diameter of the tube was insensitive to pressure over the range considered here. The first 1,2 m and last 0,3 m of the tube is rendered impermeable by the application of a commercial resin, SHOEPATCH®. These non-porous regions serve to reduce spurious entrance and exit effects. The effective length of the porous tube is thus 3,0 m, yielding an effective filtration area of 0,238 m<sup>2</sup>.

In initial experiments, the SWISS SILK tube (*Schweiz Seidengazefabrif AG Thal*), as used by Hunt (1987a), was used. However, it was found that for at least the first 20 hours of a run, suspension flowed readily through the pores of the tube and a very long run time was required before a stable cake formed and the permeate became clear. Further these tubes exhibited very little pressure integrity, expanding significantly in diameter with any increase in pressure, resulting in destruction of any cake that had formed. Investigations indicated that the poor

performance of the tubes was due to a gross mismatch between the size of the pores in the tube wall and the size of the particles used, making it difficult for particles to bridge stably across the pores to form a cake.

Subsequently the TRIPLE SEAM WOVEN POLYESTER HOSE supplied by HTW High Tech Water NV was tested. These tubes had been treated with a resin, INDOSOL®, which reduced the effective pore size of the tube and increased its pressure integrity. With this tube a stable cake and clear permeate were obtained within a minute of start-up and the tube diameter was insensitive to operating pressure. This type of tube was subsequently used for all experiments reported in this study.

The pure water flux of the bare tube is extremely high ( $> 8\,000 \text{ l/m}^2\text{h}$  at a pressure of 10 kPa). Since this flux is orders of magnitude greater than fluxes obtained with the suspension, it was assumed that the resistance of the tube wall could be regarded as negligible in comparison to that of the cake.

#### **2.2.4 Suspension**

The suspension consisted of pulverised limestone, available commercially as KULU 5, suspended in reverse osmosis (RO) permeate. Limestone particles were chosen due to their relative inertness in water, relative resistance to abrasion and shear and cheap availability [Hunt (1987a)]. RO permeate was used as the suspension medium in order to ensure consistent feed quality and to minimise the probability of any secondary membrane being formed [see Leger (1985)].

The physical properties of the limestone are given in Appendix 1.

### **2.3 EXPERIMENTAL PROCEDURE**

#### **2.3.1 Feed Preparation**

The feed suspension was prepared by mixing a weighted quantity of limestone with a known volume of RO permeate, calculated to yield the desired concentration. A new batch of feed was prepared for each experiment.

Initially, repeatability of the flux-time curves was poor. Investigations indicated that this poor repeatability was possibly due to feed suspensions being made up from different batches of limestone which seemingly had different particle size distributions. To obviate this and ensure a consistent feed for all experiments a large quantity of limestone was purchased and homogenised manually. All experiments reported here were performed with this homogenised batch.

#### **2.3.2 Start-up Procedure**

The tube was washed out with RO permeate and the suspension flow started with the back pressure valve open. The flowrate was then set to the desired value by adjusting the speed of the pump via the frequency invertor. This operating flowrate was generally achieved within 15 seconds. For the first minute, the permeate and reject were discharged to drain, to clear

out any RO water in the process lines. The permeate and reject streams were then switched back to the feed tank. The downstream pressure was then increased rapidly up to the desired operating pressure by closing the downstream back pressure valve. The flowrate did not change substantially during this pressure increase and the operating pressure was generally reached within 15 seconds. Initially the pressure tended to increase rapidly and had to be continually adjusted to the operation point by adjusting the back pressure valve. After about 5 minutes the system settled and only occasional adjustments to the back pressure valve were necessary. In all experiments reported here the permeate was clear to the eye from start-up.

The downstream pressure was selectively chosen as the control pressure on the presumption that the long non-porous entrance region would have resulted in the upstream pressure probe indicating a pressure significantly higher than the actual pressure in the porous zone. Since the pressure drop along the non-porous entrance region will be a strong function of velocity it would thus be difficult to maintain a constant operating pressure at different velocities. It subsequently occurred that this precaution was not really necessary since, at worst, the pressure drop along the tube was less than 5 % of the operating pressure, for the experiments reported here.

### 2.3.3 Measurement Techniques

- (a) Permeate flux - The flux was monitored at 5 minute intervals by measuring the time taken for the permeate to fill a 2 l measuring cylinder.
- (b) Cake thickness - An attempt was made to monitor the growth of the cake. Techniques investigated included X-rays, gamma rays and ultrasonic scanners but all proved to be unsuitable in their local commercially available form.

With respect to X-rays and gamma rays, the available industrial units are designed for the analysis of steel structures and emit relatively high energy rays. Under these circumstances, the image of the cake is relatively indistinct and the error in the measurement of cake thickness is  $\approx 0.5$  mm. A further problem is that the apparatus is relatively cumbersome and a relatively long exposure time is required, thus excluding the possibility of monitoring the growth of the cake.

Medical ultrasonic "body scanners" provided a cross-sectional view through the tube. The first problem with the apparatus is that the depth of field in the commonly available units is  $\approx 200$  mm. In these circumstances, the image of the cake is merely a thin line on the monitor, precluding accurate measurement of cake thickness. A scanner with a small depth of field ( $\approx 50$  mm) was eventually tested. This provided some qualitative observations on the cake thickness profile with time (see Section 2.5.1). However, the apparatus is extremely expensive and since it was calibrated for the sonic density of the human body could not be directly employed in the measurement of cake thickness.

It seemed that a substantial developmental time would be required before any of these techniques could be successfully applied to the measurement of cake thickness, and direct measurement of cake thickness was not pursued further in this study.

## 2.4 PROCESSING OF PRIMARY MEASUREMENTS AND ERROR ANALYSIS

### 2.4.1 Primary Measurements

The primary measurements taken, and the experimental uncertainties therein, are summarised in Table 2.1.

<b>TABLE 2.1</b> Values and Uncertainties in Primary Measurements			
	Value	Uncertainty	% Uncertainty
<b>Equipment Variables</b>			
Tube Radius ( $R$ )	0,0126 m	0,00025 m	2,0
Tube Length ( $L$ )	3,0 m	0,005 m	0,2
<b>Permeate Flow Measurements</b>			
Volume of permeate collected ( $V_{perm}$ )	2,0 $\ell$	0,02 $\ell$	1,0
Time to collect permeate ( $t_{perm}$ )	range 20 s to 80 s	0,4 seconds	range 0,6 to 2,0
<b>Operating Variables</b>			
Suspension Flowrate ( $Q$ )	range 1500 $\ell/h$ to 3500 $\ell/h$	50 $\ell/h$	range 1,4 to 3,3
Pressure ( $P$ )	range 100 kPa to 300 kPa	3 kPa	range 1,0 to 3,0
Bulk Concentration ( $C_b^*$ )	range 10 g/ $\ell$ to 80 g/ $\ell$	1 g/ $\ell$	range 1,3 to 10,0

## 2.4.2 Calculation of Permeate Flux and Superficial Inlet Velocity

### 2.4.2.1 Permeate flux

$$\begin{aligned}
 J_w \text{ (l/m}^2\text{h)} &= \frac{\text{permeate flowrate}}{\text{area}} \frac{3\ 600}{1} \frac{(\text{l/s})}{(\text{m}^2)} \left( \frac{\text{s}}{\text{h}} \right) \quad (2.1) \\
 &= \frac{V_{perm}}{t_{perm}} \frac{1}{2\pi RL} \frac{3\ 600}{1} \\
 &= \frac{2.0}{t_{perm}} \frac{1}{\pi(0.0252)(3.0)} \frac{3\ 600}{1} \\
 &= \frac{30\ 315.2}{t_{perm}}
 \end{aligned}$$

### 2.4.2.2 Superficial Inlet Velocity

$$\begin{aligned}
 \bar{U}_s \text{ (m/s)} &= \frac{\text{feed flowrate}}{\text{flow area}} \frac{1}{3\ 600} \frac{1}{1\ 000} \frac{(\text{l/h})(\text{h})}{(\text{m}^2)} \left( \frac{\text{m}^3}{\text{l}} \right) \quad (2.2) \\
 &= \frac{Q}{\pi R^2} \frac{1}{3\ 600\ 000} \\
 &= \frac{Q}{\pi(0.0126)^2} \frac{1}{3\ 600\ 000} \\
 &= \frac{Q}{1\ 795.5}
 \end{aligned}$$

## 2.4.3 Error Analysis

Let  $\Omega(F) = \% \text{ uncertainty in the measured quantity } F$

### 2.4.3.1 Uncertainty in Permeate Flux

$$\begin{aligned}
 \Omega(J_w) &= \max[\Omega(\text{permeate flowrate}); \Omega(\text{filtration area})] \\
 &= \max[\Omega(V_{perm}); \Omega(t_{perm}); \Omega(R); \Omega(L)] \\
 &= \max[1 : 2 : 1.98 : 0.17] \\
 &= 2.0\%
 \end{aligned}$$

### 2.4.3.2 Uncertainty in Superficial Inlet Velocity

$$\begin{aligned}
 \Omega(\bar{U}_s) &= \max[\Omega(\text{feed flowrate}); \Omega(\text{flow area})] \\
 &= \max[\Omega(Q); 2\Omega(R)] \\
 &= \max[3.3 : 4.0] \\
 &= 4.0\%
 \end{aligned}$$

### 2.4.3.3 Errors in Flux-Time Curves

There are two sources of errors inherent in the flux-time curves reported in Sections 2.5.1 to 2.5.3 :

- (i) Uncertainty in the flux value (see Section 2.4.3.1)
- (ii) Uncertainty in the time at which the flux is plotted - Assume that at time  $t$  after start-up a period  $t_{perm}$  was required for the permeate to fill the graduated cylinder. The flux so calculated has been plotted at time  $t$ , rather than the *mean* time of  $t + (t_{perm}/2)$ . The uncertainty in the time is thus  $\pm (t_{perm}/2)$ .

A typical flux-time, with an error envelope representing the uncertainty, is presented in Figure 2.2. It is seen that the uncertainties are insignificant when compared to the point values. For clarity, error envelopes have been excluded from subsequent presentations of flux-time curves.

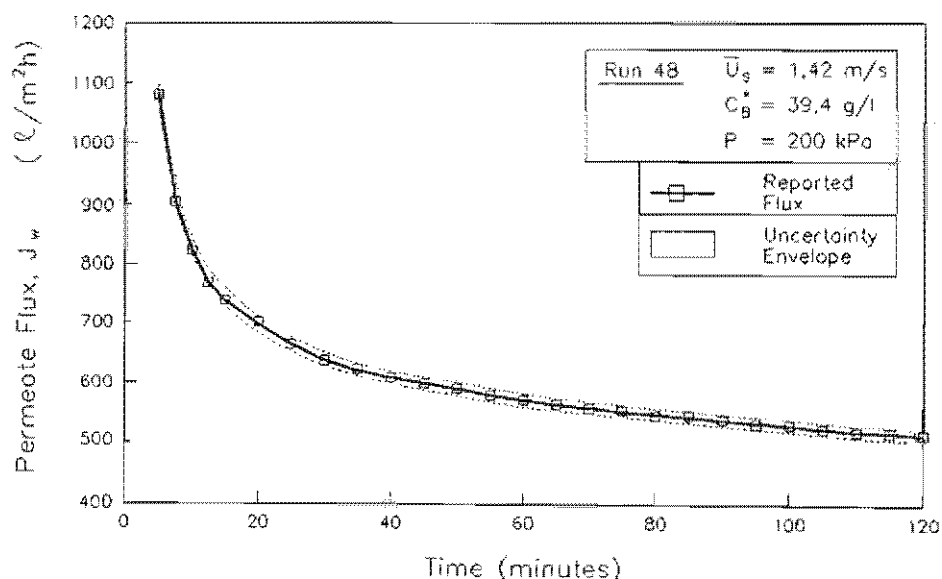


**FIGURE 2.2** Typical Uncertainties in Measured Flux Values

#### 2.4.3.4 Errors in Flux vs Operating Variables Curves

There are two inherent errors in reported curves depicting the effects of operating variables on flux :

- (a) Uncertainty in the flux value (see Section 2.4.3.1)
- (b) Uncertainty in the value of the operating velocity, pressure or concentration (see Table 2.1)

Once again, the errors are small in comparison to the point values. In any event, if error bars were employed they would be of similar size to the symbols used to represent the experimental datapoints (see e.g. Figure 2.11). In effect, the experimental errors may be inferred from the symbols used to depict the experimental datapoints, and hence error bars have been excluded from all graphs depicting the effects of inlet velocity, bulk concentration and pressure on the steady-state flux.

#### 2.4.3.5 Repeatability

Flux-time curves obtained in separate experiments conducted at similar operating conditions are depicted in Figure 2.3. Repeatability is good. However, good repeatability is subject to the feed suspensions being made up from the same batch of limestone (see Section 2.3.1).

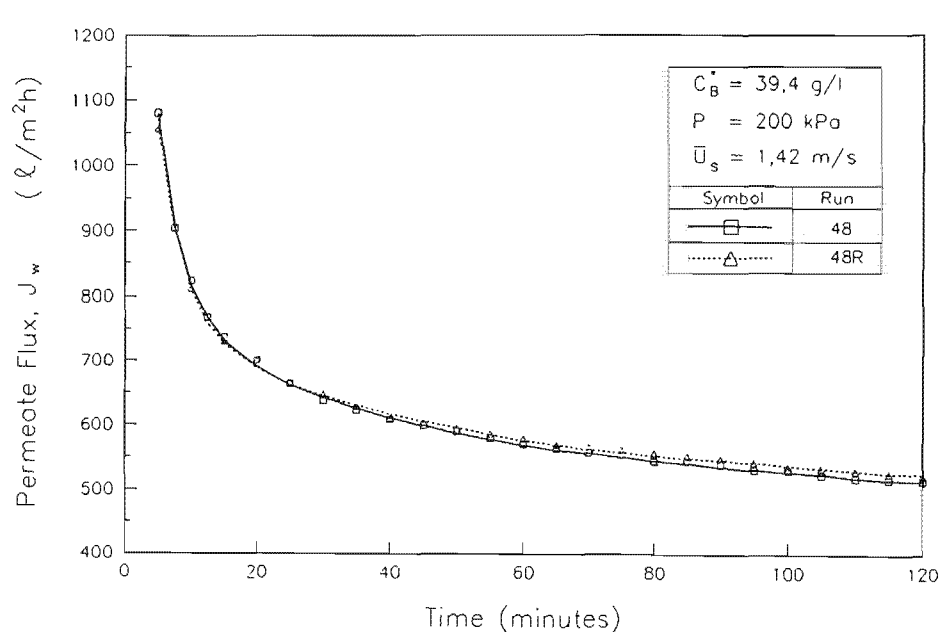


**FIGURE 2.3**      Typical Repeatability in Flux Measurements

## 2.5 RESULTS

### 2.5.1 Flux-Time Behaviour

A typical flux-time curve is presented in Figure 2.4. Consistent with previously reported trends [Baker et al. (1985), Knibbs (1981), Hunt (1987b), Saw et al. (1985), Le (1987)], the flux,  $J_w$ , exhibits an initial rapid decrease followed by a slow, almost linear decrease with time. This long-term slow decline is a feature of all results obtained in this study, and no true steady-state fluxes were obtained. In the rest of this study, the initial period of rapid flux decline will be referred to as *Period I*, and the subsequent slow decline period as *Period II*. The basis for the boundary between the periods is outlined at the end of Section 2.5.1.

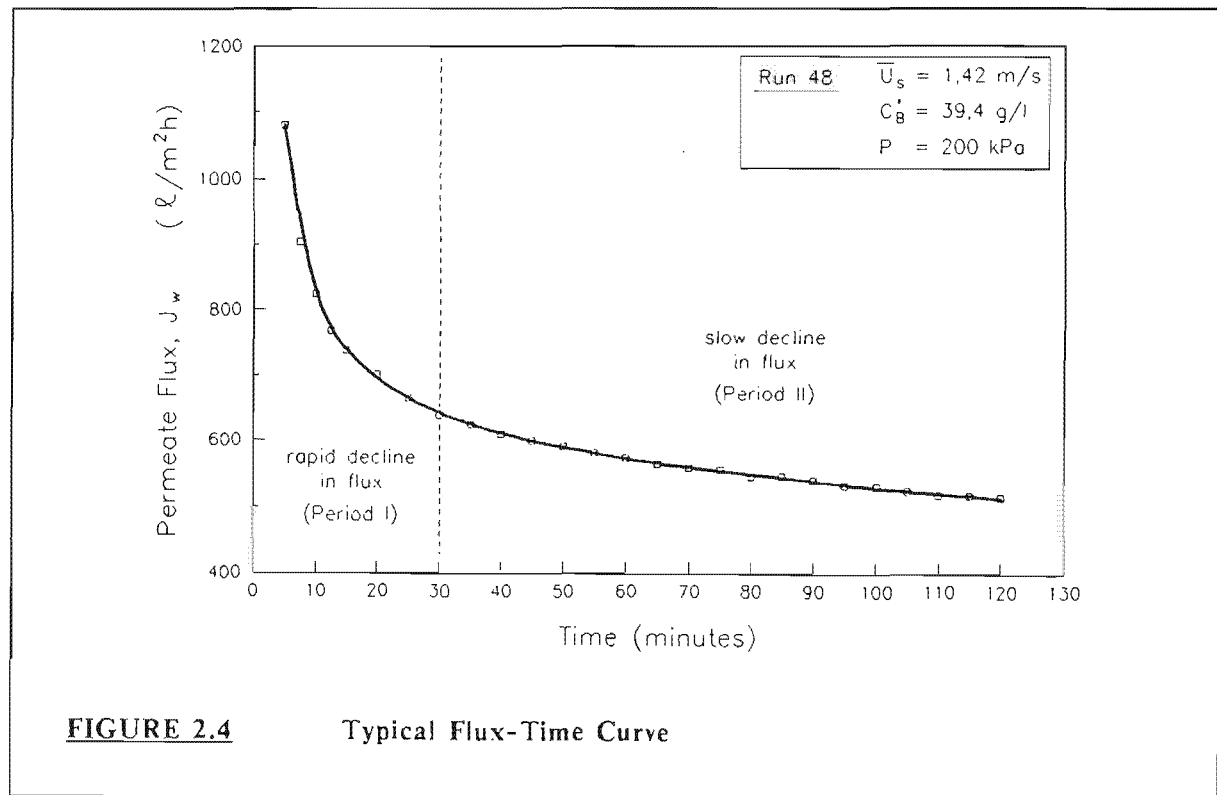


**FIGURE 2.4** Typical Flux-Time Curve

On a log-log scale, the flux-time response typically exhibits a behaviour as in Figure 2.5. After an initial highly negative value ( $\approx -0.47$ ), the gradient progressively increases and the curve eventually becomes almost linear, with a gradient of  $\approx -0.14$ , after about 35 minutes. This is in contrast to previous studies where log flux vs log time plots yielded fully linear curves [Dalheimer et al. (1970), Krause (1974)]. For a true steady-state, the log flux-log time curve will yield a slope of 0, and for ideal deposition, where the mass of cake deposited is proportional to the flux (e.g. dead-end filtration), the slope would asymptote to a slope of -0.5 [Krause (1974)]. Figure 2.5 clearly confirms that in CFMF systems cake growth becomes progressively less dependent on the permeate flux, and hence the flux declines at a slower rate than in dead-end filtration.

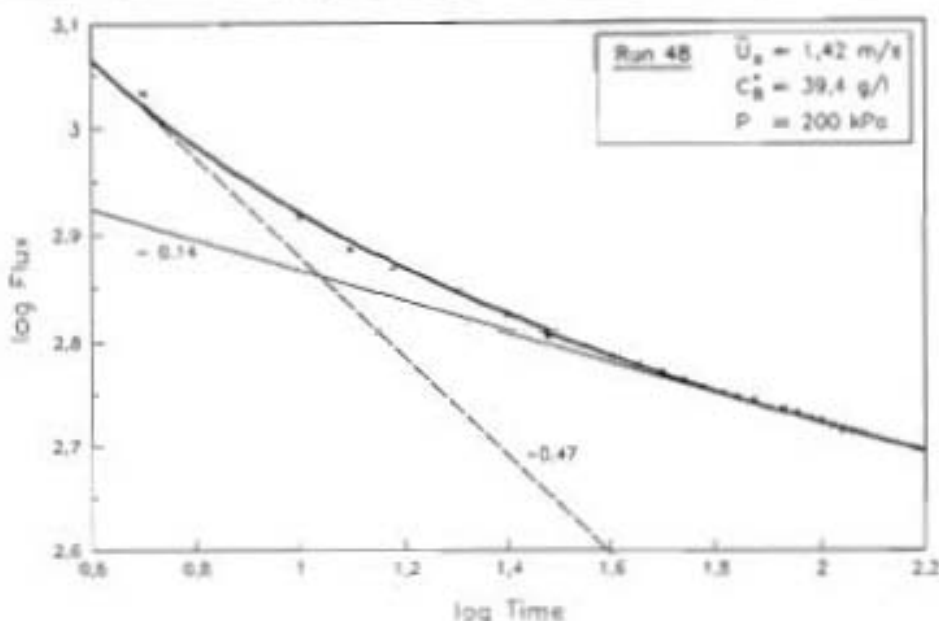


**FIGURE 2.5**      **Typical Flux-Time Curve (log-log scale)**

Since the driving force for permeate flow, i.e. the pressure drop across the tube wall, remained constant, a decrease in permeate flux indicates an increase in the hydraulic resistance to flow. In the system studied here, the controlling hydraulic resistance is the cake of solids that forms on the tube wall (see Section 2.2.3). A decrease in flux is thus due to either a growth of the cake or a change in the cake characteristics leading to a cake of lower permeability. Changes in cake characteristics may include compression and consolidation of the cake, infiltration of finer particles (*fines*) into the cake, or chemical changes within the cake.

It is generally accepted that the initial rapid decline in flux is caused by rapid cake growth. Studies in which the mass of deposited cake was monitored with time confirm this [Baker et al. (1985)]. An increase in cake mass could be due to an increase in cake thickness, and/or the formation of a more compressed, denser cake. Qualitative monitoring of the cake using an ultrasonic imaging device indicated that during the period of rapid decline in flux, the cake thickness increased rapidly and substantially (see Section 2.3.3). It is thus most likely that for the system under study, the decline of flux in Period I is due to an increase in cake thickness.

The subsequent slow decline of flux (Period II) could be due to a further, slow increase in cake thickness, or a change in cake characteristics. The study of Baker et al. (1985) indicated that the long term decline of flux is most probably due to a change in cake characteristics. In that study, the mass and particle size distribution of the cake was monitored with time. For the first 20 to 25 minutes the decrease in flux is strongly correlated with a simultaneous increase in cake mass. Thereafter, the cake mass remained approximately constant but the flux continued

to decline. The average particle size in the cake, however, progressively decreased with time. There is thus a strong indication that the long term decline in flux in that system was most probably due to preferential deposition of finer particles into the cake, leading to a cake of progressively decreasing permeability. In a later paper, Hoogland et al. (1988) found that the cake mass actually decreased with time, while the particle size also decreased. This further militates against cake growth being the cause of flux decline in Period II.

Accepting that cake growth is not the cause of the slow flux decline in Period II, the task then resolves to determining which of the following processes is responsible for flux decline in Period II for the system under study - slow compression, chemical changes within the cake or fines infiltration.

In the present study, the capturing of the cake was not feasible, and hence any change in average cake particle size with time could not be monitored. There is however strong alternate experimental evidence that the slow decline in flux in Period II is NOT due to chemical changes within the cake or slow compression of the cake, for the system under study. The experiment yielding this inference is described below.

The system was started up at a superficial inlet velocity ( $\bar{U}_s$ ) of 1.42 m/s, pressure ( $P$ ) of 200 kPa, and bulk concentration ( $C_b^*$ ) of 77.6 g/l, and the flux-time behaviour was monitored. This flux-time curve was highly repeatable. Thereafter, the system was started up as above, but the feed was switched to a second tank containing RO permeate ( $C_b^* = 0$  g/l) after 60 minutes. The resultant flux-time curves are shown in Figure 2.6.

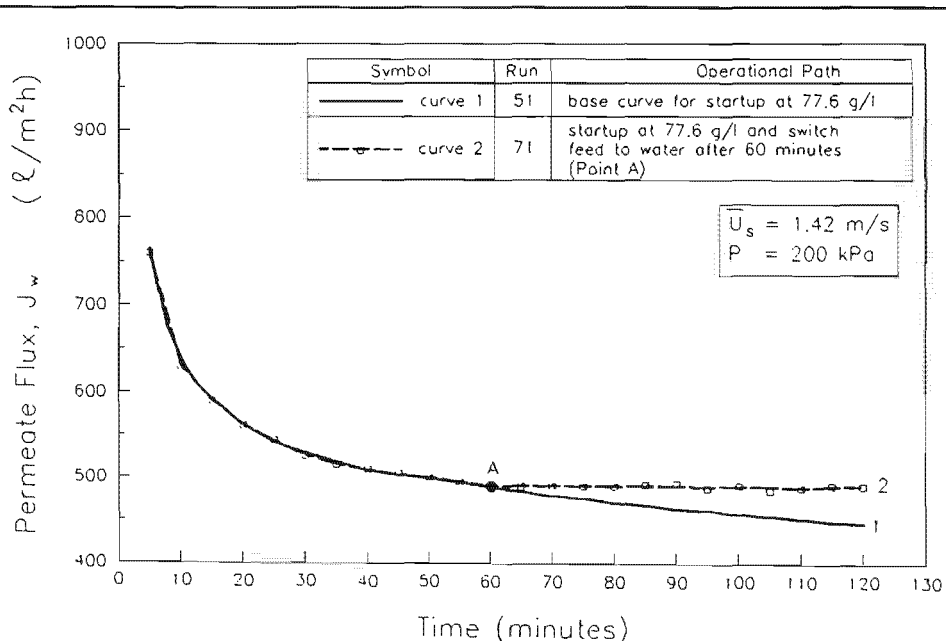


**FIGURE 2.6** Flux-Time Curve Obtained on Switching Feed Stream to Water

Curve 1 represents the (repeatable) flux-time curve obtained for the limestone suspension. Curve 2 represents the flux-time curve obtained by starting up on the suspension and then subsequently switching the feed to water.

On switching to water, the flux remains constant, and shows no noticeable decline. If the flux decline in Period II was due to slow compression or chemical activity within the cake, this decline would have continued on switching to water. If however the decline was due to finer particles from the suspension progressively infiltrating the cake, the decline would be arrested on switching the feed to water. On the basis of the above argument, Figure 2.6 indicates that the flux decline in Period II is most probably due to fines infiltration into the cake, for the system under study. (It is recognised that Figure 2.6 indicates other interesting aspects of system behaviour. This is discussed in detail in Section 2.5.3.2.)

In summary, there are strong indications that the controlling processes responsible for flux-time behaviour in the system under study are as follows :-

- The initial rapid decrease in flux is caused by an initial rapid increase in cake thickness.
- Thereafter the cake thickness remains relatively constant, but the cake is progressively infiltrated by finer particles resulting in a slow decrease in permeability, and hence the slow long term decline in flux.

It will be shown that the assumption that flux decline in Period II is caused by fines infiltration yields viable explanations for various "anomalies" that were observed in the experimental study.

The expected cake thickness profile will thus be as depicted in Figure 2.7. In the rest of this study, the maximum cake thickness i.e. that obtained at the end of Period I, will be referred to as the *steady-state* cake thickness, and the corresponding flux the *steady-state* flux.

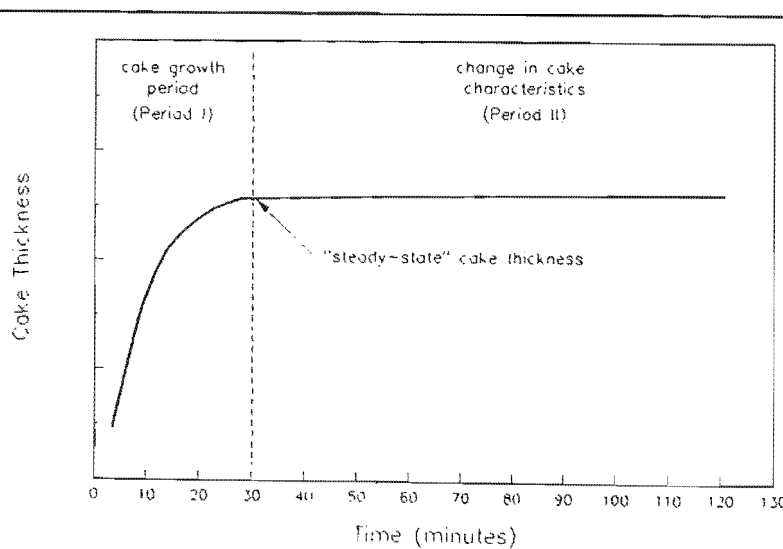


**FIGURE 2.7**

Expected Cake Thickness profile

The basis for the boundary between Periods I and II may now be outlined. The gradient of the flux-time curve indicates the rate of decline of flux, or alternatively, the rate of increase in resistance to permeate flow. It is expected that when cake growth becomes insignificant, and fines infiltration the dominant cause of increases in resistance, a significant change in the gradient of the flux-time curve would be observed. A typical  $[\partial J_w / \partial t] \text{ vs } t$  profile is shown in Figure 2.8. The curve was obtained by fitting an equation of the form :-

$$J_w = k_1 t^{\left( k_2 t + k_3 t^2 + \frac{k_4}{t} - \frac{k_5}{t^2} + \frac{k_6}{t^3} \right)} \quad . \quad (2.3)$$

to the experimental flux-time data, and numerically differentiating the curve ( $J_w$  is the flux at time  $t$  and  $k_i$  to  $k_6$  are regression constants).

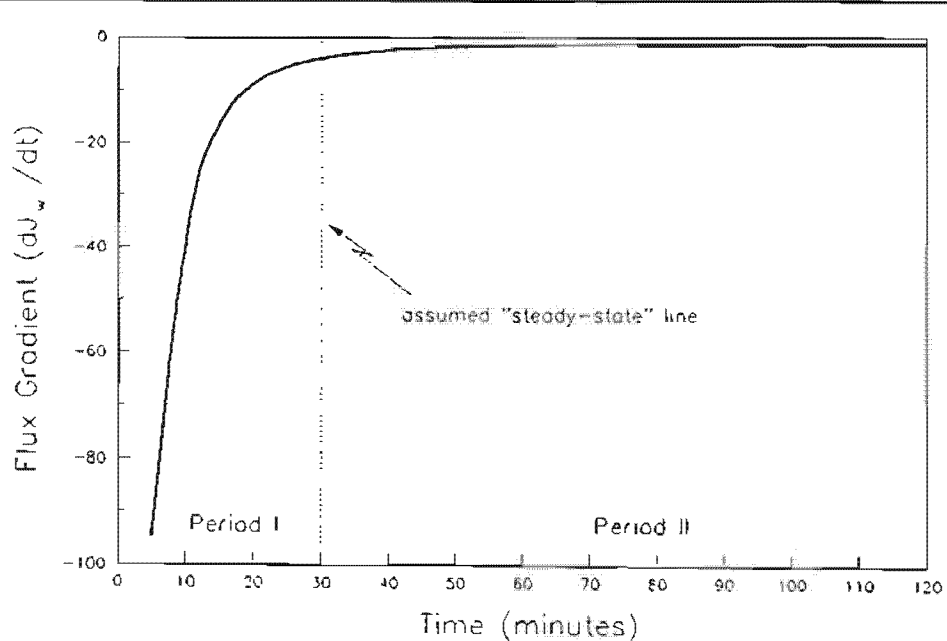


**FIGURE 2.8**      **Typical Flux Gradient Profile**

The gradient changes substantially over the period  $t < 30$  minutes, and then remains approximately constant. On this basis, the flux at 30 minutes was designated the approximate steady-state flux, and thus the approximate boundary between Periods I and II. For the experiments reported here, this steady-state point varied from  $\approx 25$  minutes to  $\approx 32$  minutes. For convenience, all steady-state values are reported at  $t = 30$  minutes.

### 2.5.2 Effects of Operating Variables on Flux

The objective here is to determine the trends that flux-time behaviour and the steady-state flux exhibit with respect to the superficial inlet velocity ( $\bar{U}_s$ ), bulk concentration ( $C_b^*$ ) and pressure ( $P$ ).

For all results presented in Sections 2.5.2.1 to 2.5.2.3, the system was started up at the specified operating conditions, with a strong emphasis being placed on reading the operating point as soon as possible. Following the start-up procedure outlined in Section 2.3.2, the operating point was generally reached within 30 seconds. The significance of this emphasis on start-up procedure will become apparent in Section 2.5.3.

#### 2.5.2.1 Effect of Superficial Inlet Velocity on Flux

The effect of superficial inlet velocity,  $\bar{U}_s$ , on flux-time behaviour is depicted in Figure 2.9 (linear scale) and in Figure 2.10 (log-log scale). All experiments were performed at the same pressure, concentration and temperature with only the inlet velocity varying. Consistent with previous studies [Dalheimer et al. (1970), Schulz and Ripperger (1989), Rautenbach and Schock (1988), Saw et al. (1985)], the flux increases with, and is highly sensitive to, inlet velocity. Of interest is the observation that the flux-time curves in Period II are all substantially parallel. On a log-log scale, the gradient appears to be a function of velocity up to  $t = 35$  minutes, whereafter all gradients are substantially the same. This is somewhat different from the results obtained by Dalheimer et al. (1970), where the log flux vs log time curves were wholly linear and the gradient was independent of velocity.

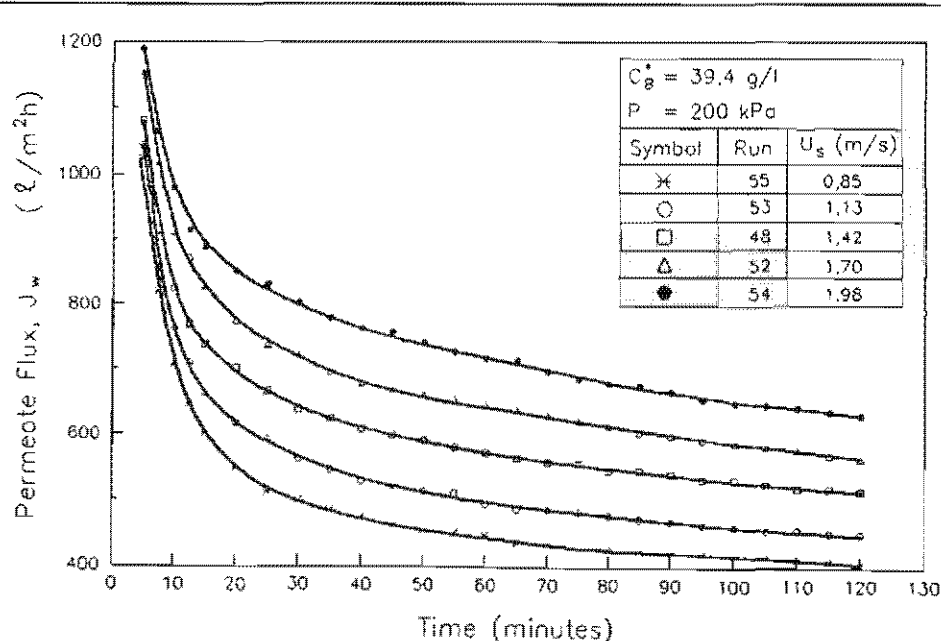


**FIGURE 2.9**      **Effect of Inlet Velocity on Flux-Time Behaviour**

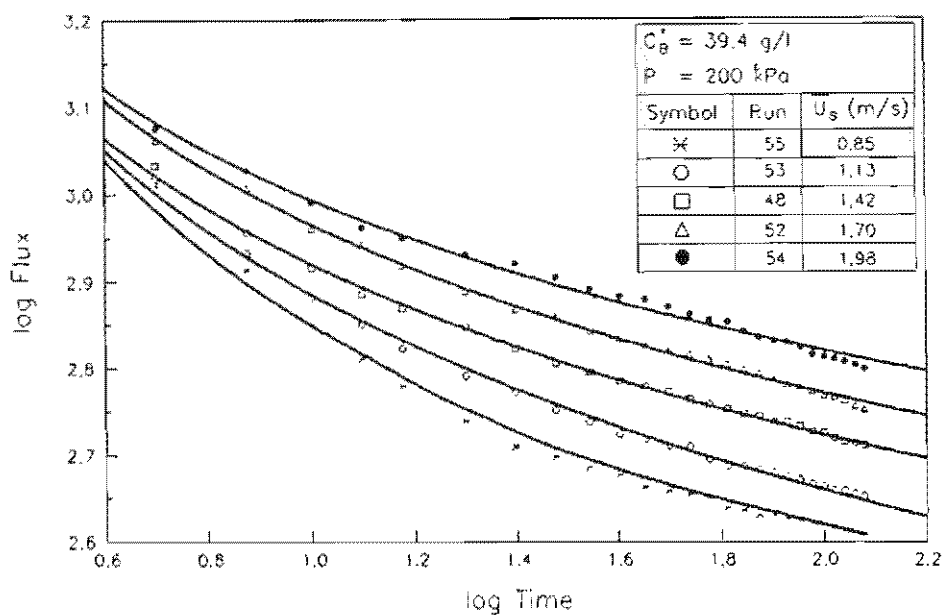


**FIGURE 2.10** Effect of Inlet Velocity on Flux-Time Behaviour  
(log-log scale)

The effect of inlet velocity on the steady-state flux, chosen at  $t = 30$  minutes, is shown in Figure 2.11.

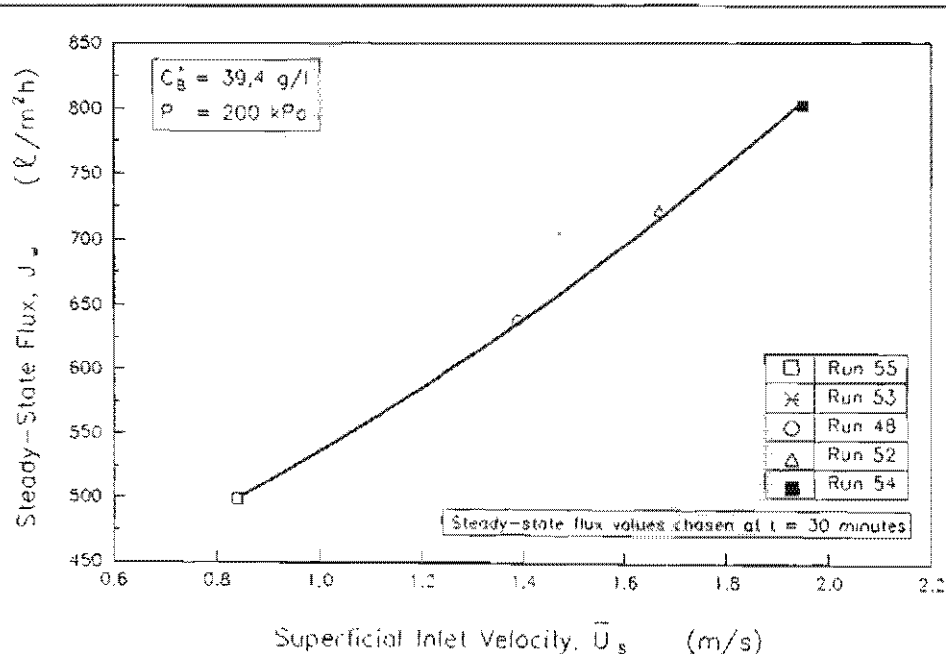


**FIGURE 2.11** Effect of Inlet Velocity on Steady-State Flux

The flux shows a progressively greater dependence on velocity as velocity increases, and may be represented by :-

$$J_w \propto \bar{U}_s^{1.1} \quad (2.4)$$

There is general consensus in the literature that the steady-state flux increases with increasing inlet velocity, although reported values for the exponents in equation 2.4 vary. In general exponents are greater than 1 [Dalheimer et al. (1970) and Schulz and Ripperger (1987) :-  $J_w \propto \bar{U}_s^{1.0}$ , Rautenbach and Schock (1988) :-  $J_w \propto \bar{U}_s^{1.2}$ ], but Baker et al. (1985) obtained exponents less than 1.

From Figure 2.11, the trend that steady-state flux exhibits with inlet velocity may be represented as :-

$$\left( \frac{\partial J_w}{\partial \bar{U}_s} \right) > 0 \quad (2.5)$$

$$\left( \frac{\partial^2 J_w}{\partial \bar{U}_s^2} \right) > 0 \quad (2.6)$$

### 2.5.2.2 Effect of Bulk Concentration on Flux

The effect of bulk concentration,  $C_B$ , on flux-time behaviour is depicted in Figure 2.12 (linear scale) and Figure 2.13 (log-log scale). Here, runs were performed at the same inlet velocity, pressure and temperature, with only the concentration varying.

A significant dependence on concentration is exhibited. Once again, the flux curves in Period II are substantially parallel. A further interesting observation concerns the rate of growth of cake. For the highest concentration, it would seem that most of the cake has already been deposited before the first flux measurement at 5 minutes after start-up. Thereafter, the curve shows a slow decline and reaches the steady-state after  $\approx 20$  to 25 minutes. For the lowest concentration it is apparent that very little cake has been deposited during the first 5 minutes. Thereafter the flux shows a substantial decline and eventually reaches its steady-state after  $\approx 35$  minutes. There are thus indications that the rate of cake growth on start-up is a strong function of concentration.

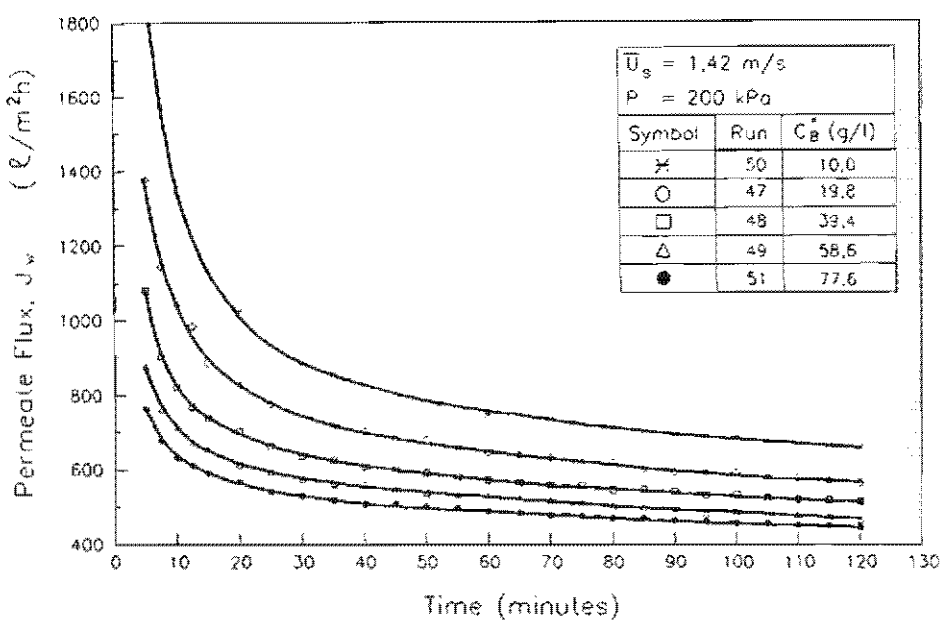


**FIGURE 2.12** Effect of Bulk Concentration on Flux-Time Behaviour

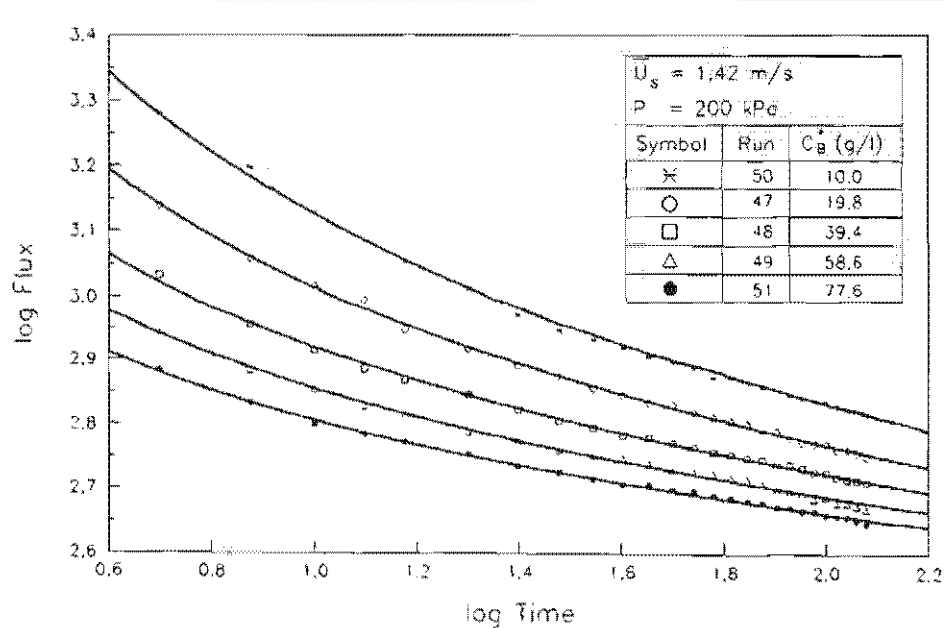


**FIGURE 2.13** Effect of Bulk Concentration on Flux-Time Behaviour (log-log scale)

The effect of bulk concentration on the steady-state flux is shown in Figure 2.14. Although the curves in Figure 2.12 apparently reach the steady-state at around 25 minutes from start-up, it can be seen that very little error in trends or values results from choosing steady-state fluxes at 30 minutes from start-up.

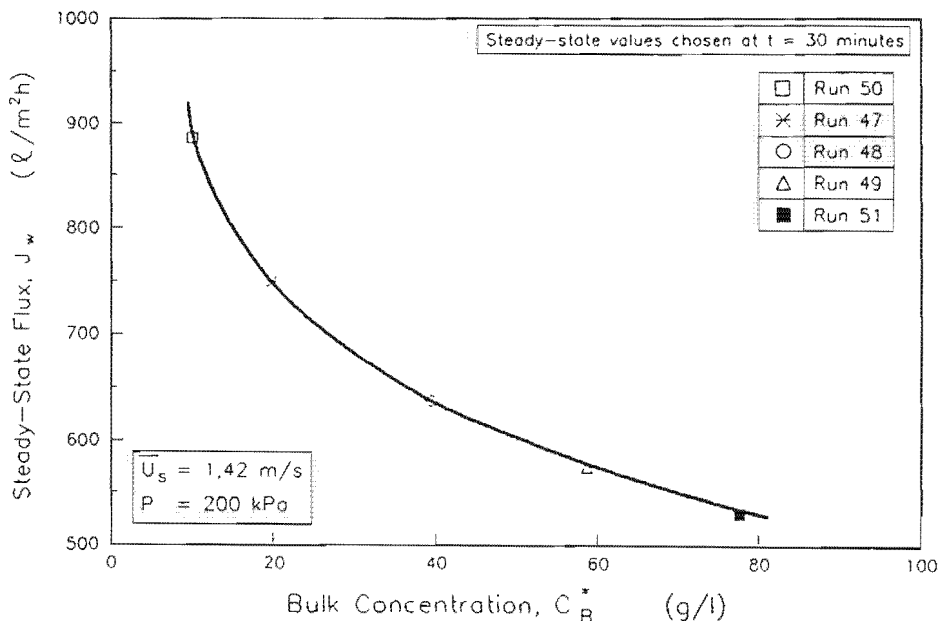


**FIGURE 2.14** Effect of Bulk Concentration on Steady-State Flux

A plot of steady-state flux vs log concentration yields a linear curve (Figure 2.15), indicative of a convection-diffusion controlled process (see Section 3.2.2).

There appears to be little consistency in the literature regarding the trend that steady-state flux exhibits with concentration. Hunt et al. (1987b) obtained trends similar to Figure 2.14. Saw et al. (1985) and Bertera et al. (1984) observed that flux decreased linearly with the log of the concentration, while Rautenbach and Schock (1988) observed a linear decrease of flux with concentration. Further, Dahlheimer et al. (1970) observed that flux was relatively insensitive to concentration, while Le (1987) found a non-linear relationship between flux and log concentration.

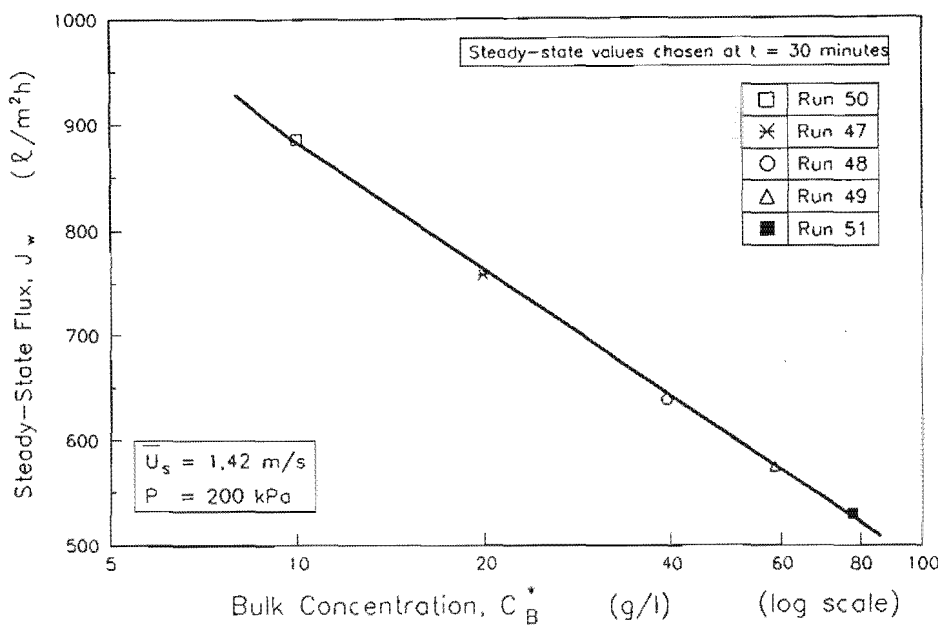


**FIGURE 2.15** Effect of Bulk Concentration on Steady-State Flux  
(concentration in log scale)

For the system under study, the flux exhibits a strong, but progressively decreasing dependence on concentration which may be represented as :-

$$\left( \frac{\partial J_w}{\partial C_B^*} \right) < 0 \quad (2.7)$$

$$\left( \frac{\partial^2 J_w}{\partial C_B^{*2}} \right) > 0 \quad (2.8)$$

#### 2.5.2.3 Effect of Pressure on Flux

The effect of pressure,  $P$ , on flux-time behaviour is shown in Figure 2.16 (linear scale) and in Figure 2.17 (log-log scale). Here, the inlet velocity and bulk concentration were held constant for all runs, while the pressure was changed. Similar to the flux-time responses obtained at different concentrations and velocities, the curves are substantially parallel in Period II.

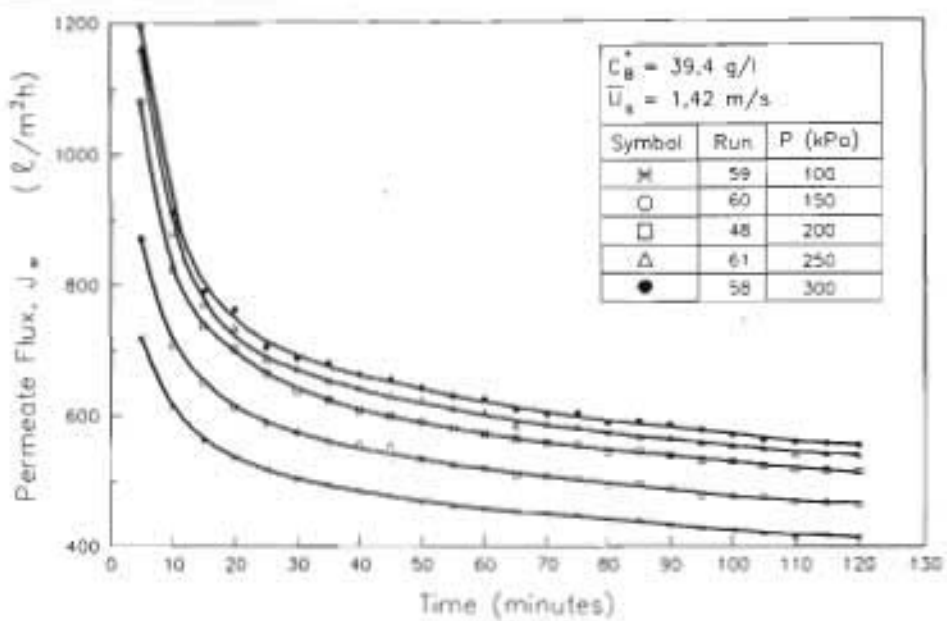


**FIGURE 2.16** Effect of Pressure on Flux-Time Behaviour

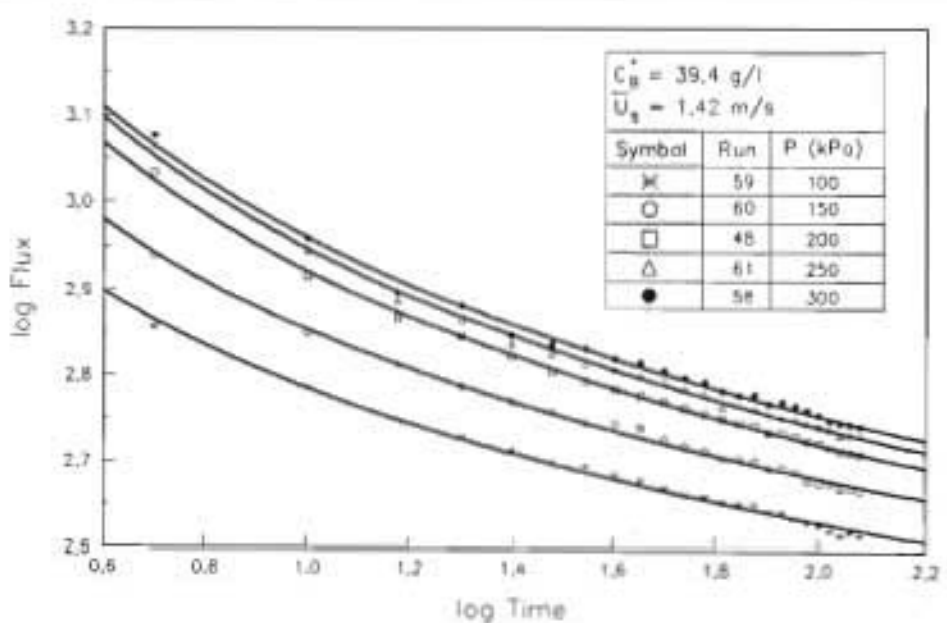


**FIGURE 2.17** Effect of Pressure on Flux-Time Behaviour  
(log-log scale)

The effect of pressure on steady-state flux is shown in Figure 2.18. The steady-state flux increases with pressure but shows a progressively decreasing dependence on it.

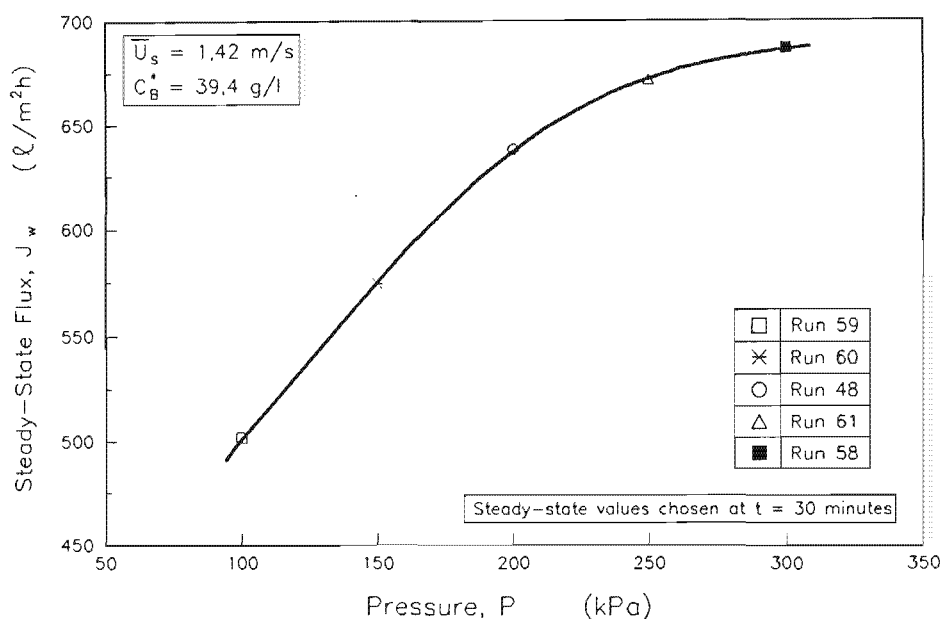


**FIGURE 2.18** Effect of Pressure on Steady-State Flux

Reported trends for the flux-pressure relationship also vary widely. Rautenbach and Schock (1988) found that flux was independent of pressure, above a pressure of 100 kPa. Saw et al. (1985) and Le (1987) noted that the flux actually decreased at high pressures, presumably caused by compression and compaction effects. Harrison et al. (1981) observed a local minimum on the flux vs pressure curve. The trends observed by Henry (1972) are similar to Figure 2.18 i.e.,

$$\left( \frac{\partial J_w}{\partial P} \right) > 0 \quad (2.9)$$

$$\left( \frac{\partial^2 J_w}{\partial P^2} \right) < 0 \quad (2.10)$$

### 2.5.3 Operational Path Dependence of Flux-time Behaviour

There are indications in the literature that the flux-time behaviour may not be a unique function of the operating variables but may also be a function of the operational path taken to reach the operating point. Harrison et al. (1981), for example, noted that the flux obtained by starting up a system at a lower velocity and then increasing the velocity is not as high as that obtained when the system is started-up at the higher velocity.

This section (2.5.3) entails an investigation into the operational path dependence of the flux-time curve. In Section 2.5.2, the system was rapidly taken up to the operating point on start-up. Effectively then the system experiences a step change up to the operating point at time zero ( $t = 0$ ). The flux-time responses obtained by starting up at the desired operating points will hereafter be referred to as the *base curves*. In this section the system is started up at conditions below (and above) the operating point and step-increased (or step-decreased) to the desired operation point after some finite time has elapsed. The flux-time responses are then compared to the base curves.

#### 2.5.3.1 Dependence of Flux-Time Behaviour on Path to Reach Operating Velocity

The system was started up at  $\bar{U}_s = 1,13$  m/s,  $P = 200$  kPa,  $C_s^* = 39,4$  g/ $\ell$ , allowed to run for 10 minutes and the inlet velocity was then rapidly increased to 1,70 m/s, while keeping the pressure constant. The experiment was then repeated, but allowing a run time of 60 minutes before the step-increase. These specific time lapses were chosen in order to assess if system response would differ depending on whether the step-change is performed in Period I or Period II. These flux-time curves are contrasted to the high and low velocity base curves in Figure 2.19.

Curves 1 and 2 represent the base curves (the data points for the base curves have been excluded for clarity). Curves 3 and 4 represent system responses obtained by step-increasing the velocity after 10 and 60 minutes, the step-increases occurring at points A and B respectively. Curve 4 is coincident with curve 1 for most points but they may be differentiated by noting that curve 1 is a solid line while curve 4 is a dashed curve with data points included.

If the flux-time behaviour were not dependent on the operating path then it would be expected that on increasing the inlet velocity at points A or B, the flux would rapidly increase to the corresponding values on curve 2, and then follow that curve substantially. On increasing the velocity during the cake growth period (point A), the flux declines at a slower rate and then follows curve 2 approximately. On increasing the velocity at point B however, the flux continues to follow the low velocity base curve. Clearly, starting up the system at the lower velocity and then increasing the velocity yields a different flux-time response from that obtained if the system is started up at the higher velocity.

The cake thicknesses at points A and B are greater than the corresponding cake thicknesses at points C and D, by inference from the flux values at those points. In order for the flux to increase in response to the velocity increases at points A and B therefore, the cake thicknesses

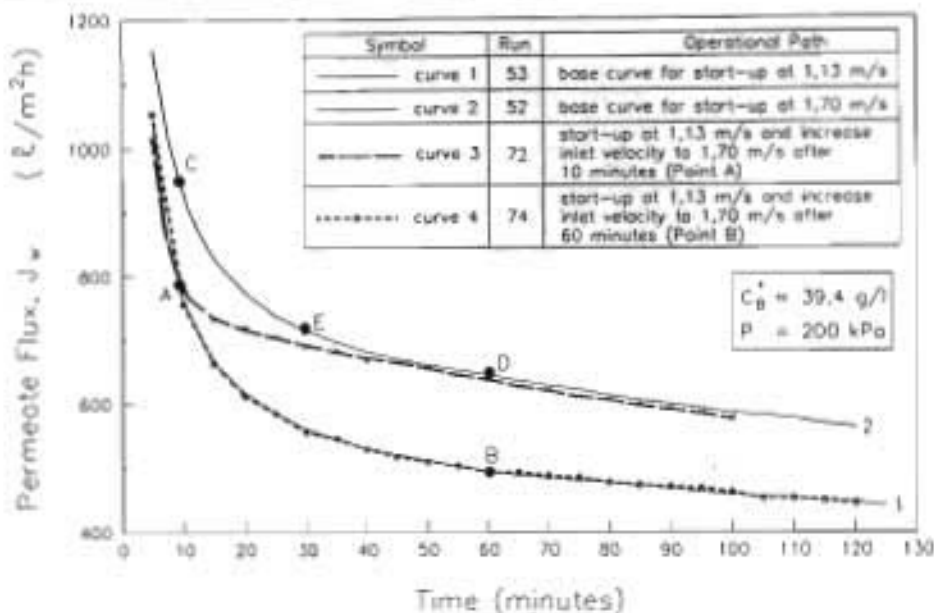


**FIGURE 2.19** System Responses to Step-Increases in Velocity

must decrease. The observed flux response indicates that the cake thickness did not decrease, possibly implying that the cake formation is irreversible. The observation that curve 3 did eventually follow curve 2 closely can be explained by noting that the cake thickness at point A is lower than the steady-state cake thickness for curve 2, point E. Thus, in response to the flowrate increase at point A the cake merely grew at a slower rate and did eventually become limited at the appropriate steady-state value for the higher flowrate.

There are strong indications therefore that the system will not respond to a velocity change requiring a decrease in cake thickness, but will respond to one requiring an increase in cake thickness.

System responses to a step-decrease in velocity are shown in Figure 2.20. Here, the system was started up at  $\bar{U}_s = 1.70 \text{ m/s}$ ,  $P = 200 \text{ kPa}$ ,  $C_B^+ = 39.4 \text{ g/L}$ , and the velocity was reduced to  $1.13 \text{ m/s}$  after time lapses of 10 and 60 minutes.

When the step-decrease is performed in Period I, the flux decreases rapidly and then follows the low velocity base curve. By inference, the cake thickness increases and then follows the cake growth profile of the low velocity base curve. When the step-decrease is performed in Period II, the flux once again decreases, but levels off at a value somewhat lower than the low velocity base curve. By inference, the final cake resistance is somewhat higher than that of the low velocity base curve at that time. Clearly, the system does respond to a velocity change requiring an increase in the cake thickness, but the response differs depending on whether the change is performed during the cake growth period or the change in cake characteristics period.

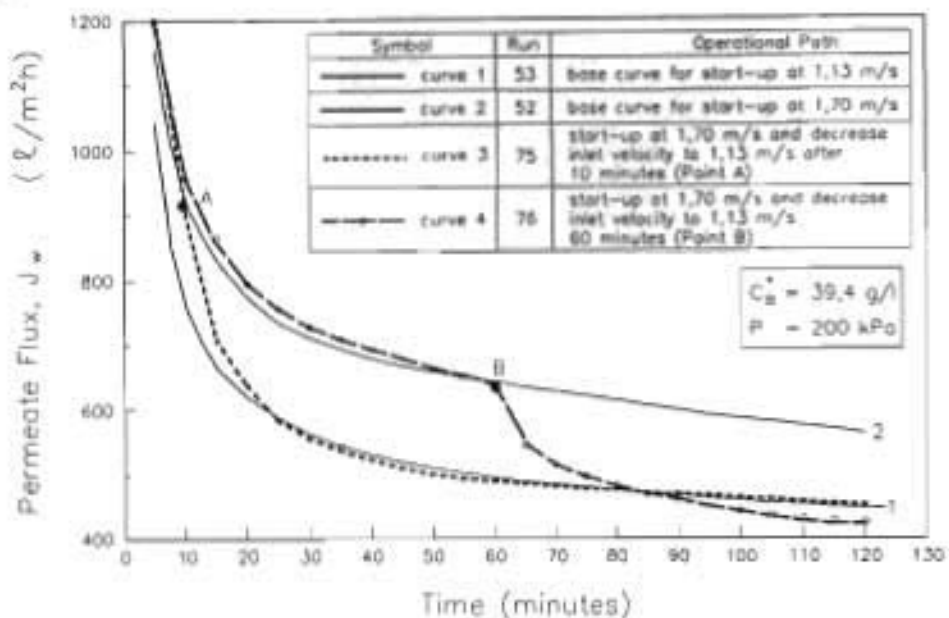


**FIGURE 2.20 System Responses to Step-Decreases In Velocity**

In Section 2.2.2 it was stated that feed samples were obtained directly from the well-mixed feed tank, and not from any sample point upstream of the tube. The reason for this is clear in the light of the above discussion. If a sample valve upstream of the tube is opened, there will be an immediate disturbance to the velocity and pressure in the tube. This disturbance could irreversibly change the flux-time behaviour of the system.

#### 2.5.3.2 Dependence of Flux-Time Behaviour on Path to Reach Operating Concentration

System response to a step-decrease in concentration was ascertained by starting up the system at  $P = 200 \text{ kPa}$ ,  $\bar{U} = 1.42 \text{ m/s}$ ,  $C_s^* = 77.6 \text{ g/l}$ , and then switching the feed to water ( $C_s^* = 0 \text{ g/l}$ ) after periods of 10 and 60 minutes, while keeping the velocity and pressure constant (Figure 2.21).

If the cake formation was fully reversible, the cake thickness would have progressively decreased on switching over to water, until the pure water flux was reached. Figure 2.26 clearly indicates that the hydraulic resistance did not change appreciably, indicating conclusively that the cake formation was irreversible. The probability that the cake was removed and that the hydraulic resistance was being provided by particles within the pores of the tube wall may be discounted since on cleaning the tube it was confirmed that a substantial cake still existed in the tube.

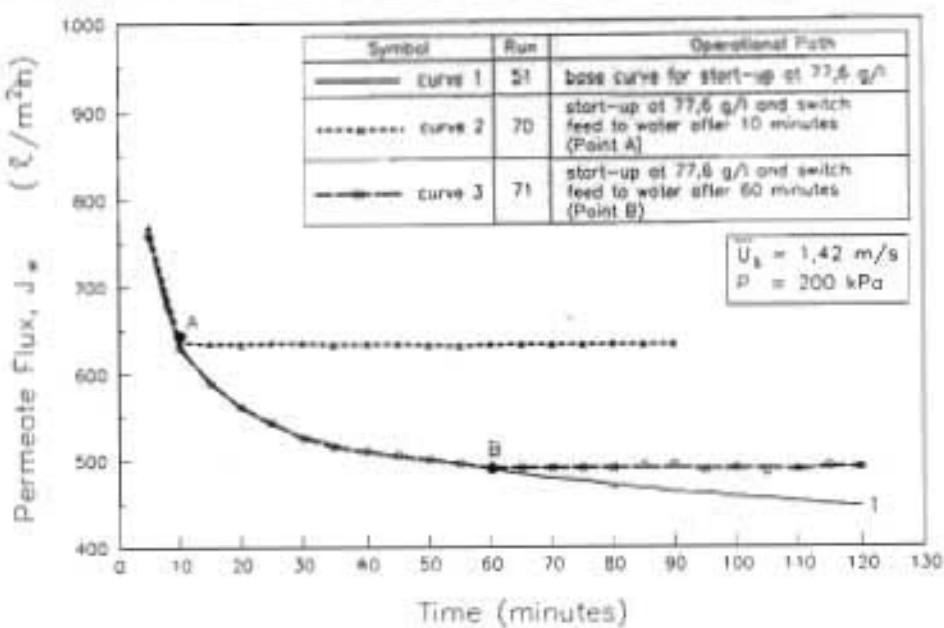


**FIGURE 2.21 System Responses to Step-Decreases in Bulk Concentration**

The observation that the cake is irreversible is not unique. Rushton et al. (1979), in an earlier study also observed that on pumping water over a cake, some critical shear needs to be exceeded before particle removal will occur. Krause (1974) notes that many filter cakes once formed are not easily removed. Further, Baker et al. (1985) have noted that in some of their experiments, the cake was sufficiently cohesive to remain on the tube wall until backwashed.

Monitoring the turbidity of the reject stream in the view-glass during the course of the above experiment led to some interesting qualitative observations. On switching the feed to water the turbidity progressively decreased, and the reject stream was clear to the eye after about 4 minutes. At the conclusion of the above experiment, the inlet velocity was progressively step-increased in steps of approximately 0.28 m/s, with water as the feed stream, while maintaining the pressure constant. With each step in velocity, a "puff" of slightly turbid water appeared in the view-glass and then rapidly cleared away. The concentration of each puff seemed to be very low, and further, no significant change in the permeate rate was noted. Each puff generally lasted for a few seconds and then the reject stream remained clear until the next step-increase in velocity.

Clearly, with each step-increase in velocity, a few layers of particles were being stripped off the cake. However, the resultant change in cake resistance was insufficient to significantly change the permeate rate. This possibly indicates that the cake removal process was being limited by the shear at the cake surface, and indicates that some *critical shear stress* needs to be exceeded in order to remove cake particles. Thus, with each increase in velocity a few

layers of cake, whose *critical shear for removal* was now exceeded, were stripped off into the bulk flow. Further, since only a few layers of particles were removed with each velocity increase, it would seem that this *critical shear for removal* is not uniform through the cake but possibly increases towards the wall. At very high velocities it would be expected that sufficient cake would be stripped off to significantly increase the flux. For the operating range investigated here, however, this did not occur.

System responses to a step-increase in concentration are shown in Figure 2.22. The system was started up at a concentration of 19.8 g/l and the feed was switched to a second feed tank containing a suspension of 77.6 g/l after periods of 10 and 60 minutes.

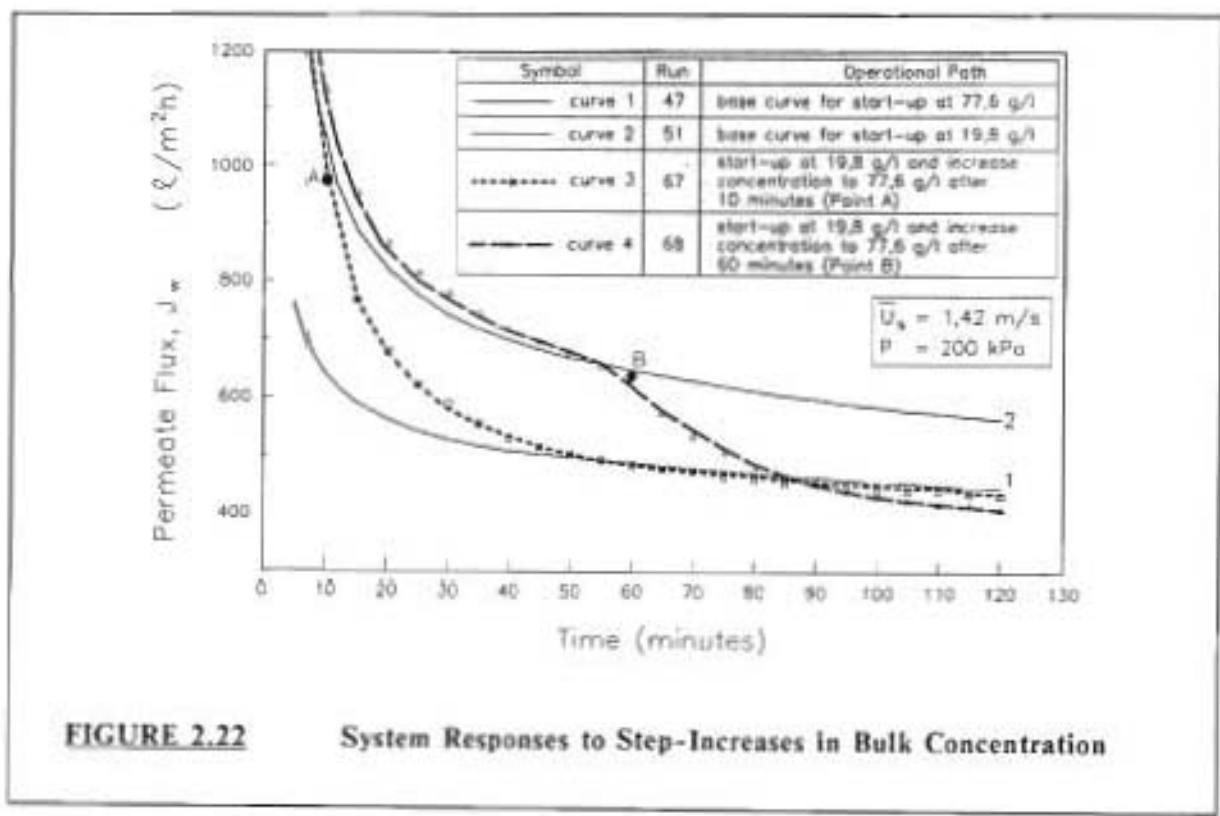
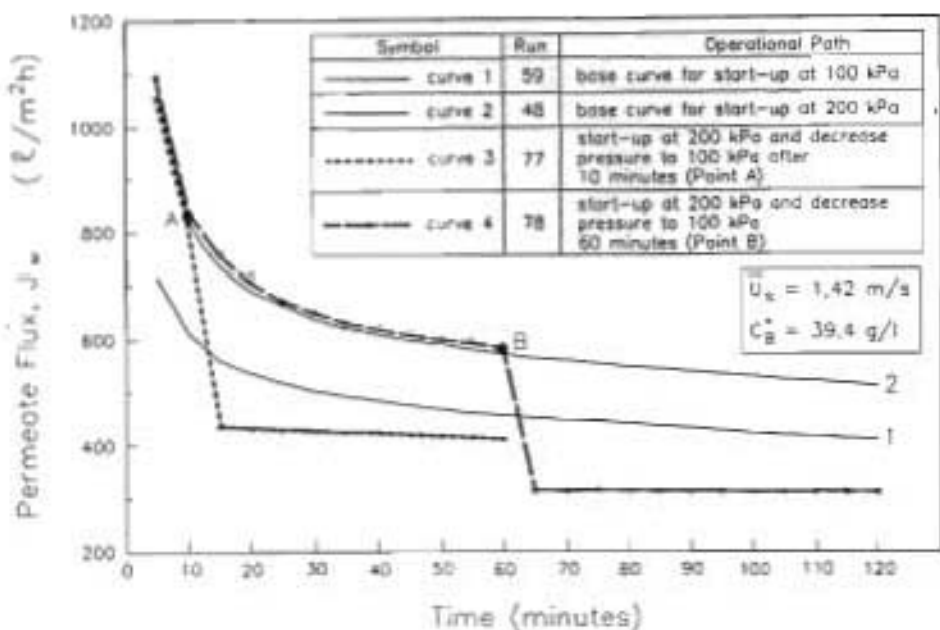


FIGURE 2.22 System Responses to Step-Increases in Bulk Concentration

The flux-time responses are similar to those obtained by the step-decrease in velocity. When the step-increase in concentration is performed in either Period I or Period II, the cake thickness increases with a corresponding decrease in flux. When the change is performed in Period II however, the flux drops to a level somewhat below the high concentration base curve.

#### 2.5.3.3 Dependence of Flux-Time Behaviour on Path to Reach Operating Pressure

System response to a step-decrease in pressure was investigated by starting up the system at a pressure of 200 kPa and then reducing the pressure to 100 kPa after intervals of 10 and 60 minutes, while keeping all other operating variables constant (Figure 2.23).



**FIGURE 2.23 System Responses to Step-Decreases in Pressure**

In both instances, the flux obtained after the step-decrease are substantially lower than the corresponding values for the low pressure base curve. On comparing the normalised fluxes (i.e. flux/pressure) before and after the step changes, it is seen that they are similar (Table 2.2), indicating that the hydraulic resistance did not decrease significantly. This further confirms the irreversibility of the cake formation.

**TABLE 2.2 Normalised Fluxes Before And After Pressure Decreases**

Lapse time before pressure decrease (minutes)	Normalised Flux before decrease ( $\ell/\text{m}^2\text{h}$ )/(100 kPa)	Normalised Flux after decrease ( $\ell/\text{m}^2\text{h}$ )/(100 kPa)
10	407	431
60	298	309

System responses to step increases in pressure are shown in Figure 2.24. Here start-up occurred at 100 kPa and the pressure was step-increased to 200 kPa in both periods.

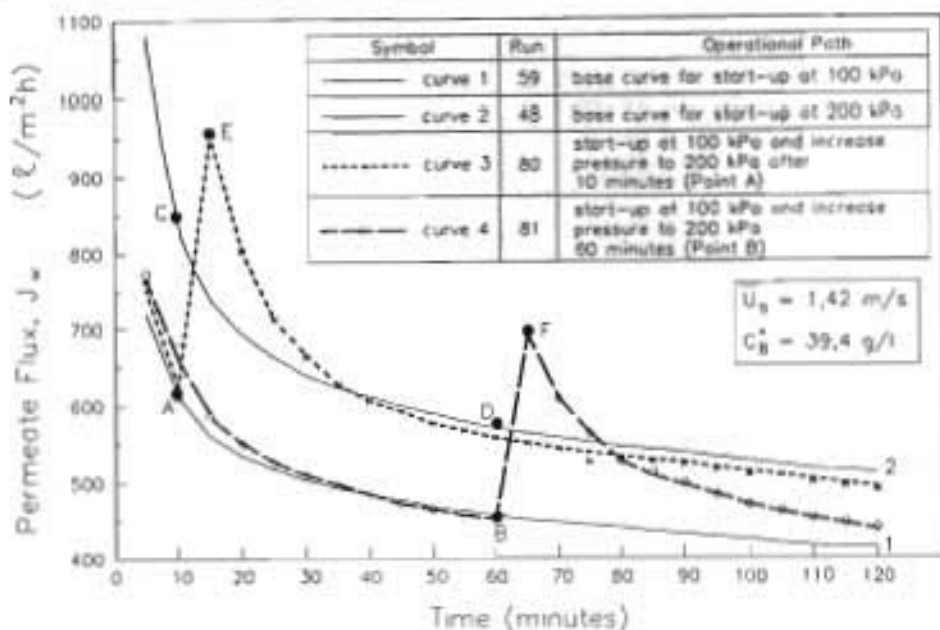


**FIGURE 2.24 System Responses to Step-Increases in Pressure**

In Period I, the flux increases to a value higher than the high pressure base curve, decreases rapidly, and then levels off at a value slightly below the high pressure base curve. If the normalised fluxes are considered (Flux/100 kPa = 608 at point A and 419 at point C), it is seen that the cake thickness at point A is actually smaller than the cake thickness at point C. Hence, after increasing the pressure, the system experiences the same permeate driving force as at point C, but has a lower hydraulic resistance. The flux thus increases to above point C. The lines between points A and E (and points B and F) do not represent the actual path described by the flux, but have merely been drawn in to indicate continuity between data points. Point E represents the flux value five minutes after the pressure increase at point A. A more realistic representation of the flux response may be obtained by extrapolating curve 3 back to the line  $t = 10$  minutes (Figure 2.25). Here points A and A' represent the flux immediately before and after the pressure increase. It is seen that on doubling the pressure at point A, the flux immediately doubles. Thereafter cake growth occurs, decreasing the flux, and the cake eventually becomes limited at a value slightly higher than the high pressure base curve.

In Period II, the flux exhibits a similar behaviour, but drops to a value substantially below the high pressure base curve, eventually approaching the low pressure base curve. Once again, as in the instance of a flowrate decrease or a concentration increase in Period II, the final resistance obtained by increasing the cake thickness in Period II is greater than that obtained in the base case. In the instance of a pressure increase, this difference is substantial.

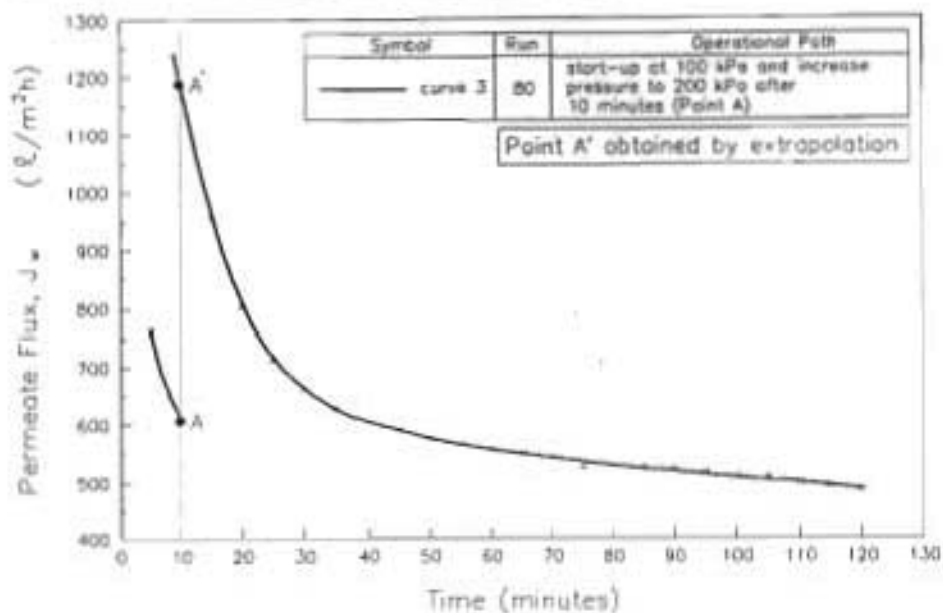


**FIGURE 2.25** Extrapolation to Ascertain Flux Immediately After Step-Increase in Pressure

Curve 4 in Figure 2.24 indicates that approximately 60 minutes after the pressure increase, the flux has dropped to the value it had before the increase. Further, it is clear that curve 4 is asymptotizing to the low pressure base curve. This could erroneously be interpreted as indicating that flux is independent of pressure. It must be noted however that this apparent independence is uniquely obtained when a step-increase is performed in Period II. When the system is started up at different pressures, the flux is most certainly a function of pressure, for the system under study (Figure 2.16). Dahlheimer et al. (1970) performed an experiment similar to that above i.e. step-increased the pressure and monitored the flux response. After an hour, the flux had returned to the value it had before the increase. This was interpreted as indicating that the flux was relatively insensitive to pressure. In view of the above statements, this could possibly have been an erroneous conclusion.

## 2.6 SUMMARY OF EXPERIMENTAL STUDY

The characteristic flux-time curve may be divided into two regions – *Period I*, where the flux decreases rapidly, followed by *Period II*, where the flux exhibits a slow, long-term decline with time. The rapid decrease in *Period I* may be attributed to a rapid increase in cake thickness. Thereafter, the cake thickness levels off to some steady-state value, but changes within the cake lead to the slow long-term decline. There are indications that, for the system under study, the slow decline in *Period II* is due to the progressive infiltration of fines into the cake, leading to a cake of progressively decreasing permeability.

The limiting or *steady-state* permeate flux, is a function of inlet velocity, bulk concentration and pressure. The trends that the steady-state permeate flux exhibits with respect to these operating variables are summarised in Table 2.3 :

<b>TABLE 2.3</b> <b>Summary of Effects of Operating Variables on Steady-State Permeate Flux</b>	
<b>Operating Variable</b>	<b>Effect on Steady-state flux</b>
Inlet velocity	$\left(\frac{\partial J_w}{\partial \bar{U}_s}\right) > 0$ $\left(\frac{\partial^2 J_w}{\partial \bar{U}_s^2}\right) > 0$
Concentration	$\left(\frac{\partial J_w}{\partial C_s^*}\right) < 0$ $\left(\frac{\partial^2 J_w}{\partial C_s^{*2}}\right) > 0$
Pressure	$\left(\frac{\partial J_w}{\partial P}\right) > 0$ $\left(\frac{\partial^2 J_w}{\partial P^2}\right) < 0$

There are unequivocal indications that the flux-time behaviour is dependent on the path taken to reach the operating point. If the operating path includes a change in operating variables that requires a decrease in cake thickness in order to be effective, the system will not respond as expected. This is due to an apparent irreversibility of the cake formation. There are indications that this irreversibility is due to the cake removal being limited by the shear stress at the cake surface.

If the change in operating variables requires a further growth in cake, system response will differ slightly depending on whether the change is performed during Period I or Period II. If the change is implemented during Period I, the final flux, and hence cake resistance, will be similar to that obtained by starting up at the "thicker cake" condition. When the change is performed in Period II, the final cake resistance is slightly higher than that obtained by starting up at the "thicker cake" condition. This difference is substantial in the instance of a pressure increase.

## *Chapter 3*

# **QUALITATIVE MECHANISTIC MODEL OF STEADY-STATE CONDITION**

---

### **3.1 INTRODUCTION**

The major characteristic of a cross-flow microfiltration (CFMF) system is that after an initial period of rapid decline the permeate flux either remains constant or alternatively decreases at a relatively slow rate. This behaviour may be explained in terms of the cake growth dynamics. On start-up the cake rapidly increases in thickness and then became limited at some maximum, or *steady-state* value. This steady-state cake thickness, and hence the steady-state permeate flux, is a function of the suspension velocity, suspension bulk concentration and operating pressure. After the steady-state cake thickness has been attained, the cake experiences changes in its characteristics resulting in the long-term slow decline in flux.

This chapter concerns the development of a model to describe the steady-state condition. The main objective here is to develop and present a clear, physically realistic and consistent picture of the mechanisms that determine cake growth and its eventual limit. To that end the model is developed and presented qualitatively. This qualitative model will be formulated into a mathematical model in Chapter 5.

#### **3.1.1 A Note on State and Measured Variables**

In Chapter 2, the global effects of superficial inlet velocity, pressure and concentration on permeate flux were identified. This superficial velocity,  $\bar{U}_s$ , is given by :-

$$\bar{U}_s = \frac{Q}{\pi R^2} \quad (3.1)$$

where  $\bar{U}_s$  = superficial inlet velocity (bulk average) (m/s)

$Q$  = suspension inlet flowrate ( $m^3/s$ ).

$R$  = tube radius (m).

The permeate flux,  $J_w$ , was based on the circumferential area of the tube :-

$$J_w = \frac{Q_p}{2\pi RL} \quad (3.2)$$

and is related to the permeate velocity at the wall,  $V_w$ , by :-

$$V_w = J_w \frac{1}{3600} \frac{1}{1000} \left( \frac{s}{h} \right) \left( \frac{l}{m^3} \right) \quad (3.3)$$

where  $J_w$  = permeate flux at tube wall ( $\ell/m^2h$ )

$Q_p$  = permeate flowrate ( $m^3/s$ )

$L$  = length of tube (m)

$V_w$  = permeate velocity at tube wall (m/s)

If it is assumed that the cake grows until some form of hydrodynamic balance is established at the cake surface, the velocities of significance in this balance will be the permeate velocity at the cake surface,  $V_{cs}$ , and the axial velocity in the free channel,  $\bar{U}_c$ , given by :-

$$V_{cs} = \frac{Q_p}{2\pi(R-t_c)L} \quad (3.4)$$

$$\bar{U}_c = \frac{Q}{\pi(R-t_c)^2} \quad (3.5)$$

where  $V_{cs}$  = permeate velocity at cake surface (m/s)

$\bar{U}_c$  = axial velocity in free channel (m/s)

$t_c$  = cake thickness.

These velocities,  $V_{cs}$  and  $\bar{U}_c$ , are the "true" velocities seen by particles at the cake surface, and are referred to as the *state* velocities. These are related to the *measured* velocities,  $V_w$  and  $\bar{U}_s$ , by :-

$$\bar{U}_c = \bar{U}_s \frac{R^2}{(R-t_c)^2} \quad (3.6)$$

$$V_{cs} = V_w \frac{R}{(R-t_c)} \quad (3.7)$$

If the cake thickness is significant in relation to the tube radius, the state velocities and measured velocities could differ appreciably in value. Implications of this are seen in, for example, the experiments conducted to ascertain the effect of suspension concentration on permeate flux. Although the experiments were conducted at a constant superficial inlet velocity, the steady-state cake thickness would have increased with concentration, by inference from the steady-state fluxes (see Figure 2.14). This implies that the free channel velocity,  $\bar{U}_c$ , increased with

concentration. Thus, although the inlet velocities measured by the experimenter were constant for all concentrations, the actual velocity that determined the system behaviour increased with concentration.

Despite the difference in value between state and measured velocities, it is expected that trends expressed in terms of the state velocities will be similar to trends expressed in terms of the measured velocities, since  $V_{cs}$  and  $\bar{U}_c$  are positive, monotonic functions of  $V_w$  and  $\bar{U}_s$ , respectively. Thus,

$$\text{if } \left( \frac{\partial F}{\partial \bar{U}_s} \right) > 0 \quad \text{then} \quad \left( \frac{\partial F}{\partial U_c} \right) > 0$$

$$\text{if } \left( \frac{\partial V_w}{\partial F} \right) > 0 \quad \text{then} \quad \left( \frac{\partial V_{cs}}{\partial F} \right) > 0$$

where  $F$  is some arbitrary variable. It is feasible, however, that the trends exhibited by the second derivative may differ in certain instances, depending on whether  $V_{cs}$  and  $\bar{U}_c$  or  $V_w$  and  $\bar{U}_s$  are used.

The purpose of the above discussion is solely to highlight the fact that a difference may exist between the velocities measured by the experimenter and the velocities "seen" by the system. Clearly, the variables of practical interest are the measured variables and any model must eventually relate  $V_w$  to  $\bar{U}_s$ ,  $P$  and  $C_B$ . However, in developing the mechanistic basis for the model, or evaluating the mechanistic bases of other models, it is invariably  $V_{cs}$  and  $\bar{U}_c$  that will be significant in determining drag forces on particles, axial shear stresses on cake surface, diffusion coefficients etc. Most previous modelling attempts reported in the literature have concerned either planar systems, or systems in which the cake thickness is negligible in comparison to the tube radius. In those instances, clearly, the state and measured velocities are equivalent. In reporting literature in the present study, an attempt will be made to interpret variables as being either *state* or *measured*, in order to ensure consistency with the present study. Thus, in instances where a previous worker has merely referred to *axial velocity*, it will be interpreted here as being either a *superficial velocity*,  $\bar{U}_s$ , or a *channel velocity*,  $\bar{U}_c$ . Similarly, where a previous worker has referred to *permeate velocity*, it will be reported here as being either the *permeate velocity at the tube wall*,  $V_w$ , or the *permeate velocity at the cake surface*,  $V_{cs}$ .

### **3.2 STATEMENT OF PROBLEM AND LITERATURE REVIEW**

The driving force for cake growth is the convection of solids towards the cake by the radial fluid flow. Even after the steady-state cake thickness has been attained, solids will still be convected towards the wall. Hence some mechanism must exist to offset this cake growth driving force and prevent these "excess" particles from becoming incorporated into the cake structure. It is the identification of this mechanism that poses the greatest problem in the modelling of the steady-state in CFMF.

Earliest attempts at modelling CFMF-type of behaviour involved the solution of the Fickian-diffusion equation using the classic Leveque solution for convective diffusion (film theory) [Blatt et al. (1970), Romero and Davis (1988)]. In that approach, the steady-state is attained when the convection towards the wall is balanced by a Brownian back-diffusion away from the cake. However, when this theory is applied to the UF of colloids or the CFMF of particles, using the Stokes-Einstein Brownian diffusivity coefficient, predicted fluxes are orders of magnitude below that observed experimentally [Blatt et al. (1970), Reed and Belfort (1982)]. The possible reason for this is that the Stokes-Einstein diffusivity for even small particles is extremely small, being inversely related to particle size. It was subsequently suggested that either the back diffusion of particles was substantially greater than that predicted by the Stokes-Einstein equation, or that the polarised layer did not provide the controlling hydraulic resistance to permeate flow [Blatt et al. (1970)]. Porter (1972) showed that the latter argument was highly unlikely and further proposed that the back diffusion of particles could be augmented by a radial migration of particles away from the cake.

Subsequent modelling approaches may be classified into 4 main categories : *force-balance* models, *enhanced back-diffusion* models, *axial convection* models and *scour* or *erosion* models. Significant studies in this regard are reviewed below. Most of the models have been developed for laminar flow CFMF. They are included here for completeness and since it is feasible that even in turbulent systems the controlling processes may occur in the laminar sublayer.

### **3.2.1 Force Balance Models**

In this category of models, the forces acting on individual particles are considered. The steady-state is attained when some particular balance of forces is achieved.

#### **3.2.1.1 Inertial Lift (Lateral Migration) Models**

Neutrally buoyant particles in a laminar flow field tend to experience an inertial lift force which causes a migration away from the wall to some equilibrium position between the wall and centreline [Altena and Belfort (1984)]. The phenomenon has variously been termed the *Poiseuille effect*, the *tubular pinch effect* and the *inertial lift effect*. Porter (1972) initially suggested that this inward migration could offset the convection of solids towards the wall. The most recent and comprehensive models based on the inertial lift theory are those of Belfort et al. [Altena and Belfort (1984), Green and Belfort (1980), Belfort and Nagata (1985)]

In the inertial lift model it is proposed that particles are subject to two significant forces viz a fluid drag force,  $F_D$ , directed towards the wall and the inertial lift force,  $F_L$ , directed away from the wall. These correspond to a lift velocity,  $V_L$ , and a permeation velocity,  $V_{cs}$  (Figure 3.1). When the permeation velocity exceeds the lift velocity, particles convect to the wall and cake growth occurs. Cake growth becomes limited when the lift velocity equals or exceeds the permeation velocity.

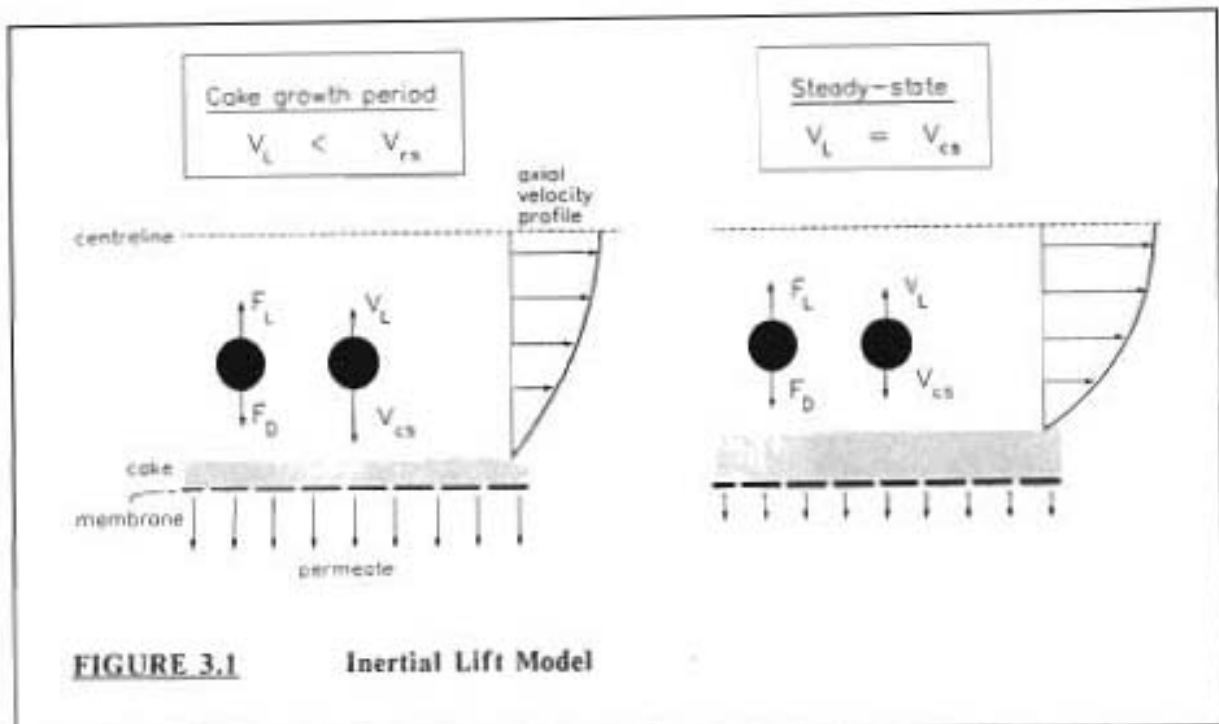


**FIGURE 3.1** Inertial Lift Model

The general form of the lift velocity is given as [Green and Belfort (1980)] :-

$$V_L = k_T \bar{U}_c Re \left( \frac{r_p}{R_c} \right)^{k_B} h_1(r) \quad (3.8)$$

where  $V_L$  = lift velocity on particle (m/s)  
 $\bar{U}_c$  = suspension velocity in free channel (m/s)  
 $Re$  = Reynolds Number (based on  $\bar{U}_c$  and  $R_c$ )  
 $R_c$  = radius of free channel (m) ( $= R - t_c$ )  
 $r_p$  = particle radius (m)  
 $h_1(r)$  = some function of radial distance  
 $k_T, k_B$  = constants ( $> 0$ )

It is seen that the lift velocity increases as particle size increases. Further, for a specified particle size and permeation velocity,  $V_{CS}$ , some minimum axial velocity exists above which  $V_L > V_{CS}$  and hence no convection towards the wall will occur.

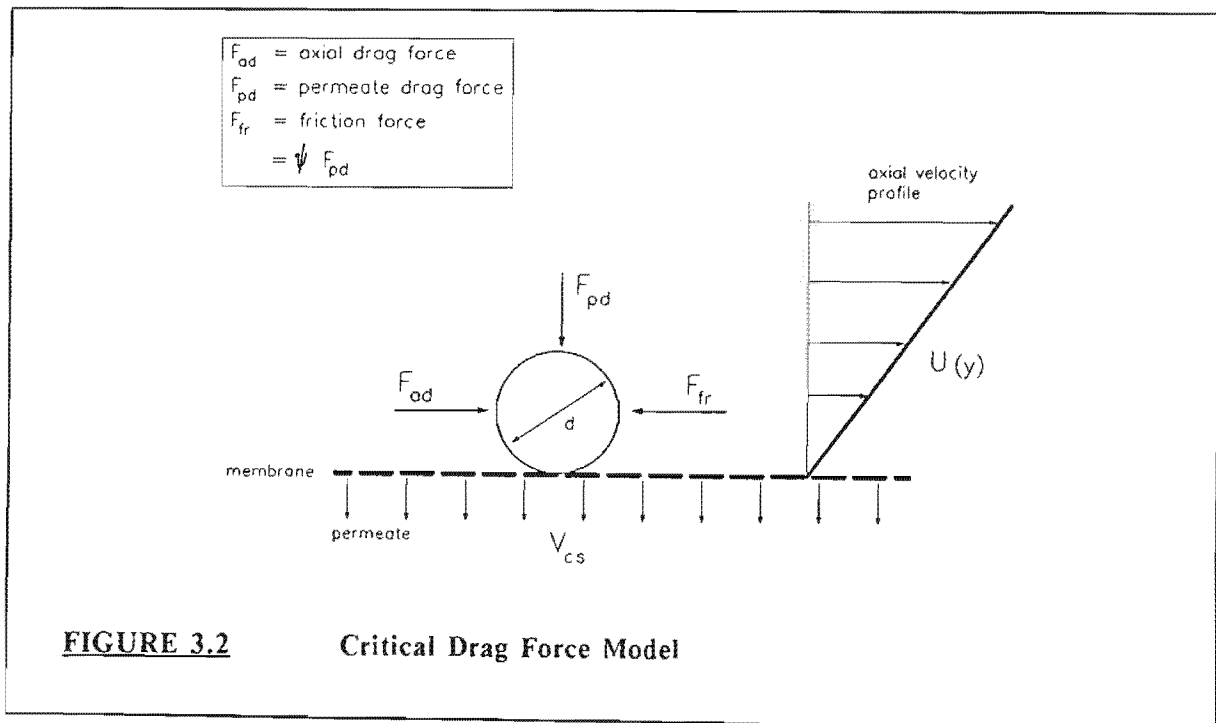
Green and Belfort (1980) combined an inertial lift equation with an hydraulic resistance equation and applied the model to the data obtained on a latex suspension. The effect of cake growth on  $\bar{U}_c$ , and hence on  $V_L$ , was explicitly included. Predicted fluxes were in order of magnitude agreement with experimental observations, although the predicted cake thickness occupied over 70 % of the channel. The inertial lift model was also tested on the data of Thomas et al. (1973) and Reed et al. (1980), who had measured the critical axial velocities necessary to prevent catastrophic fouling in UF and HF systems. It was shown that the observed critical velocities were consistent with the predictions of the inertial lift model.

The applicability of inertial lift theory to turbulent CFMF is questionable. As noted by Romero and Davis (1988), most inertial lift models are generally limited to dilute suspensions of non-interacting particles and cannot be applied close to the wall. Zydny and Colton (1986) state that the "model fails to predict a dependence on bulk particle concentration". This is not strictly correct since the right hand side of equation 3.8 is a function of concentration via the Reynolds Number. However, in general the Reynolds number would only show a significant dependence on concentration at high concentrations, or for suspensions whose viscosity is a strong function of concentration. Noting that the inertial lift effect is inapplicable under such circumstances, Zydny's statement is, in effect, valid. The lateral migration model has found limited favour with Baker et al. (1985) and Hoogland et al. (1988), who note that the model does explain their observations that finer particles are preferentially deposited as the axial velocity is increased.

### 3.2.1.2 Critical Drag or Critical Shear Models

Rautenbach and Schock (1988) and Fischer and Raasch (1986) proposed that a critical force balance condition existed for particle stability on a cake (or membrane) surface. Below this critical condition particles which reach the cake surface will deposit stably. At or above this critical condition, particles which reach the surface will be destabilised and will not deposit. Conceptually, the work of Fischer and Raasch is not significantly different from that of Rautenbach and Schock, and only Rautenbach and Schock's model will be detailed here.

Rautenbach and Schock's critical condition is derived by an equilibrium of drag forces normal and parallel to the membrane (Figure 3.2).



$$C_D \frac{1}{2} \rho \overline{U_p}^2 \frac{\pi d^2}{4} \geq \psi C_D \frac{1}{2} \rho V_{cs}^2 \frac{\pi d^2}{4} \quad (3.9)$$

where  $C_D$  = drag coefficient for spheres  
 $\overline{U_p}$  = mean axial velocity over particle (m/s)  
 $\psi$  = friction coefficient (or proportionally constant)  
 $V_{cs}$  = permeate velocity (m/s)  
 $d$  = particle diameter (m)  
 $\rho$  = suspension density (kg/m<sup>3</sup>)

Rautenbach and Schock reduced equation 3.9 to the form

$$\overline{U_p} \geq \psi V_{cs} \quad (3.10)$$

and utilised the *Universal Velocity Profile* for turbulent flow to evaluate  $\overline{U_p}$ . In the near wall region, the universal velocity profile may be differentiated into three zones : the laminar zone, the laminar/turbulent intermediate (or buffer) zone and the fully turbulent zone (see Section 3.4.2). This led to three expressions for  $\overline{U_p}$  and hence  $V_{cs}$ , depending on the particular zone being considered.

Laminar zone :  $V_{cs} \propto Re^{1.75} \left( \frac{v}{2R} \right) \left( \frac{d}{2R} \right)$  (3.11)

Buffer zone :  $V_{cs} \propto Re^{1.26} \left( \frac{v}{2R} \right) \left( \frac{d}{2R} \right)^{0.44}$  (3.12)

Fully turbulent zone :  $V_{cs} \propto Re^{1.0} \left( \frac{v}{2R} \right) \left( \frac{d}{2R} \right)^{1/7}$  (3.13)

where  $Re$  = Reynolds Number  
 $v$  = suspension kinematic viscosity (m<sup>2</sup>/s)

It was found that the best agreement between experiment and theory was given by equation 3.12. The correspondence between the model and Rautenbach and Schocks' experimental observations is quite impressive. Rautenbach and Schock obtained steady-state fluxes for clay/water and quartz/water suspensions at concentrations ranging from 1 % to 15 % by volume in thin tube, as well as channel, modules. When the fluxes are plotted against the right hand side of equation 3.11, all points lie along a straight line. The proportionality constant, reported in Schulz and Ripperger (1989), is given as  $0.22 \psi^{-1}$ , with  $\psi = 4.680$ . Schulz and Ripperger (1989) applied the model to various systems and found a good correspondence between predictions and observations. Various workers [Harrison et al. (1981)] have observed that the average particle size of the cake decreases as the operating velocity is increased. This is explicable in

terms of Figure 3.2 by noting that at a specific velocity, particles above a certain size will be destabilised while particles below a certain size will deposit, leading to a preferential deposition of small particles as the velocity is increased. In Section 2.5.3.2 it was observed that layers of the cake were progressively removed as the velocity was step-increased. This is also seemingly explicable in terms of a critical drag force model.

A flaw with equation 3.12 is that no pressure dependence of flux is predicted. This is consistent with Rautenbach and Schocks' experimental results, where fluxes were independent of pressure over the range 100 kPa to 200 kPa. The results of the present, and other studies [Henry (1972), Saw et al. (1985), Le (1987)], however, indicates that flux can exhibit a dependence on pressure, indicating that equation 3.12 may not be generally applicable. It is in principle feasible, however, to couple equation 3.12 with a hydraulic resistance equation potentially yielding a model that will show a pressure dependence of flux.

Comparison between model predictions for the effects of concentration and velocity on steady-state flux with the results of this study requires that the steady-state cake thickness be known.  $Re$  in equation 3.12 should be based on the suspension velocity in the free channel,  $\bar{U}_s$ , and not on the superficial velocity,  $\bar{U}_s$ . Similarly  $V_{cs}$  in equation 3.12 is the permeate velocity at the cake surface and not at the tube wall,  $V_w$ .

Since the steady-state cake thickness were not known, the model was tested at two extreme limits i.e. a minimum cake thickness of 0.0 mm and a maximum thickness of 2.0 mm. A typical comparison is shown in Table 3.1<sup>1</sup>.

**TABLE 3.1** Comparison Between Fluxes Predicted by Rautenbach and Schocks' Model and Experimental Results Obtained in This Study

Assumed Cake thickness (mm)	Flux at cake surface ( $J_{cs}$ ) ( $\ell/m^2h$ )	
	Rautenbach and Schocks' Model	This experimental study
0.0	88.6	638
2.0	141	758
<u>Data for Run 48</u>		
$\bar{U}_s$	= 1.42 m/s	
$C_s$	= 39.4 g/l	
$P$	= 200 kPa	

<sup>1</sup> Suspension physical properties were calculated using the expressions in Section 3.4.4.

The fluxes predicted by equation 3.12 are considerably below experimental observations in both extreme cases. It is possible that the poor fit may be due to the proportionality constant being a function of the specific system, and hence inapplicable to the limestone system studied here. It is thus more instructive to compare the trends predicted by the model with the trends observed in this study. From equation 3.12 it is seen that  $V_{cs}$ , and hence  $J_{cs}$ , scales with  $\bar{U}_c^{1.26}$ . This trend is depicted in Figure 3.3 for the particle properties and velocity range considered here, and exhibits a similar trend to that observed experimentally (equations 2.5 and 2.6).

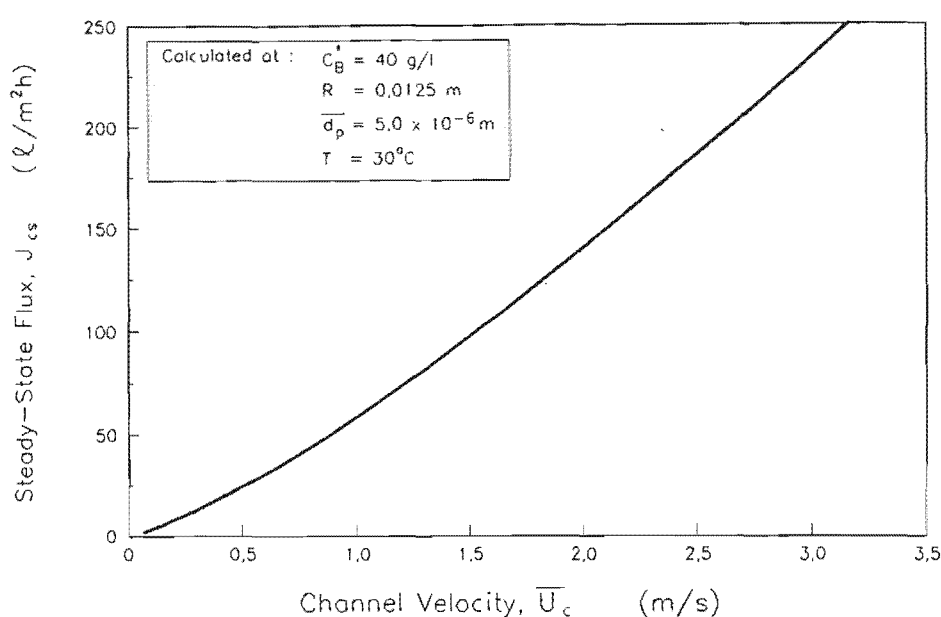


**FIGURE 3.3** Trend for Effect of Inlet Velocity on Steady-State Flux, as Predicted by Rautenbach and Schock's Model

The trend predicted for the effect of concentration on steady-state flux (Figure 3.4) is however, substantially different from observations (Figure 2.14, equations 2.7 and 2.8). Over the concentration range considered here the model predicts that the flux is virtually independent of concentration. From equation 3.12 it is seen that  $V_{cs}$  scales with  $v^{-0.26}$ . This indicates that the model would only predict a significant dependence on concentration at high concentrations and for suspensions whose viscosity is a strong function of concentration. Further, noting that the steady-state cake thickness increases with concentration (by inference from Figure 2.14) it is seen that for a constant inlet velocity the channel velocity,  $\bar{U}_c$ , will also increase as concentration increases. Since  $V_{cs}$  is a stronger function of channel velocity than of kinematic viscosity ( $V_{cs}$  scales with  $\bar{U}_c^{1.26}$  and  $v^{-0.26}$ ) it is most probable that if the increase in  $\bar{U}_c$  with concentration is incorporated into Figure 3.4, the model will predict an increase in flux with concentration.

Clearly, while the model predicts correct trends with respect to velocity, no trend is predicted with respect to pressure and the predicted trend with respect to concentration is contrary to experimental observations.

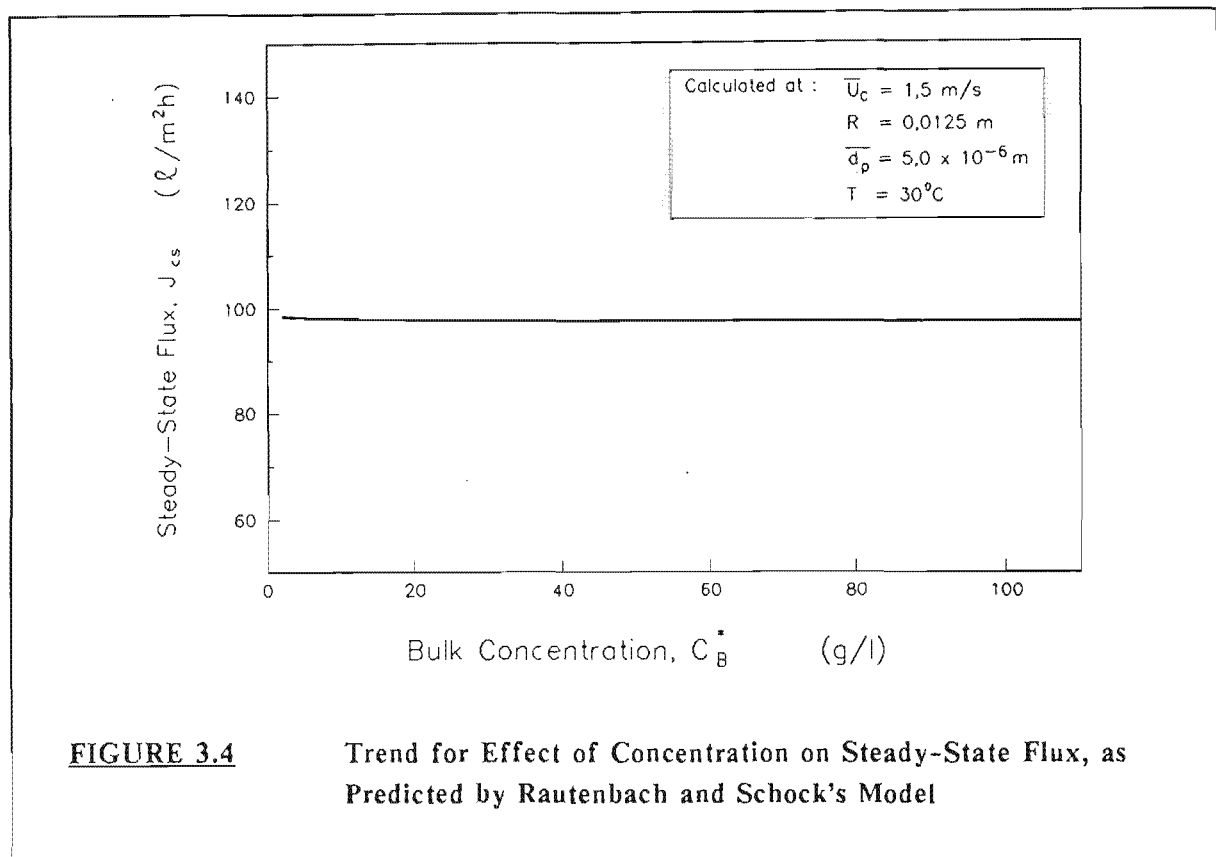


**FIGURE 3.4** Trend for Effect of Concentration on Steady-State Flux, as Predicted by Rautenbach and Schock's Model

A second criticism of the model stems from the observation that the best fit is provided by equation 3.12, the *buffer zone* equation. Rautenbach and Schock also note that this is surprising since with the small particle size concerned it would be expected that the demixing zone would occur in the laminar region. This discrepancy is best visualised by comparing the theoretical thickness of the laminar zone with the particle sizes used in their experiments. For the conditions used in those experiments, the theoretical thickness of the laminar zone ranges from 40 to 80  $\mu\text{m}$ <sup>2</sup>. In contrast the particles had an average size of 2 to 2,5  $\mu\text{m}$ . Further, particles "on the surface" will in fact be embedded partially below the mean cake surface, further decreasing their protrusion into the flow field. Thus, particles will unequivocally lie within the laminar zone and very little physical basis exists for the application of the equation 3.12. Rautenbach and Schock propose that the presence of particles may destroy the laminar zone and thus enable particles to be affected by forces in the intermediate zone. In Section 3.4 it will be shown that it is most likely that particles will dampen out turbulence and thus increase the laminar zone.

<sup>2</sup> Calculated using equation 3.44 with suspension properties and operating velocities obtained from Rautenbach and Schock (1988)

It is feasible, however, that the radial flow through the wall may reduce the thickness of the laminar zone (this is discussed in Section 3.4). However, if any substantial change to the velocity profile occurs then equations developed from the universal velocity profile may no longer be applicable and the forms of equations 3.11 to 3.13 would have to change. It would seem therefore that various contradictions exist between the best fit equation and the fluid dynamics and particle geometry in the near wall region.

There are further conceptual inconsistencies with models based solely on a critical drag force or critical shear stress concept. These form a major part of the discussion in the chapter on Model Development, and are postponed to Section 3.6.

### 3.2.2 Enhanced Back Diffusion Models

In this class of models it is proposed that the convection of solids towards the wall is offset by a simultaneous back transport from cake to the bulk suspension. The steady-state is attained when these rates equalise, and may be represented by the one dimensional Fickian diffusion equation :

$$VC = D \frac{\partial C}{\partial r} \quad (3.14)$$

where  $V$  = permeate velocity (or flux, depending on the units for  $D$ )  
 $C$  = concentration  
 $D$  = diffusion coefficient

In contrast to the simple concentration polarisation models, however, the diffusivity used in the solution of equation 3.14 is not the Stokes-Einstein diffusivity, but some alternative diffusivity that has a substantially higher value.

On integrating equation 3.14, a linear relationship between flux and log concentration is predicted [Fane et al. (1982)]. This is consistent with flux-concentration relationship observed in this study (see Figure 2.15). This point will be pursued further in Section 3.6, Model Development.

#### 3.2.2.1 Shear Enhanced Back-Diffusion

Prior to reviewing models based on shear enhanced back diffusion, it is instructive to briefly review the concept.

When a suspension is subjected to a viscous shear field, particle-particle interactions result in a displacement of particles from the bulk flow streamlines. A marked particle will subsequently exhibit a random walk behaviour, termed *self diffusion*. If a concentration gradient exists in the suspension then a particle in any given plane will experience a greater number of interactions with particles on its side that has the higher concentration than on its side with the lower concentration. This causes a net drift of particles in the direction of decreasing concentration, the drift velocity being proportional to the concentration gradient. This net drift down a

concentration gradient may be characterised by an effective particle diffusivity, the *shear induced diffusivity* [Davis and Leighton (1987)]. This process has variously been termed *shear induced hydrodynamic diffusion* and *shear enhanced diffusion*.

Ekstein et al. (1977) investigated this effective particle diffusivity by tracking labelled particles in a Couette device. The diffusivity increased with the square of the particle radius and linearly with the shear rate. It was also found that the diffusivity increased linearly with concentration up to a volume fraction of 0.2 and thereafter remained constant at a value :-

$$D_{p2} = 0.03r_p^2 \gamma \quad (3.15)$$

where  $D_{p2}$  = shear induced diffusivity of particle ( $\text{m}^2/\text{s}$ )

$r_p$  = particle radius (m)

$\gamma$  = shear rate ( $\text{s}^{-1}$ )

Recently, Leighton and Acrivos (1987a, 1987b) showed that this apparently constant value above a volume fraction of 0.2 was due to a geometric limitation in the apparatus of Ekstein et al. With the elimination of these limitations the diffusivity was found to increase rapidly with concentration. Their measurements were represented by an empirical correlation [Leighton and Acrivos (1986)]:-

$$D_{p3} = r_p^2 \gamma \hat{D} \quad (3.16)$$

with

$$\hat{D} = 0.33C^2(1 + 0.5e^{0.8C}) \quad (3.17)$$

where  $C$  = volume fraction of solids.

Equation 3.17 was found to be valid up to  $C = 0.5$ .

Zydney and Colton (1986) proposed that the discrepancy between the simple concentration polarisation model, using the Stokes-Einstein diffusivity, and experimental observations could be attributed to an augmentation of particle back transport by the shear induced diffusion mechanism. They incorporated Ekstein's expression for the diffusivity into the Leveque equation for the local mass transfer coefficient yielding

$$k_m(x) = 0.052 \left( \frac{r_p^4}{x} \right)^{\frac{1}{3}} \gamma_w \quad (3.18)$$

where  $k_m$  = mass transfer coefficient ( $\text{m}/\text{s}$ )

$\gamma_w$  = shear rate at the wall ( $\text{s}^{-1}$ )

$x$  = axial coordinate (m)

Substituting this into the Fickian Diffusion equation and integrating along the length of the tube,  $L$ , yields :-

$$\overline{V_{cs}} = 0,078 \left( \frac{r_p^4}{L} \right)^{\frac{1}{3}} \gamma_w \ln \left( \frac{C_w}{C_B} \right) \quad (3.19)$$

where  $\overline{V_{cs}}$  = length averaged permeate velocity (m/s)

$C_w$  = concentration at the wall (volume fraction)

$C_B$  = bulk concentration (volume fraction)

Evaluation of equation 3.19 on twelve sets of data showed that the model yielded better agreement with experimental observations than previous models.

Explicit in the model is the assumption that the flux has reached some pressure-independent value. Zydny and Colton seem to regard this "*pressure independence of flux*" as a characteristic behaviour of CFMF systems. Clearly equation 3.19 can only apply to laminar systems which exhibit a pressure-independant behaviour. The shear induced diffusion mechanism could however, apply in the laminar sublayer of turbulent system.

### 3.2.2.2 Turbulent Back Diffusion

Hunt (1987a, 1987b) proposed that in turbulent CFMF systems, particles will be transported down a concentration gradient by turbulent eddies and their motion could thus be characterised by an *effective turbulent diffusivity*. Following Flemmer et al. (1982), this diffusivity is given as :-

$$D' = k_9 U^* \quad (3.20)$$

where  $D'$  = particle diffusivity (kg/ms)

$k_9$  = proportionality constant

$U^*$  = friction velocity

$$= \sqrt{\frac{\tau_w}{\rho}}$$

with  $\tau_w$  = shear stress at the cake surface.

The turbulent diffusion of particles would result in a back transport from the cake to the bulk suspension. When the rate of this back diffusion is exceeded by the rate of convection to the wall, cake growth occurs. Cake growth is accompanied by both a decrease in the rate of convection to the wall and an increase in the rate of back transport, leading eventually to a cake thickness at which these rates are equal. This defines the steady-state condition, whereafter no net particle transport to the cake will occur.

The Hunt model entails the simultaneous solution of the steady-state mass balance and the hydraulic resistance equations :

mass balance :

$$J' C' = D' \frac{\partial C'}{\partial r} \quad (3.21)$$

pressure balance :

$$\Delta P = \frac{\mu_l J' t_c}{K' \rho_l} \quad (3.22)$$

where  $J'$  = permeate flux ( $\text{kg}/\text{m}^2\text{s}$ )

$C'$  = concentration (mass fraction)

$\Delta P$  = pressure difference across cake (Pa)

$\mu_l$  = fluid viscosity (PaS)

$\rho_l$  = fluid density ( $\text{kg}/\text{m}^3$ )

$K'$  = cake permeability ( $\text{m}^2$ )

$t_c$  = cake thickness (m)

It was assumed that the bulk of the mass transfer occurred within a thin concentration boundary layer close to the cake surface. Based on the non-dimensional distance coordinate in turbulent flows (see equation 3.43) it was proposed that the boundary layer thickness could be represented by :-

$$\delta = k_{10} \frac{v}{U^*} \quad (3.23)$$

where  $\delta$  = boundary layer thickness (m)

$k_{10}$  = a constant

$v$  = suspension kinematic viscosity ( $\text{m}^2/\text{s}$ )

Using the Blasius equation for friction factors in smooth tubes, the friction velocity required in equations 3.20 and 3.23 was modelled as:

$$U^* = k_{11} \overline{U}_c \left( \frac{v}{\overline{U}_c R_c} \right)^{1/8} \quad (3.24)$$

where  $k_{11}$  = a constant

Integration of equation 3.21 over the boundary layer requires the relationship between flux and radius. On the assumption that the axial velocity profile may be approximated by plug flow, this relationship was given as :-

$$J'(r) = J'_0 \frac{r}{R_c} \quad (3.25)$$

where  $J'(r) = \text{flux at radius } r \text{ in the boundary layer (kg/m}^2\text{s)}$

$J_s = \text{flux at tube wall (kg/m}^2\text{s)}$

$R_t = \text{radius of free core (m)}$

Substituting equation 3.25 into equation 3.21 and integrating over the boundary layer with boundary conditions :-

$$\begin{aligned} \text{at } r &= R_t - b & C &= C_s \\ r &= R_t & C &= C_0 \end{aligned}$$

yields

$$J'_0 = \frac{k_{12} \bar{U}_c^2 \left[ \frac{v}{\bar{U}_c K} \right]^{1/4} \ln \left[ \frac{C_s}{C_0} \right]}{\sqrt{1 - \frac{k_{12}}{\bar{U}_c K} \left[ \frac{v}{\bar{U}_c K} \right]^{1/8}}} \quad (3.26)$$

$$\Delta P = \frac{\mu J'_0 t_c}{p_z K} \quad (3.27)$$

where  $k_{12,13}$  = constants

$C_0$  = boundary concentration

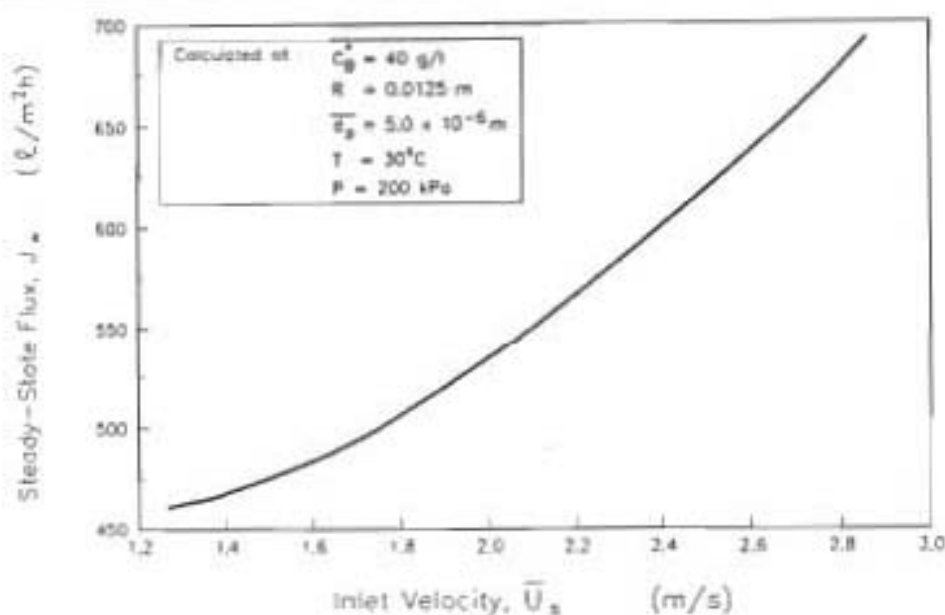
The model has four parameters :-  $k_{12}$ ,  $k_{13}$ ,  $C_0$  and  $K'$ . Hunt evaluated these parameters for a limestone suspension by regression on experimental results (Table 3.2). Comparison between the regressed model and experimental observations was good except at low concentrations, where predictions tended to be too high.

TABLE 3.2 Hunt's Regressed Parameters for a Limestone Suspension

Parameter	Regressed Value
$C_0$	0.5465
$k_{12}$	$3.752 \times 10^{-8}$
$k_{13}$	4914
$K'$	$1.262 \times 10^{-18}$

A comparison was made between model predictions and experimental fluxes obtained in this study, using the regression parameters from Table 3.2. Evaluation of model predictions for the effect of inlet velocity on steady-state flux was not possible since the model did not converge

for two of the velocities studied here (the reason for this non-convergence will be discussed shortly). However, the general trend predicted by the model (Figure 3.5) is consistent with the trend observed in this study (equations 2.5 and 2.6).



**FIGURE 3.5** Trend for Effect of Inlet Velocity on Steady-State Flux, as Predicted by Hunt's Model

The model also predicts the correct trend for the effect of concentration on steady-state flux, although the predicted values are substantially below observations (Figure 3.6). Although the regression parameters were evaluated on a limestone suspension, it is not unexpected that the predicted and experimental fluxes differ since the limestone used in this study could possibly have had a different size distribution and specific cake resistance from that used by Hunt.

The trend predicted for pressure is not consistent with the trend observed in this study (Figure 3.7). Experimental fluxes show a decreasing dependence on pressure while predicted fluxes show a linear, almost increasing, dependence. It has been shown by Pillay et al. (1989) that the incorrect pressure trend could be due to the model assumption that the cake is incompressible. Incorporating a compressible cake resistance equation into the model does yield the correct trend for flux dependence on pressure [Pillay et al. (1989)].

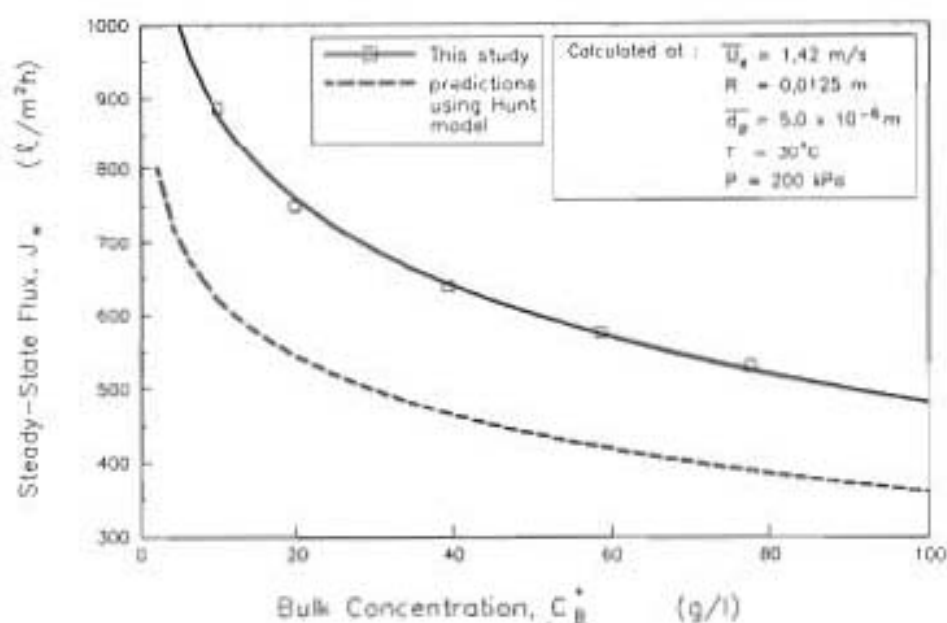


**FIGURE 3.6** Trend for Effect of Concentration on Steady-State Flux, as Predicted by Hunt's Model

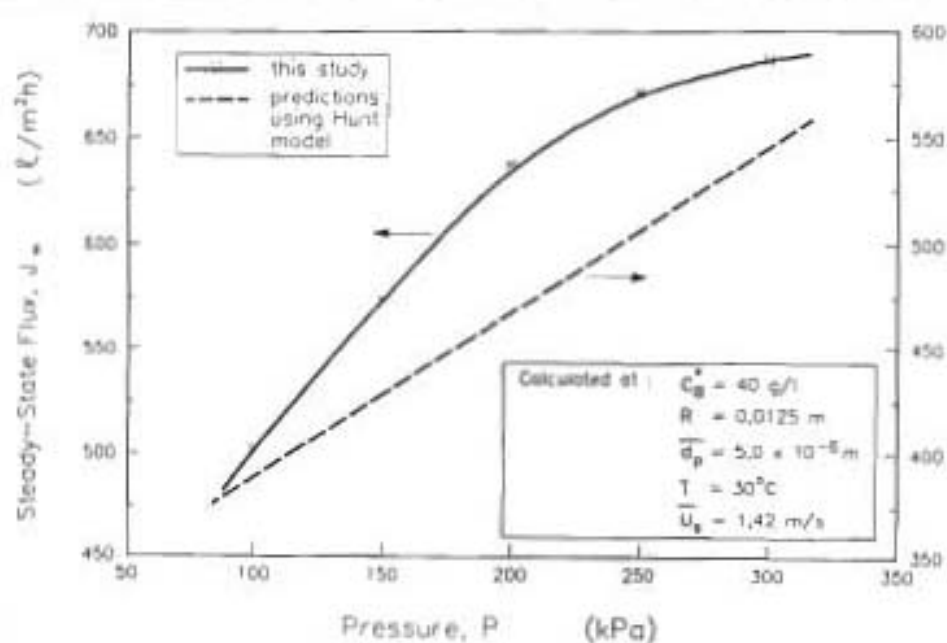


**FIGURE 3.7** Trend for Effect of Pressure on Steady-State Flux, as Predicted by Hunt's Model

Seemingly, the turbulent back diffusion model can yield the correct trends for flux dependence on velocity and concentration. Incorporation of a compressible cake expression into the model could result in the correct trend for the effect of pressure on flux. There are however, major mechanistic inconsistencies with a model based on the assumption that particles experience a turbulent back diffusion from cake to bulk suspension. This forms a major part of the chapter on **Model Development** and is postponed to Section 3.6.

There are, however, some significant errors with Hunt's model, which will be detailed here. For most of the data points on which Hunt's regressions were performed, the predicted boundary layer thicknesses are greater than half of the tube radius, and in some instances greater than the radius. Clearly boundary layer thicknesses that are greater than half the radius contradict the entire concept of a concentration boundary layer, and thicknesses greater than the radius are physically impossible<sup>3</sup>. This unrealistic boundary layer thickness is the major cause of the non-convergence of the model in certain regions, the non-convergence occurring when the boundary layer thickness exceeds the tube diameter.

Secondly, equation 3.25 is most certainly wrong.  $J_0$  in equation 3.25 should be the flux at the cake surface and not the flux at the tube wall. For the typical cake thicknesses achieved by Hunt (2 mm to 7 mm in a tube of radius 14 mm) a significant difference would exist between the fluxes at the cake surface and tube wall. There has apparently been a confusion between the state and measured variables. Attempts to re-regress Hunt's model using the correct formulation for equation 3.25 proved unsuccessful, the regression package used being unable to locate an optimal set of parameters.

### **3.2.3 Axial Convection Models**

The axial convection models propose that the convection of solids towards the wall is offset by a simultaneous axial convection of solids along the wall and out of the tube (Figure 3.8).

Leonard and Vassilieff (1984) proposed a simple convection flow model in which analytical solutions were obtained for the particle layer by assuming that the velocity profile in the vicinity of the layer was linear and that the layer could be regarded as either an immobile solid or a Newtonian fluid with the same effective viscosity as the bulk suspension. The permeate flux was assumed to be constant in the axial direction.

The model was subsequently extended by Davis and Birdsell (1987), relaxing some of the assumption made by Leonard and Vassilieff. Fully developed parabolic velocity profiles were determined for both the suspension and the particle layer, permeate fluxes were allowed to vary axially, and the particle layer was assigned a concentration-dependant viscosity greater than that of the bulk suspension.

---

<sup>3</sup> It will be shown in Section 5.2.1 that the one-dimensional Fickian Diffusion equation is only applicable if the boundary layer thickness is small in comparison to the radius of the tube.

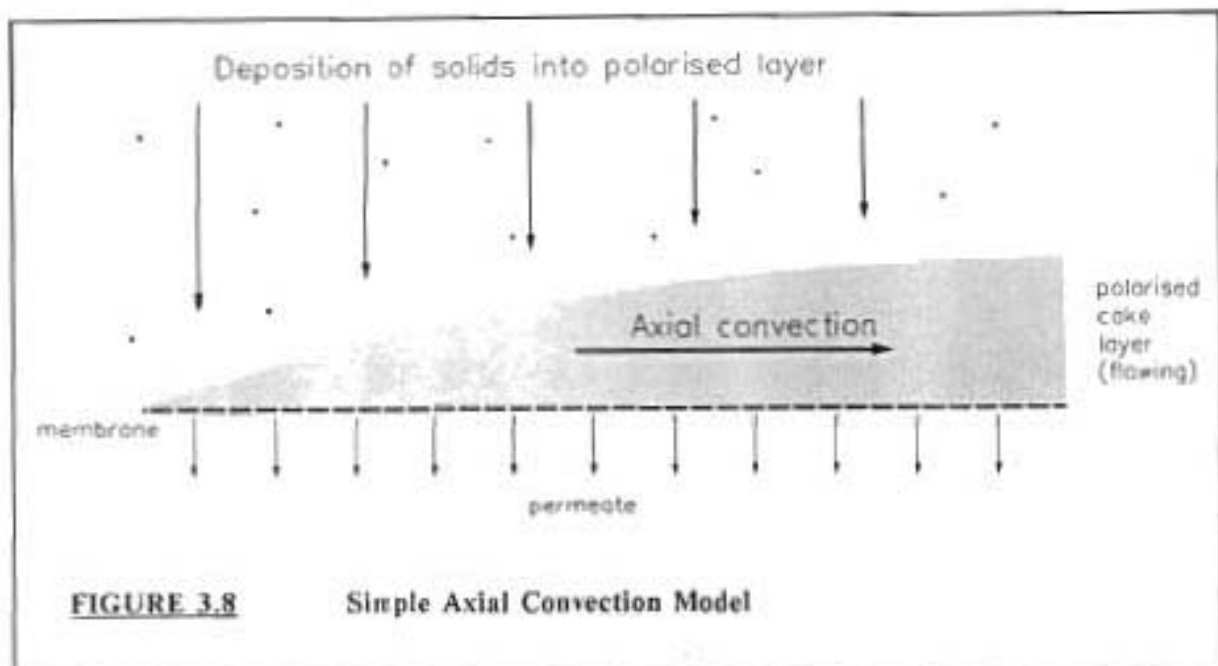


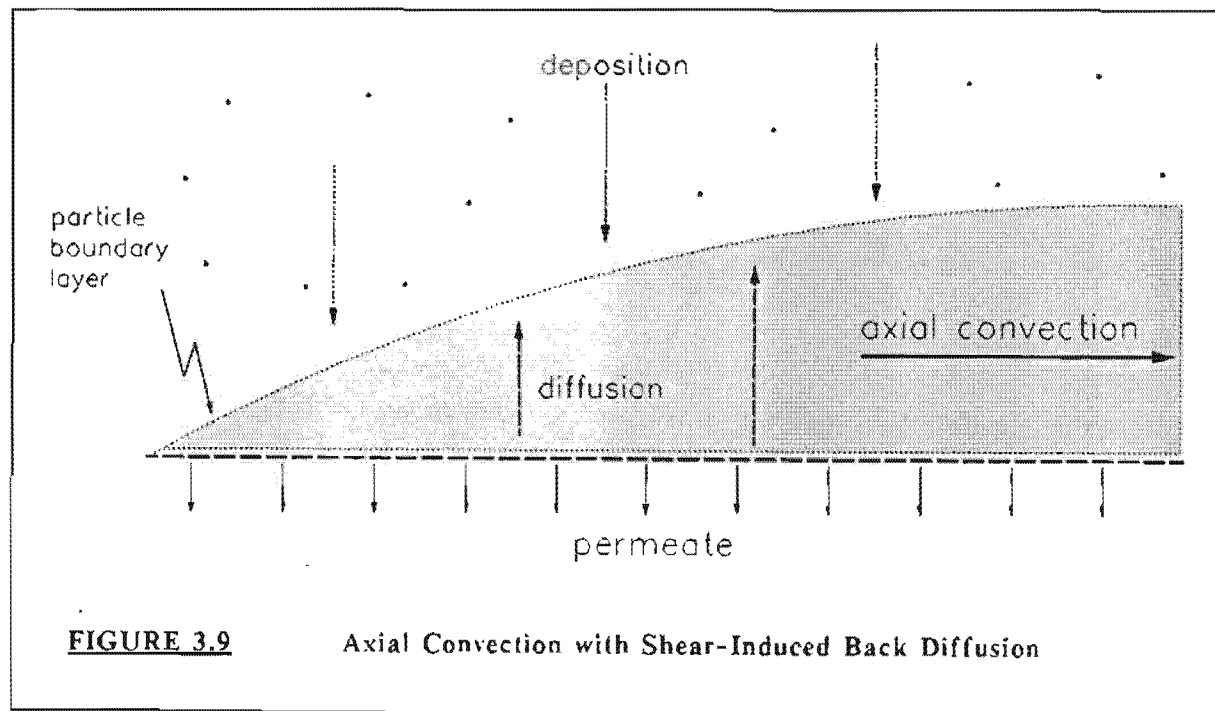
**FIGURE 3.8** Simple Axial Convection Model

To test model predictions and to visually monitor the convection phenomenon a CFMF channel with transparent side walls was constructed. At high fluxes it was observed that thick stagnant cake layers were formed. At lower fluxes thin layers formed within which it was observed that particles did indeed flow axially. Theoretical predictions for the thickness of these flowing layers were in order of magnitude agreement with observations, except at high thicknesses.

The observation that axially flowing particle layers do exist could superficially be viewed as proof of the mechanistic superiority of the convection model over other laminar CFMF models (e.g. lateral migration, shear enhanced diffusion). There are, however, a few points which militate against this conclusion. Firstly in Davis and Birdsell's experiments the resistance of the particle layer was negligible compared to the membrane resistance, and thus not typical of most CFMF systems. Secondly, for those data points where the theory approximates observations, the thickness of the flowing layers ranged from 180  $\mu\text{m}$  to 500  $\mu\text{m}$ . Noting that the particles used had a size range of 150 to 212  $\mu\text{m}$ , the flowing layers would have only consisted of one to three particles, hardly typical of CFMF. Lastly, there are indications that if particles flow axially along the tube in preference to forming a cake, this may merely be an effect associated with particle size. In the present study an attempt was made to filter a suspension consisting of spherical polystyrene beads of size range 100  $\mu\text{m}$  to 400  $\mu\text{m}$ . It was found that the particles did not form a cake but merely travelled along the tube, eventually blocking up the reject line. In contrast when limestone ( $d_p = 5 \mu\text{m}$ ) was used at the same operating conditions, a cake formed readily. These are thus strong indications that Davis and Birdsell's observation of flowing particle layers may only be limited to a narrow range of axial flow, flux and particle size.

In an improvement over the simple convection flow model, Davis and Leighton (1987) introduced the convection-diffusion model. A particle layer concentrated at or near its maximum packing density will not flow easily. Davis and Leighton proposed that within the particle layer the mechanism of shear induced hydrodynamic diffusion will result in a fluidisation and resuspension of the layer, which will then flow axially. The significant transport mechanisms in this model are depicted in Figure 3.9. A "local" model was developed, enabling the prediction of the particle layer thickness, velocity and concentration profiles with the layer and the wall concentration at any point along the tube, for an assumed permeate flux. The improved viscosity and shear induced diffusivity correlations developed by Leighton and Acrivos (1986) were employed. The "local" model also predicts the conditions at which a stagnant cake layer will form below the flowing layer.

The "local" model was subsequently incorporated into a "global" model by Romero and Davis (1988). The global model enables the prediction of the thickness of the flowing layer, thickness of stagnant cake layer (if any) and permeate flux with axial distance. No direct comparison with experimental observations has been made for either the local or global models, although it is claimed that the model is in qualitative agreement with experimental trends.



### 3.2.4 Scour/Erosion Models

In this class of models, correlations and models developed for the fields of sedimentation and slurry transport in pipelines are adapted to CFMF. It is instructive to firstly briefly review those fields and their relevance to the problem at hand.

Sedimentation includes the processes of erosion, entrainment, transportation, deposition and compaction of sediment. Of major interest to workers in the sedimentation field are the critical conditions at which a bed of sediment at the bottom of a river or canal will erode. This is probably analogous to the critical conditions at which deposition will cease in a CFMF system. The general approach adopted in sedimentation has been to define a *critical shear stress* at which sediment motion is incipient. Notable amongst these is the work of Shields - the classical Shields curve for incipient sediment motion [Raudkivi (1967)]. A review of these efforts is presented by Simons and Senturk (1976) and Raudkivi (1967). A large body of work has also been performed on the turbulent dispersion of suspended sediment, analogous to the turbulent radial mixing in CFMF systems. Good reviews of these dispersion models are presented by Raudkivi (1967) and Yalin (1972).

The differences between CFMF and sedimentation are, however, significant. Sedimentation correlations and models have been developed for length scales orders of magnitude greater than that in CFMF. The driving force for deposition differs in each instance. Further, very little hydrodynamic similarity exists between the system. These aspects preclude the direct application, or easy adaptation, of sedimentation technology to CFMF.

Closer to the field of CFMF in terms of length scales is the field of slurry transportation in pipelines. A vast body of work has been performed on the *critical threshold velocity* required to maintain a bedload-free flow of suspension. This has resulted in a proliferation of semi-empirical correlations which, in general, show very little correspondence to each other [Turian et al. (1987)].

A good review and evaluation of the better critical velocity correlations is presented by Turian et al. (1987) and Wasp et al. (1977). Recently, there has been a trend towards models with a strong mechanistic and theoretical basis, especially for models to predict the velocity and concentration profiles in a pipe. Significant amongst these are the works of Roco and Shook (1985) and Hsu et al. (1989). In general, slurry transport models and correlations have been developed for bulk concentrations substantially higher than that in CFMF systems, concentrations at which particle-particle interactions and slurry velocity may exert a significant influence on system behaviour.

An example of a model developed from sedimentation technology is the Scour Model of Fane et al. (1982). They proposed that at the steady-state the rate of convective transport towards the cake is balanced by the rate of scour away from it :

$$V_{cs} C_b^* = - \left( \frac{\partial \delta_{ss}}{\partial t} \right) C_w^* \quad (3.28)$$

where  $(\partial \delta_{ss} / \partial t)$  = rate of scour

$C_b^*$  = bulk concentration (mg/l)

$C_w^*$  = wall concentration (mg/l)

Following Raudkivi :

$$\left( \frac{\partial \delta_{ss}}{\partial t} \right) = - K_e \gamma \quad (3.29)$$

where  $K_e$  = erosion coefficient

= function(*concentration, nature of solids*)

$\gamma$  = shear rate

= function( $U_c$ )

Assuming a power law relationship between  $K_e$  and  $C_b^*$ :

$$K_e \propto (C_b^*)^{k_{14}} \quad (3.30)$$

where  $k_{14}$  = a constant

From equations 3.28 to 3.30, and noting that  $C_w^*$  is a constant for a given suspension,

$$V_{cs} \propto \frac{K_e (\bar{U}_c)^{k_{15}}}{C_b^*} \\ = k_{16} (C_b^*)^{k_{17}} (\bar{U}_c)^{k_{15}} \quad (3.31)$$

where  $k_{15}, k_{16}, k_{17}$  are regression constants.

The utility of the scour model is limited to the correlation of experimental results and does not elucidate the mechanistic particle transport processes. As a correlation method it proves useful, showing a good agreement between observed and predicted fluxes for a wide range of systems [Fane et al. (1982)]. Since the main objective here is to develop a mechanistic model, the scour model will not be pursued further. It should also be noted that equation 3.31 predicts a log-log relationship between flux and bulk concentration, in contrast to the semi-log relationship observed in the present study (see Figure 2.15).

An example of a model developed from slurry transport technology is that of Scarlett and Treasure (1974), reported in Murkes and Carlsson (1988). The model is an adaptation of Durand's correlation for the critical velocity :

$$\bar{U}_{crit} = 2,43 \frac{C^{1/3}}{C_D^{1/4}} \left[ 4gR \left( \frac{\rho_s}{\rho_l} - 1 \right) \right]^{1/2} \quad (3.32)$$

where  $\bar{U}_{crit}$  = critical deposition velocity (m/s)  
 $C$  = bulk concentration (volume fraction)  
 $C_D$  = drag coefficient for spheres  
 $\rho_s, \rho_l$  = densities of solids and liquid ( $\text{kg/m}^3$ )  
 $g$  = gravity ( $\text{m/s}^2$ )  
 $R$  = pipe radius (m)

Scarlett and Treasure proposed that the gravity,  $g$ , in equation 3.30 could be replaced by an *equivalent gravity*,  $g'$ , derived from fluidisation theory :

$$g' = \frac{\Delta P}{(1-\beta)(\rho_s - \rho_l)t_c} \quad (3.33)$$

where  $\Delta P$  = pressure drop across cake (Pa)  
 $\beta$  = cake voidage  
 $t_c$  = cake thickness (m)

The hydraulic resistance equation is given by :

$$V_w = k_{18} \frac{\Delta P}{\mu(t_{eo} + t_c)} \quad (3.34)$$

where  $k_{18}$  = permeability constant  
 $t_{eo}$  = equivalent resistance of filter medium (m)  
 $V_w$  = permeate velocity (m/s)

Combining equations 3.32 to 3.34 and rearranging yields :

$$V_w = \frac{k_{18} \Delta P}{\mu} \left( \frac{h_2^2 \Delta P}{(h_3 \bar{U}_{crit}^3 + h_4 \bar{U}_{crit}^{3.5} + 0,28 \bar{U}_{crit}^4)^{1/2}} + t_{eo} \right)^{-1} \quad (3.35)$$

where

$$h_2 = 2,43 C^{1/3} \left( \frac{4R}{(1-\beta)\rho_l} \right)^{1/2}$$

$$h_3 = \frac{21 \mu}{d_p \rho_f}$$

$$h_4 = 6 \left( \frac{h_3}{21} \right)^{1/2}$$

Evaluation of the mechanistic basis of the model is difficult. The Durand correlation is highly empirical. Further, the rationale for the combination of equations 3.32 to 3.34 is not blatantly obvious and neither is the *equivalent gravity* concept represented by equation 3.33. Murkes and Carlsson, however, assert that the above model is "... *the only complete theoretical approach known...*".

### **3.3 MODELLING APPROACH**

From the literature review in Section 3.2 it is clear that proposed mechanisms for cake growth and limit vary widely. The two models proposed specifically for turbulent flow, viz. the critical drag force model and the turbulent back diffusion model, are based on completely different controlling mechanisms, yet each provides a reasonable fit, in terms of trends and values, to its particular experimental data set. It must be noted that in each instance there is an *a priori* assumption for the mechanism responsible for limiting cake growth.

Clearly, there must be some 'common thread' in turbulent CFMF systems. The processes responsible for the convection of the solids to the cake, the growth of the cake and transport away from the cake must be similar in all systems. The controlling process could, however, differ from system to system, and could be a function of the operating regime, suspension physical properties, cake properties etc. The logical point of departure in modelling the system, therefore, would be to firstly develop a complete overview of particle transport processes in turbulent CFMF systems, detailing the likely mechanisms by which particles may be exchanged between the cake and the bulk suspension. Then system behaviour under the action of different controlling mechanisms may be assessed and compared to experimental observations.

It was previously noted that for particles of size ranges typical in CFMF, *inherent* or Brownian movement is negligible. Any particle motion which does occur is due solely to the fluid motion and fluid-particle interactions (neglecting gravity effects). The point of departure in resolving the particle transport processes in the system, therefore, is to examine the fluid dynamics and fluid-particle interactions in the system.

In Section 3.4, the fluid dynamics of turbulent flow in a porous tube is examined and radial flow regimes identified. In Section 3.5 fluid-particle interaction and particle dynamics in these various flow regimes are investigated. These are then combined in Section 3.6 and Section 3.7 to yield a description of particle transport processes in a CFMF tube and hence a qualitative model of the mechanisms responsible for cake growth and its eventual limit.

### **3.4 FLUID DYNAMICS OF TURBULENT FLOW IN A POROUS TUBE**

The objective here is to identify fluid flow regimes and transport mechanisms that are likely to exist in turbulent CFMF systems. Most studies on the fluid dynamics of turbulent flows have been limited to pure fluids in non-porous tubes. Relevant concepts from these studies will be outlined, and the effects that flow through the wall and the presence of particles are likely to have on the fluid dynamics will be investigated.

Unless otherwise stated, the contents of Sections 3.4.1 and 3.4.2 may be referenced in Brodkey (1967), Hinze (1975) or Schlichting (1968).

#### **3.4.1 General Description of Turbulence**

The major feature of turbulent flows is the spontaneous, chaotic, random motion of lumps of fluid, called *turbulent eddies* or *balls of turbulence*, superimposed on the bulk flow. This manifests as a fluctuation in fluid properties (velocity, pressure etc.) superimposed on the time-averaged mean values. The presence of these velocity fluctuations contribute a mean  $x$ -directional momentum flux of  $\rho \bar{U}'V'$ , where  $U'$  and  $V'$  are the instantaneous fluctuating components of the velocity in the  $x$  and  $y$  directions respectively, at the point being considered ( $x$  refers to the direction of the bulk flow, and  $y$  refers to the direction normal to the bulk flow). In analogy to the microscopic exchange of momentum in viscous flows, this macroscopic exchange of momentum by turbulent eddies may be regarded as a turbulent shear stress :-

$$\tau_t = -\rho \bar{U}'V' \quad (3.36)$$

where  $\tau_t$  = turbulent shear stress (Pa)

$\bar{U}'V'$  = time averaged value of  $U'V'$  ( $m^2/s^2$ )

$\rho$  = fluid density ( $kg/m^3$ )

The effects of this macroscopic momentum transfer by eddies is most significant in the direction normal to the bulk flow, resulting in velocity profiles that are substantially flatter over most of the flow field than velocity profiles in viscous flows.

Two phenomenological theories of turbulent transport that are of interest are Boussinesq's *eddy viscosity* concept and Prandtl's *mixing length* concept. Boussinesq proposed that parameters of turbulent transport could be defined by analogy with the parameters of molecular transport. In analogy to Newton's viscosity relationship, he introduced the concept of eddy viscosity,  $\mu_t$ , relating the turbulent shear stress to the mean velocity gradient :-

$$\tau_t = \mu_t \frac{\partial \bar{U}}{\partial y} \quad (3.37)$$

where  $\bar{U}$  = time averaged axial velocity ( $m/s$ )

$\mu_t$  = eddy viscosity ( $kg/ms$ )

Subsequent refinements led to the introduction of the *eddy diffusivity of momentum*,  $\epsilon$ , defined by :

$$\epsilon = \frac{\mu_t}{\rho} \quad (3.38)$$

where  $\epsilon$  = eddy diffusivity of momentum ( $m^2/s$ )  
(also called *eddy kinematic viscosity*)

Thus,

$$\tau_t = \rho \epsilon \frac{\partial \bar{U}}{\partial y} \quad (3.39)$$

Prandtl proposed the concept of mixing length, akin to the mean free path in molecular transport. Packets of fluid would move through some distance in the longitudinal and transverse directions while maintaining their  $x$ -momentum. Relative to the surrounding fluid, the packet will cover a distance,  $l$ , proportional to its diameter, before it loses its integrity and mixes into the surroundings. This mixing length,  $l$ , is related to the turbulent shear stress by :-

$$\tau_t = \rho l^2 \left| \frac{\partial \bar{U}}{\partial y} \right| \frac{\partial \bar{U}}{\partial y} \quad (3.40)$$

The eddy diffusivity, is thus related to the mixing length by :-

$$\epsilon = l^2 \left| \frac{\partial \bar{U}}{\partial y} \right| \quad (3.41)$$

Neither  $\epsilon$  nor  $l$  may be predicted independent of experiment. However, these phenomenological concepts are valuably utilised in the correlation of turbulent velocity profiles and subsequently yield information on the turbulent transport in the system. In general,  $\epsilon$  and  $l$  are calculated from measured velocity profiles and known shear stress distributions, yielding the distributions of  $\epsilon$  and  $l$  across the flow field, and the effects of operating conditions on these distributions. Phenomenologically the  $l$  distribution indicates the eddy length scales and the  $\epsilon$  distributions the momentum diffusivity in the flow field.

### 3.4.2 Turbulent Flows in Non-Porous Tubes

Prior to examining the fluid dynamics in tubes, it is necessary to clarify the concept of *wall*. Fluid dynamics studies often refer to the *wall*, *distance from the wall*, and the *wall region*. This *wall* refers to any solid surface that bounds the flow field. In normal pipe flow, the boundary is the *wall* of the pipe itself. In CFMF systems, however, the boundary to the flow field is the *inner surface of the cake*, and not the tube wall. Hence, when reference is made to the *wall* in the rest of this text, it is important to note that this refers to the *inner cake surface*, if a CFMF system is being considered. If it becomes necessary to refer to the *wall* of a CFMF tube, this will specifically be referred to as the *tube wall*.

Pipe flow is a specific instance of *wall flows* i.e. flows in which the turbulence is affected by the presence of a solid boundary. The flow field may divided into three sub-regions (Figure 3.10). At the solid boundary, the axial velocity is zero due to the no-slip boundary condition. Next to the wall is a thin region, the *viscous sublayer*, where the velocity gradient is at its maximum and where viscous effects dominate over inertial ('turbulence') effects. Above this sublayer, inertial effects progressively increase and are of the same order of magnitude as the viscous effects. This constitutes the *buffer* or *intermediate zone* and is also the zone of maximum turbulence intensity ( $U''/\bar{U}$ ). Far from the wall the flow becomes fully turbulent with dominating inertial effects and negligible direct viscous effects - the *fully turbulent zone*.

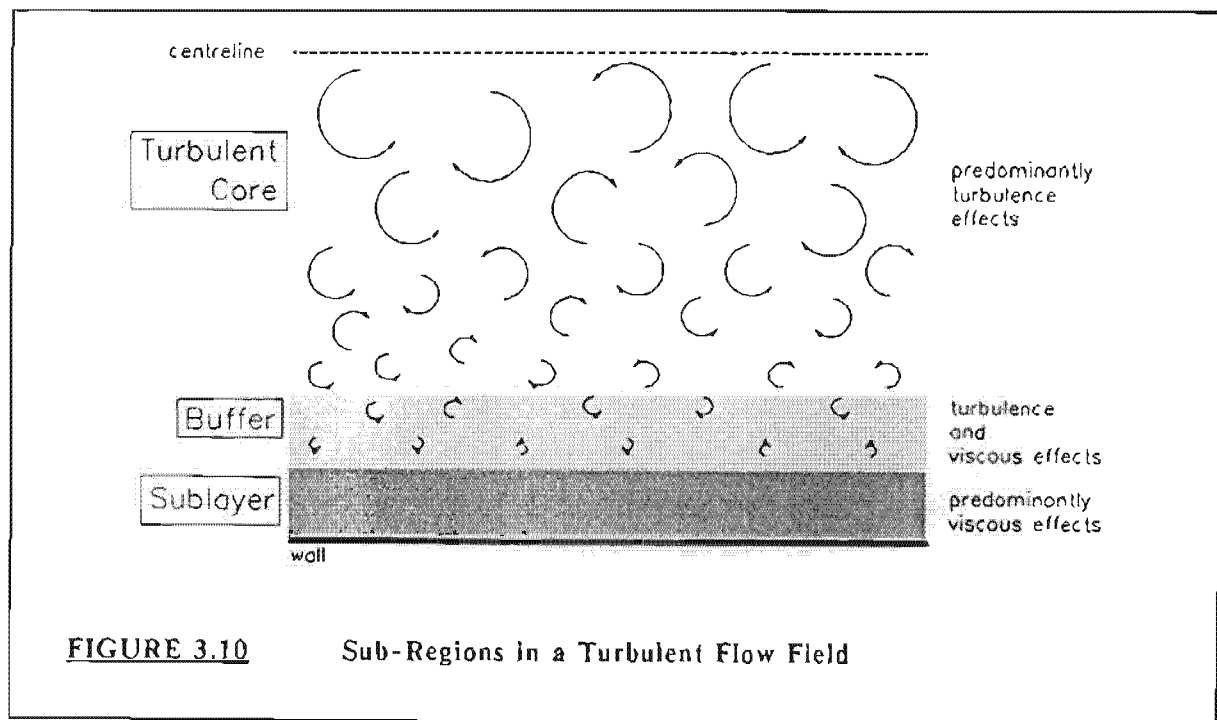


**FIGURE 3.10** Sub-Regions in a Turbulent Flow Field

Various researchers have measured the velocity profiles in, and thicknesses of, these zones. This has resulted in *universal velocity profile* for wall flows (Figure 3.11), in which a non-dimensional velocity,  $U^*$ , has been correlated with a non-dimensional distance from the wall,  $Y^*$ , where :-

$$U^* = \frac{U}{U'} \quad (3.40)$$

$$Y^* = \frac{Y}{\nu} \quad (3.43)$$

with     $U$     = axial velocity (m/s)  
            $Y$     = distance from wall (m)

$\nu$  = kinematic viscosity ( $m^2/s$ )

$U^*$  = friction velocity

$$= \sqrt{\frac{\tau_w}{\rho}}$$

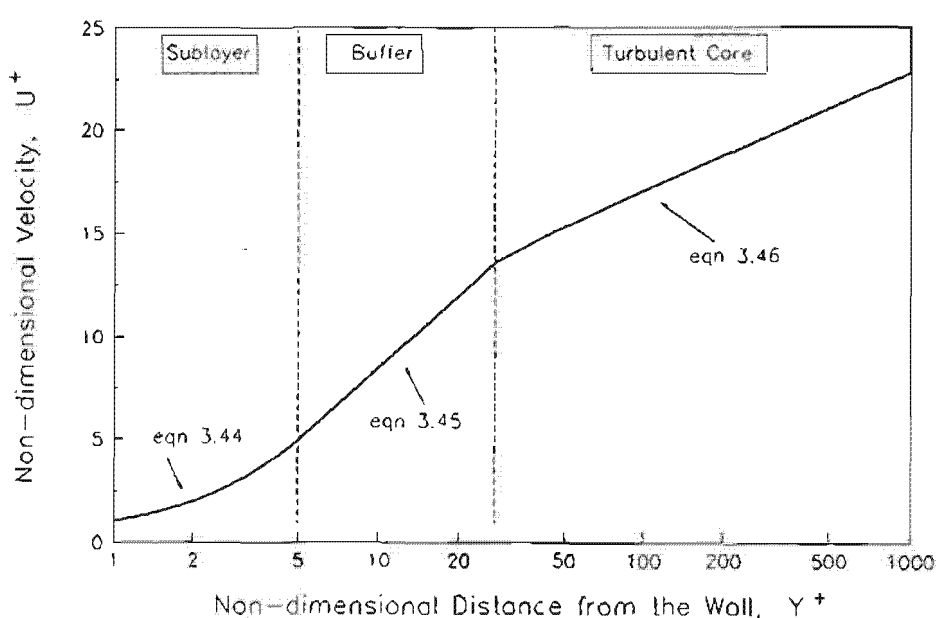


**FIGURE 3.11**      **Universal Velocity Profile for Turbulent Flow**  
 [from Welty et al. (1976)]

The profile may be represented by three equations :-

laminar sublayer      ( $Y^+ < 5$ )       $U^* = Y^*$       (3.44)

buffer zone      ( $5 < Y^+ \leq 30$ )       $U^* = 5 \ln Y^* - 3.05$       (3.45)

fully turbulent zone      ( $Y^+ > 30$ )       $U^* = 2.5 \ln Y^* + 5.5$       (3.46)

The universality of Figure 3.11 is seen in that it applies equally well to cartesian and cylindrical geometries, and to gases and liquids [Nedderman (1961)].

A dimensional version of the velocity profile is presented in Figure 3.12, calculated at typical conditions used in this study. The viscous sublayer is typically one order of magnitude greater than the diameter of the particles used in this study ( $d_p = 5\mu m$ ). This indicates that the important mechanism governing particle transport near the cake will occur in the sublayer and buffer zones, warranting a more detailed investigation into those regions. This is pursued further a few paragraphs henceforth.

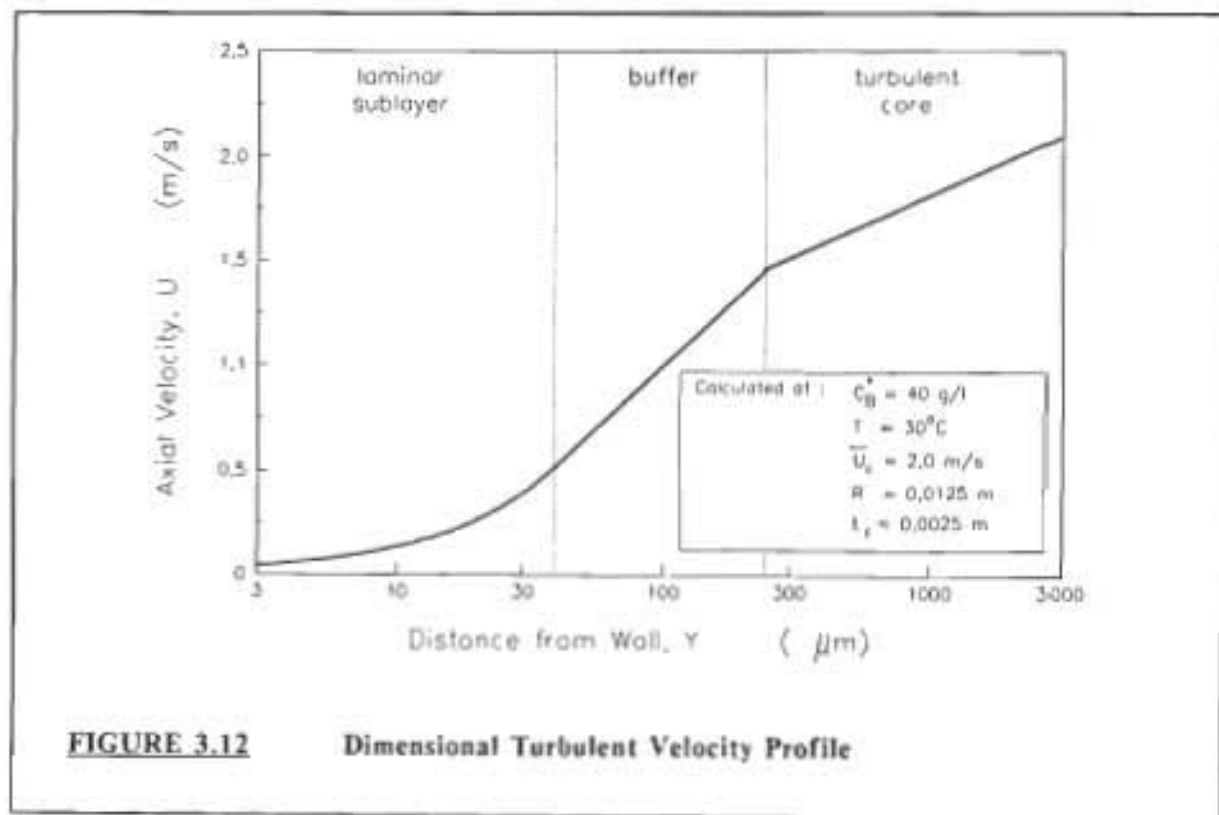


**FIGURE 3.12** Dimensional Turbulent Velocity Profile

From the universal velocity profile, the radial distribution of  $\epsilon$  and  $I$  may be calculated using equations 3.37 to 3.40, and the well known distribution of shear stress in pipes<sup>4</sup> :-

$$\tau(r) = \tau_w \frac{r}{R} \quad (3.47)$$

where  $\tau(r)$  = shear stress at radius  $r$

$\tau_w$  = shear stress at wall

$R$  = tube radius (m)

<sup>4</sup> It will be shown in Chapter 8 that calculation of the eddy diffusivity of momentum from the universal velocity profile is invalid. For the present purpose, where only trends are required, this is acceptable.

The radial distribution of  $\ell$  for high Reynolds Numbers is depicted in Figure 3.13. The distribution is relatively insensitive to  $Re$ , and is almost independent of  $Re$  for values above  $10^5$ . The mixing length, and hence phenomenological eddy size, progressively increases from the wall and levels off towards the centreline. This is consistent with statistically correlated eddy sizes which also indicated that eddies are largest in the centre of the tube and progressively decrease in size towards the wall, eventually vanishing in the sublayer. Statistical studies on turbulence structure have, however, also shown that eddies at any point in the flow field do not possess a unique size but consist of a spectrum of sizes. For the purposes of this study,  $\ell$  may be assumed to be the *effective* eddy size as defined by equation 3.40.

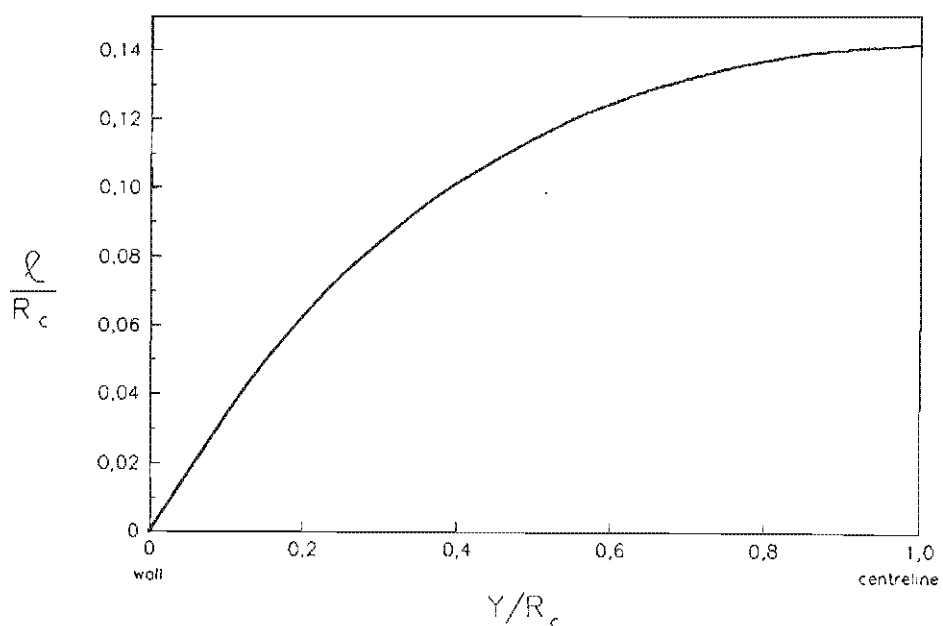


**FIGURE 3.13** Radial Distribution of Prandtl's Mixing Length  
[from Schlichting (1968)]

The distribution of  $\epsilon$  in pipes is shown in Figure 3.14. The diffusivity of momentum is high in the core, and progressively decreases towards the wall, eventually vanishing in the sublayer where the molecular viscosity becomes predominant.

What emerges clearly from both the  $\ell$  and  $\epsilon$  distributions is that the core of the tube is highly turbulent with relatively large eddies, and both the eddy size and the effective diffusivity that results from the eddies progressively decreases towards the wall, eventually diminishing in the viscous sublayer.

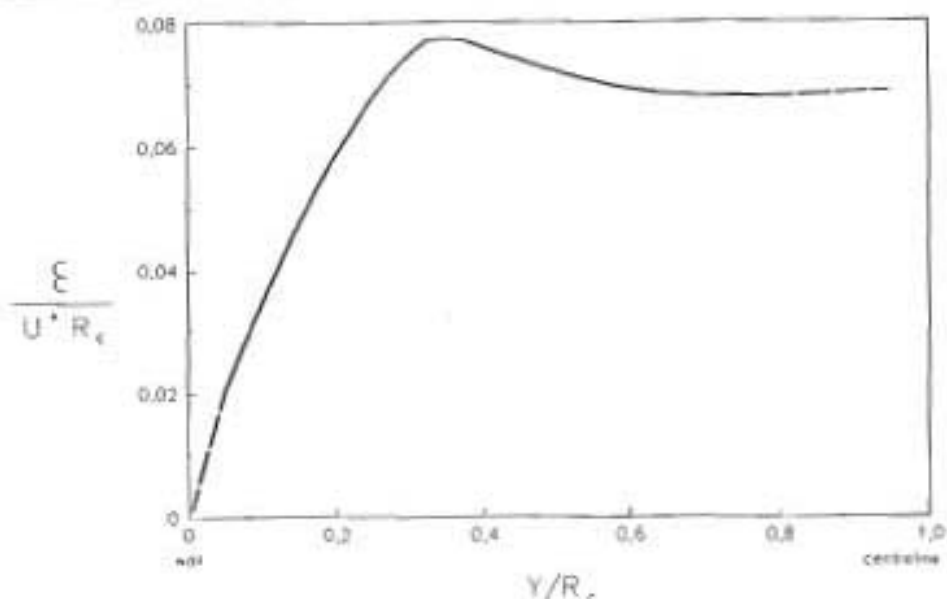


**FIGURE 3.14** Radial Distribution of Eddy Diffusivity of Momentum [from Schlichting (1968)]

Classically, the viscous sublayer has been regarded as a steady, laminar flow region [Schlichting (1968)]. Various workers in the fields of heat and mass transfer in turbulent systems have noted that the assumption that  $\epsilon = 0$  in the sublayer leads to the calculation of wall fluxes that are too low when compared to experimental values [Notter and Sleicher (1971)]. This led to the postulation that some eddy activity does exist in the sublayer and resulted in a proliferation of studies on the likely form of the eddy diffusivity relationship in this region [e.g. Notter and Sleicher (1971), Son and Hanratty (1967), Hughmark (1968, 1971, 1973)]. In general, the proposed relationships have the form :-

$$\frac{\epsilon}{v} = \text{function } (Y^+) \quad (3.48)$$

The expressions are all empirically evaluated, by fitting the equation to measured heat and mass transfer rates.

Recently, detailed visual observations of the sublayer indicate clearly that the zone is not laminar in the strictest sense, but that large scale, cyclic motions occur within the sublayer [Corino and Brodkey (1969)]. The major feature of these motions is the sudden, violent ejection of lumps of fluid from the sublayer into the buffer zone, in a direction almost normal to the wall. This phenomenon has been termed a *turbulent burst*, and consists of three phases (Figure 3.15).

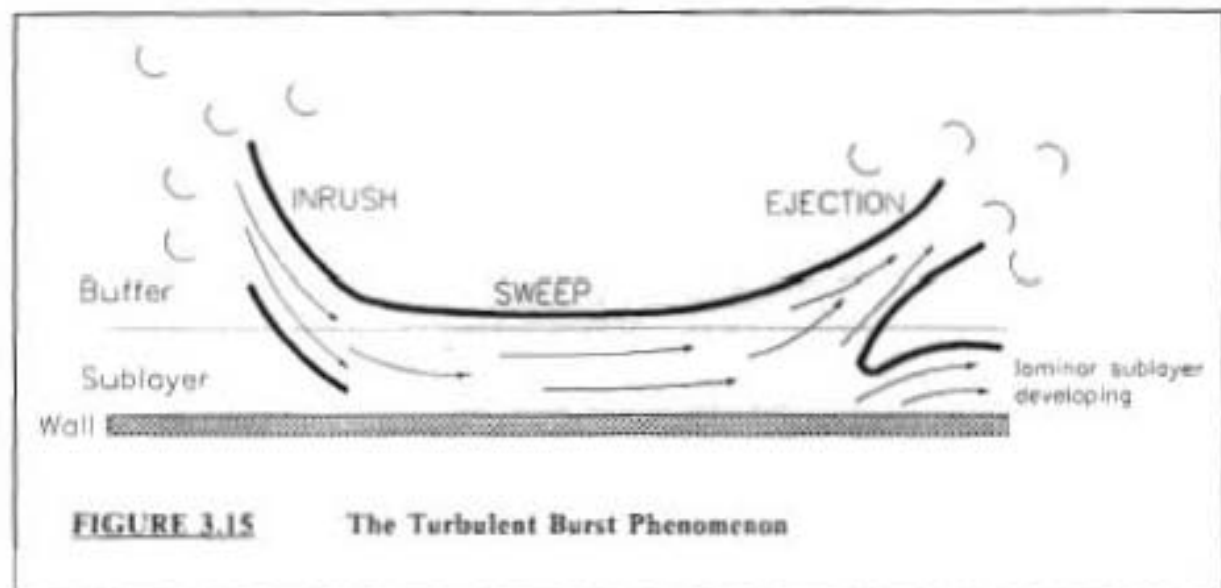


**FIGURE 3.15** The Turbulent Burst Phenomenon

High-speed fluid from the outer region enters the sublayer - the *inrush* phase. The fluid then travels for some distance parallel to the wall, progressively becoming more unstable - the *sweep* phase. The fluid is then suddenly ejected out of the zone in the form of a discrete fluid lump - the *ejection* phase. The ejection generally originates from the region  $5 < y^+ < 15$ , although ejections have been observed down to  $y^+ = 2.5$ . Below  $y^+ = 2.5$  the velocity gradient is essentially linear at all times, but with a widely varying slope, indicating that although this region is not active in the ejection phase it is nevertheless affected by the events occurring above it. The outer penetration depth of the ejected fluid element is random and the fluid is eventually accelerated and swept along with the axial flow. In terms of a 25 mm tube with water flowing at 2 m/s, the statistical average axial distance between bursts will be 6.35 mm and the frequency about 100 Hz [Yung et al. (1989)]. Although each burst may only cover a small fraction of the sublayer, the high frequency of bursts will result in the entire sublayer being swept within a short time.

Clearly the turbulent burst phenomena will result in transport rates from sublayer to buffer and turbulent zones being substantially greater than that predicted by purely viscous transport mechanisms. This is consistent with the view noted earlier, i.e. that the assumption of pure viscous flow in the sublayer leads to the prediction of heat and mass flows that are too low. Noting that the expressions for  $\epsilon$  in the wall region are evaluated by comparison with measured transport rates, it is most likely that the final correlations implicitly include the contribution of turbulent bursts to transport in the system. This will be addressed further in Chapter 5.

Davies (1975) expressed the view that turbulent bursts were merely turbulent eddies that had managed to penetrate the sublayer. The author of this thesis is clearly inadequately equipped to decisively comment on this. There are some superficial aspects, however, which mitigate against the equivalence of eddies and turbulent bursts. Firstly, Davies' viewpoint has not been reflected in the recent papers published by workers in that field, who all still refer to "turbulent bursts" [Yung et al. (1989)]. Secondly it is difficult to conceptualise how an eddy, a discrete

a lump of fluid, that penetrates the sublayer could result in the well defined three-stage activity that has been observed in the wall region. It is feasible that the initial inrush of fluid could be due to an eddy, but the subsequent sweep and ejection phases are not characteristic of eddy behaviour. In that instance it could be stated that the burst is caused by an eddy, but is a structurally different phenomenon. Finally, the burst activity has been observed to occur with a statistical regularity, both in distance and time, that is not consistent with the occasionally random penetration of the sublayer by an eddy. On the basis of these superficial comments, eddies and bursts will be regarded as separate phenomena in the rest of this study. Bursts will refer to inrush-sweep-ejection sequences that occur in the near wall region, and eddies will refer to large-scale random motions of lumps of fluid that occur in the buffer and turbulent zones.

### 3.4.3 Fluid Dynamics in Porous Tubes

The fluid dynamics of turbulent flow in porous tubes has not been studied as extensively as that of non-porous tubes. The most significant experimental work in this regard is that of Weissberg (1955, 1956). This section will be limited to the identification of the major differences between turbulent flow in porous and non-porous tubes.

The obvious difference is that in porous tubes the flow has a radial component,  $V$ , in addition to the axial velocity component,  $U$ . This radial velocity progressively increases from the centre of the tube towards the wall, but shows a decrease in the immediate vicinity of the wall (Figure 3.16). The effect of this radial flow on the fluid dynamics is seen in the axial velocity profile, turbulence levels, as well as the shear stress distribution.

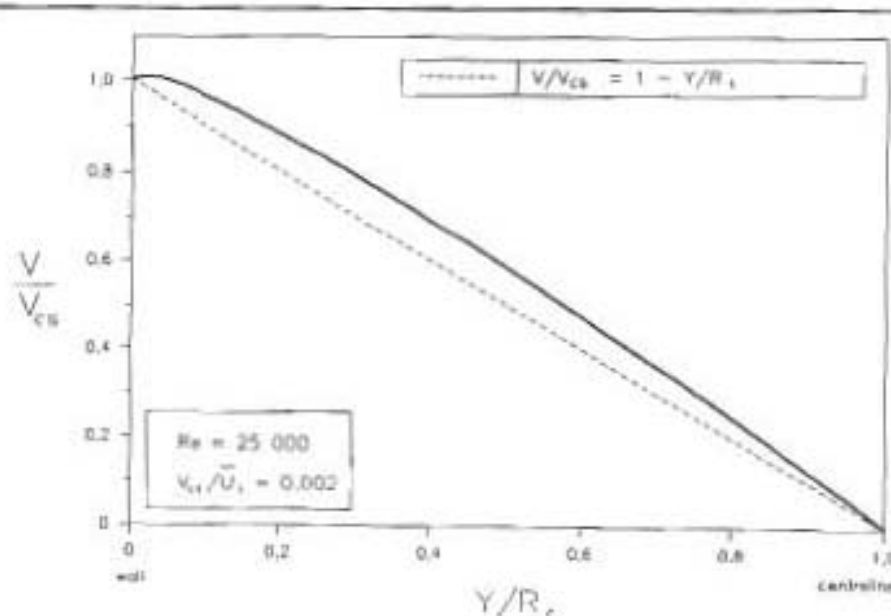


**FIGURE 3.16**

Typical Radial Velocity Profile  
[from Kinney and Sparrow (1970)]

The typical effect of radial flow through the wall (suction) on the axial velocity profile is shown in Figure 3.17. Over most of the cross section, the velocity gradient is flattened by suction, but is increased in the near wall region. Effectively, the shear rate at the wall increases, and the boundary layer thickness decreases, as suction is increased. Attempts to determine a universal velocity profile in the normal  $U^*$  vs  $Y^*$  form were unsuccessful, the data points not falling along a common curve as in the case of non-porous tubes [Weissberg (1955)]. Weissberg did, however, correlate his results in an empirical form. This will be addressed in Chapter 5.

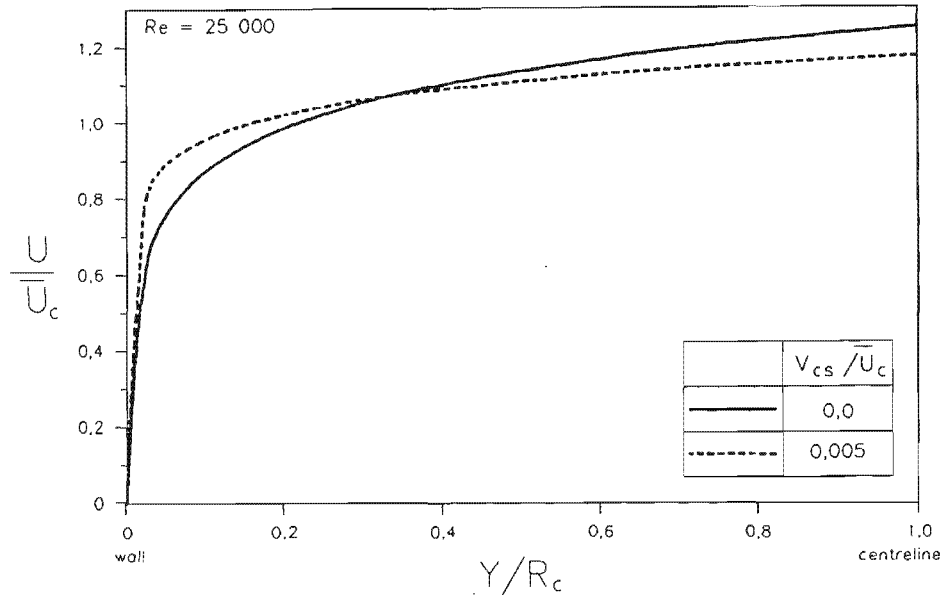


**FIGURE 3.17** Effect of Radial Fluid Flow on Axial Velocity Profile  
[following Weissberg (1956)]

Beavers and Joseph (1967) have shown that for flow in porous tubes the no-slip condition is not met at the wall since fluid can move axially within the porous wall. As noted by Belfort and Nagata (1985), however, for most common instances the deviation from the no-slip condition is negligible.

Weissberg observed that for all suction rates, turbulence levels across the entire cross section of the tube were lowered as suction increased. By implication, transport levels are likely to decrease with increasing suction. In the near wall region, however, the decrease in velocity fluctuations would to some degree be offset by the increased velocity gradient and the net effect on transport coefficients is difficult to ascertain. Skin friction coefficients for turbulent flow in porous tubes are greater than that in non-porous tubes, and increases as the suction rate is increased. This is in direct contrast to viscous flow in porous tubes, where the skin

friction coefficients are less than that in non-porous tubes and decreases as suction increases [Yuan and Finkelstein (1956), Pillay et al. (1988a, 1988b)]. The effect of suction on the stability or frequency of turbulent bursts is not known.

Effectively then the major effects of radial flow through the wall are a decrease in turbulence levels across the tube, an increase in the skin friction coefficient and a thinning of the boundary layer.

#### 3.4.4 Effect of Particles on Fluid Dynamics

The effect of particles on turbulence is dependent on particle concentration and size [Brodkey (1967), Soo (1967)]. If the particles are very small compared to the scale of turbulence ("size of eddies") they act as tracers, following the fluid elements closely. In this instance the presence of particles does not alter the turbulence structure substantially. As particle size increases relative to the scale of turbulence, a fraction of the available energy in the system is lost in dissipation to the particles, effectively dampening the turbulence. This dampening increases as the particle concentration increases. Eventually a total dampening of turbulence occurs as the maximum packing density of the particles is approached.

The turbulent burst phenomenon is also affected by the presence of particles. Grass (1974) observed that, similarly to eddies, bursts are also damped by the presence of particles.

#### 3.4.5 Summary of Fluid Dynamics

The major feature of turbulent flows is the presence of turbulent eddies which, *inter alia*, promote good momentum transport in the direction normal to the bulk flow. This momentum transport may be characterised by an *eddy diffusivity of momentum*,  $\epsilon$ . The length scale of eddies, and  $\epsilon$ , is high in the centre of the tube, the *turbulent core*, and progressively decreases towards the wall, eventually vanishing in the viscous zone next to the wall, the *sublayer*. Although predominantly viscous, the sublayer is periodically destabilised by the outward ejection of relatively discrete lumps of fluid, or *turbulent bursts*. These bursts enhance transport out of the sublayer. Above the sublayer lies a region where both viscous and turbulence effects are significant, the *buffer*.

In a porous tube, the fluid also has a radial velocity component which increases towards the wall. In general this results in the axial velocity profiles, turbulence levels and shear stress distributions in porous tubes differing from that in non-porous tubes, the extent of deviation increasing as the radial flow increases. By implication, radial transport coefficients in porous tubes would differ from that in non-porous tubes.

The presence of solid particles within the flow field tends to dampen the level of turbulence, the dampening increasing with particle size and concentration.

## 3.5 FLUID PARTICLE INTERACTIONS AND PARTICLE DYNAMICS

The objective here is to identify the likely particle transport mechanisms in the various flow regions identified in Section 3.4.

### 3.5.1 Particle Motion in a Turbulent Flow Field

Particle motion in a turbulent flow field is determined by the particle size and inertia, characterised by a *particle relaxation time*, and some characteristic scale of the turbulence [Brodkey (1967), Ni (1986)]. If the particle is large in comparison to the scale of the turbulence it will not respond to the fluctuating velocity components, and the main effect will be a dampening of the level of turbulence. On the other extreme, if the particle is small compared to the smallest eddies (i.e. *microscale of turbulence*) it will also act as a tracer particle and follow the detailed motion of the fluid elements in the eddy. Particles within these extremes are likely to have some mean velocity relative to the fluid and respond to some range of eddy sizes.

Particles which do respond to the fluctuating velocity components will also experience the random, chaotic motion associated with eddies. Clearly if a concentration gradient exists this eddy transport of particles will result in a transport in the direction of decreasing concentration, and may be characterised by an *effective turbulent particle diffusivity*,  $D_{\mu t}$ . Formally,  $D_{\mu t}$  accounts for the random motion of particles in a turbulent flow field, as induced by the diffusivity of the fluid [Soo (1967)].  $D_{\mu t}$  will be related to the diffusivity of momentum,  $\epsilon$ , but will not necessarily be equal to it. A quantitative discussion of this relationship is postponed to the chapter on Mathematical Modelling, Chapter 5.

### 3.5.2 Particle Motion in a Viscous Flow Field

In considering viscous flow fields, it is convenient to consider separately particle motion that occurs in arbitrary viscous flow fields, and particle motion that will specifically occur in the viscous sublayer of turbulent flow fields.

Two phenomena that apply to any viscous flow field have previously been discussed in Section 3.2, viz. the inertial lift effect and the shear induced hydrodynamic diffusion. To recap, the inertial lift theory proposes that particles in a viscous shear field will experience a lift force directed away from the wall, and will migrate across streamlines to some equilibrium position between wall and centreline. The shear induced hydrodynamic diffusion theory proposes that particles in a viscous shear field will experience particle-particle interactions that will result in a net diffusion in the direction of decreasing concentration.

The issue of particle motion in the viscous sublayer of a turbulent flow has for many years been of major interest to workers in the fields of fouling in exchangers, pipe transport of suspensions and river hydrology. The objective was to determine the mechanisms by which particles may travel across the sublayer to deposit on the wall and the mechanisms by which they may be re-entrained from the wall back into the bulk flow.

The question of how particles at a wall may be re-entrained back into the bulk flow is somewhat more problematic than may be initially perceived. Simplistically, it may be presumed that turbulent eddies could directly re-entrain particles from a wall. Mechanistically this is inconsistent with the known fluid dynamics in the near wall region which clearly indicates that eddies die out at some finite distance from the wall. Consequently, investigations into the re-entrainment process have focussed on developing alternative mechanisms for the detachment of particles from a surface and transportation of particles across the sublayer.

Most workers have tended to use a Saffman-type lift force to explain particles transport across the sublayer [see e.g. Soo and Tung (1972)]. Observations on the unsteady nature of the sublayer have resulted in mechanistically more attractive models, significant among which are Sutherland's *eddy entrainment* model [Sutherland (1967)], and Cleaver and Yates' *updraft under a burst* model [Cleaver and Yates (1973)]. Although Sutherland's model is based on the questionable concept of re-entrainment by eddies, the model is reviewed here since the experimental observations are of interest to the problem at hand.

Sutherland's proposals were based on the observation of grain motion and sublayer structure in a laboratory flume. At low axial fluid velocities (well below the *critical condition for particle entrainment* criterion used in the field of hydrology) isolated grains which protruded above the mean bed surface were observed to move axially along the surface. At slightly higher velocities, grains moved in the form of short intermittent bursts. With each burst, many grains moved simultaneously and then the motion subsided and the area remained relatively undisturbed until the next burst. The frequency of these bursts increased with increasing velocity and, at the critical condition, occurred about every two seconds at any specified point. At and above this critical condition, grain motion occurred mainly in the axial direction, parallel to the bed surface, with a few grains occasionally moving at a slight angle away from the bed. In further experiments, the structure of the sublayer was observed using a dye injection technique. A major feature was the sudden ejections of lumps of fluid out of the sublayer. The more violent ejections resulted in particles on the bed surface being set into motion, whereafter they moved axially with the flow<sup>5</sup>.

Sutherland proposed that the unsteady nature of the sublayer could be explained in terms of eddy penetration into that region. Particle entrainment will occur by eddies disrupting the sublayer and impinging onto the surface layer of grains. The swirling motion within the eddy will increase the local shear stress and cause some particles to roll along the surface. This defines the incipience of motion. This swirling motion within eddies will also exert a drag force on exposed particles, thereby accelerating them. The drag will consist of vertical as well as axial components. If the vertical component is sufficiently large, the resultant force on exposed particles will be inclined away from the bed resulting in these grains leaving the bed. Since each eddy would cover a number of particles, motion away from the bed would occur as bursts of particles. Evaluation of Sutherland's model is postponed to a few paragraphs hence.

<sup>5</sup> It is not clear from the paper whether, at the incipience of motion, particles were suddenly lifted vertically or whether they merely rolled over neighbouring particles into the flow field.

Cleaver and Yates (1973) model is based on the turbulent burst phenomenon described in Section 3.4.2. There, Corino and Brodkey's observations on fluid flow in the near wall region is described. Here, some of their observations on particle motion in that region will be outlined. Their investigations into the structure of the viscous sublayer were based on the monitoring of  $0.6\text{ }\mu\text{m}$  tracer particles in the near wall zone [Corino and Brodkey (1969)]. As noted previously, results indicated that violent ejections of the fluid occurred from the region  $5 < y' < 100$  and occasionally occurred down to  $y' = 2.5$ . The fluid below  $y' = 2.5$  remained passive with respect to the bursts. However, particles below  $y' = 2.5$  exhibited some motion "in sympathy" with the ejection. Particles were observed to move axially at a slight angle away from the wall, this *ejection angle* generally being  $-5^\circ$ . Particles rarely escaped the region  $y' < 2.5$  during the period of single burst. Particles then either moved back to the wall, presumably convected there by a new inrush phase, or reached the region  $y' > 2.5$  and were entrained by the next ejection phase.

On the basis of these observations, Cleaver and Yates proposed at the instance of an ejection, the fluid flow around a single, isolated particle would be as in Figure 3.18.

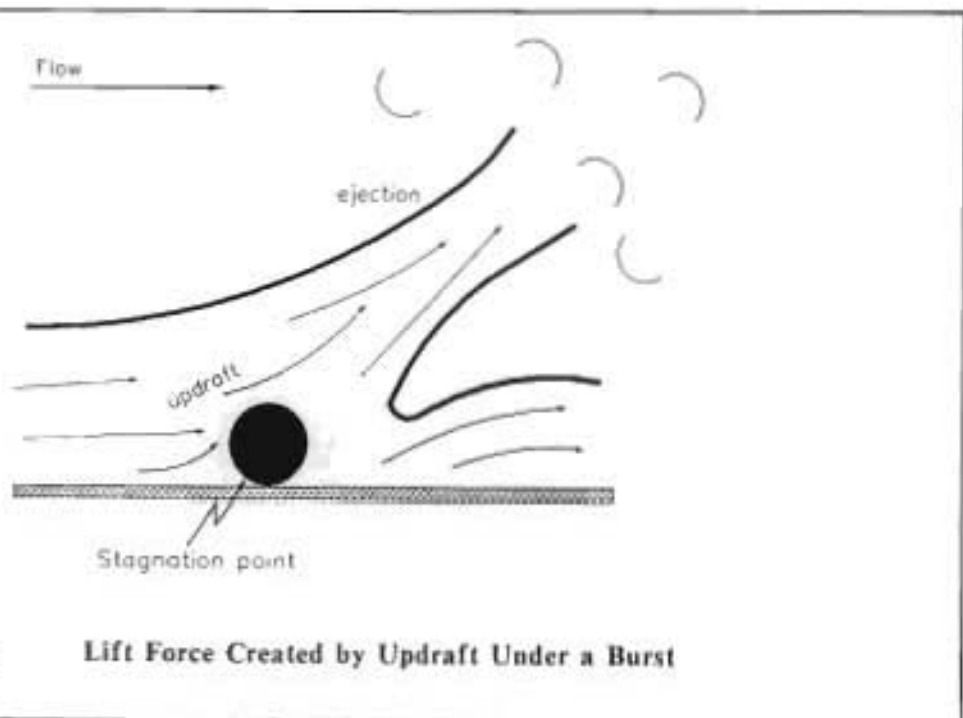


**FIGURE 3.18** Lift Force Created by Updraft Under a Burst

The ejection would induce a quasi-steady updraft of fluid. Near the wall, the flow would behave like a viscous stagnation point flow and would thus consist of both horizontal and vertical velocity components. The particle would, under the action of this vertical force, be lifted off the substrate and would subsequently describe a trajectory inclined slightly to the horizontal.

It was noted that the theoretical lift force experienced by the particle was extremely small, and orders of magnitude smaller than the axial drag force. However, this force was regarded as being sufficient to detach the particle from the substrate and move it through a vertical distance of one particle diameter during the period of the burst. Phillips (1980) has expressed the view that Cleaver and Yates' proposal of a lift force created by the updraft under a burst is the most satisfactory model for re-entrainment in turbulent flows.

Yung et al. (1989), however, have recently questioned whether the lift force created by the updraft would be sufficient to lift particles off the surface. In their experiments, the burst-particle interactions in the sublayer were monitored using dye injection together with high speed photography and a dual laser beam illumination technique. Their observations indicated that the lift force experienced by a particle during a burst is not as strong as suggested by Cleaver and Yates. Generally, particle motion occurred axially along the surface. The motion was intermittent, particles remaining stationary for a short time before resuming motion. Particles did not generally exhibit any upward motion when a fluid lump was ejected out of the sublayer. In a few instances, particles did exhibit an instantaneous vertical velocity component, but this was statistically rare. Their observations showed that at the incipience of particle re-entrainment, the horizontal force is dominant in the entrainment mechanism, in contrast to Yates' hypothesis of an instantaneous lift force that would be sufficient to detach particles from the surface. They concluded that "... the turbulent burst activity is insignificant in the re-entrainment of deposited particles completely submerged within the viscous sublayer".

A further significant study on burst-particle interactions is that of Grass (1974). In his experiments, the boundary layer was formed on a flat plate towed through still water, and the re-entrainment process recorded using a high-speed photographic technique. His observations indicated that the ejection events carried particles from the bed region through the entire boundary layer in single, continuous motions. The detailed mechanisms by which this re-entrainment occurred were not stated in the paper.

Clearly, diverse opinion exists on the role of turbulent bursts in particle re-entrainment. Prior to attempting to resolve the role, if any, of bursts in particle re-entrainment, it is instructive to contrast the experiments of Sutherland, and Corino and Brodkey. In both instances, the observations of fluid behaviour in the sublayer were similar. Sutherland attributed this behaviour to eddy penetration into the zone. Corino and Brodkey, in a more detailed examination, identified a three-step turbulent burst event as the cause of the behaviour. It is significant that Sutherland's proposal of eddy penetration was made solely to explain how sublayer destabilisation may occur, and further that his study was published two years earlier than the more detailed sublayer study of Corino and Brodkey. It thus likely that Sutherland's observations of the sublayer behaviour were in fact due to turbulent bursts, although he did not recognise it in terms of a three-phase event distinct from the phenomenon of eddies.

The role of bursts in particle re-entrainment may now be addressed. Grass' observations indicated that the ejection events do transport particles out of the wall region. Conversely, Yung et al. observed that particle motion occurs mainly in the axial direction, and particles rarely exhibited any vertical motion that could be correlated with the ejection events. This predominantly axial motion was also observed by Sutherland. It is difficult to identify specific differences in experimental conditions that may have led to these contradictory results. The particle size used by Grass ( $150 \mu\text{m}$ ) falls between the sizes used by Yung et al. ( $50 \mu\text{m}$ ) and Sutherland ( $268$  to  $512 \mu\text{m}$ ). The bulk and friction velocities used in Grass' experiment ( $U = 0,7 \text{ m/s}$ ,  $U^* = 0,029 \text{ m/s}$ ) are, however, slightly higher than that used by Yung et al. ( $U = 0,1$  to  $0,5 \text{ m/s}$ ,  $U^* = 0,01$  to  $0,026 \text{ m/s}$ ). From the available experimental evidence, no unequivocal conclusion may be drawn regarding the role of turbulent bursts in particle re-entrainment from the sublayer.

An alternative approach to the problem would be to identify the various steps involved in the re-entrainment of particles and to assess the possible role of turbulent bursts in these steps. The re-entrainment process may be divided into two stages :-

- (a) Step 1 - a particle must be detached from its stable position on the bed surface.
- (b) Step 2 - the particle must be transported across the sublayer and into the buffer zone.

From the available experimental evidence, it seems that ejection events will be capable of transporting particles that have reached the region  $y^* > 2,5$  across the rest of the sublayer, providing of course that the particles are not too large. The problem then resolves to assessing whether bursts can detach particles from the bed surface and transport them across the region  $y^* < 2,5$ .

Cleaver and Yates' proposal of a *lift force created under an updraft* that is capable of detaching particles from a surface is highly idealistic. The experimental observations of Yung et al. indicate clearly that this lift force, if it exists, does not manifest itself in terms of observed particle motion. A second criticism of the model is that the lift force arises solely as a result of the existence of the stagnation point. If a bed of particles is considered, it is seen that all particles will be embedded below some mean bed surface (Figure 3.19) and the fluid flow around each particle will differ from the simple picture presented in Figure 3.18. It is then difficult to conceptualise how stagnation points, and subsequently lift forces, may arise. Clearly, Cleaver and Yates lift force under an updraft cannot be the mechanism by which particles are initially detached from a bed surface.

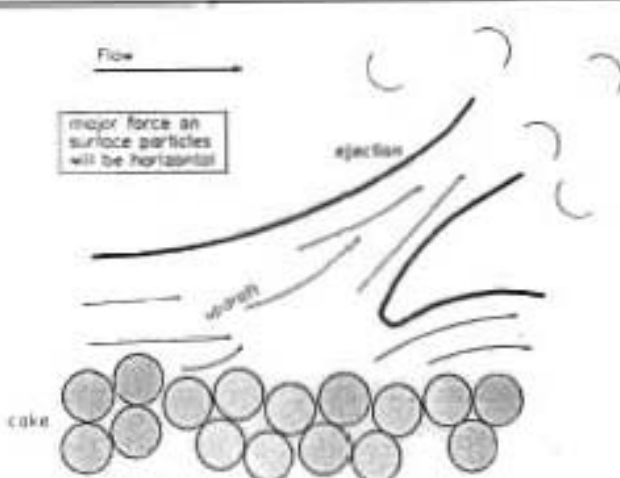


**FIGURE 3.19** Expected Fluid Flow Patterns at Cake Surface

A possible mechanism for the detachment of particles from a bed surface is as follows, based partially on Sutherland's model. A particle on a bed surface will be held there by, *inter alia*, its weight and various inter-particle forces. The axial fluid flow will exert an axial shear on the particle which if in excess of some critical value will cause the particle to roll about its point of contact with its neighbouring particles and thus off the bed surface. Thus, the initial step in the re-entrainment process is caused by the axial shear on the particles.

This proposed mechanism for the initial step in particle re-entrainment is consistent with the observation of Yung et al. (1989) that "... in the initial stage of particle re-entrainment, the horizontal force is the dominant force acting on the particle". Accepting this, it is seen that the only pre-requisite for this initial detachment of the particle is that the shear stress at the wall must exceed some critical value. Turbulent bursts may contribute to this by causing local increases in the wall shear stress, but in principle this initial stage is not dependent on the existence of bursts.

A particle that has been removed from the bed surface is then exposed to the predominantly axial fluid flow in the region  $y^* < 2.5$ . Now although the fluid in this region seems to be passive with respect to the ejection event, the fluid will be accelerated by inrush and sweep events and will subsequently decelerate when the ejection event occurs. This is confirmed by the observation that the region  $y^* < 2.5$  has an essentially linear velocity profile that varies widely and randomly [Corino and Brodkey (1969)]. Since the inrush event is directed towards the wall and the ejection event away from it, the fluid in this region will experience a periodic velocity component inclined away from the wall. Effectively then a particle in the region  $y^* < 2.5$  will experience a fluctuating drag force which is predominantly axial but with a periodic component normal to the wall. If the particle is relatively large, it may not respond to the normal component and will exhibit an intermittent axial motion. This is consistent with the observations of Yung and Sutherland. Smaller particles may respond to the periodic normal

drag and describe a trajectory inclined away from the wall. Such particles could then reach the region  $y' > 2.5$  and be entrained by ejection events. Thus, turbulent bursts could, indirectly, cause the transport of smaller particles across the region  $y' < 2.5$ , whereafter they may be directly entrained across the rest of the sublayer.

It would seem then that the initial step in the re-entrainment of particles from a bed could occur in the absence of bursts, but can be promoted by them. Larger particles which have been removed from the bed surface will tend to move axially along the surface and are not likely to be transported across the sublayer by bursts. Smaller particles may be transported across the region  $y' < 2.5$  by the indirect action of bursts and may subsequently be transported across the rest of the sublayer by direct entrainment by bursts.

In terms of the above model, re-entrainment, either directly or indirectly, by bursts will increase as particle size decreases and as the frequency and density of bursts increases. In typical CFMF system, the particle size is substantially smaller, and the bulk and friction velocity somewhat higher than that used in the studies of Yung, Grass and Sutherland. Since the frequency of bursts scales with  $U^{*2}$  and the density with  $U^*$  [Yung *et al.* (1989)] it is highly likely that transport of particles across the sublayer by turbulent bursts could be a significant transport mechanism in CFMF systems.

### 3.5.3 Summary of Particle Dynamics

Particles in the turbulent core and the buffer zone could also be entrained by eddies and will thus experience a transport in the direction of decreasing concentration. This may be characterised by an *effective turbulent particle diffusivity*,  $D_{\mu}$ , which will be a function of the eddy diffusivity of momentum,  $\epsilon$ .

Various mechanisms exist by which particles may be transported out of the sublayer and into the buffer zone. These include *shear induced hydrodynamic diffusion*, *lateral migration*, and *turbulent bursts*.

There appears to be little clarity on the mechanism by which particles are initially detached from a surface. On the basis of a simple model, consistent with detailed observations of particle motion in the near-wall region, it is most likely that the initial detachment occurs when a particle rolls over neighbouring particles and into the flow field, under the action of the axial shear stress at the surface.

### 3.6 MODEL DEVELOPMENT

In the Sections 3.4 and 3.5, the fluid dynamics in the tube and particle dynamics in the various flow regimes were examined. Prior to combining these into an overview of particle transport in the system, two "intuitively obvious" cake limiting mechanisms will be examined in greater detail. Criticism of these simpler models could possibly provide some indications as to the significant mechanisms that must be included in the final overview of particle transport in the system.

The major effects of turbulence include high momentum transport rates in the direction normal to fluid flow and hence high shear stresses and shear rates at the wall. Particles may also be transported by turbulent eddies and will thus also experience a high rate of transport down concentration gradients normal to the bulk flow. The two obvious cake growth limiting mechanisms that may be deduced from this are as follows :-

- Critical shear/drag model - it may be assumed that the cake grows until the fluid shear stress or drag at the cake surface reaches some critical value. Thereafter all particles which reach the cake surface will be unstable and will be sheared off the surface. The models of Rautenbach and Shock (1988) and Fischer and Raasch (1986) are examples of this.
- Turbulent back diffusion model - it may be assumed that the convection of solids towards the cake is offset by an eddy-induced turbulent back diffusion of particles from cake to bulk suspension. The limiting cake thickness is achieved when the rate of back diffusion equals the rate of convection to the cake. An example of this type of model is that of Hunt et al. (1987b)

As noted in Section 3.2, the critical shear model explains the observation that smaller particles are preferentially deposited as the operating velocity increases. Further, the observations made in Section 2.5.3.2, when the feed was switched to water, seem to be consistent with the postulation that removal of particles from the cake surface is controlled by the shear stress at the surface. Predicted trends for the effect of velocity on steady-state flux and cake thickness are also consistent with experimental observation.

The first criticism of the critical shear model is that it is not consistent with the flux-time behaviour obtained in Section 2.5.2. Assume that for some superficial inlet velocity  $\bar{U}_w$ , the limiting cake thickness is  $t_{cr}$ . During the growth of the cake when  $t_c < t_{cr}$ , all particles convected to the wall will deposit stably i.e. the system should behave like a dead-end filter. Hence, the cake thickness and flux profiles should follow the dead-end filtration profiles until  $t_{cr}$  is reached. Thereafter, the cake thickness will remain constant, but the flux could decline due to fines infiltration etc. Now assume that the system is operated at a velocity  $\bar{U}_{w*}$  such that  $\bar{U}_{w*} < \bar{U}_{w*}$ . The limiting cake thickness in this instance will be  $t_{cr}$  and will be greater than  $t_{cr}$ . Once again, for  $t_c < t_{cr}$  the system should follow the dead-end filtration flux and cake thickness profiles. Hence, the flux profile obtained at  $\bar{U}_{w*}$  should be the same as the profile obtained at  $\bar{U}_w$ , up to the steady-state point for  $\bar{U}_w$ . For all velocities therefore, the flux should follow the same dead-end filtration profile until the particular steady-state cake thickness is reached.

This expected behaviour is depicted in Figure 3.20. Curve 1 represents the expected flux-time curve for dead-ended filtration. Curves 2 to 6 represent the flux curves that will be obtained at different velocities if indeed the system behaved as inherently predicted by the critical shear model. Taking into account preferential deposition of sizes at different velocities curves 2 to 6 may deviate slightly from those depicted in Figure 3.20, but in principle the flux decline profiles and steady-state points should all derive from a common dead-end curve if indeed the critical shear model holds.

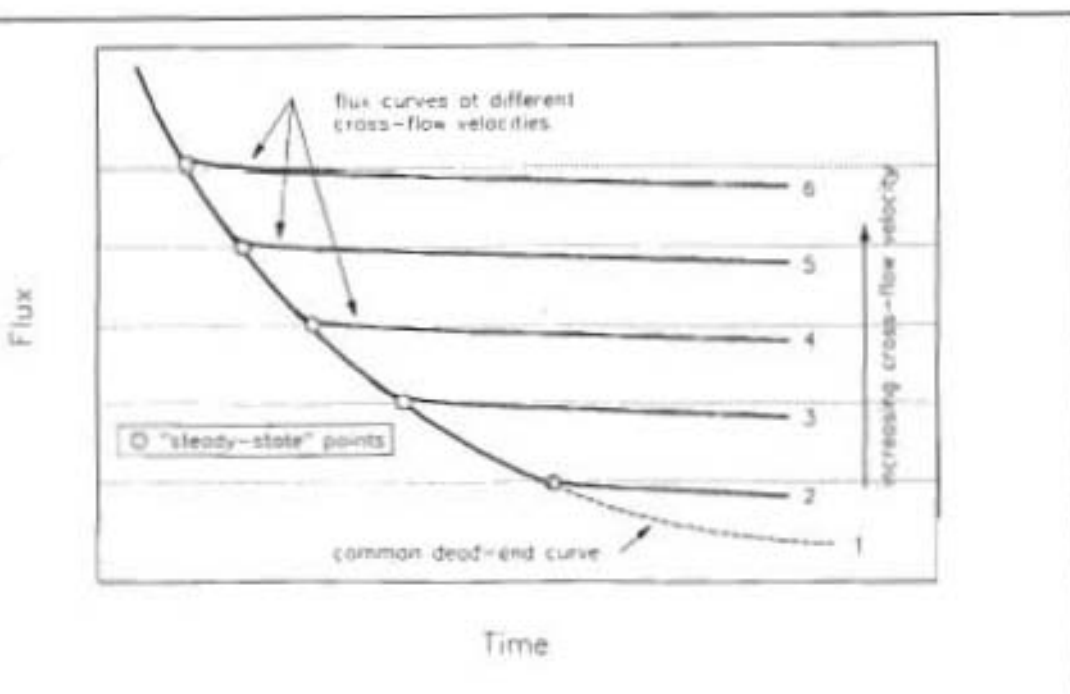


**FIGURE 3.20**      Expected Flux Decline Curves if Critical Shear/Drag Model Applies

This predicted behaviour has been observed in the CFMF of a Bingham plastic under laminar-flow conditions [Fordham and Ladva (1990)]. This predicted behaviour is, however, clearly different from the experimental flux-time responses obtained at different velocities in this study (Figure 2.9, repeated here for convenience). In the case of the experimental curves, each curve exhibits a different rate of decline almost from start-up and the flux-time curves up to the steady-state points clearly do not derive from a common dead-end curve. It would seem therefore that the rate of cake growth is a function of inlet velocity, and thus contradictory to predictions of the critical shear model.

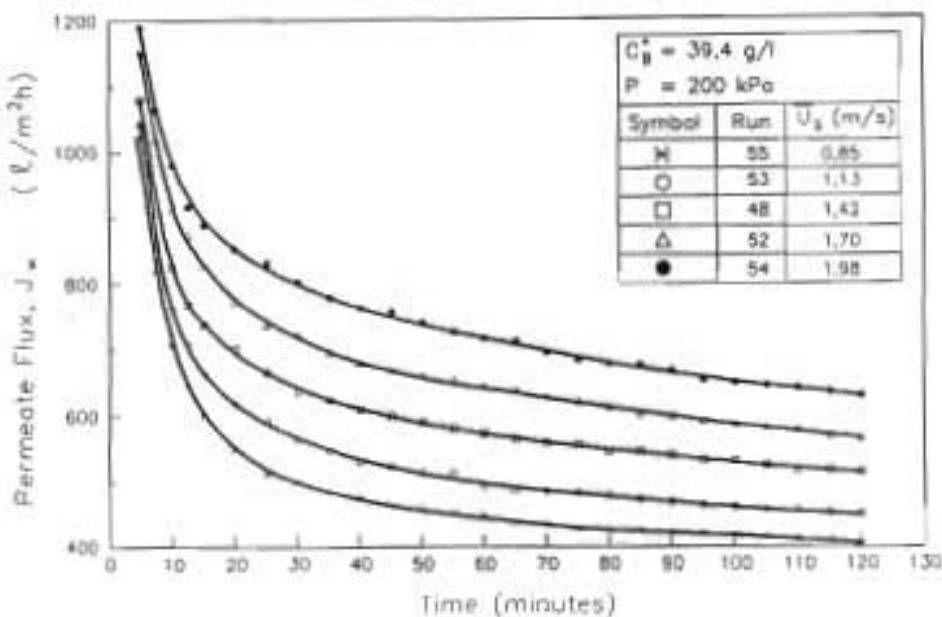


**FIGURE 2.9** Flux-Time Curves at Different Inlet Velocities  
(repeated)

The second flaw in the critical shear model concerns the trend predicted for the effect of concentration on steady-state flux and cake thickness. The drag force on a particle at the cake surface, or shear stress at the surface, will decrease as the concentration increases, indicating correctly that the cake thickness will increase with increasing concentration. In the mathematical formulation of the surface shear or drag, the effect of concentration manifests in the viscosity term [see e.g. Rautenbach and Schock (1988)]. In general, the viscosity of a suspension is a weak function of concentration at low concentration but increases substantially as concentration is increased. This implies that steady-state flux and cake thickness should show a weak dependence on concentration at low concentrations, but a strong dependence on concentration at high concentrations. This is completely contradictory to the trends observed in this study, where the flux is strongly dependent on concentration at low concentrations, but weakly so at higher concentrations.

Finally, although not explicitly stated in the critical shear model, some other back transport mechanism must be occurring simultaneously with the shearing mechanism at the cake surface. After the critical shear or drag has been achieved at the cake surface, particles will still be convected towards the cake by the radial fluid flow, although they will not deposit. A mass balance over any control volume next to the cake surface indicates that unless some mechanism exists to remove particles from the volume at the same rate at which they convect into it, then the concentration in the control volume will increase continuously. Effectively then, the critical shear model is only applicable if some other back transport mechanism exists, and occurs at a rate equal to or greater than the rate of convection of solids towards the cake.

The turbulent back diffusion model, similarly to the critical shear model, predicts the correct trend for the effect of velocity on steady-state flux and cake thickness. With regards to concentration, any diffusion model (e.g. equation 3.14) predicts a linear relationship between flux and log concentration. This is consistent with experimental observations made in this study, indicating the superiority of the turbulent diffusion model with respect to concentration effects.

In the diffusion model, the cake will not grow at the same rate as in a dead-end filter, since deposition of particles onto the cake is offset by a simultaneous back diffusion of particles from the cake. The rate of growth of cake is thus given as :-

$$\begin{aligned} \text{Net rate of deposition} &= (\text{rate of convection to cake}) \\ &\quad - (\text{rate of back diffusion}) \end{aligned}$$

Now,

$$\begin{aligned} \text{rate of convection to cake} &= \text{function}(V_{zr}, C) \\ \text{rate of back diffusion} &= \text{function}(\bar{U}_r, \text{suspension properties}) \end{aligned}$$

Thus, the turbulent back diffusion model predicts that the rate of growth of cake should be a function of  $\bar{U}_r$ , and hence a function of  $\bar{U}_r$  and  $t_c$ . According to this model therefore the rate of decline of flux would be a function of inlet velocity and should differ appreciably from a dead-end curve. This is consistent with the experimental obtained flux-time responses (Figure 2.9), once again indicating the superiority of the turbulent back diffusion model over the critical shear model.

The turbulent back diffusion model alone, however, fails completely to explain the observation that smaller particles are preferentially deposited as velocity increases, or that smaller particles preferentially infiltrate the cake after its formation. Indeed, an opposite effect is predicted. It was noted in Section 3.4.2 that a spectrum of eddy sizes would exist at any point in a turbulent flow field. For each eddy size range there would be a maximum size of particle that may be entrained by those eddies. Thus, larger particles will only be transported by the larger eddies while smaller particles will be transported by a greater range of eddy sizes, leading to the conclusion that smaller particles will exhibit a greater diffusivity than larger particles. Effectively, smaller particles should experience a greater rate of transport away from the cake, leading to a cake preferentially composed of larger particles. Clearly, a simple diffusion model alone cannot explain the preferential deposition effect.

A diffusion model alone also fails to explain the apparent irreversibility of the cake. If the only mechanisms of significance were the convection of solids towards the cake and a diffusion away from the cake, then on switching the feed over to water the rate of back diffusion would have greatly exceeded the rate of convection towards the cake, resulting in progressive removal of the cake. Similarly, when the velocity is increased, or concentration decreased, during a run the imbalance in rates of convection and back diffusion would cause the cake to decrease to the appropriate value, and the system would not exhibit any dependence on operating path.

A further flaw concerns the contradiction between the mechanistic basis of a simple turbulent back diffusion model and the known fluid dynamics of the near-wall region. Turbulent back-diffusion models generally assume that back transport occurs by eddies transporting solid from the high concentration cake to the low concentration bulk suspension. As stated by Hunt et al. (1987b) and Flemmer et al. (1982), "...random eddies penetrate the boundary layer to scour the cake beneath". In view of the known fluid dynamics in the near wall region, this is clearly unlikely. It cannot be over emphasised that detailed studies of the near wall region and of the re-entrainment process contradict the concept of direct re-entrainment by eddies. Further, it should be noted that if any form of back diffusion occurs from the cake, the opposing process of convection towards the cake and back diffusion away from it will result in a concentration profile being established between cake and suspension, the concentration increasing towards the cake. The concentration of the sublayer, and probably a part of the buffer zone, will be substantially above bulk concentration, and will approach the cake concentration in the layer adjacent to the cake. In Section 3.4.5 it was noted that the presence of particles tends to dampen out turbulence, the degree of dampening being a strong function of concentration. Thus, the effect of a high concentration in the near-cake region would be to dampen out turbulence, increase the thickness of the sublayer and further reduce the probability of direct re-entrainment by turbulent eddies. Clearly, the mechanistic presentability of any turbulent back-diffusion model will be greatly improved if known transport mechanisms in the near wall region (e.g. turbulent bursts, shear induced diffusivity) were incorporated into the model.

It emerges that neither the simple critical shear nor the turbulent diffusion models stands up to criticism in terms of experimental observations and known fluid and particle dynamics. Each model does, however, have specific merits. The global flux-time behaviour up to the steady-state point, as well as the effect of concentration on the steady-state flux, seem to be "rate controlled" phenomena, consistent with a diffusion model. The preferential deposition effect and apparent irreversibility of the cake are seemingly controlled by the shear at the cake surface, consistent with the critical shear model.

In the following sections, the applicable elements of these simple models are combined with the fluid and particle dynamics developed earlier, yielding an overview of plausible transport mechanisms in the system and hence the qualitative model for cake growth and limit.

### 3.7 PARTICLE TRANSPORT MECHANISMS

In this section, an overview of particle transport in a turbulent CFMF is developed, with particular emphasis being placed on identifying the mechanisms by which particles may be exchanged between the cake and the bulk suspension. This is then applied to determine the concentration distribution in the system and the mechanism by which cake growth occurs.

Firstly, the concept of *cake* must be clarified. In all filtration systems, solids accumulate at the filtration barrier and form a densely packed structure. If the particles are of uniform size and do not exhibit any form of back-diffusion, a distinct interface will exist between the dense

structure at the wall and the bulk suspension. The concentration profile will exhibit a step change at this interface (Figure 3.21 a) and it could be assumed that this interface delineates cake from suspension.

If, however, some form of back-diffusion does exist, the opposing processes of convection to the cake and back-diffusion away from it will result in the establishment of a smooth, continuous concentration profile from bulk to cake. Further, if the solids form a compressible cake the concentration will increase marginally through the cake itself (Figure 3.21 b). In this instance the distinction between cake and suspension is not as clear.

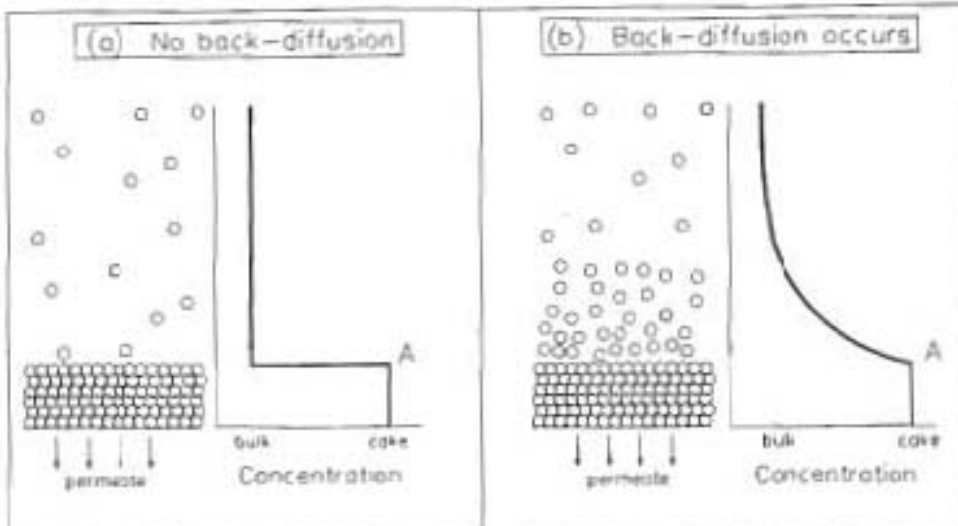


**FIGURE 3.21**      Expected Concentration Profiles in Systems With and Without Back Diffusion

The difference between *cake* and *suspension* may be determined by considering how the mobility or fluidity of a flowing suspension changes as its concentration is increased. With increasing concentration, the mean distance between particles decreases, particle-particle interactions increase and the viscosity of the suspension increases. Each particle is however, still suspended in the flowing fluid. Further increases in concentration will result in further decreases in the mean inter-particle distance until at some critical condition particles will be fully bounded by other particles i.e. the particles will have reached their maximum random packing density. Now, in contrast to being suspended in a flowing fluid, the particles form a coherent, stable structure which is permeated by the flowing fluid. This structure can be regarded as *cake*.

Formally then, *cake* may be defined as particles at a concentration corresponding to the maximum random packing density for the specified size distribution and particle shape. In the case of

compressible cakes, the packing density will be a function of the solids compressive pressure (see Section 4.2). In this instance the minimum concentration that can be regarded as cake will be that concentration corresponding to the random packing density at zero consolidation pressure.

In terms of this definition, point A in Figure 3.21b delineates cake from suspension. The region above point A consists of suspension and is mobile. The region below point A consists of cake, at varying consolidation pressures, and is stagnant.

Cake growth and limit may thus be viewed in terms of concentration. Mobile suspension will consolidate into stagnant cake if its concentration reaches some critical value,  $C_{crit}$ <sup>6</sup>. Cake growth occurs if accumulation of solids in the layer next to the existing cake leads to this layer reaching this critical concentration. The layer of suspension immediately next to the cake, and hence that which could potentially turn into cake, is referred to frequently in the discussion that follows and will hereafter be referred to as the *precake* layer. Cake growth will cease when, by mechanisms to be determined, the concentration of the precake layer is prevented from reaching  $C_{crit}$ .

The particle transport mechanisms in the system may now be addressed. The discussion that follows concerns a *differential tube* i.e. it is assumed that axial gradients are negligible in comparison to radial gradients and hence only transport processes occurring in the radial direction will be considered<sup>7</sup>.

The tube is regarded as consisting of 3 zones - the *cake*, the *precake* layer and the *suspension* zone (Figure 3.22).

The cake consists of solids at their maximum packing density. It will be assumed that the particles are mono-disperse, spherical and do not form a compressible cake, so that radial variations in packing density through the cake will not exist. Further, it will be assumed that axial flow in the cake is negligible, so that fluid flow within the cake occurs only in the radial direction. The precake is a hypothetical layer above the cake and consists of suspension flowing axially over the cake. This layer is in fact a control volume that lies within the viscous sublayer. It has been assigned a special significance since it is this region that will be involved in any cake growth. Fluid flow within the precake layer occurs in both the radial and axial directions. The suspension zone consists of the rest of the viscous sublayer, the buffer zone and the turbulent core. Fluid flow in this zone also occurs in both the axial and radial directions.

<sup>6</sup> Although the cake is at the maximum random packing density,  $C_{crit}$  could be slightly below this packing density. This is discussed further in Chapter 5.

<sup>7</sup> The circumstances under which the above assumptions apply will be addressed in Chapter 5.

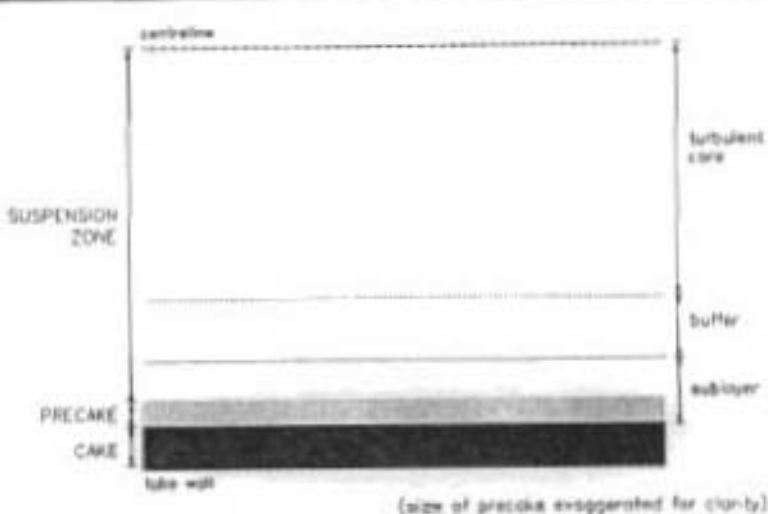


**FIGURE 3.22 Hypothetical Zones in CFMF Tube**

Two inter-zonal particle exchange processes may be defined - exchange between cake and precake, and exchange between precake and suspension zone.

(a) *Cake - precake exchange processes*

Firstly, the distinction between *cake particle* and *precake particle* must be drawn. Considering the cake - precake boundary, particles may at any time occupy one of three positions (Figure 3.23).

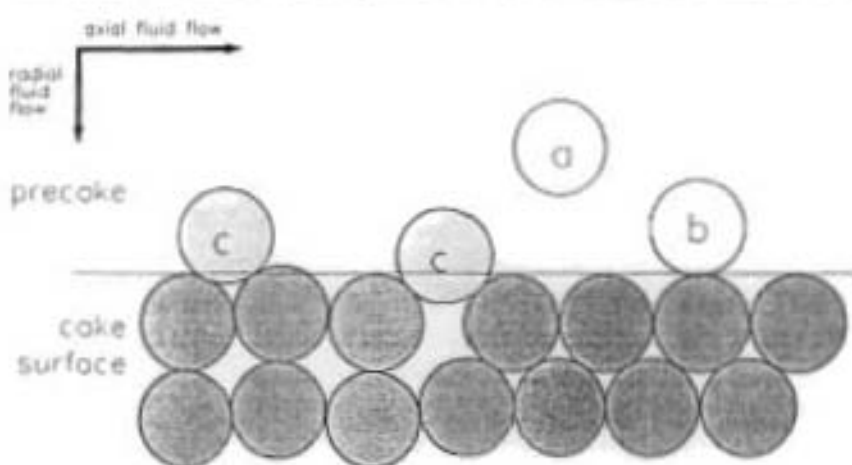


**FIGURE 3.23 Differences Between Cake and Precake Particles**

The particle may unequivocally lie within the precake (particle  $a$ ), the particle may touch a point on the cake surface (particle  $b$ ), or the particle may occupy a *hole* in the cake surface (particle  $c$ ). *Holes* refer to the three-dimensional spaces in the undulating surface of the cake into which particles may deposit. It is clear that particles  $a$  and  $b$  will possess an axial velocity component while particle  $c$  will not. In terms of a stability criterion, particles  $a$  and  $b$  are unstable, while particle  $c$  is potentially stable. In this discussion, particle  $c$  will be regarded as a cake particle and both the particles  $a$  and  $b$  will be regarded as precake particles. Thus, cake particles are only those that unequivocally occupy potentially stable positions in the cake surface.

Particles in the precake are subject to both radial and axial fluid drag forces. They will thus move axially in the tube, describing a trajectory towards the cake surface. On reaching the cake surface, the particle may immediately occupy a hole or be convected axially along the surface to eventually fall into a hole. Thus the radial fluid flow is the driving force for precake particles to become cake particles.

A particle in the cake surface is subjected to radial fluid drag and interparticle forces (*particle friction*) that tends to hold it stably in the surface, and an axial shear stress that tends to destabilise it (Figure 3.24). The axial shear experienced by a particle in the cake surface will be significantly greater than the axial drag experienced by a particle in the precake, since in the former instance the relative velocity between particle and the axially flowing fluid is at a maximum.

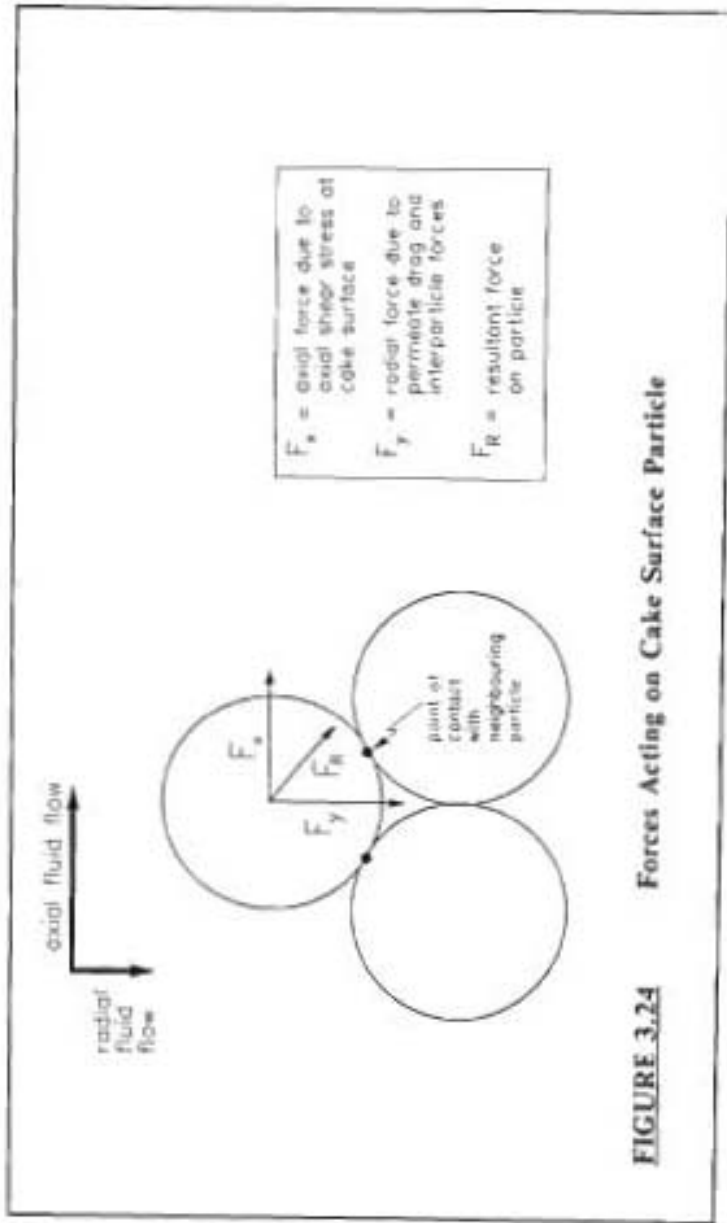


**FIGURE 3-24** Forest Action on California Sustainable Biomaterials.

If the resultant of these forces falls below the point of contact with neighbouring particles, then the particle will remain stable (Figure 3.25a). If, however, the resultant is directed above the point of contact with neighbouring particles, the particle is inherently unstable (Figure 3.25b). Thus, the radial fluid drag and the inter-particle forces define some *critical shear stress*,  $\tau_{crit}$ , which must be exceeded in order to destabilise the particle.

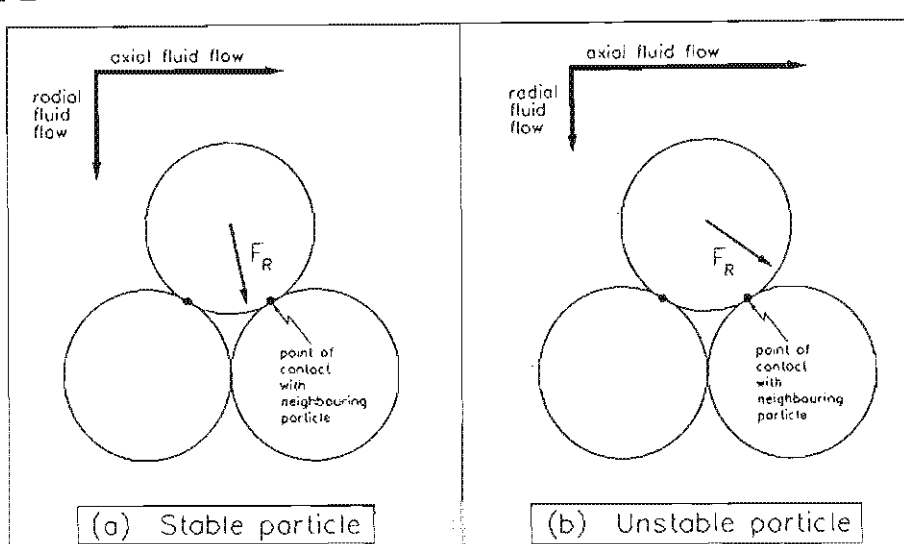


**FIGURE 3.25**      Stable and Unstable Cake Surface Particles

If the available fluid shear stress at the surface is below  $\tau_{crit}$ , particles will remain stably in the cake surface. If however,  $\tau_{crit}$  is exceeded, the particle will roll out of its hole and become a precake particle. The particle could, once again, be convected back to the cake.

It is seen that if the available shear stress is below  $\tau_{crit}$ , a net transfer of particles from the precake to the cake will occur, driven by the radial fluid flow. If  $\tau_{crit}$  is exceeded, no net movement from precake to cake will occur, since all particles which are convected to the cake, as well as existing particles in the cake surface, will be inherently unstable and could be sheared off back into the precake. In this instance there will be a continuous exchange of particles between the flowing precake and the stagnant cake, with no net deposition occurring onto the cake (Figure 3.26).

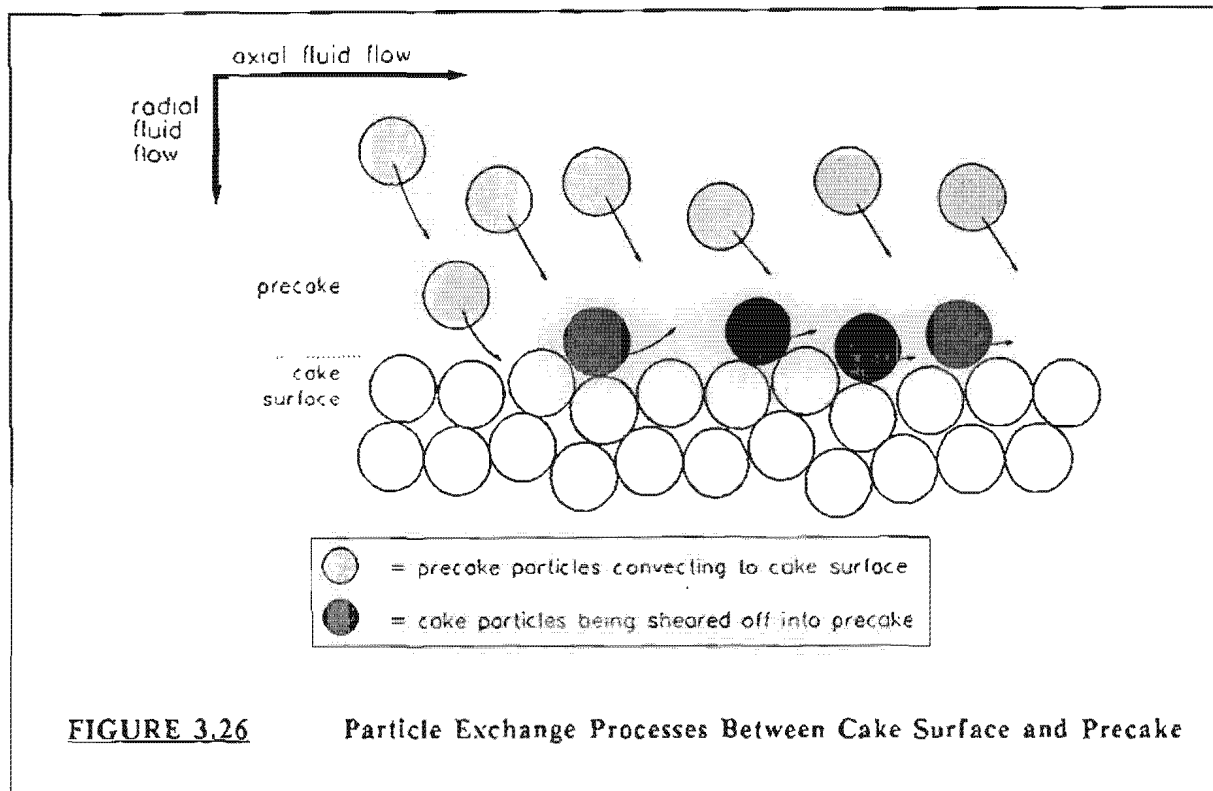


**FIGURE 3.26** Particle Exchange Processes Between Cake Surface and Precake

(b) *Precake - suspension zone exchange processes*

Particles are convected into the precake from the suspension zone by the radial fluid flow. It is convenient to divide particle transport from the precake to the suspension zone into two stages – transport from the precake across the sublayer and into the buffer zone, and transport from the buffer zone into the turbulent core (Figure 3.27).

The most significant mechanism of transport from buffer to turbulent core is by turbulent eddies i.e. turbulent diffusion of particles. Two mechanisms are likely to be significant in transporting particles from the precake across the sublayer and into the buffer zone – transport by turbulent bursts, for particles above  $y^+ = 2.5$ , and shear induced hydrodynamic diffusion, which could apply over the whole precake and sublayer zones. The question of which mechanism will dominate will be addressed in the chapter on Mathematical Modelling (Chapter 5). Lateral migration has not been included as a feasible mechanism for transport out of the precake. The reason for this will be addressed in Section 3.9.

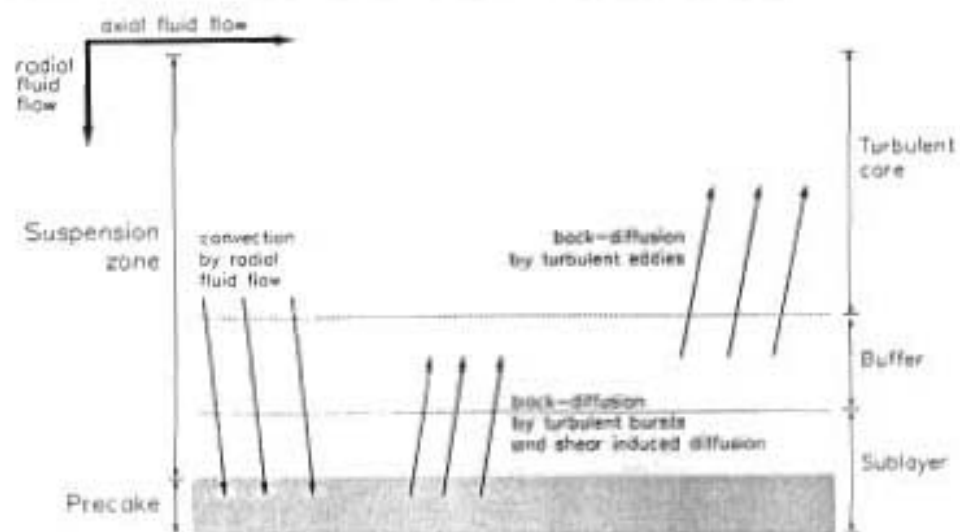


**FIGURE 3.27** Particle Exchange Processes Between Precake and Suspension Zone

It is important to note that the back-transport mechanisms mentioned above i.e. transport by turbulent eddies and bursts and shear induced hydrodynamics diffusion, are *diffusive* processes and will only result in an effective particle transport from the precake to the turbulent core if the concentration of the precake is greater than the bulk concentration. Effectively then, if the concentration of the precake is the same as the suspension zone, the only significant particle exchange process will be the convection of solids into the precake by the radial fluid flow. If, however, the concentration of the precake is greater than that in the turbulent core, a back-diffusion of solids from precake to turbulent core will occur simultaneously with the convection of solids into the precake.

The effects of the above particle exchange mechanisms on concentration distribution in the system may now be examined.

If the available shear stress at the cake surface does not exceed  $\tau_{c,s}$ , all particles which convect to the wall will deposit stably on the cake surface. The concentration of the whole free channel (i.e. precake + suspension zone) will be uniform and will show a step-increase at the cake surface (see Figure 3.21a). Since no concentration gradient exists between the precake and the turbulent core, no back-diffusion can occur. The system will then behave like a dead-end filter and the cake will grow at a rate defined by the permeate flux and the bulk concentration.

If, however,  $\tau_{crit}$  is exceeded by the available fluid shear stress at the surface no net transport from precake to cake will occur. A mass balance over the precake now indicates that the concentration of the layer will increase and exceed the bulk concentration, as particles are convected into the precake from the suspension zone. The back transport mechanisms now become operative and a back-diffusion of particles will occur from the precake to the turbulent core, via the viscous sublayer and buffer zone. The opposing processes of convection and back diffusion will result in the establishment of a concentration profile, the concentration being a maximum in the precake and progressively decreasing away from it to eventually reach bulk concentration at the edge of some boundary layer (see Figure 3.21b).

If the rate of convection of solids into the precake is greater than the rate of back diffusion out of it, the concentration of the precake will obviously increase, and vice versa. If the concentration of the precake increases, however, this will also cause the rate of back-diffusion to increase, due to the increased concentration difference between precake and bulk suspension. Thus, increases in the precake concentration will result in simultaneous increases in the rate of back-transport until at some concentration the rate of back-diffusion will equal the rate of convection into the precake. Now, no net transport into, or out of, the precake will occur and the system will be in a dynamic equilibrium. The precake thus has a theoretical equilibrium concentration,  $C_{eq}$ , which will be attained when the rates of convection and back-diffusion equalise.

For a differential tube, this theoretical equilibrium concentration may be evaluated from a one-dimensional Fickian Diffusion equation. The circumstances under which the one-dimensional equation is applicable, and the assumptions inherent in its application, will be addressed in Chapter 5. At any radius,  $r$ , within the boundary layer,

$$\text{rate of convection into precake} = V(r) C \quad (3.49)$$

$$\text{rate of back-diffusion from precake} = D_p(r) \frac{\partial C}{\partial r} \quad (3.50)$$

where  $V(r)$  = radial velocity at radius  $r$  (m/s)

$D_p(r)$  = particle diffusivity at radius  $r$  ( $\text{m}^2/\text{s}$ )

$C$  = concentration at radius  $r$  (volume fraction)

Equating equations 3.49 and 3.50, and integrating over the boundary layer,  $\delta$ , with boundary conditions :-

$$\text{at precake : } r = R_c \quad C = C_{eq}$$

$$\text{at edge of boundary layer : } r = R_c + \delta \quad C = C_B$$

yields

$$\int_{R_c}^{R_c + \delta} \frac{V(r)}{D_p(r)} dr = \ln \left( \frac{C_{eq}}{C_B} \right) \quad (3.51)$$

where  $R_c$  = radius of free channel, or core (m)  
 $(= R - l_c)$   
 $\delta$  = boundary layer thickness (m)  
 $C_{eq}$  = theoretical equilibrium concentration of precake (volume fraction)  
 $C_b$  = bulk concentration (volume fraction)

It is seen that this theoretical equilibrium precake concentration,  $C_{eq}$ , is determined by the  $V(r)/D_p(r)$  distribution. As  $V(r)$  increases relative to  $D_p(r)$ ,  $C_{eq}$  will increase, and conversely.

There is however a physical limitation to the concentration of the precake. As noted in the beginning of Section 3.7, at some critical concentration,  $C_{crit}$ , a suspension will reach its maximum packing density and consolidate into cake. If  $C_{eq}$  is less than  $C_{crit}$ , the equilibrium may be achieved. If however, at the specified  $V(r)$  and  $D_p(r)$  distribution,  $C_{eq}$  is greater than  $C_{crit}$ , the equilibrium cannot be achieved. In this instance, the concentration of the precake will increase up to  $C_{crit}$ , whereafter the precake will consolidate into cake. Effectively then cake growth occurs when the concentration of the precake, as determined by the radial fluid flow and particle diffusivity distributions, reaches the critical concentration for consolidation.

In summary, the initial step in the back-transport of particles from the cake is the shearing of particles off the cake surface. If this initial step does not occur, the system will behave like a dead-ended filtration system. If the shearing of particles off the cake surface does occur, the systems behaviour becomes controlled by a convection-diffusion process. The radial fluid velocity and particle diffusivity distributions will determine the concentration of the precake, and hence whether the precake will reach the critical concentration and consolidate into cake. Cake growth ceases when the equilibrium concentration of the precake falls below the critical concentration for consolidation.

### 3.8 QUALITATIVE MODEL FOR THE GROWTH AND LIMIT OF THE CAKE

It is proposed that the available shear stress at the cake surface always exceeds the critical shear stress necessary to destabilise cake surface particles, except possibly for a short period immediately after start-up.

On start-up, the radial fluid flow convects particles to the tube wall where, faced with a barrier to their motion, they accumulate to form a cake. Particles are sheared off this cake surface and the concentration of the layer immediately adjacent to the cake (*precake*) subsequently increases and exceeds bulk concentration. Back-diffusion of particles occurs from this precake to the turbulent core and a concentration profile is established. This back-diffusion is effected by three mechanisms. Shear induced hydrodynamic diffusion and turbulent bursts transport particles from the precake across the rest of the sublayer and into the buffer zone. Subsequently, turbulent eddies transport particles from the buffer zone into the turbulent core.

Initially the radial fluid flow,  $V(r)$ , is high and the theoretical equilibrium concentration of the precake,  $C_{eq}$ , exceeds the critical concentration at which suspension will consolidate into cake,  $C_{crit}$ . Thus the concentration of the flowing precake increases rapidly up to  $C_{crit}$ , at which this flowing layer consolidates and becomes part of the stagnant cake structure. Now particles are sheared off this "new" cake surface and a new precake layer develops. Thus cake growth occurs by progressive precake layers reaching the critical concentration and consolidating into cake.

The increase in cake thickness has 2 significant effects on the system :-

- (i) the hydraulic resistance to permeate flow increases. Thus  $V(r)$  and the rate of convection towards the wall decreases.
- (ii) the free channel area decreases, causing an increase in the suspension velocity in the channel. All the back-transport mechanisms are strong functions of velocity, and hence  $D_p(r)$  and the rate of back-transport of particles increases.

Effectively, as the cake grows the theoretical equilibrium concentration of the precake decreases, and further, the time taken for the precake to reach  $C_{crit}$  progressively increases. At some cake thicknesses,  $V(r)$  will have decreased, and  $D_p(r)$  increased, to a level where  $C_{eq}$  falls below  $C_{crit}$ . The rates of convection and back-diffusion may now reach equilibrium, the precake will remain at a sub-critical equilibrium concentration, and no further cake growth will occur.

Formally, the critical condition at which the limiting, or steady-state, cake thickness is attained is given by :-

$$C_{eq} \leq C_{crit}$$

where  $C_{eq}$  is the theoretical equilibrium concentration of the precake, defined by the equilibrium mass balance :-

$$\int_{R_c - \delta}^{R_c} \frac{V(r)}{D_p(r)} dr = \ln \left( \frac{C_{eq}}{C_B} \right)$$

### 3.9 DISCUSSION

Stated simply, the model proposes that back transport of particles occurs in two stages - shearing of particles off the cake surface and subsequent back-diffusion to the turbulent core. If the shearing step does occur, system behaviour becomes determined by the convection and back-diffusion processes i.e. it becomes *rate-controlled*.

Mathematically, the proposed model for the steady-state condition resolves to the same convection-diffusion mass balance equation employed in the simple diffusion models discussed in Section 3.2.2, with the entire proposed mechanism for cake growth and limit manifesting solely as a boundary condition to the equation. Mechanistically however the proposed model is more attractive than the simple turbulent diffusion model, being based on realistic particle dynamics in the near-wall region. These particle dynamics will manifest in the specific formulation of the particle diffusivity,  $D_p$ .

In Chapter 4 it will be shown that the model is consistent with the phenomena associated with shear stresses at the cake surface i.e. the apparent irreversibility of the cake and the preferential deposition of smaller particles as velocity increases. Further, since the steady-state condition is determined by the convection-diffusion processes, the predicted trends for the effects of velocity and concentration on flux will be consistent with experimental observations. This is illustrated in the chapter on Mathematical Modelling, Chapter 5. In order for model trends for the effect of pressure on flux to be consistent with observations, however, the compressibility of the cake must be taken into account. This is also addressed further in Chapter 5.

In Section 3.7, it was stated that lateral migration was not regarded as a viable mechanism for the back-transport of particles from the precake to the suspension zone. The motivation for this is that the concentration of the precake will be substantial, and will approach the cake concentration. In these circumstances, the basic assumptions of the lateral migration model i.e. dilute suspension of non-interacting particles, are invalid.

## *Chapter 4*

### **INVESTIGATIONS INTO CHANGES IN CAKE STRUCTURE AND CHARACTERISTICS**

---

#### **4.1 INTRODUCTION**

The limiting cake thickness, and hence *steady-state* flux, is primarily determined by the hydrodynamics in the tube i.e. fluid-induced shears and particle transport. Hence, the observed effects of operating variables on the steady-state flux are explicable in terms of system hydrodynamics. However, various system behaviours observed in the experimental study are seemingly determined by the behaviour of the cake e.g. the observed path dependence of flux-time behaviour, the long-term decline in flux. In this chapter an attempt is made to explain these observations in terms of the cake structure and characteristics.

In Chapter 3, only spherical, uniformly sized particles were considered. In most real suspensions, including the limestone system studied here, the suspension will consist of particles of a wide size distribution. The major effect that this will have on the system will be to change the structure and characteristics of the cake (i.e. voidage, permeability and critical shear stress). In this chapter, three phenomena attributable to the presence of polydisperse particles will be discussed - hydraulic compression of the cake (*hydraulic compression effect*), preferential deposition of smaller particles (*preferential deposition effect*) and infiltration of finer particles into the cake structure (*fines infiltration effect*).

In Sections 4.2 to 4.4 the mechanisms of these phenomena are discussed together with their individual effects on the cake structure. Mechanisms are proposed for the preferential deposition effect and the fines infiltration effect, based on the model of cake growth developed in Chapter 3. In Section 4.5, these individual effects are combined to indicate the net effect on cake structure and characteristics during the cake growth period as well as the slow decline in flux period. This is subsequently applied, in Section 4.6, to explain the various system irreversibilities and anomalies observed in the experimental study.

Most of the discussion in this chapter is of a qualitative nature. The major intention is to determine how changes in cake characteristics may influence flux-time behaviour, and hence to explain the various seemingly anomalous behaviours observed in the experimental study.

## 4.2 HYDRAULIC COMPRESSION EFFECT

The flow of fluid through a cake consisting of particles of a wide range of sizes could cause a rearrangement of the particulate structure, leading to a cake of decreased voidage [Tiller and Yeh (1987)]. This process is termed *hydraulic compression* and arises by particles being forced into the existing void spaces by fluid drag forces. It must be noted that this compression of the cake is not due to the deformation of individual particles, but to a re-arrangement of the particles. The extent of hydraulic compression at any plane in the cake, and hence the voidage at that plane, is determined by the effective compressive force,  $F_s$ , experienced by particles in that plane.

A hypothetical *solids compressive pressure*,  $P_s$ , may be introduced, given by :-

$$P_s = \frac{F_s}{A} \quad (4.1)$$

where  $F_s$  = compressive force experienced by particles at a plane in the cake (kN)

$A$  = superficial area of the plane ( $\text{m}^2$ )

Stated alternatively, the voidage decreases as the solids compressive pressure,  $P_s$ , increases.

The fluid flow around each particles generates friction and drag forces which manifest as a decrease in the liquid hydraulic pressure,  $P_L$ , in the direction of flow. These drag forces are transmitted from particle to particle and eventually to the support medium. At equilibrium, the effective compressive force,  $F_s$ , experienced by particles at a plane in the cake is equal to the cumulative drag forces up to that plane (Figure 4.1), i.e.

$$F_s = \sum F_d \quad (4.2)$$

where  $F_d$  = fluid drag force on particle

Also, at any plane in the cake, the cumulative drag forces up to that point equal the liquid hydraulic pressure drop up to that point :-

$$\sum F_d = (P - P_L) A \quad (4.3)$$

where  $P$  = liquid pressure at free cake surface (kPa)  
(i.e. operating pressure)

$P_L$  = liquid hydraulic pressure (kPa)

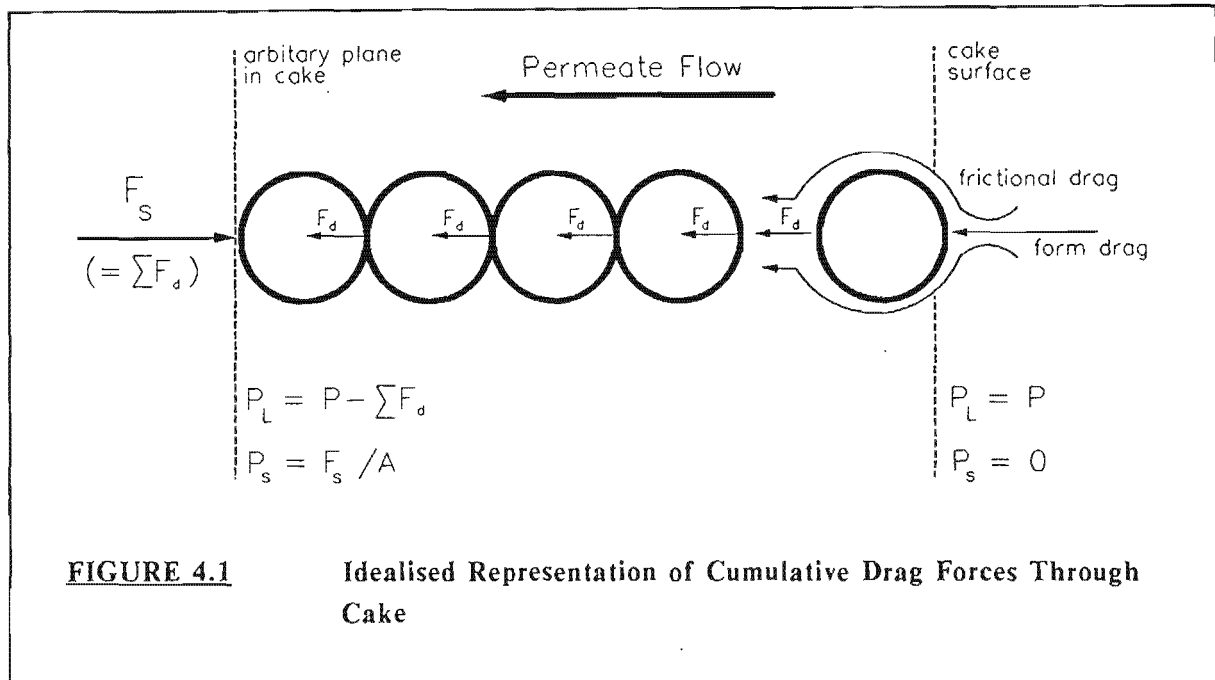


**FIGURE 4.1**      **Idealised Representation of Cumulative Drag Forces Through Cake**

From equations 4.1 to 4.3 :-

$$P_s + P_L = P \quad (4.4)$$

Differentiating with respect to distance through the cake,  $w$ ,

$$\frac{dP_s}{dw} + \frac{dP_L}{dw} = 0 \quad (4.5)$$

where  $w$  = distance through cake (m)

Equations 4.4 and 4.5 describe the variations in  $P_s$  and  $P_L$  through a cake formed on a flat surface. For a cake formed on a radial surface, the force balance is somewhat complicated since the drag forces are also transmitted in the azimuthal direction ("hoop stress") [Tiller and Yeh (1985)]. The pressure balance equation for a cylindrical cake is :-

$$\frac{dP_L}{dr} + \frac{dP_s}{dr} + (1 - E_o) \frac{P_s}{r} = 0 \quad (4.6)$$

where  $E_o$  = earth stress ratio

= lateral stress / radial stress

$r$  = radial distance through cake (m)

Except for thick, relatively incompressible cakes, the  $P_s$  and  $P_L$  profiles described by equation 4.6 do not differ substantially from that obtained from equation 4.5 [Tiller and Yeh (1985)]. Stated alternatively, if the thickness of the cake is not great compared to the

radius of the tube, the  $P_s$ , and  $P_t$ , may be approximated by the flat cake equations, equations 4.4 and 4.5. In the rest of this discussion, it will be assumed that equations 4.4 and 4.5 adequately represent the  $P_s$ , and  $P_t$ , profiles through the cake.

The hydraulic pressure,  $P_t$ , is a maximum at the cake surface and progressively decreases towards the medium, due to fluid drag losses. The solids compressive pressure,  $P_s$ , is zero at the cake surface and progressively increases towards the support medium as the cumulative drag forces experienced by the particles increase. Hence, the local voidage,  $\beta$ , will progressively decrease towards the medium. For a slightly compressible cake, and assuming that the hydraulic resistance of the support medium is negligible,  $P_s$ ,  $P_t$  and  $\beta$  will typically exhibit profiles as in Figure 4.2.

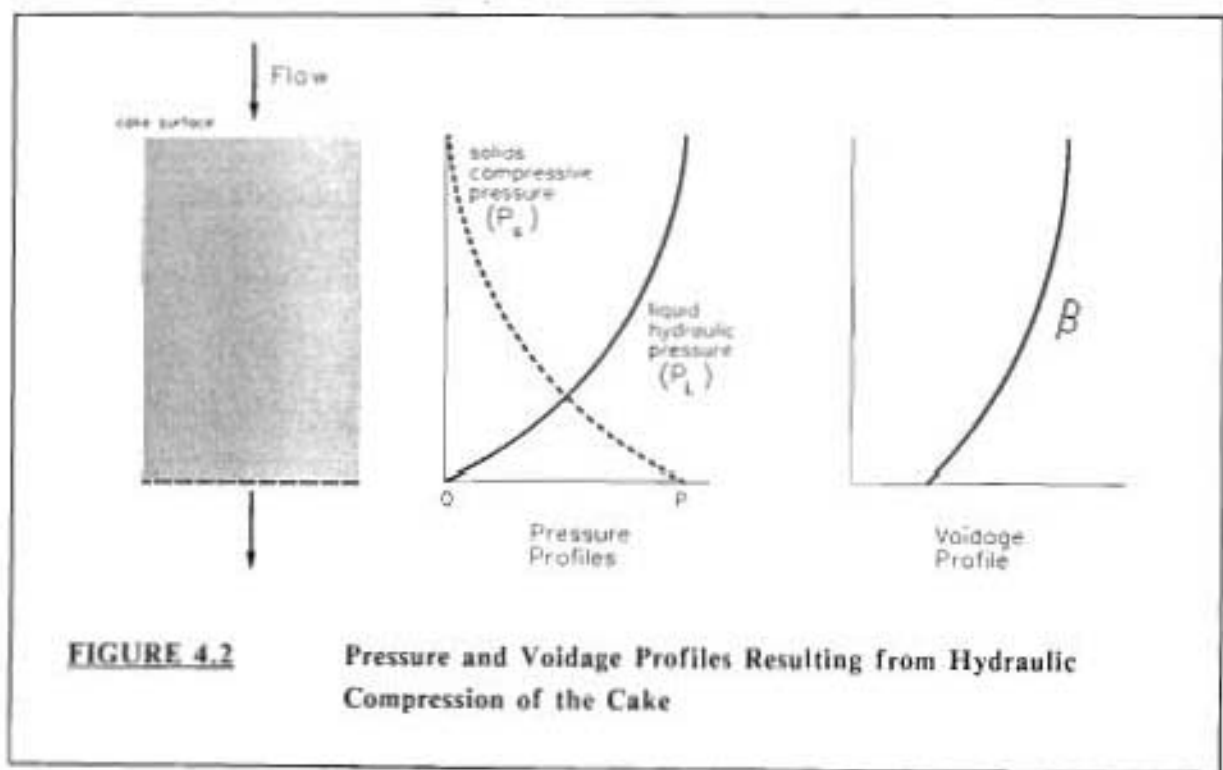


**FIGURE 4.2**

Pressure and Voids Profile Resulting from Hydraulic Compression of the Cake

This hydraulic compression of the cake is highly irreversible i.e. if  $P_s$  at a point is now decreased, e.g. by decreasing the fluid flow through the cake, particles cannot retrace paths out of the void spaces, and hence the voidage will remain at the level determined by the higher  $P_s$ . As a cake grows, the  $P_s$  and  $P_t$  profiles will change. However, particles at any point in the cake will always be exposed to an increasing  $P_s$  (Figure 4.3).

The hydraulic compression and variation in  $P_s$  through the cake has two significant effects on the cake characteristics – variations in permeability and variations in critical shear stress through the cake.

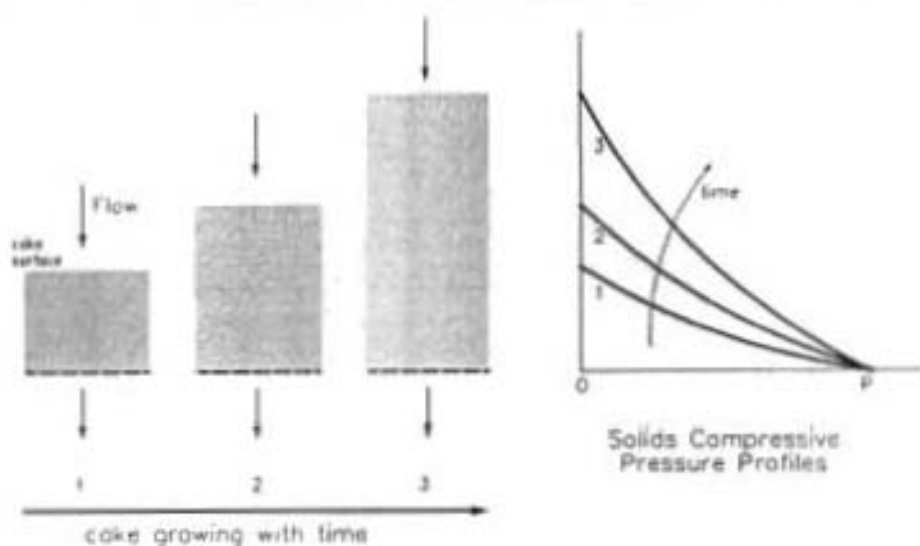


**FIGURE 4.3** Change in Solids Compressive Pressure Profiles as Cake Grows

#### 4.2.1 Radial Variation in Permeability

The permeability at a point in the cake ( $K$ ) is related to the voidage at that point, and will decrease as the  $P_s$  at that point increases. The general relation between permeability,  $K$ , and  $P_s$  is given by [Foust et al. (1980)]:-

$$K = K_a P_s^{q_1} \quad (4.7)$$

where  $K$  = permeability ( $\text{m}^2$ )

$P_s$  = compressive pressure (kPa)

$K_a$  = a constant

$q_1$  = a constant ( $< 0$ )

Thus, the permeability decreases towards the wall. Typical permeability profiles are shown in Figure 4.4 for slightly compressible and highly compressible cakes.

A major significance of this permeability profile is that most of the overall cake resistance is offered by cake layers closer to the wall. On moving away from the wall, the contribution that each layer makes to the overall cake resistance progressively decreases.

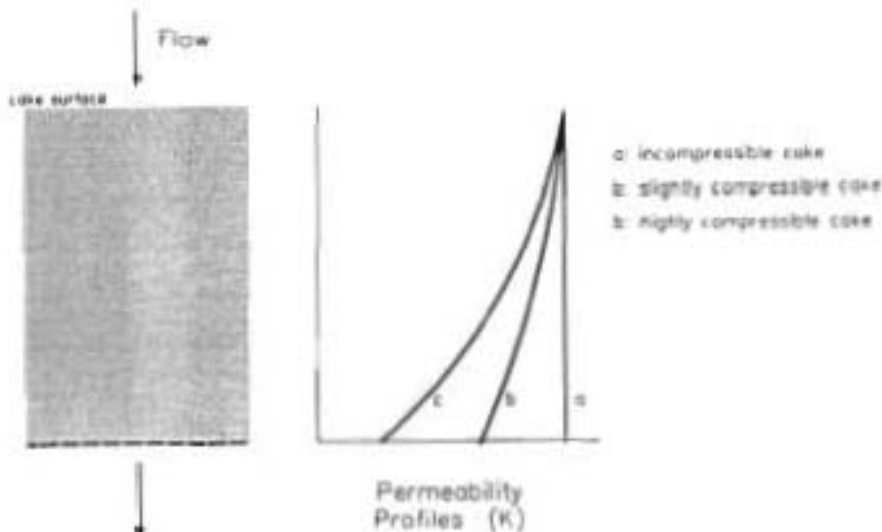


**FIGURE 4.4** Permeability Profiles Resulting from Hydraulic Compression of Cake

#### 4.2.2 Radial Variation in Critical Shear Stress

In Section 3.7, the concept of critical shear stress,  $\tau_{crit}$ , was introduced. This is the minimum axial shear stress required to destabilise particles at the cake surface. It was further noted that  $\tau_{crit}$  is a function of the fluid drag forces around the particle and inter-particle forces (*particle friction*) experienced by the particle. The inter-particle forces will increase as particle-particle contact increases i.e. as the voidage decreases. The critical shear stress will thus be a positive function of solids compressive pressure.

$$\tau_{crit} = \text{function } [P_s^{q_2}, F_d] \quad (4.8)$$

where  $q_2$  = a constant ( $> 0$ )

$F_d$  = fluid drag force

This is analogous to the *powder yield locus* in soil mechanics, where the critical shear stress for failure in a powder is a function of the compressive stress being experienced by the powder [Smith (1982)].

In the surface layers of the cake,  $P_s$  is small and  $\tau_{crit}$  will be determined predominantly by the fluid drag force. On moving towards the wall,  $P_s$  increases and is likely to be the major determinant of  $\tau_{crit}$ . By the earlier definition of  $\tau_{crit}$  it could be argued that the concept cannot be applied to particles within the cake. For particles within the cake  $\tau_{crit}$  may be conceptualised by noting that if particle layers above the layer being considered were removed,

thereby making the layer a surface layer, the layer will remain at the voidage it attained when it was an inner cake layer. Thus although the effective  $P_s$  on the layer will now be approximately zero, the  $\tau_{crit}$  for the layer will be determined by the maximum  $P_s$  that it was exposed to when it was an inner cake layer.

Hydraulic compression of the cake will thus result in the critical shear stress progressively increasing towards the wall (Figure 4.5). It can be seen that if the available shear stress due to the axial fluid flow is  $\tau_1$ , only a fraction of the cake can potentially be destabilised and removed.

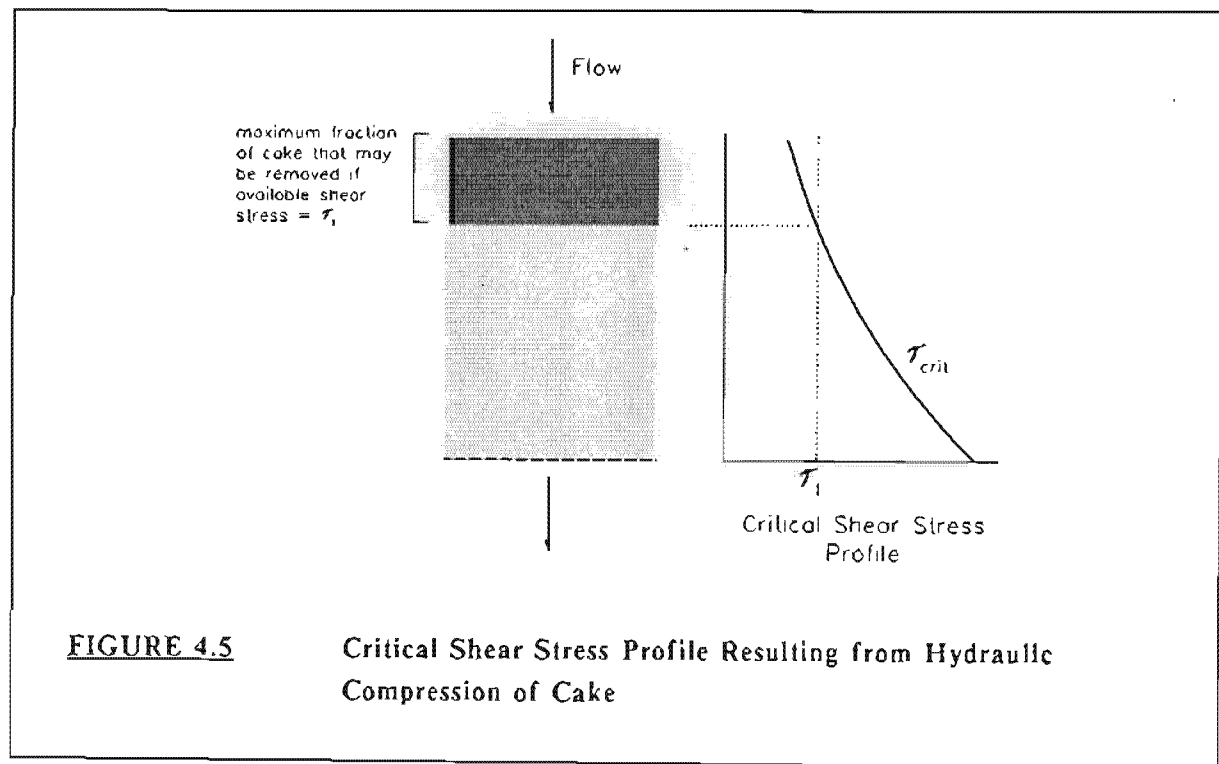


**FIGURE 4.5** Critical Shear Stress Profile Resulting from Hydraulic Compression of Cake

#### 4.2.3 Summary of Hydraulic Compression Effect

Hydraulic compression of the cake results in a  $P_s$  profile being established, the  $P_s$  being small at the cake surface and progressively increasing towards the wall. This manifests as variations in the permeability,  $K$ , and the critical shear stress,  $\tau_{crit}$ , through the cake. The permeability is at a maximum at the cake surface and decreases towards the wall. Resultantly the contribution that each layer makes to the overall cake resistance progressively decreases on moving away from the wall. The  $\tau_{crit}$  is relatively small at the cake surface and increases towards the wall.

### 4.3 PREFERENTIAL DEPOSITION EFFECT

Various workers have observed that on cross-flow filtering a suspension containing polydisperse particles, the cake would preferentially be composed of the smaller particle size fractions, and further that the average particle size decreases as the operating velocity is increased [Baker et al. (1985), Harrison et al. (1981)]. In this study, this phenomenon is termed the *preferential deposition effect*. It should be noted that unlike the *fines infiltration effect*, i.e. penetration of finer particles into the existing cake structure, the preferential deposition effect dictates the size of particles deposited during the growth of the cake. In this section (4.3), the mechanism of this preferential deposition and the effect that this has on cake characteristics is investigated.

Baker et al. (1985) proposed a mechanism by which finer particles could preferentially be deposited based on the inertial lift effect (see Section 3.2.1.1 for a discussion of the inertial lift effect). The lift force on a particle is a function of, *inter alia*, the particle size. Thus, at a given velocity larger particles could experience a net lift force directed away from the wall while small particles would experience a net convective force directed to the wall, leading to a cake preferentially composed of the smaller size fractions.

An alternative mechanism for the preferential deposition effect is proposed here, based on the cake growth and limit mechanism discussed in Section 3.7. The initial step in the back transport of particles is the shearing of particles off the cake surface to form a layer whose concentration is greater than the bulk concentration (the precake). This shear removal will occur if the fluid shear stress at the cake surface,  $\tau$ , is greater than some critical shear,  $\tau_{crit}$ . If mono-disperse particles are considered, all particles which reach the cake surface will be inherently unstable and will be sheared off into the precake if  $\tau \geq \tau_{crit}$ . If polydisperse particles are considered, three scenarios are feasible.

Consider three particles, *a*, *b* and *c*, arriving at similar holes in the cake surface (Figure 4.6). Under the action of the available shear stress, Particle *a* will be inherently unstable and will be sheared off into the precake. Particle *b*, however, will be stable and will remain in the cake surface. Particle *c* does not perceive a barrier to its motion and will penetrate the cake surface. The effect that particle penetration will have on cake characteristics is discussed in Section 4.4. Here, the effects that particles *a* and *b* have on the cake formation will be addressed.

For simplicity, it will be assumed that the bulk suspension consists only of two sizes - *a* and *b*. Consider 4 control volumes, as in Figure 4.7 - around the cake surface ( $C_{ss}$ ), the precake ( $C_{ps}$ ), the suspension zone ( $C_{sz}$ ) and the cake surface and precake combined ( $C_{sp}$ ).

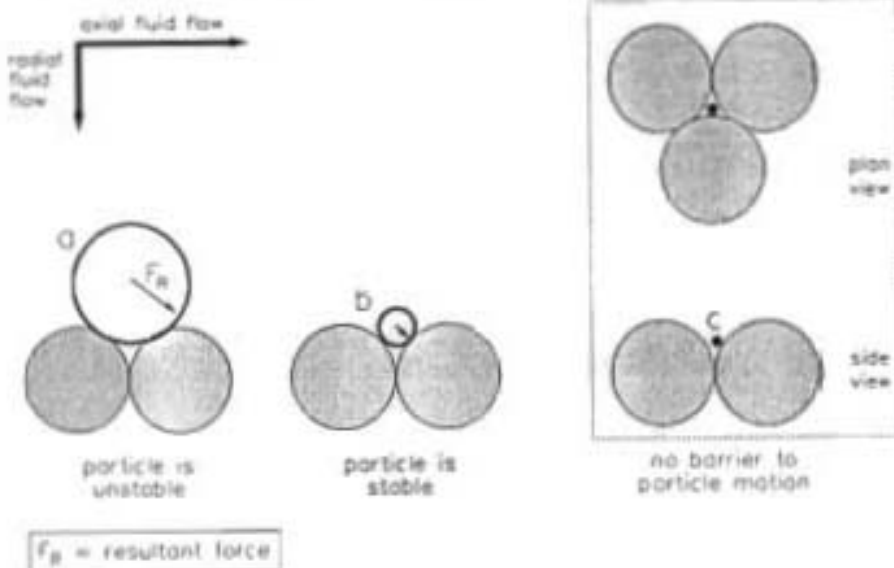


**FIGURE 4.6** Particles of Different Sizes at Cake Surface

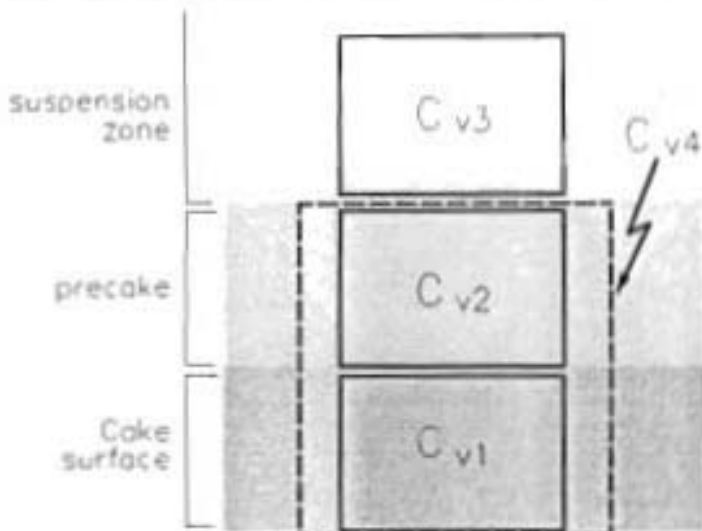


**FIGURE 4.7** Control Volumes Near Cake Surface

The *number fractions* of particles *a* and *b* in each zone are denoted by  $x_{ai}$  and  $x_{bi}$  where *i* represents the particular control volume. Further,  $x_{ai} + x_{bi} = 1$ . The significant particle exchange mechanisms that occur are depicted in Figure 4.8. Particles are convected from the

suspension zone into the precake and simultaneously a back-transport of particles occurs from the precake to the suspension zone. Particles from the precake are convected onto the cake surface and may be sheared off back into the precake.

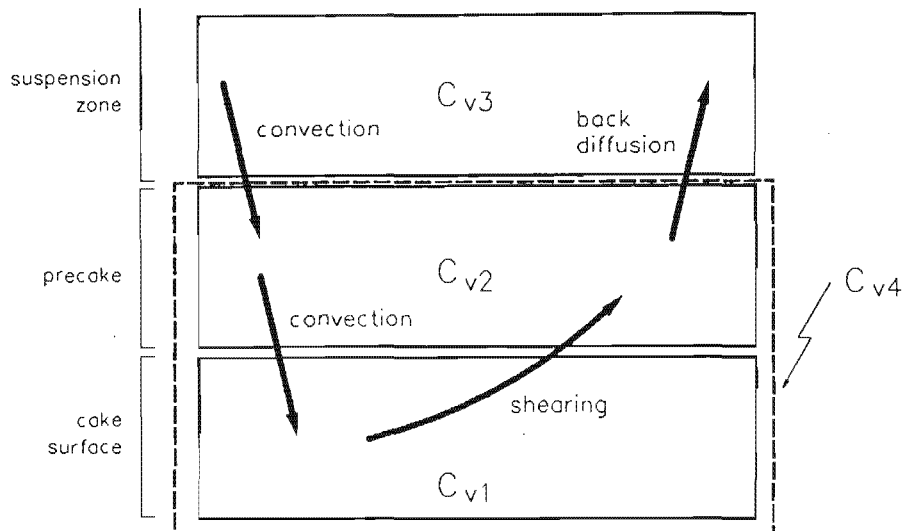


**FIGURE 4.8** Particle Transport Processes Between Control Volumes

Assume that initially all control volumes have the same size distribution i.e.  $x_{a1} = x_{a2} = x_{a3}$  and  $x_{b1} = x_{b2} = x_{b3}$ . At some time,  $t_1$ , particles of both sizes  $a$  and  $b$  are convected onto the cake surface. Assume further that at the given surface shear stress *most* particles of size  $b$  deposit stably while *all* particles of size  $a$  are sheared off into the precake.

At this instant, the fractions of  $a$  and  $b$  in the cake surface and precake will differ from the bulk size distribution. However, the mean size distribution in the cake and precake combined ( $C_{v4}$ ) will be the same as the bulk i.e.

At time  $t_1$ :

$C_{v1}$ (cake surface)	$x_{a1} < x_{a3}$	$x_{b1} > x_{b3}$
$C_{v2}$ (precake)	$x_{a2} > x_{a3}$	$x_{b2} < x_{b3}$
$C_{v4}$ (cake surface and precake)	$x_{a4} = x_{a3}$	$x_{b4} = x_{b3}$

Now there is a continuous convection of particles from  $C_{v3}$  to  $C_{v2}$  simultaneous to the back-transport from  $C_{v2}$  to  $C_{v3}$ . During the cake growth period, the rate of convection into the precake will exceed the rate of back-diffusion. The overall concentration of the precake will thus increase until at some time  $t_1 + \Delta t$  the critical concentration will be reached and  $C_{v2}$  will consolidate into cake. The cake will now consist of both  $C_{v1}$  and  $C_{v2}$  i.e.  $C_{v4}$ . The mean

size distribution of the cake will be indicated by  $x_{a4}$  and  $x_{b4}$ . The objective here is to determine how  $x_{a4}$  and  $x_{b4}$  will compare to the bulk size distribution, immediately after  $C_{v2}$  has consolidated into cake.

Particles convected into  $C_{v2}$  from  $C_{v3}$  will have a size distribution of  $x_{a3}$  and  $x_{b3}$ . Particles experiencing back-transport from  $C_{v2}$  to  $C_{v3}$  will have a size distribution of  $x_{a2}$  and  $x_{b2}$ . This exchange serves to decrease the difference in size distributions between  $C_{v2}$  and  $C_{v3}$ . Thus, at the instant of consolidation of  $C_{v2}$  into cake,  $x_{a2}$  and  $x_{b2}$  will be determined by the extent of particle exchange that has occurred between  $C_{v2}$  and  $C_{v3}$  during the period  $\Delta t$ .

The extent of this particle exchange between  $C_{v2}$  and  $C_{v3}$  will be indicated by the ratio (*rate of back diffusion / rate of convection*) i.e.  $(R_d/R_c)$ . During the cake growth period, of course, this ratio will be less than 1. If the ratio is relatively small, then the time taken to reach the critical concentration,  $\Delta t$ , will be small and very little gross particle exchange would have occurred before  $C_{v2}$  reaches the critical concentration.

Thus, if  $(R_d/R_c) \rightarrow 0$ ,

$$\begin{aligned} (x_{a2})_{\text{at time } t_1 + \Delta t} &\approx (x_{a2})_{\text{at time } t_1} \\ (x_{b2})_{\text{at time } t_1 + \Delta t} &\approx (x_{b2})_{\text{at time } t_1} \end{aligned}$$

Hence

$$\begin{aligned} (x_{a4})_{\text{at time } t_1 + \Delta t} &\approx (x_{a4})_{\text{at time } t_1} \\ &\approx (x_{a3}) \\ (x_{b4})_{\text{at time } t_1 + \Delta t} &\approx (x_{b4})_{\text{at time } t_1} \\ &\approx (x_{b3}) \end{aligned}$$

Thus, for a small  $(R_d/R_c)$  the mean cake particle size will be similar to the mean particle size in the bulk suspension.

If the ratio  $(R_d/R_c)$  is relatively large,  $\Delta t$  will also be relatively large and substantial particle exchange would have occurred between  $C_{v2}$  and  $C_{v3}$ , minimising the differences in size distributions between these regions.

Thus, if  $(R_d/R_c) \rightarrow 1$ ,

$$\begin{aligned} (x_{a2})_{\text{at time } t_1 + \Delta t} &\approx (x_{a3}) \\ (x_{b2})_{\text{at time } t_1 + \Delta t} &\approx (x_{b3}) \end{aligned}$$

However,

$$(x_{at})_{\text{at time } t_1 + \Delta t} = (x_{at})_{\text{at time } t_1} \\ < (x_{a2})$$

$$(x_{bt})_{\text{at time } t_1 + \Delta t} = (x_{bt})_{\text{at time } t_1} \\ > (x_{b2})$$

Hence,

$$(x_{at})_{\text{at time } t_1 + \Delta t} < (x_{a2}) \\ (x_{bt})_{\text{at time } t_1 + \Delta t} > (x_{b2})$$

In this case, the mean particle size in the cake would be less than the mean size of the bulk suspension.

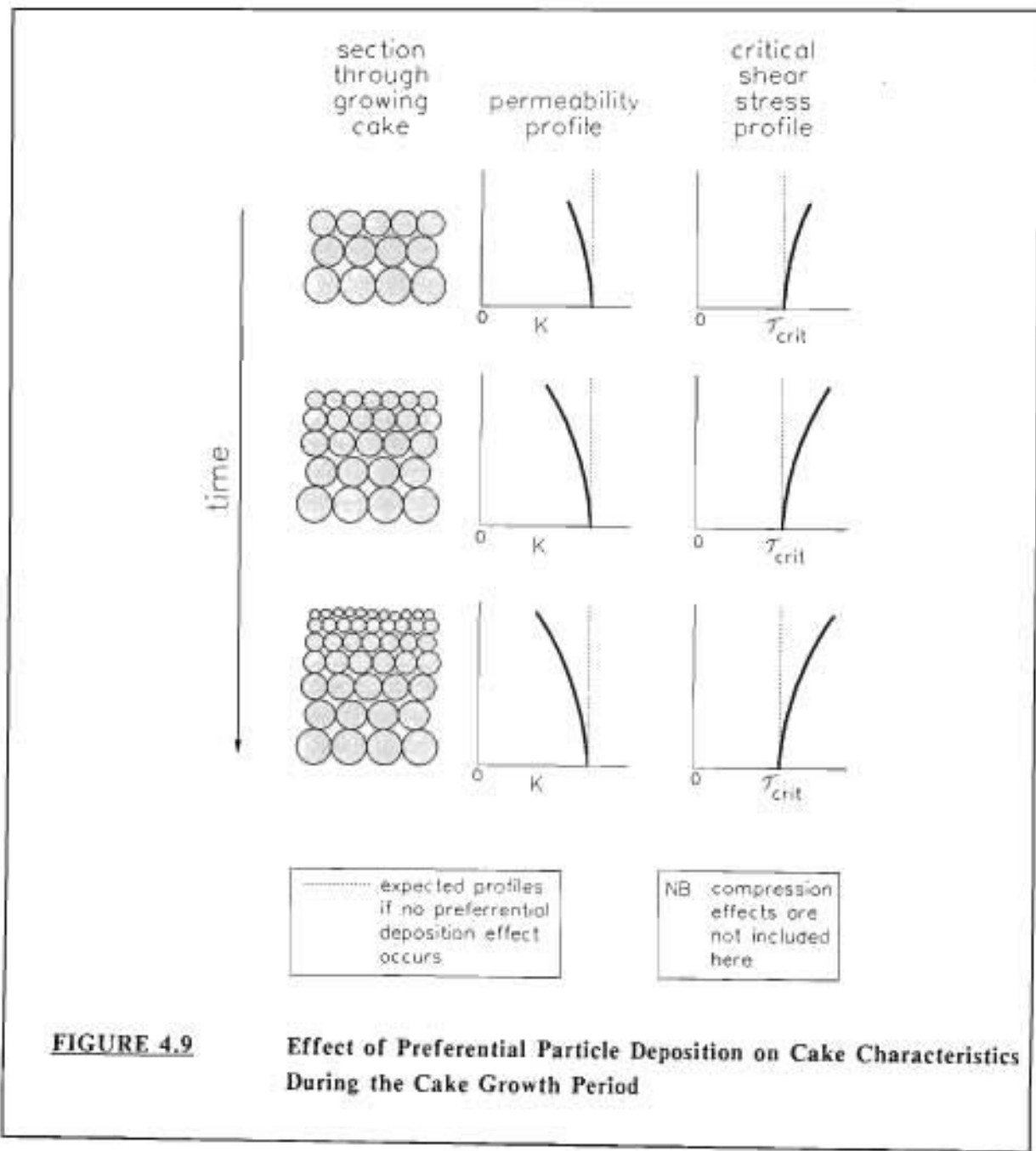
The above discussion is simplistic, in that variations in size distribution through the suspension zone have been neglected. The important point, however, is that the mean particle size in the cake may be close to or substantially less than the mean particle size in the bulk suspension, and will be determined by the relative rates at which the convective and back-diffusive transport mechanisms occur.

To summarise thus far, during the cake growth period particles below some critical size would deposit stably onto the cake surface or alternatively penetrate the surface, while larger particles will be sheared off into the precake. This critical particle size will decrease as the surface shear stress increases. The extent of particle exchange between the precake and suspension zone will subsequently determine the size distribution in the precake and hence the mean particle size in the cake. The ratio ( $\bar{x}_d/\bar{x}_e$ ) indicates this gross exchange. If the ratio is low, the mean cake particle size will be similar to the bulk mean size. This mean cake particle size will decrease as the ratio increases.

Both the surface shear stress and the ratio ( $\bar{x}_d/\bar{x}_e$ ) will increase as the suspension velocity increases. One implication of this is that the mean cake particle size will decrease as operating velocity is increased - the experimentally observed *preferential deposition effect*. A second implication of this is that the cake will have a radial variation in particle size distribution. On start-up the shear stress at the surface and the ratio ( $\bar{x}_d/\bar{x}_e$ ) are relatively small. Hence, the particle size distribution of the cake layers next to the wall will be close to the bulk distribution. As the cake grows, the suspension velocity in the free channel increases. Thus the mean particle size in each cake layer will progressively decrease on moving away from the wall, reaching a minimum at the surface of the steady-state cake. To the best of the authors knowledge, no experimental studies into radial variations in cake particle size distribution have

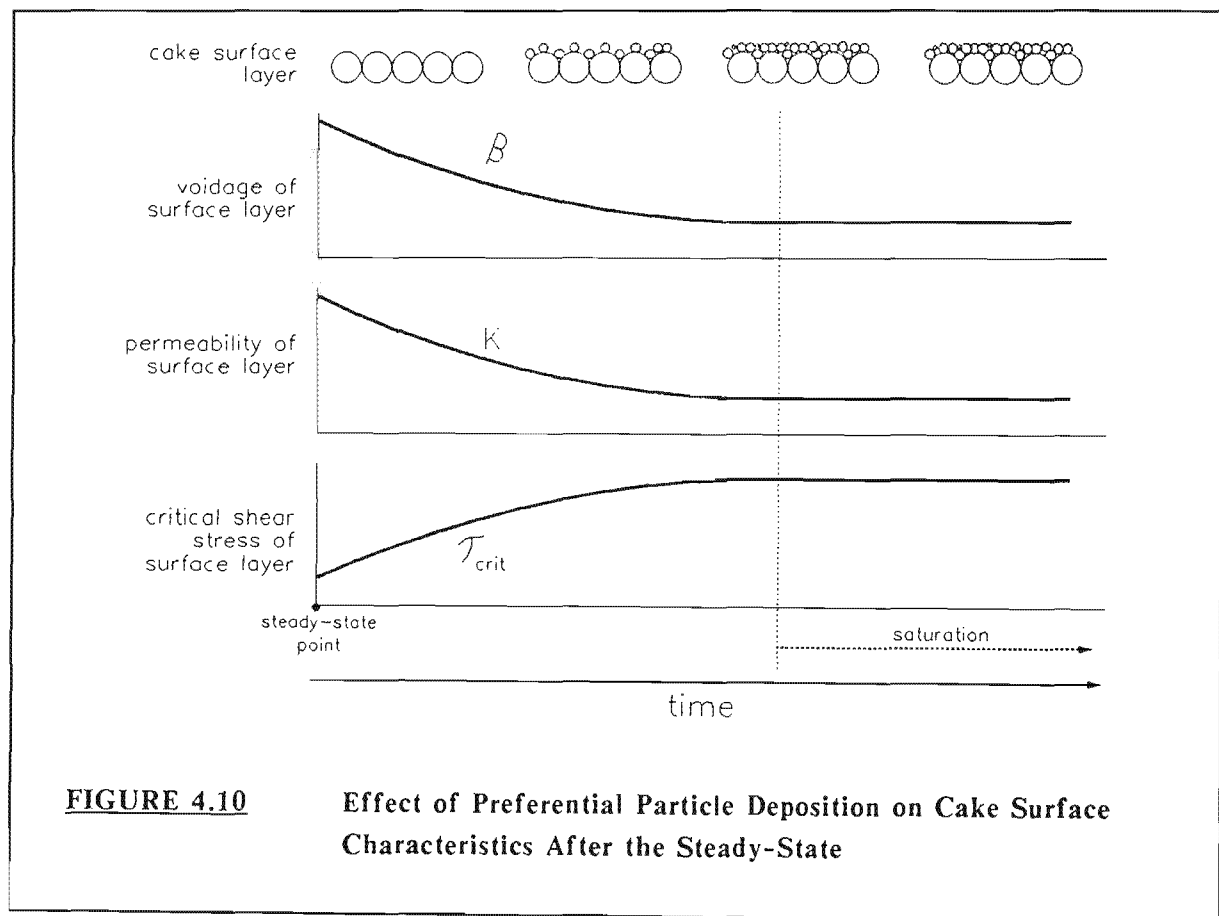
been reported, and the above effect cannot be confirmed. The observation that the mean cake particle size decreases with time [Baker et al. (1985), Hoogland et al. (1988)] could possibly be a manifestation of this radial variation in particle size.

The variation in particle size distribution through the cake will result in the local voidage also varying through the cake. It is thus expected that the local permeability,  $K$ , and local critical shear stress,  $\tau_{crit}$ , will also exhibit profiles through the cake. The qualitative effect that the preferential deposition of particles will have on cake characteristics during the cake growth period is illustrated in Figure 4.9.



In view of the preferential deposition effect, it is necessary to modify the conceptual picture presented earlier (Section 3.8) of particle activity at the cake surface after the limiting cake thickness has been reached.

After the limiting cake thickness has been attained, particles will still be convected to the cake surface. If the particles are monodisperse, all will be sheared off back into the precake. If polydisperse particles are considered, some fraction of the particles which convect to the surface will deposit stably into holes in the surface. However, the number of holes in a cake surface that may be stably occupied by particles of a particular size range is finite. As these holes become progressively occupied, particles of that particular size range will no longer be able to deposit stably onto the cake surface. Thus, after the limiting cake thickness is reached, preferential deposition of small particles will continue only until the cake surface becomes "saturated" with these smaller size fractions. This will result in the  $\beta$ ,  $K$  and  $\tau_{crit}$  of the surface layer progressively changing after the steady-state has been reached, until some saturation value is attained (Figure 4.10).



#### 4.4 FINES INFILTRATION EFFECT

In Section 2.5.1 it was shown that, for the system under study, there are strong indications that the slow long-term decline in flux is due to a progressive infiltration of finer particles into the existing structure, leading to a cake of progressively decreasing permeability. Here, the mechanism of this infiltration and the effects that this has on cake characteristics will be examined.

If the suspension consists of polydisperse particles, some of the particles which convect to the cake surface may be smaller than the void spaces between the particles in the surface. In contrast to depositing stably in the voids or being sheared off into the precake, these smaller particles will penetrate the cake surface. These *fines* may travel for some distance in the pores between the cake particles, eventually coming to rest at a smaller void space, when a group of fines bridge across a void, or by adhering to other cake particles. The local voidage, and hence local permeability of any layer in the cake will decrease as the layer becomes impregnated with fines.

Fines infiltration will occur during the cake growth period as well as after the limiting cake thickness has been attained. During the cake growth period, however, the increase in cake resistance due to fines infiltration is likely to be insignificant compared to the increase in resistance due to cake growth. Hence, the effects of fines infiltration on cake resistance will be most noticeable only after the steady-state cake thickness is reached.

The volume of voids in the cake is finite. Further, the size of particles that may infiltrate a particular pore in the cake is limited by the geometric arrangement of the cake particles. If, for example, spherical particles of diameter  $d$  are considered, the maximum size of particle that may penetrate the void is  $\approx 0,15 d$ . If this void is subsequently occupied by a particle, the diameter of the new voids decreases to  $\approx 0,01 d$  (Figure 4.11).

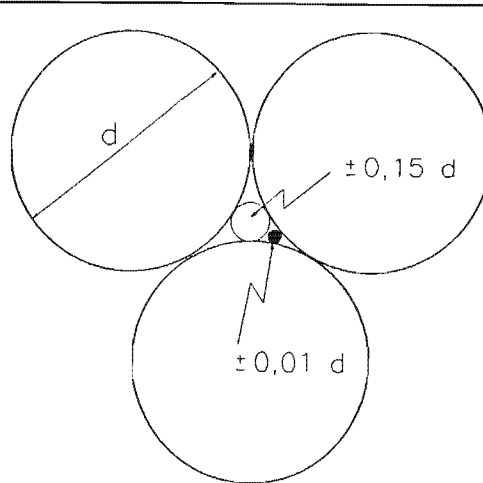


**FIGURE 4.11** Geometric Limit of Infiltrating Particles

Thus, for any layer in the cake there exists some maximum, or *saturation* volume fraction that may be occupied by fines. Effectively then, the fines content of a cake will increase with time and asymptotically approach some value corresponding to a fully saturated cake. The flux will thus decline and asymptotically approach some *ultimate* flux value.

The question arises as to whether fines saturate the entire cake volume, (*volume effect*) or whether this saturation is limited to the layers near the cake's surface (*surface effect*). This has significant implications for system behaviour, as will be demonstrated shortly.

There are strong indications that saturation by fines is limited to the surface layers of a cake. The first stems from the flux-time curves obtained at different operating conditions, as explained below.

The time taken to approach full saturation will be proportional to the volume of cake to be saturated and inversely proportional to the rate at which fines are convected into the cake. Assume firstly that the full cake volume is to be saturated. The saturation volume,  $V_{sat}$  will be given by :-

$$V_{sat} = \pi(R^2 - (R - t_c)^2)L \quad (4.9)$$

where  $V_{sat}$  = volume of cake available for saturation by fines ( $\text{m}^3$ )

$R$  = radius of tube (i.e. outer radius of cake) (m)

$t_c$  = thickness of cake (m)

$L$  = length of cake (m)

Thus,  $V_{sat}$  will increase as the cake thickness increases.

If the system is operated at a high superficial inlet velocity, the cake thickness will be relatively small and the flux relatively high. Thus,  $V_{sat}$  will be relatively small and the rate of convection of fines into the cake relatively high, indicating that the cake will rapidly approach its full saturation level. The flux will thus asymptote to its *ultimate* value shortly after the steady-state cake thickness has been attained. Conversely, if the system is operated at a low inlet velocity, the steady-state cake thickness will be relatively large and the flux relatively low. In this instance, the flux should exhibit a long period of decline before asymptoting to its ultimate value. Thus, if fines saturate the entire cake, the expected flux decline curves obtained at different operating velocities will be as depicted in Figure 4.12.

Alternatively, assume that fines saturate the cake only to some depth  $\bar{w}$  below the cake surface. The volume available for saturation in this instance is given by :-

$$V_{sat} = \pi[(R - t_c + \bar{w})^2 - (R - t_c)^2] \quad (4.10)$$

where  $\bar{w}$  = distance below cake surface to which fines penetrate (m)

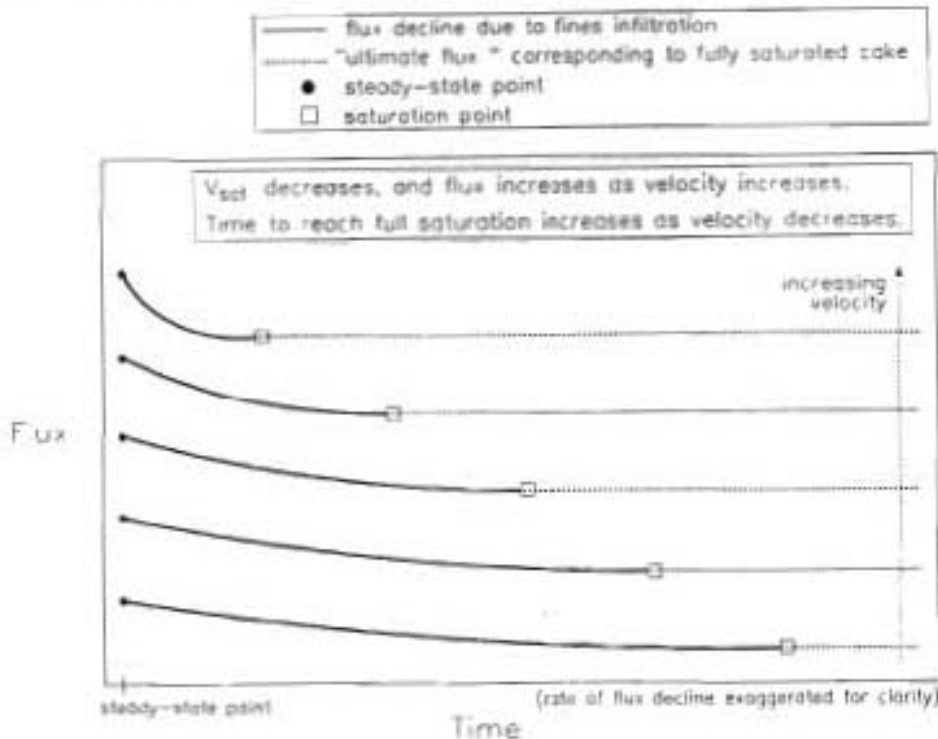
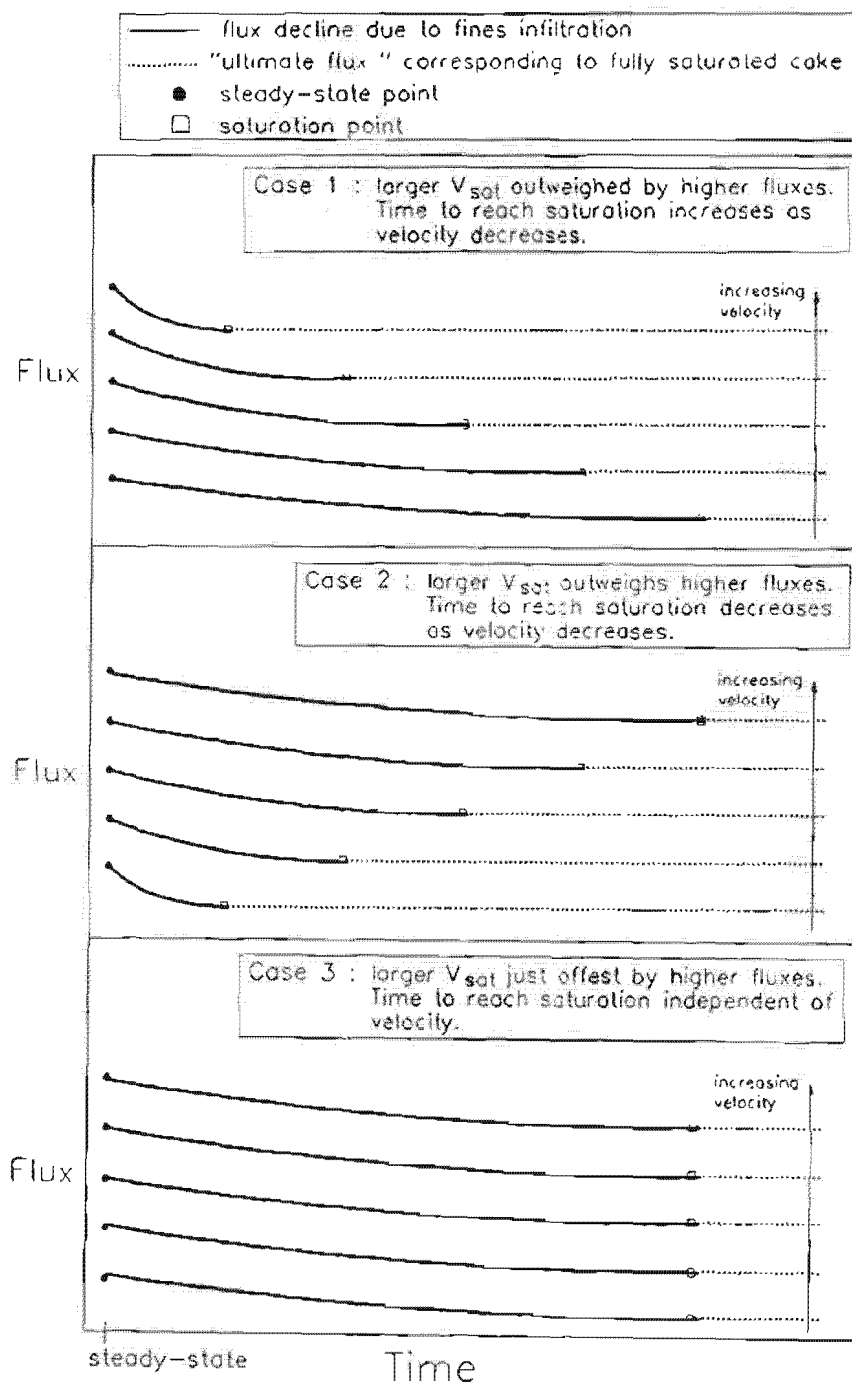


**FIGURE 4.12**      **Expected Flux Decline Curves If Fines Saturate Entire Cake Volume**

Equation 4.10 indicates that the volume available for saturation *decreases* as the cake thickness increases, due to the effects of the cylindrical geometry. Hence both  $V_{sat}$  and the rate of convection of fines into the cake will increase as operating velocity increases. Now three possible trends exist for flux decline curves obtained at different velocities, depending on the values of flux,  $t_c$  and  $\bar{w}$ .

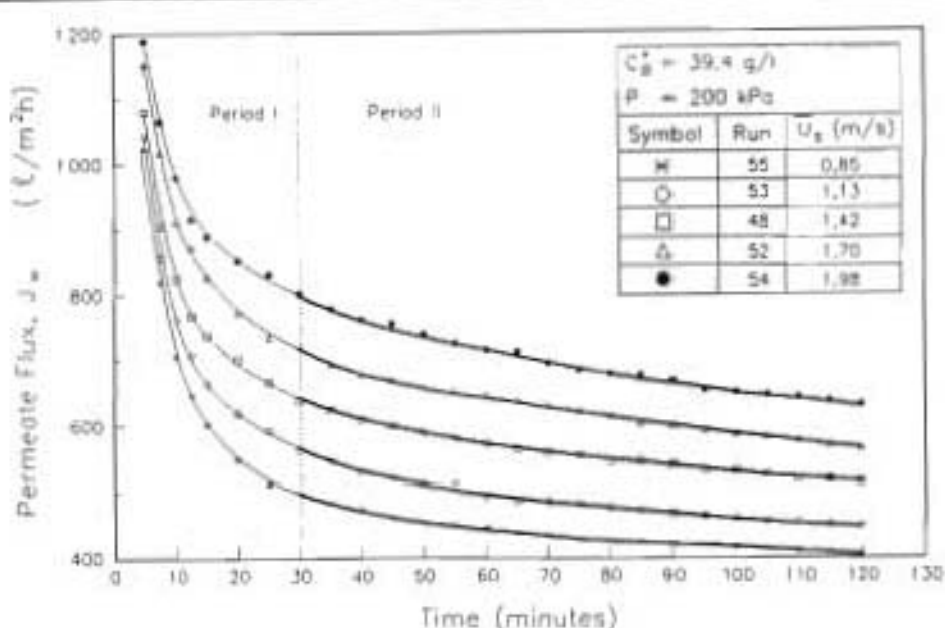
- Case 1** If at higher operating velocity the greater  $V_{sat}$  is outweighed by the higher flux, the time to reach full saturation will be less than if the system were operated at a lower velocity. In this instance the time to reach saturation will increase as operating velocity decreases.
- Case 2** If at the higher operating velocity, the higher flux is outweighed by the greater  $V_{sat}$ , a longer time would be taken to reach the saturation value than if the system were operated at a lower inlet velocity. Hence the time to reach saturation will decrease as operating velocity decreases.
- Case 3** The last possibility is that higher  $V_{sat}$ 's are just offset by higher fluxes. Here the time to reach saturation will be relatively independent of operating velocity.

These possible trends for flux decline at different operating velocities are depicted in Figure 4.13.



**FIGURE 4.13** Possible Trends for Flux Decline Curves if Fines Saturate Only the Surface Layers of the Cake

The experimental flux-time curves in Period II, obtained at different inlet velocities, are presented in Figure 2.9 (repeated here for convenience). The trend exhibited is contradictory to Figure 4.12, but is relatively consistent with Case 2 and Case 3 of Figure 4.13, indicating a strong probability that fines saturation is likely to be a surface effect.

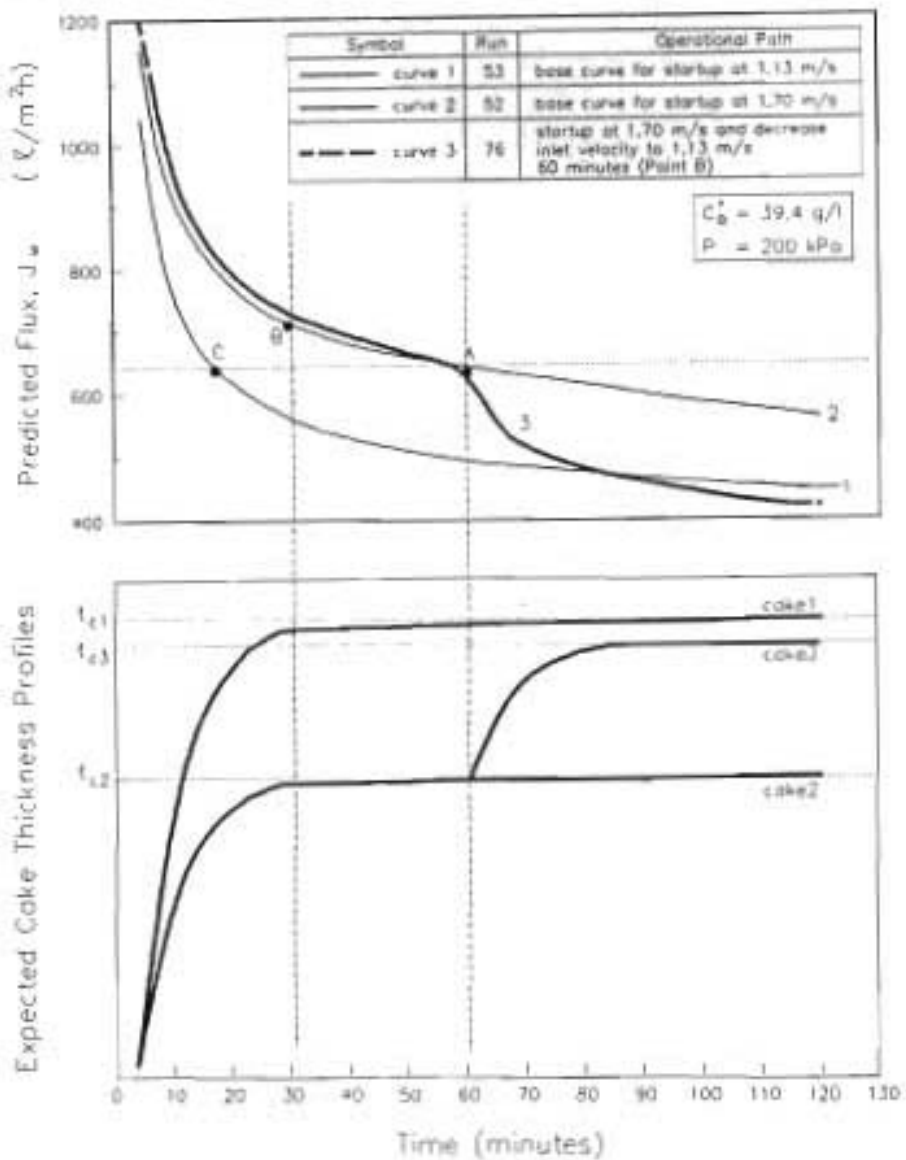


**FIGURE 2.9** Flux Decline Curves from Experimental Study (repeated)

The second indication that saturation by fines is likely to be limited to the surface layers concerns the observed system response to a step decrease in velocity (Figure 2.20, repeated in Figure 4.14). To recap, curves 1 and 2 were obtained by starting up the system at inlet velocities of 1.13 m/s and 1.70 m/s respectively, and curve 3 was obtained by starting up the system at 1.70 m/s and then step-decreasing the velocity to 1.13 m/s after 60 minutes. The likely cake thickness profiles for curves 1 and 2 (cake 1 and cake 2) are shown in Figure 4.14.

After an initial increase, the cake thicknesses reach their steady-state values and then remain approximately constant. The cake thickness profile for curve 3 (cake 3) will follow cake 2 up to  $t = 60$  minutes. At this point the velocity decreases, and hence the cake thickness will increase.

After the velocity decrease at point A, the axial and radial fluid velocities in the system will be equivalent to those at point C. If cake 3 had not experienced any changes in its characteristics during the period  $t = 30$  minutes to  $t = 60$  minutes, the cake would grow and eventually become limited to the steady-state value for curve 1, i.e.  $t_{ss}$ .

**FIGURE 4.14****Expected Cake Thickness Profiles for a Step-Decrease in Velocity**

However, over the period  $t = 30$  minutes to  $t = 60$  minutes, the specific cake resistance of cake 3 would have increased to above that of a "fines free" cake. Hence, the final cake thickness obtained after the velocity decrease,  $t_{c3}$ , must be somewhat lower than  $t_{c1}$ . It must be emphasised that, due to the increase in the specific cake resistance of cake 3 over the period  $t = 30$  minutes to  $t = 60$  minutes,  $t_{c3}$  cannot be greater than  $t_{c1}$ .

Assume, firstly, that fines saturate the entire cake volume. Since  $t_{c3} \leq t_{c1}$ , the final saturation resistance for cake 3 will be less than or equal to the final resistance for cake 1. Hence, the ultimate flux for curve 3 should be greater than that of curve 1. This is inconsistent with Figure 4.14, which clearly indicates that curve 3 drops to a value below curve 1.

Alternatively, assume that fines saturate only the surface layers of the cake. In this instance, cross-sectional profiles through cakes 1 and 3 will be as in Figure 4.15. Cake 1 reaches its steady-state thickness whereafter its surface layers become progressively saturated with fines. Similarly, cake 3 reaches its limiting value whereafter the surface layer becomes progressively saturated with fines. At  $t = 60$  however, cake 3 experiences a growth in thickness. Now a "fines free" cake grows above the existing partially saturated surface. This new surface will now become progressively infiltrated with fines.

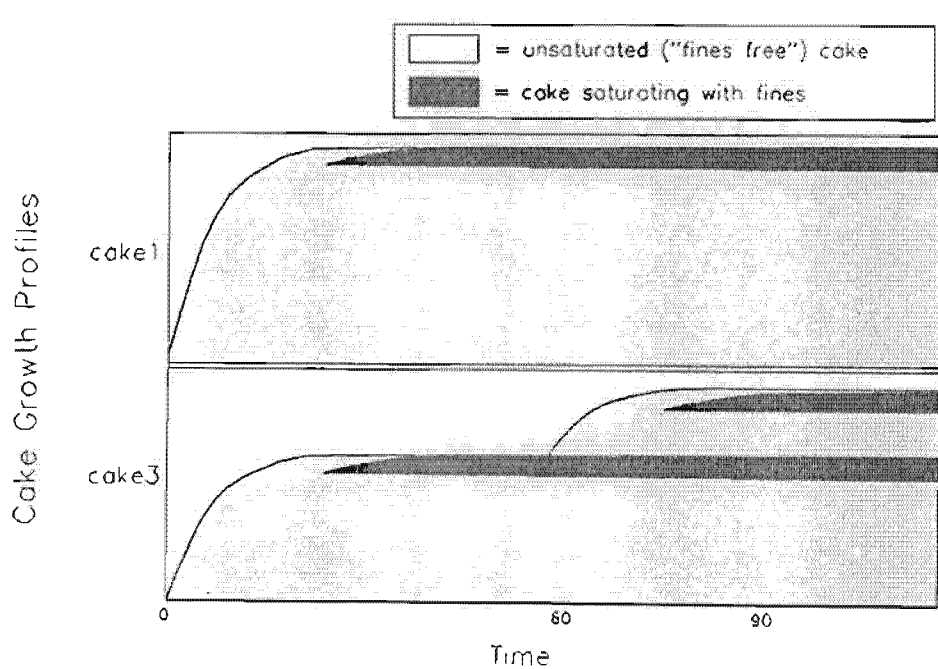
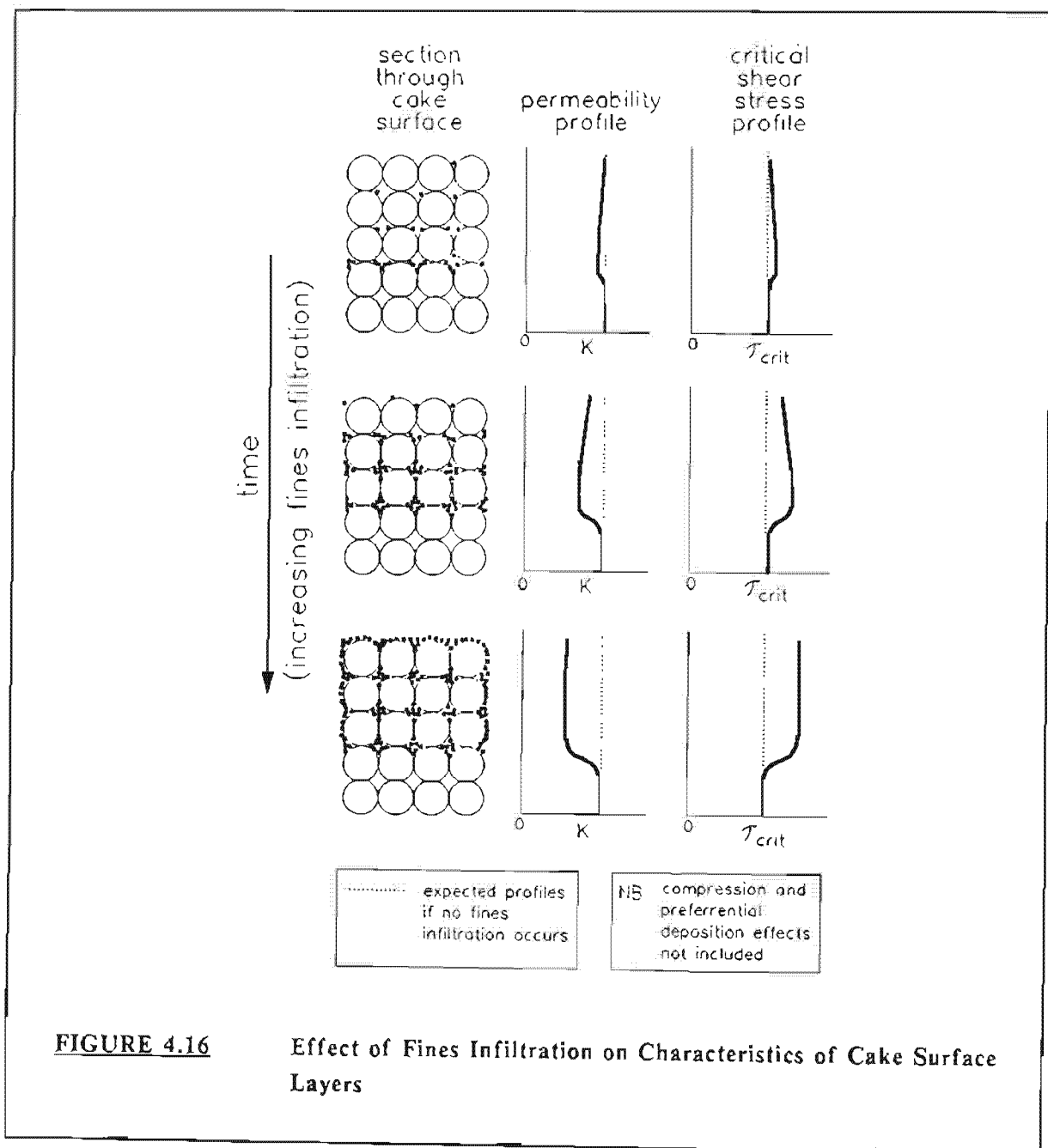


**FIGURE 4.15**      **Expected Cake Cross-Sections if Fines Saturate Only The Surface Layers of the Cake**

On comparing cakes 1 and 3 at  $t = 90$ , it is seen that cake 1 consists of one region that is fairly saturated with fines and a substantial fraction that is relatively fines free. Conversely, cake 2 consists of two regions that are fairly saturated with fines. The resistance of cake 3 is thus likely to be greater than that of cake 1, indicating that the flux for curve 3 should be lower

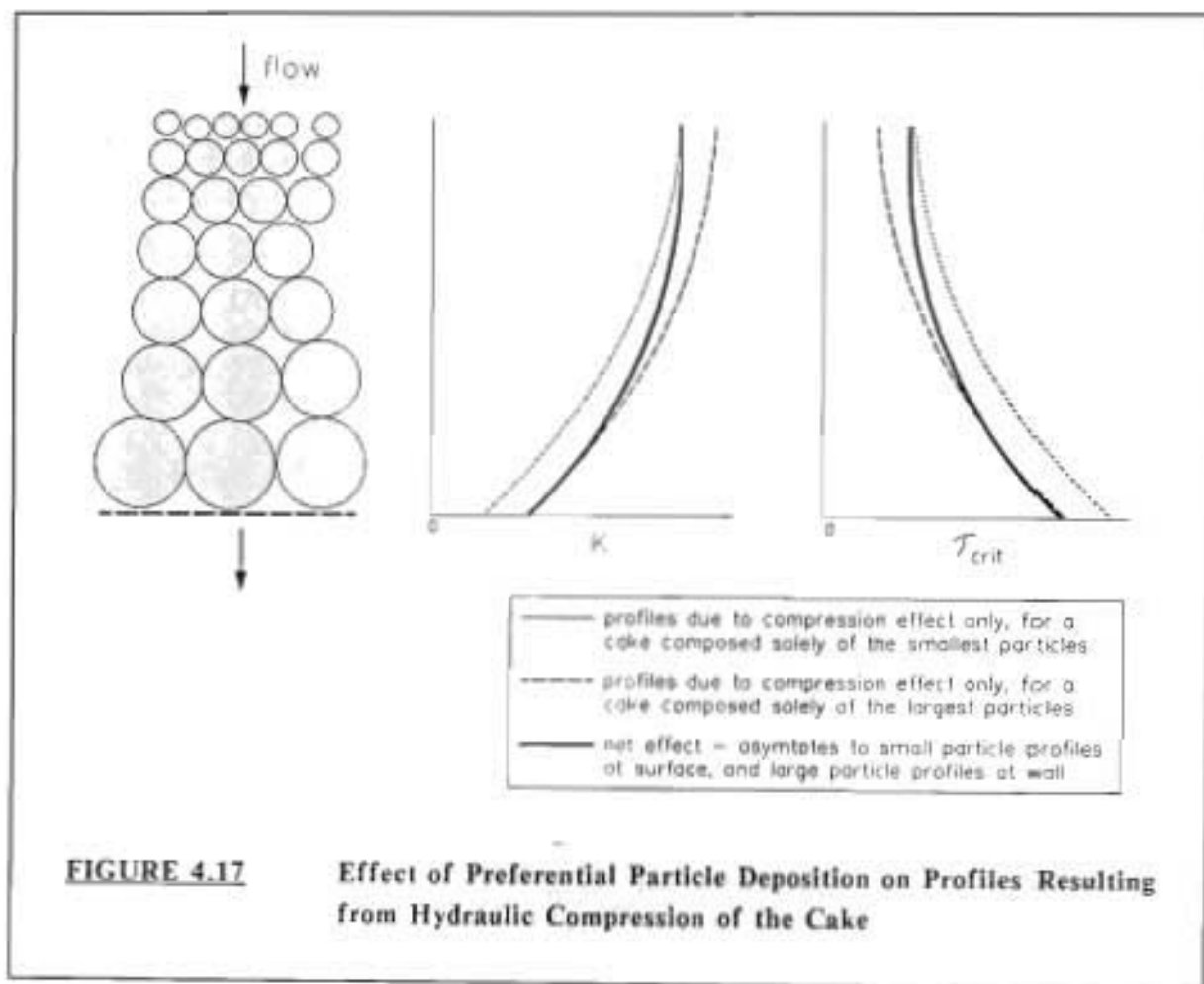
than that of curve 1. This is consistent with Figure 4.14, indicating that the observed flux-time response obtained by step-decreasing the operating velocity is consistent with the assumption that fines saturation is limited to the surface layers of the cake.

Unequivocal determination of whether fines saturation is a surface or a volume effect will necessitate sampling and analysis of the cake. On the basis of the above arguments, however, it seems most likely that this saturation is limited to the surface layers. This progressive saturation of the surface layers will change the voidage, and hence the permeability and critical shear stress profiles, of the surface layers. The effect of fines infiltration on cake characteristics may thus be represented as in Figure 4.16.



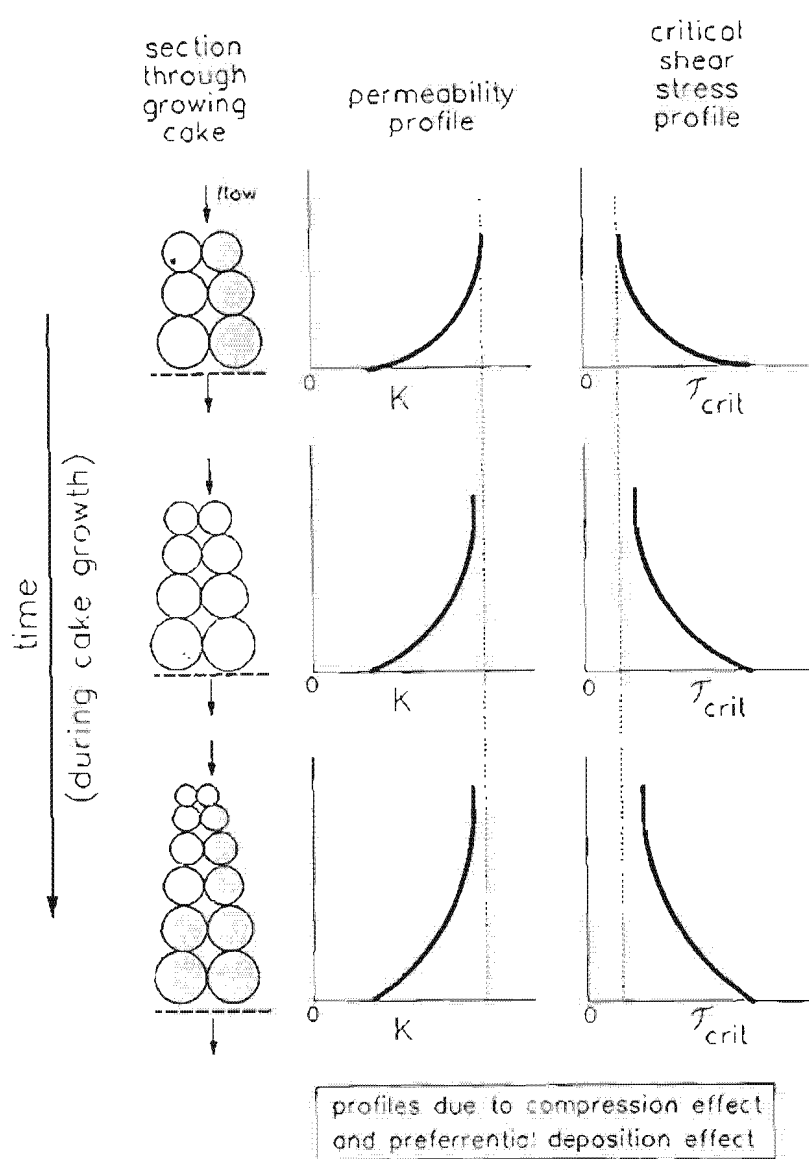
#### 4.5 NET EFFECT ON CAKE STRUCTURE AND CHARACTERISTICS

During the cake growth period, the significant effects that will determine cake characteristics will be the compression effect and the preferential deposition effect. The dominant effect is likely to be hydraulic compression. Preferential deposition may be regarded as *distorting* the profiles that result from hydraulic compression, causing the voidage at the surface layers to be slightly lower than that determined solely by compression (Figure 4.17).



**FIGURE 4.17** Effect of Preferential Particle Deposition on Profiles Resulting from Hydraulic Compression of the Cake

Since the preferential deposition effect is a strong function of the rates of exchange between the precake and the bulk, the observed influence on cake characteristics is likely to be small during the initial stage of cake growth, but will increase as the limiting cake thickness is approached. Hence, the likely voidage, permeability and critical shear stress profiles during the cake growth period will be as in Figure 4.18.

**FIGURE 4.18**

**Net Effects on Cake Characteristics During the Cake Growth Period  
(due to hydraulic compression and preferential deposition)**

After the limiting cake thickness has been attained, the main influences on cake characteristics will be the preferential deposition effect at the cake surface and the infiltration of fines into the surface layers. Both effects will eventually be limited by saturation of the surface and surface layers respectively. Effectively, after the limiting cake thickness has been reached, the change in cake characteristics will be limited to the surface layers and will be as in Figure 4.19.

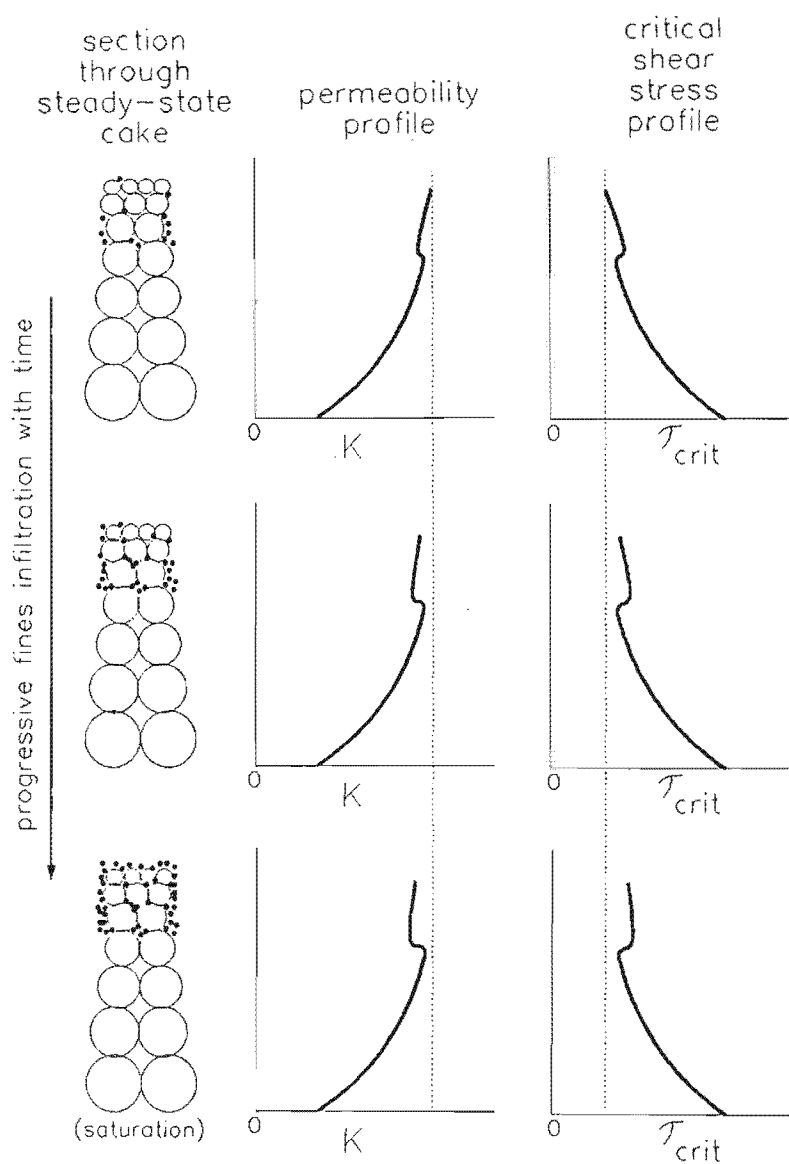


**FIGURE 4.19** Net Effects on Cake Characteristics After the Steady-State (due to fines infiltration)

## 4.6 APPLICATIONS

The effects of the various changes in characteristics on flux-time behaviour will be as follows :-

### 4.6.1 Long-term Flux Decline

The slow long-term decline in flux has already been explained in Section 2.5.1 and Section 4.4. Fine particles progressively infiltrate the surface layers of the cake resulting in a progressive decline in the cake permeability and hence in the permeate flux. However, there is some maximum or *saturation* fines fraction that may occupy the surface layers. Thus, the fines content asymptotically approaches this saturation value and the flux will asymptotically approach some *ultimate* flux value<sup>1</sup>.

### 4.6.2 Irreversibility of Cake

The initial step in the removal of particles from the cake is the shearing of particles off the cake surface. This will only occur if the shear stress at the surface exceeds the critical shear stress of the layer.

The shear stress at the surface is determined by the suspension velocity and physical properties. The critical shear stress exhibits a profile through the cake and in general increases towards the wall. It is thus feasible that at a specified suspension velocity, only some fraction of the cake may potentially be destabilised.

It is proposed that at normal operating conditions, the available shear stress only exceeds the critical shear stress of a small fraction of the cake. This fraction will decrease with time, as fines saturation of the surface layers progressively increases the  $\tau_{crit}$  of these layers (Figure 4.16).

Thus, when an attempt is made to decrease the cake thickness e.g. by increasing the velocity, decreasing the concentration or decreasing the pressure, a fraction of the cake surface layers will be removed. However, since the contribution of these surface layers to the overall cake resistance is small (see Section 4.2), the net effect on the measured permeate flux will not be significant. Cake removal will eventually become limited when the available shear is unable to exceed the critical shear stress of the current surface layer.

Clearly, at higher axial shear stresses, the fraction of cake that is removed will increase, eventually manifesting as an increase in permeate flux. For the operating range investigated in this study, however, this did not occur. A further effect to be noted is that the suspension velocity in the free channel will decrease as cake is removed, thereby decreasing the available axial shear stress at the surface. The effect of this would be to further decrease the fraction of cake that may be removed by a specified increase in inlet velocity or decrease in pressure.

---

<sup>1</sup> This ultimate flux is probably not attainable in a system that operates on a closed recycle basis, as in this study, since the fines content of the feed stream progressively decreases with time. Hence if a constant flux is obtained after some time this cannot unequivocally be attributed to saturation of the cake but could merely be due to depletion of fines.

#### 4.6.3 Cake Growth in Period II

In Section 2.5.3 it was observed that if the velocity is decreased, bulk concentration is increased, or pressure is increased during the slow decline in flux period, the final cake resistance is higher than that obtained by starting up the system at the lower velocity, higher concentration or higher pressure. As noted in Section 4.4, this apparent anomaly is explicable if it is assumed that fines saturation is limited to the surface layers of the cake.

A cross-section through the cake obtained by starting up the system at the "thicker cake" condition indicates that the surface layers will be relatively saturated with fines while the rest of the cake will be relatively fines free (Figure 4.15). Conversely, a cake obtained by starting up the system at the "thinner cake" condition and then increasing the cake thickness after a significant time lapse will consist of two regions that are relatively saturated with fines. Since the permeability of a cake layer is a strong function of particle size, the total resistance of this latter cake will be somewhat higher than the resistance of the cake obtained by starting up the system at the "thicker cake" condition.

### 4.7 SUMMARY OF CHANGES IN CAKE STRUCTURE AND CHARACTERISTICS

For the system under study, three phenomena that are likely to cause changes in the cake characteristics are *hydraulic compression* of the cake, the *preferential deposition effect* and the *fines infiltration* effect. These phenomena are mainly due to the presence of a wide size range of particles in the suspension.

Hydraulic compression occurs when fluid drag forces cause an irreversible collapse of the particulate structure, leading to a cake of decreased voidage. The preferential deposition effect concerns the deposition of smaller particles onto the cake, in preference to the larger size fractions. This is explicable in terms of a simple model based on rates of transport to and from the precake. The fines infiltration effect concerns the progressive infiltration of very fine particles into the existing cake structure, until some saturation fines content is achieved. There are strong indications fines saturate only the surface layers of the cake, and not the entire cake volume.

The above phenomena change the voidage profile and hence the permeability and critical shear stress profiles of the cake. The individual effects are summarised in Table 4.1.

<b>TABLE 4.1</b> Individual Effects on Cake Characteristics			
	Effect on :		
	Voidage $\beta$	Permeability $K$	Critical shear stress $\tau_{crit}$
<b>Hydraulic Compression</b>	Decreases towards tube wall	Decreases towards tube wall	Increases towards tube wall
<b>Preferential Deposition</b>	Decreases towards cake surface	Decreases towards cake surface	Increases towards cake surface
<b>Fines Infiltration</b>	Decreases in cake surface layers	Decreases in cake surface layers	Increases in cake surface layers

Hydraulic compression is most likely to be the dominant cause of changes in cake structure and characteristics during the cake growth period. The fines infiltration effect is most observable after the limiting cake thickness has been achieved.

The apparent irreversibility of the cake, the long-term flux decline, and the observation that the final cake resistance is dependent on the operating path taken to reach the operating point, are explicable in terms of the above phenomena.

# *Chapter 5*

## **MATHEMATICAL MODEL OF THE STEADY-STATE CONDITION**

---

### **5.1 INTRODUCTION**

In Chapter 3 it was shown that, for the limestone system used in the present study, the steady-state condition is determined by a convection-diffusion process. The radial fluid flow towards the wall convects particles to the cake surface. The mechanisms of shear induced hydrodynamic diffusion, entrainment by turbulent bursts and entrainment by turbulent eddies, effect particle diffusion from the concentrated suspension layer next to the cake back to the bulk suspension. The steady-state cake thickness is attained when the equilibrium concentration of this concentrated suspension layer falls below the critical concentration for consolidation.

In this Chapter, this qualitative mechanistic model is formulated into a mathematical model of the steady-state.

Convection-diffusion models for turbulent CFMF have been formulated by previous workers, as discussed in Chapter 3. In general, previous workers assumed loose forms for model functions (e.g. diffusivity) and model parameters were subsequently evaluated by regression on experimental results. Thus, despite mechanistic inconsistencies associated with those models, their mathematical formulations do permit effective correlation of experimental results. In view of this, the formulation of yet another model based on loose, albeit different, forms for model functions and sufficient regression parameters to enable successful correlation with experimental results will not necessarily be a significant contribution towards modelling of CFMF.

The approach adopted here is to attempt to formulate model functions rigorously from existing technology and correlations for fluid and particle dynamics, with minimum recourse to regression parameters. Noting the considerable differences between a CFMF system and systems usually employed in rigorous fluid and particle dynamics studies, it is recognized *a priori* that this modelling approach is unlike to yield as good a fit with experimental observations as the previous "full regression" models. However the evaluation of the applicability and short falls of current technology is an important point of departure towards the ultimate aim of a fully predictive turbulent CFMF model.

In Section 5.2, the appropriate steady-state continuity and hydraulic resistance equations are identified. The differences between a CFMF system and those systems usually employed in fluid and particle dynamics investigations are briefly reviewed in Section 5.3, in order to identify differences that may be ignored and those that must be explicitly accounted for when applying existing transport correlations to CFMF. In Section 5.4, mathematical formulations are developed for the various model functions needed to solve the steady-state equations. The numerical solution procedure is outlined in Section 5.5 and the approach adopted in quantifying model parameters is discussed in Section 5.6. Model predictions are presented and discussed in Section 5.7. Finally, the model is evaluated and summarised in Section 5.8.

### **5.1.1 A Reminder on State and Measured Variables, and the Wall**

In this chapter, frequent reference is made to fluid and particle dynamics technology and correlations developed by other workers. Most of these previous studies have concerned systems where no *cake* exists, and hence the superficial and channel velocities are the same. In applying these correlations to CFMF, it must be realised that velocities should be based on the free channel radius,  $R_c$ , and not on the tube radius,  $R$ . Accordingly, in reporting correlations, their nomenclature has been suitably adapted to reflect this fact. Hence, where a correlation refers to a *bulk average axial velocity*,  $\bar{U}$ , this is reported here as a *bulk average channel velocity*,  $\bar{U}_c$ , and *permeate velocities at the wall* are reported here as *permeate velocities at the cake surface*,  $V_{cs}$ .

Reiterating the points made in Section 3.4.2, it should be noted that *wall* refers to the surface that bounds the flow field. In systems where no cake exists, the *wall* resolves to the wall of the tube or pipe. In CFMF, however, the *wall* is the inner surface of the cake, and not the tube wall. This should be remembered when interpreting graphs and correlations in this chapter. Where it becomes necessary to refer to the wall of the CFMF tube, this will be specifically referred to as *tube wall*.

## **5.2 THE STEADY-STATE EQUATIONS**

### **5.2.1 Continuity Equation**

The one-dimensional continuity equation applicable to convection-diffusion controlled processes i.e.

$$VC = D \frac{\partial C}{\partial r}$$

is widely known and applied in the modelling of membrane separation processes. Here the origin of the equation is briefly reviewed in order to highlight the assumptions inherent in the equation and hence to ascertain whether the equation is applicable to the system used in the present study.

The equation of continuity for the particles in radial co-ordinate systems is :-

$$\frac{\partial C}{\partial t} + \nabla \cdot (C \mathbf{V}) = \nabla \cdot (D_p \nabla C) \quad (5.1)$$

where  $C$  = particle concentration (volume fraction)  
 $\mathbf{V}$  = suspension velocity vector (m/s)  
 $D_p$  = particle diffusivity vector (m<sup>2</sup>/s)  
 $t$  = time (s)

The following simplifying assumptions are made :

- (i) azimuthal gradients, i.e. ( $\partial/\partial\theta$ ), are negligible.
- (ii) the concentration profiles are at a "steady-state"<sup>1</sup> i.e.  $\partial C/\partial t = 0$ .
- (iii) radial concentration gradients are confined to a thin concentration boundary layer, of thickness  $\delta$ , next to cake surface.

With the above assumptions, equation 5.1 reduces to :

$$r < (R_c - \delta)$$

$$C = C_B$$

$$r > (R_c - \delta)$$

$$\frac{1}{r} \frac{\partial}{\partial r} (r V C) + \frac{\partial (C U)}{\partial z} = \frac{1}{r} \frac{\partial}{\partial r} \left( r D_{p,r} \left( \frac{\partial C}{\partial r} + \frac{\partial C}{\partial z} \right) \right) + \frac{\partial}{\partial z} \left( D_{p,z} \left( \frac{\partial C}{\partial r} + \frac{\partial C}{\partial z} \right) \right) \quad (5.2)$$

where  $C_B$  = bulk concentration (volume fraction)  
 $r$  = radial distance from tube centreline (m)  
 $R_c$  = core radius (m) ( $= R - t_c$ )  
 $R$  = tube radius (m)  
 $V$  = suspension velocity in radial direction (m/s)  
 $U$  = suspension velocity in axial direction (m/s)  
 $D_{p,r}$  = particle diffusivity in radial direction (m<sup>2</sup>/s)  
 $D_{p,z}$  = particle diffusivity in axial direction (m<sup>2</sup>/s)  
 $t_c$  = cake thickness (m)

---

<sup>1</sup> Note that the "steady-state" referred to in assumption (ii) refers solely to time-invariant concentration profiles. The steady-state in CFMF is a unique situation where concentration profiles are time-invariant and there is no net radial solids transport across the boundary layer. It is, however, entirely possible to have systems where the concentration profile is time-invariant while a net solid transport does occur.

Equation 5.2 describes the concentration distribution in a tube of arbitrary length, explicitly including gradients in the axial direction. A substantial simplification may be made by considering a *differential element* of a tube, where concentration gradients in the axial direction are negligible in comparison with gradients in the radial direction. Most systems may be divided into differential elements fulfilling the above criterion. A model developed for the differential element may then be integrated to yield the approximate concentration distribution along the whole tube [see e.g. Pillay et al. (1988)].

For such a differential element, from equation 5.2, and denoting the radial particle diffusivity,  $D_{p,r}$ , simply as  $D_p$  :

$$r > (R_c - \delta)$$

$$\frac{1}{r} \frac{\partial}{\partial r} (r V C) = \frac{1}{r} \frac{\partial}{\partial r} \left( r D_p \frac{\partial C}{\partial r} \right) \quad (5.3)$$

Integration of equation 5.3 yields

$$r V C - r D_p \frac{\partial C}{\partial r} = Q_s \quad (5.4)$$

The constant of integration,  $Q_s$ , indicates the net solids flowrate across any unit length cylindrical surface in the boundary layer.

Equation 5.4 indicates an interesting implication of the differential element assumption. Since axial gradients are assumed to be zero, continuity must be observed in the radial direction. Hence if a net solids transport does occur across the boundary layer (e.g. during cake growth), the net solids flowrate across any unit length cylindrical surface in the boundary layer must be constant, as indicated by equation 5.4.

Rearrangement of equation 5.4 yields

$$V C - D_p \frac{\partial C}{\partial r} = \frac{Q_s}{r} \quad (5.5)$$

Here  $(V C - D_p \partial C / \partial r)$  indicates the net solids velocity at a particular radius  $r$ . Since the net solids flowrate remains constant, the net solids velocity must decrease through the boundary layer, due to the increase in circumferential area. This is indicated by the term  $(Q_s/r)$ . Hunt et al. (1987c), adopting a one-dimensional differential element approach in modelling cake growth, assumed that the net solids velocity increases through the boundary layer. This is clearly not feasible from the point of view of continuity.

A further implication of equation 5.5 is that the concentration boundary layer cannot be large in comparison with the tube radius. In the extreme instance, when the thickness of the boundary layer approaches the radius of the tube, the net solids velocity at the inner edge of the boundary layer approaches infinity, implying that an infinite source of solids exists along the centreline. Thus, if the boundary layer is large, a differential element analysis is inapplicable and axial gradients must be explicitly included in order to obtain a realistic solution.

At the steady-state in CFMF, the net solids velocity is zero. This is a unique instance of equation 5.5 with  $Q_s = 0$ . Hence

$$\nu C = D_p \frac{\partial C}{\partial r} \quad (5.6)$$

It should be noted that  $\nu$  in equations 5.2 to 5.5 represents the *suspension velocity*, comprised of both the net fluid and net solids velocities relative to the tube co-ordinate system. For the unique case of zero net solids velocity,  $\nu$  in equation 5.6 reduces to the fluid velocity.

To summarise thus far, equation 5.6 is the one-dimensional convection-diffusion continuity equation applicable to systems where the concentration profile is time-invariant, the net solids velocity is zero and axial gradients are negligible in comparison with radial gradients. The question arises as to whether equation 5.6 is applicable to the system used in the present study. Fractional changes in operating variables along the tube are presented in Table 5.1 (overleaf).

Since the steady-state cake thickness is a function of pressure, concentration and velocity, it follows from Table 5.1 that this steady state thickness will exhibit only a small variation in the axial direction. Further, the variation of concentration in the axial direction is indeed negligible in comparison with the concentration variation in the radial direction (low bulk concentration increasing up to packing density). Accordingly the tube used in the present study may reasonably be modelled as a differential element.

**TABLE 5.1** Summary of Fractional Changes in Operating Variables along Tube

Run Number	Change in Superficial Velocity $\Delta(\bar{U}_s)\%$	Change in Bulk Concentration $\Delta(C_B^*)\%$	Change in Pressure $\Delta(P)\%$
55	8	8	3
53	7	7	3
48	6	6	3
52	6	6	3
54	5	6	3
50	8	9	3
47	7	8	3
49	5	6	3
51	5	5	3
59	5	5	6
60	5	6	4
61	6	7	2
58	6	7	2

$$\Delta(\bar{U}_s)\% = \frac{\bar{U}_s(\text{in}) - \bar{U}_s(\text{out})}{\bar{U}_s(\text{in})} \times 100$$

$$\Delta(C_B^*)\% = \frac{C_B^*(\text{out}) - C_B^*(\text{in})}{C_B^*(\text{in})} \times 100$$

$$\Delta(P)\% = \frac{P(\text{in}) - P(\text{out})}{P(\text{in})} \times 100$$

where  $\bar{U}_s$  = superficial velocity (m/s)

$C_B^*$  = bulk concentration (g/ℓ)

$P$  = pressure (kPa)

(in) refers to inlet of tube

(out) refers to outlet of tube

$\bar{U}_s(\text{in})$ ,  $C_B^*(\text{in})$ ,  $P(\text{in})$  and  $P(\text{out})$  were measured.  $\bar{U}_s(\text{out})$  and  $C_B^*(\text{out})$  were calculated by mass balance.

From the qualitative model presented in Chapter 3, the appropriate boundary conditions for equation 5.6 are :

$$r = R_c \quad C = C_{crit}$$

$$r = R_c - \delta \quad C = C_B$$

where  $R_c$  = radius of free core (m)

$\delta$  = boundary layer thickness (m)

$C_{crit}$  = critical concentration (volume fraction)

$C_B$  = bulk concentration (volume fraction)

Integration of equation 5.6 with the above boundary conditions yields :

$$\int_{R_c-\delta}^{R_c} \frac{V}{D_p} dr = \ln\left(\frac{C_{crit}}{C_B}\right) \quad (5.7)$$

The steady-state continuity equation is thus given by equation 5.7. Note that  $V$  and  $D_p$  in equation 5.7 are not constants, but are the radial distributions of the radial velocity and particle diffusivity respectively across the boundary layer.

### 5.2.2 Hydraulic Resistance Equation

Following Darcy's Law, the hydraulic resistance equation for a planar cake (cartesian co-ordinate system) is as follows :-

$$\Delta P = \frac{\mu_t V}{K} t_c \quad (5.8)$$

where  $\Delta P$  = pressure drop across cake (Pa)

$\mu_t$  = permeate viscosity (Pa.s)

$V$  = permeate velocity (m/s)

$t_c$  = cake thickness (m)

$K$  = permeability ( $m^2$ )

Equation 5.8, however, cannot be directly applied to cylindrical co-ordinate or CFMF systems. Firstly, although the permeate flowrate remains constant through the cake, the permeate velocity will change, due to the change in circumferential area. Thus  $V$  in equation 5.8 will vary radially through the cake.

The second problem concerns the cake permeability,  $K$ . Most real cakes are compressible to some extent. Hydraulic compression, arising from fluid flow through the cake, will cause a solids compressive pressure ( $P_s$ ) profile to be established through the cake (See Chapter 4). In cylindrical cakes this  $P_s$  profile is further complicated by the presence of "hoop" stresses. The cake permeability is a function of  $P_s$ , and thus  $K$  is expected to exhibit some complex

profile through the cake. There are also indications that the permeability (or conversely the specific cake resistance) of a cake formed under cross-flow conditions may be a function of cross-flow velocity, operating pressure and time from start-up [Baker et al. (1985), Hoogland et al. (1988)]. It emerges therefore that  $K$  may be a complex function of distance through the cake, velocity, pressure and time from start-up.

A hydraulic resistance equation which explicitly caters for all the various effects on  $K$  is beyond the scope of the present study. For the present purpose it will be assumed that variations in permeability through the cake, the effect of cross-flow velocity on permeability and the change in permeability with time are "second order" effects and may be ignored. Accordingly, the permeability is only a function of the operating pressure in the system,  $P$ , and the dependence of  $K$  on  $P$  arises solely from compression effects.

An approximate hydraulic resistance equation applicable to cylindrical cakes may now be derived.

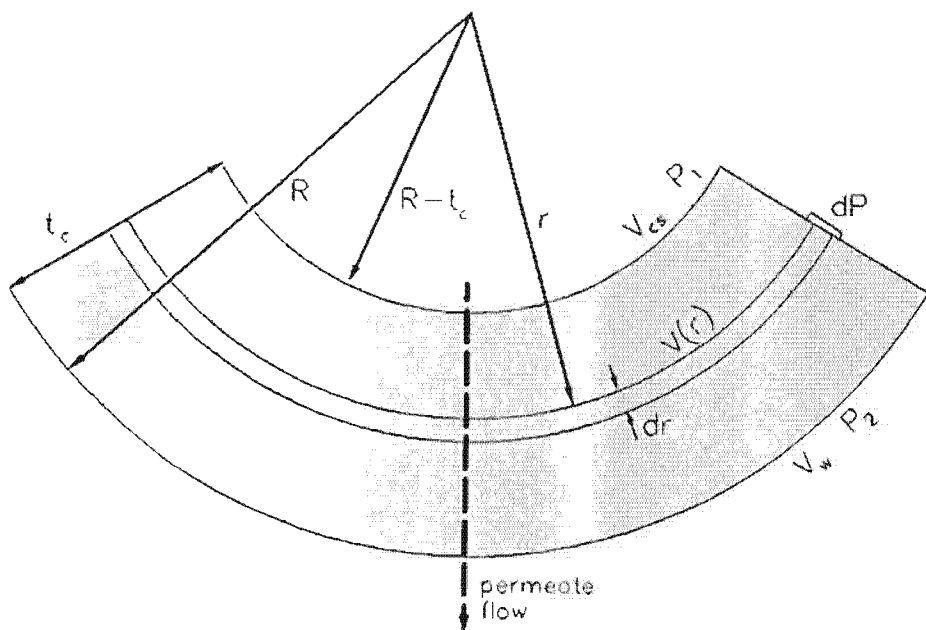


**FIGURE 5.1** Section Through a Cake Formed on a Cylindrical Surface

Across a thin section of the cake at radius  $r$  (Figure 5.1),

$$-\frac{dP}{dr} = \frac{\mu_1 V(r)}{K} dr \quad (5.9)$$

where  $V(r)$  = permeate velocity at radius  $r$  (m/s).

From a mass balance, for a cake of unit length in the axial direction :-

$$V(r)2\pi r = V_w 2\pi R$$

where  $V_w$  = permeate velocity at tube wall (m/s)  
 $R$  = tube radius (m)

Thus,

$$V(r) = V_w \frac{R}{r} \quad (5.10)$$

Substituting equation 5.10 into equation 5.9 and integrating with the limits :-

$$r = R - t_c \quad P = P_1$$

$$r = R \quad P = P_2$$

yields

$$-\int_{P_1}^{P_2} dP = \frac{\mu_l}{K} V_w R \int_{R-t_c}^R \frac{dr}{r}$$

whence

$$\Delta P = \frac{\mu_l V_w R}{K} \ln\left(\frac{R}{R-t_c}\right) \quad (5.11)$$

### 5.2.3 Summary of Steady-State Equations

The system used in the present study may be approximated as a differential element. The steady-state condition is thus represented by the simulation solution of the following equations :

$$\int_{R_c-\delta}^{R_c} \frac{V}{D_p} dr = \ln\left(\frac{C_{crit}}{C_B}\right) \quad (5.7)$$

$$\Delta P = \frac{\mu_l V_w R}{K} \ln\left(\frac{R}{R-t_c}\right) \quad (5.11)$$

In order to solve the above steady-state equations for the steady-state cake thickness ( $t_c$ ) and permeate velocity ( $V_w$ ) mathematical formulations for  $\delta$ ,  $V$  and  $D_p$  in terms of the operating variables are needed, together with values for  $C_{crit}$  and  $K$ .

## 5.3 APPLICABILITY OF CURRENT FLUID AND PARTICLE DYNAMICS TECHNOLOGY TO CFMF

The major aim is to formulate model functions that are required to solve the steady-state equations from existing technology in fluid and particle dynamics. Direct application of a correlation requires complete similarity between the system for which the correlation was developed and the system to which it is to be applied. There are, however, significant differences between CFMF systems and the systems used in most turbulent fluid and particle dynamics studies. The first is that most transport correlations have been developed for non-porous tubes, whereas in CFMF a significant radial velocity component exists. The second difference is that most studies have involved systems where the viscosity is uniform across the cross section of the tube while in CFMF the viscosity is expected to exhibit a significant radial variation due to the existence of a radial concentration profile. This section (5.3) addresses the issue of whether these differences must be explicitly accounted for, or whether they may be ignored.

### 5.3.1 Applicability of Correlations Developed for Non-porous Tubes to CFMF

The obvious approach is to compare results obtained from studies of turbulent flow in porous tubes with predictions from correlations developed for non-porous tubes, at the typical conditions used in this study.

Probably the most significant experimental studies of the fluid dynamics of turbulent flow in porous tubes are those of Weissberg (1955, 1956). Other experimental studies include those of Aggarawal et al. (1972), Hirata et al. (1982a) and Mizushina et al. (1972). In a theoretical approach, Kinney and Sparrow (1970) developed an integro-differential model for turbulent flow in porous tubes. The model was subsequently extended by Merkine et al. (1971), and Na (1972). A theoretical model, based on the extension of the mixing length concept, was developed by Hirata et al. (1982b). These theoretical models, although mechanistically attractive, are somewhat difficult to implement. In any event, the models of Kinney and Sparrow, Merkine et al., and Na, used Weissberg's experimental results for model evaluation. Accordingly only Weissberg's studies will be referred to here.

Weissberg measured axial velocity profiles, turbulence levels and friction factors for air flowing in a porous pipe, for a wide range of axial inlet and radial wall velocities. In contrast to non-porous tubes, where the non-dimensional velocity,  $U^*$ , is well correlated with the non-dimensional distance from the wall,  $Y^*$ , no such universal relationship could be found for porous tubes. Following the correlation approach of Laufer, Weissberg correlated the mean (time-averaged) axial velocity profiles as follows :-

$$Y^* < 20 \quad (\text{wall region})$$

$$sY^* = \frac{E\left(sU^* + \frac{v^*}{s}\right) - E\left(\frac{v^*}{s}\right)}{E'\left(sU^* + \frac{v^*}{s}\right)} \quad (5.12)$$

$Y^+ \geq 20$  (inner region)

$$U^+ = h_5 + h_6 \log(Y^+) \quad (5.13)$$

where

$$s = 0,1037(1 - 2,486V^+)$$

$$V^+ = \frac{V_{cs}}{U^+}$$

$$E(sU^+) = \frac{1}{\sqrt{2\pi}} \int_0^{sU^+} e^{-t^2} dt$$

$$E'(sU^+) = \frac{1}{\sqrt{2\pi}} e^{-\frac{(sU^+)^2}{2}}$$

$$h_5 = 3,07 (1 + 20,7 V^+)$$

$$h_6 = 6,75 (1 - 7,67 V^+)$$

with  $U^+$  = non-dimensional axial velocity

$$= (U/U^+)$$

$Y^+$  = non-dimensional distance from the wall

$$= (YU^+/\nu)$$

$Y$  = distance from the wall (or cake surface) (m)

$\nu$  = kinematic viscosity ( $m^2/s$ )

$U^+$  = friction velocity (m/s)

$$= \sqrt{\frac{\tau_w}{\rho}}$$

$V_{cs}$  = radial velocity at wall (or cake surface) (m/s)

Note that

$$E(x) = \frac{1}{2} \operatorname{erf} \left( \frac{x}{\sqrt{2}} \right)$$

where  $\operatorname{erf}(x)$  is the error function.

Comparison between friction coefficients in porous tubes with the standard Blasius equation for smooth non-porous tubes yielded the following :

$$\frac{f}{f_0} = 1 + 115,8 \frac{V_{cs}}{\bar{U}_c} \quad (5.14)$$

where  $f$  = friction factor in porous tubes

$f_0$  = Blasius friction factor for smooth non-porous tubes

$$= 0,079 (Re)^{0,25}$$

$V_{cs}$  = radial velocity at wall (cake surface) (m/s)

$\bar{U}_c$  = bulk average axial velocity in free channel (m/s)

Note that for turbulent flow, friction factors in porous tubes are greater than those in non-porous tubes (see equation 5.14). As noted in Chapter 3, this is contrary to that in laminar flow, where friction coefficients decrease as suction through the wall increases.

The typical effect of radial flow on the axial velocity profile is depicted in Figure 5.2 (a) and (b). The profiles were calculated from equations 5.12 and 5.13. Figure 5.2(a) depicts profiles over the whole tube, and Figure 5.2(b) that in the near wall region. Suction of fluid through the wall results in a flattening of the velocity profile over the core with a subsequent steepening of the gradient in the wall region.

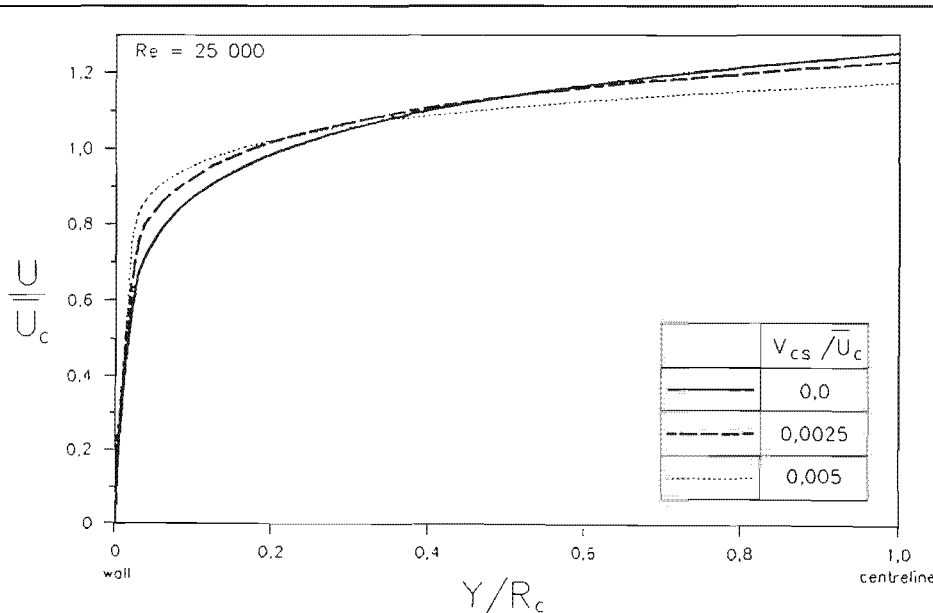


**FIGURE 5.2(a)** Effect of Radial Fluid Flow on Axial Velocity Profile (whole tube)

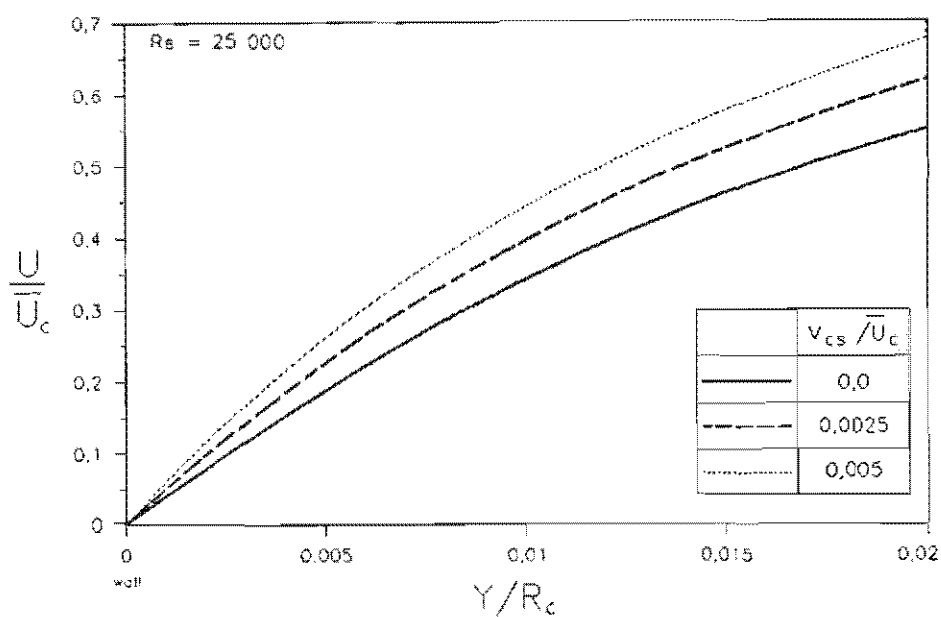


**FIGURE 5.2(b)** Effect of Radial Fluid Flow on Axial Velocity Profile (near wall region)

In this study, as well as in most membrane systems, the radial velocity is generally small relative to the axial velocity. The question arises as to whether, for low radial velocities, the actual axial velocity profile in a porous tube would differ significantly from non-porous tube profiles.

In applying the above correlations to CFMF, the velocities based on the free channel radius, i.e.  $V_{cs}$  and  $\bar{U}_c$ , must be employed in place of velocities based on the tube radius, i.e.  $V_w$  and  $\bar{U}_s$ . Since the cake thicknesses obtained in the present study are not known, four *worst case* scenarios were investigated (Table 5.2, overleaf). Axial velocity profiles calculated from Weissberg's correlations for these scenarios are compared to a non-porous tube profile calculated from Von Karmans universal velocity profile correlations (equations 3.44 to 3.46) in Figure 5.3. Note that over most of the graph the curves are co-incident, and hence show up as a single curve.

It is clear that at these low radial velocities the axial velocity profile does not differ substantially from non-porous tube profiles. For the system under study therefore the axial velocity profiles may reasonable be approximated as non-porous tube profiles.

The axial velocity profile in a system is determined by the radial momentum transport processes occurring in that system. Figure 5.3 thus also indicates that radial transport correlations developed for non-porous tubes may confidently be applied to porous tubes if the radial velocity component is small.

**TABLE 5.2** Velocity Combinations Investigated to Ascertain Whether Axial Velocity Profiles at Low Radial Flows are Similar to Non-Porous Tube Profiles

Assumed highest Flux at Tube Wall ( $J_w$ )			( $\ell/\text{m}^2\text{h}$ )	1 000	
Assumed Superficial Axial Velocities ( $\bar{U}_s$ )			(m/s)	1,4 and 2,0	
Assumed Cake Thicknesses ( $l_c$ )			(m)	0,0 and 0,002	
Case	Permeate Velocity at Tube Wall $V_w$ (m/s)	Superficial Suspension Velocity $\bar{U}_s$ (m/s)	Assumed Cake Thickness $l_c$ (m)	Permeate Velocity at Cake Surface $V_{cs}$ (m/s)	Suspension Velocity in Free Channel $\bar{U}_c$ (m/s)
1	2,78E-4	1,4	0,0	2,78E-4	1,4
2	2,78E-4	2,0	0,0	2,78E-4	2,0
3	2,78E-4	1,4	0,002	3,31E-4	1,98
4	2,78E-4	2,0	0,002	3,31E-4	2,83

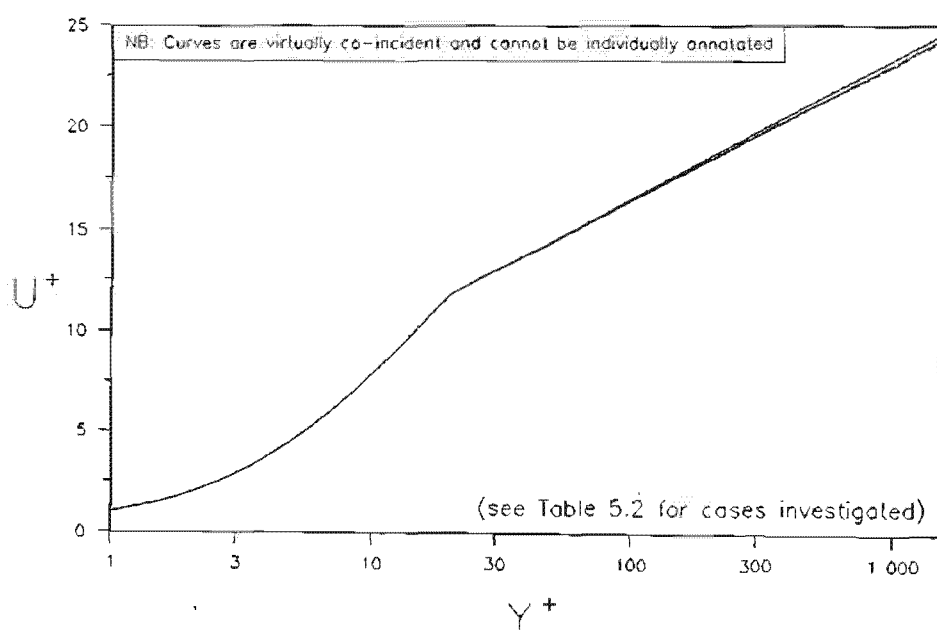


**FIGURE 5.3** Comparison of Axial Velocity Profiles Obtained at Low Radial Flows, With Non-Porous Tube Profiles

### 5.3.2 Applicability of Correlations Developed for Radially-Invariant Viscosity Systems to CFMF

In most systems employed in fluid dynamics studies, the viscosity is radially invariant. In CFMF a radial concentration profile exists, the concentration increasing from a relatively low value in the tube core to a value approaching the maximum packing density of the solids near the cake surface. Resultantly, the viscosity is expected to show a radial variation, increasing from a low core value to a value approaching infinity at the cake surface.

It is known that turbulence levels are significantly damped by the presence of solids [Hsu et al. (1989), Brodkey (1967)]. It is thus expected that turbulence transport coefficients in regions of high concentration and viscosity will differ significantly from those obtained in pure fluids. This will in turn result in a difference between the actual velocity profiles in CFMF systems and those obtained in systems without a radial concentration gradient, at the same inlet Reynolds numbers. Accordingly, the effects of the radial concentration gradients may not be ignored and must be explicitly accounted for.

### 5.3.3 Summary of Applicability of Current Technology

The effects of radial velocity on radial transport coefficients is seemingly negligible at the typical radial and axial velocities encountered in this study. Correlations developed for non-porous tubes may thus be confidently applied to CFMF. The effect of the radial concentration profile, however, must be taken into account. Thus, correlations developed for non-porous, uniform concentration systems must be suitably adapted to take into account radial concentration gradients before being applied to CFMF.

## 5.4 FORMULATION OF MODEL PARAMETERS

The steady-state is represented by equations 5.7 and 5.11. Typically, the operating variables  $\bar{U}_s$ ,  $P$  and  $C_\beta$  will be specified. The task then resolves to finding the cake thickness at which equations 5.7 and 5.11 will be simultaneously satisfied. In order to solve the equations, the following model functions are required :

- $D_p$  - particle diffusivity distribution over the boundary layer ( $m^2/s$ )
- $V$  - radial fluid velocity distribution over the boundary layer ( $m/s$ )
- $C_{crit}$  - the critical concentration for consolidation (volume fraction)
- $K$  - average cake permeability ( $m^2$ )
- $\delta$  - boundary layer thickness (m)

$D_p$ ,  $V$  and  $\delta$  are to be formulated from current technology. The approach adopted here is to formulate these functions from correlations developed for pure fluids flowing in non-porous tubes, based on the bulk viscosity, bulk density and bulk average velocity, and to then adapt these to CFMF systems by inferring the effects of the radial concentration profile on the resultant formulations.

### 5.4.1 Particle Diffusivity Distribution - $D_p$

Particle diffusion arises from three mechanisms - shear induced hydrodynamic diffusivity, transport by turbulent bursts and transport by turbulent eddies.

#### 5.4.1.1 Particle Diffusivity due to Turbulent Bursts and Eddies

##### (a) Introduction

In a fully turbulent flow field, particle dispersion is effected by the random motion of turbulent eddies. Accordingly, the particle diffusivity due to turbulence,  $D_{pt}$ , is related to the eddy diffusivity of momentum,  $\epsilon$  [Soo (1967), Ni (1986)]. In analogy to molecular mass transfer, an inverse particle Schmidt number may be defined [Im and Chung (1983)] :

$$S_c' = \frac{D_{pt}}{\epsilon} \quad (5.15)$$

where  $S_c'$  = inverse particle Schmidt Number

$D_{pt}$  = particle diffusivity due to turbulence ( $m^2/s$ )

$\epsilon$  = eddy diffusivity of momentum ( $m^2/s$ )

Formulation of the  $D_{pt}$  distribution in a fully turbulent flow field thus resolves to ascertaining the distribution of the momentum diffusivity,  $\epsilon$ , and the inverse particle Schmidt number  $S_c'$ .

Cleaver and Yates (1986) modelled particle transport due to turbulent bursts by explicitly considering the action of individual bursts. Each burst would sweep some finite area of a surface and entrain some small fraction of the particles covering that area. Hence the net particle entrainment may be determined from the removal efficiency of a single burst, the statistical distribution of burst frequencies and the statistical distribution of burst sizes.

The alternative approach to modelling bursts adopted here follows from the approach used in modelling the particle diffusivity in a fully turbulent zone. As noted in Section 3.4.2, numerous investigations have focussed on developing eddy diffusivity distributions in the near wall region, including the buffer and sub-layer zones. These studies were motivated by the observation that the assumption of a zero eddy diffusivity in the sub layer leads to calculated heat and mass transfer fluxes being lower than that observed experimentally. In general, diffusivity expressions for the near wall region take the form

$$\frac{\epsilon}{v} = function(Y^*)$$

and the exact forms are determined by regression on experimental results.

In view of the current knowledge of the sub-layer, it is obvious that the assumption of purely viscous transport mechanisms in that region will lead to low calculated fluxes, since transport in that region is substantially augmented by turbulent bursts. It also follows that the empirical expressions developed for the eddy diffusivity in that region will implicitly include the

contribution of turbulent bursts to transport in that region. In analogy to the particle diffusivity due to eddies, the particle diffusivity due to bursts may also be modelled from an inverse particle Schmidt number and an appropriate momentum diffusivity distribution for the near wall region.

Modelling of  $D_{pr}$  due to both bursts and eddies thus resolves to ascertaining the  $S_c'$  and the  $\epsilon$  distribution over the entire flow field.

(b) Inverse Particle Schmidt Number -  $S_c'$

The inverse particle Schmidt number is determined by the particle size and inertia, characterised by a *particle relaxation time* and the characteristics of the underlying fluid turbulence [Im and Chung (1983)]. At each point in a turbulence field there exists a spectrum of eddy sizes and frequencies. If the particle is very small and light it will respond to every velocity fluctuation and hence the particle diffusivity will approach the momentum diffusivity i.e.

$$S_c' \rightarrow 1 \quad \text{as} \quad d \rightarrow 0 : \rho_s \rightarrow \rho_f$$

Conversely very heavy, dense particles may only respond to the larger eddies, resulting in the particle diffusivity being substantially lower than the momentum diffusivity i.e.

$$S_c' \rightarrow 0 \quad \text{as} \quad d \rightarrow \infty : \rho_s \rightarrow \infty$$

Prediction of  $S_c'$  from fluid and particle properties and bulk flow conditions is not at present feasible. Although this has been the topic of theoretical studies, solution of the equations requires a detailed knowledge of the underlying turbulence e.g. the Eulerian and Lagrangian time scales [Soo (1967), Ni (1986)]. Experimental studies of  $S_c'$  include Calabrese and Middleman (1979), Snyder and Lumley (1971) and Ni (1986). Calabrese and Middleman investigated the dispersion of immiscible drops of liquid ( $\bar{d}_p = 600$  to  $900 \mu\text{m}$ ,  $\rho_s/\rho_f = 0,69$  to 1,6) in water flowing in a 50 mm tube. Inferred  $S_c'$  ranged from 0,5 to 0,8. Snyder and Lumley obtained  $S_c'$  values ranging from 0,1 to 0,5. Ni, studying the dispersion of dust particles in air obtained a radial distribution for  $S_c'$ . At the centreline,  $S_c' \approx 0,6$ , increasing to  $\approx 1$  in the near wall region.

In terms of current technology therefore, the *a priori* prediction of  $S_c'$  is not possible and  $S_c'$  will have to remain an adjustable model parameter. In view of the high relative density of limestone particles ( $\rho_s/\rho_f = 2,55$ ) it is expected that  $S_c'$  will be small.

(c) Momentum Diffusivity Distribution -  $\epsilon$ 

In turbulent flows, the total (laminar and turbulent) shear stress may be related to the gradient of the time-averaged velocity by :-

$$\frac{\tau}{\rho} = (\nu + \epsilon) \frac{d\bar{U}}{dY}$$

where  $\tau$  = total shear stress (Pa)

$\rho$  = density ( $\text{kg}/\text{m}^3$ )

$\nu$  = molecular kinematic viscosity ( $\text{m}^2/\text{s}$ )

$\epsilon$  = eddy kinematic viscosity (eddy diffusivity of momentum) ( $\text{m}^2/\text{s}$ )

$\bar{U}$  = time averaged axial velocity (m/s)

$Y$  = distance from wall (m)

Rearrangement leads to

$$\frac{\tau}{\tau_w} = \left( \frac{\epsilon}{\nu} + 1 \right) \frac{dU^+}{dY^+} \quad (5.16)$$

where  $\tau_w$  = shear stress at wall (cake surface) (m/s)

In principle therefore  $\epsilon$  may be obtained from a measured velocity profile and a knowledge of the shear stress distribution. For example, using Von Karman's universal velocity profile (equations 3.44 to 3.46) with equation 5.16 yields the following [Notter and Sleicher (1971)] :

$$Y^+ < 5 \quad \epsilon = 0 \quad (5.17)$$

$$5 < Y^+ < 30 \quad \frac{\epsilon}{\nu} = 0.2Y^+ - 1 \quad (5.18)$$

$$30 < Y^+ \quad \frac{\epsilon}{\nu} = 0.4Y^+ - 1 \quad (5.19)$$

In practise, the above distributions are inconsistent with those inferred from measured heat and mass fluxes, especially in the near wall region. The reason for the inapplicability of equation 5.17 has been addressed in previous sections i.e. the universal velocity profile assumes that purely viscous transport processes occur in the sub-layer, contrary to current knowledge of that region. Notter and Sleicher (1971) attribute the failure of equations 5.18 and 5.19 to the fact that  $\epsilon$  is a sensitive function of velocity, and even the most rigorous measurements of velocity show significant scatter. They also note that it would probably be impossible to determine the  $\epsilon$  distribution for the near wall region from measurement of velocity profiles in that region, due to the practical difficulty associated with accurate measurement close to the wall.

Consequently, the approach adopted by most workers has been to assume some function form for  $\epsilon$ , and to evaluate function constants from measured heat and mass fluxes. Strictly, these studies yield distributions of the eddy diffusivity of heat,  $\epsilon_H$ , and the eddy diffusivity of mass,  $\epsilon_m$ . However,  $\epsilon$ , may be inferred from  $\epsilon_H$  and  $\epsilon_m$ , as discussed a few paragraphs hence. Most studies have concentrated on the region  $Y^+ < 30$  since in most cases of heat and mass transfer the boundary layer lies in this region. A good review of studies in this regard is presented by Notter and Sleicher (1971).

For the present purpose distributions of  $\epsilon$  for both the fully turbulent and the near wall regions are required. A summary of the better correlations, i.e. those which show a good fit with their particular experimental data, is presented in Table 5.3.

**TABLE 5.3** Correlations for Turbulent Diffusivities

Reference	Correlation
Notter and Sleicher (1971)	$Y^+ < 45$ $\frac{\epsilon_H}{\nu} = \frac{0.0009(Y^+)^3}{[1 + 0.0067(Y^+)^2]^{0.5}} \quad (5.20)$
	$Y^+ > 45 \quad \text{and} \quad Y^+ < 0.15$ $\frac{\epsilon_H}{\nu} = 1.3(0.4Y^+r^* - 1) \quad (5.21)$
	$Y^+ > 0.15$ $\frac{\epsilon}{\nu} = \frac{0.25 Re \sqrt{f_m/8}}{dh_7/dr^{*2}} - 1 \quad (5.22)$ <p> <math>f_m</math> = Moody friction factor  <math>Re</math> = Reynolds Number  <math>h_7</math> = velocity defect function  <math>Y^+ = Y/R_e</math>  <math>r^* = r/R_e</math> </p>
Son and Hanratty (1967)	$Y^+ \rightarrow 0$ $\frac{\epsilon_m}{\nu} = 0.00032(Y^+)^4 \quad (5.23)$

**TABLE 5.3** Correlations for Turbulent Diffusivities  
(continued)

Reference	Correlation
Hughmark (1971)	$4.3 < Y' < 12$ $\frac{\epsilon}{\nu} = 0.00096(Y^+)^3$ (5.24)
	$12 < Y' < 35$ $\frac{\epsilon_H}{\nu} = 0.0155(Y^+)^{1.9}$ (5.25)
de Pinho and Fahien (1981)	<p>whole tube</p> $\frac{1}{\dot{\epsilon}_H} = \frac{1}{\dot{\epsilon}_{ch}} + \frac{1}{\dot{\epsilon}_{wh}}$ (5.26) $\dot{\epsilon}_H = \frac{\epsilon_H}{\langle \epsilon_H \rangle}$ <p><math>\langle \epsilon_H \rangle</math> = average diffusivity over tube  <math>= 0.069 U^* R_e</math></p> <p><math>\dot{\epsilon}_{ch}</math> = diffusivity of heat for core region  <math>= 1.123[1 + 2.345(r')^2][1 - (r')^2]</math></p> <p><math>\dot{\epsilon}_{wh}</math> = diffusivity of heat for wall region  <math>= 0.000137 Re^{1.75}(1 - r')^2</math></p>

**TABLE 5.3**

(continued)

**Correlations for Turbulent Diffusivities**

Reference	Correlation
Hsu et al. (1989)	<p>whole tube</p> $\epsilon = U^* l \left[ 0,4 \left( \frac{r}{R_c} \right)^2 + (0,6 - h_8) \left( \frac{r}{R_c} \right) + h_8 \right] h_9 h_{10} \quad (5.27)$ <p><math>h_8 = 1.74 - 0.6705 \log(Re) + 0.0655 [\log(Re)]^2</math></p> <p><math>l = \text{mixing length}</math></p> $= R_c \left[ 0,14 - 0,08 \left( 1 - \frac{Y}{R_c} \right)^2 - 0,06 \left( 1 - \frac{Y}{R_c} \right)^4 \right]$ <p><math>h_9 = \text{correction for } Re &lt; 10^5</math></p> $= 1 + \frac{0,12}{0,14} \exp \left[ -0,0475 \left( \frac{Re}{1000} - 4 \right) \right]$ <p><math>h_{10} = \text{damping factor near wall}</math></p> $= \left[ 1,0 - \exp \left( -\frac{\gamma U^*}{26v} \right) \right]$ <p>(NB : in Hsu's paper equation 5.27 is stated as follows :</p> $\epsilon = U^* R_c l \left[ 0,4 \left( \frac{r}{R_c} \right)^2 + (0,6 - h_8) \left( \frac{r}{R_c} \right) + h_8 \right] h_9 h_{10}$ <p>The units are inconsistent, and it was assumed that the first <math>R_c</math> on the right hand side was a misprint).</p>

In order to evaluate  $\epsilon$  from the correlations in Table 5.3, the relationships between  $\epsilon$ ,  $\epsilon_H$  and  $\epsilon_M$  are required. This has been investigated by, *inter alia*, Notter and Sleicher (1971). Typically the approach was to assume that  $\epsilon = k\epsilon_M$  (or  $\epsilon = k\epsilon_H$ ), where  $k$  is some constant, hence calculate a velocity profile from an  $\epsilon_M$  or  $\epsilon_H$  distribution, and compare the calculated velocity profile to known profiles.

It was found that, on average :

$$Y' < 45 \quad (\text{near wall region})$$

$$\epsilon_M \approx \epsilon_H \approx 1.3 \epsilon \quad (5.28)$$

$$Y' \geq 45 \quad (\text{core region})$$

$$\epsilon_M \approx \epsilon_H \approx \epsilon \quad (5.29)$$

Equations 5.28 and 5.29 may thus be used with Table 5.3 to obtain the radial distribution for  $\epsilon$ . The question arises as to which of the correlations should be used. A comparison between the various correlations is shown in Figures 5.4(a) (near wall region) and 5.4(b) (rest of tube).

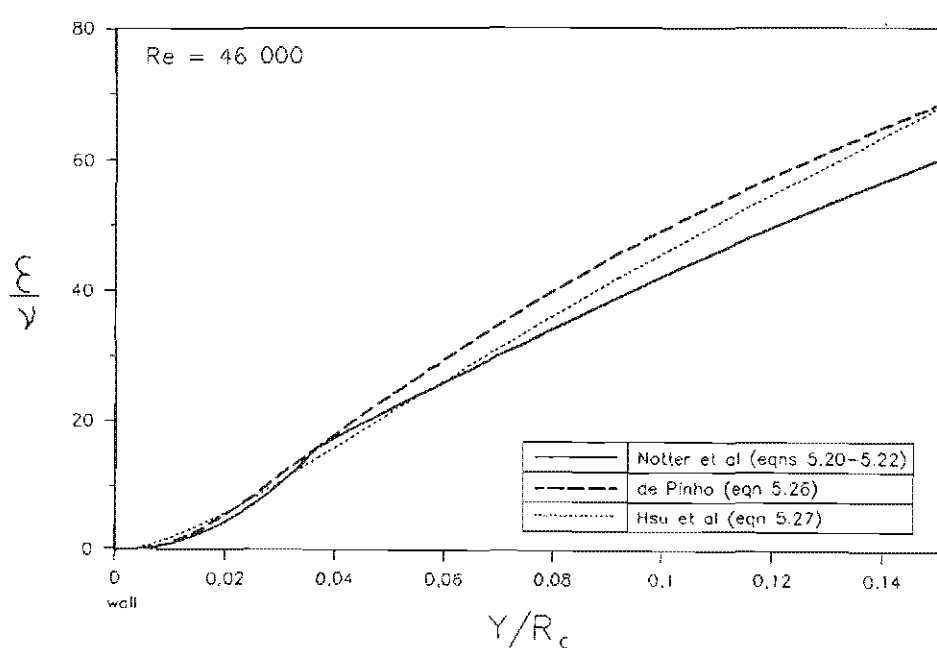


**FIGURE 5.4(A)** Comparison of Eddy Diffusivity Correlations  
(near wall region)

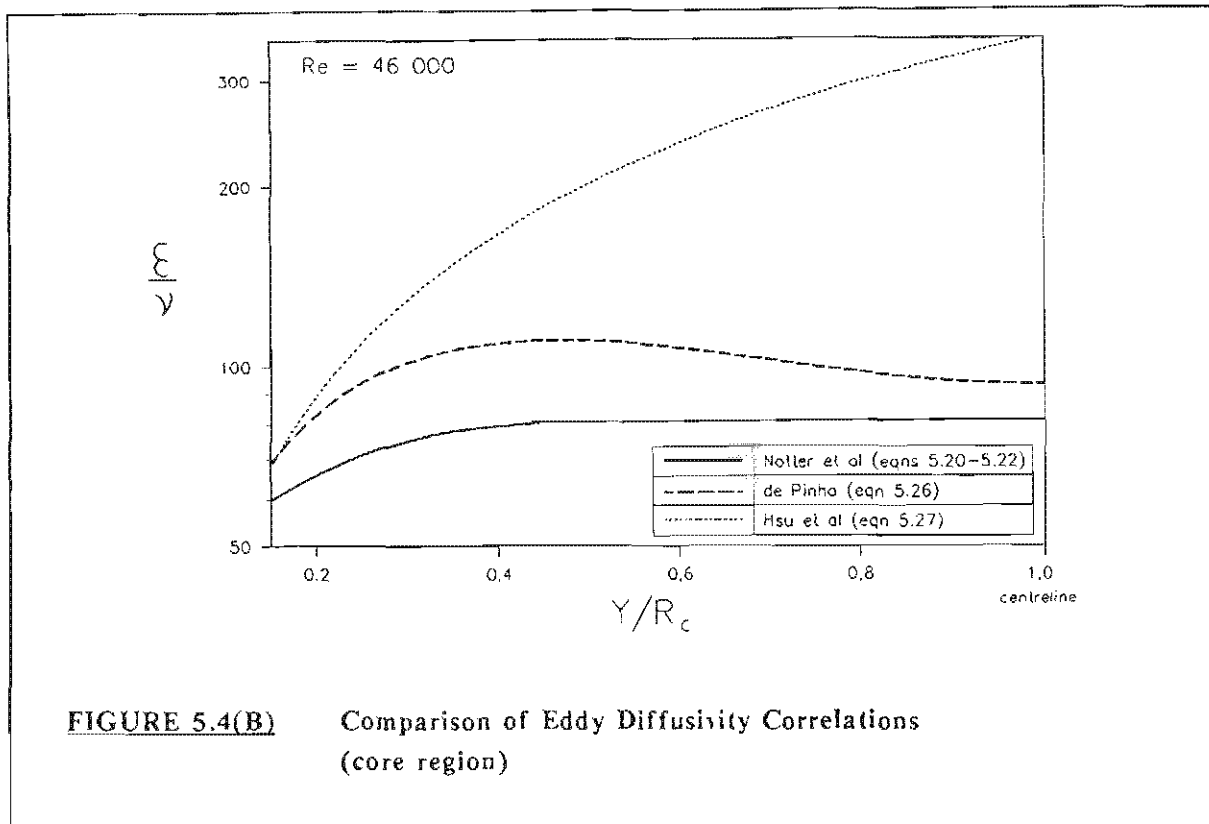


**FIGURE 5.4(B)** Comparison of Eddy Diffusivity Correlations  
(core region)

In the near wall region, the  $\epsilon$  distributions are similar. In the core, the correlation of Hsu et al. differs significantly from that of de Pinho and Notter et al.<sup>2</sup>.

The significant discrepancy amongst the correlations for  $Y' > 0.15$  is not of major importance here, since it will be shown that all boundary layers obtained in the model fall well within the region  $Y' < 0.15$ . With regard to which correlation should be used, that of de Pinho (equation 5.26) is particularly attractive, since it is fairly recent, is based on a wide range of data and consists of smooth, easily computed equations. Accordingly, equation 5.26 will be used in the present study.

The above  $\epsilon$  correlations apply to systems of constant viscosity. The effect of radial concentration profiles on the  $\epsilon$  distribution will now be addressed.

The presence of solids affects the turbulence level in a complex way. A good review of studies in this regard is presented by Hsu et al. (1989). In general, it is found that solids tend to dampen the level of turbulence, the dampening increasing as solids concentration and size increases. This is, in part, due to the dissipation of the fluid turbulence energy to the solids.

<sup>2</sup> Note the logarithmic vertical scale in Figure 5.4(B).

Burst activity is also damped by the presence of solids [Grass (1974)]. Thus the momentum diffusivity in a region of significant solids concentration will be lower than that obtained in a pure fluid i.e.

$$\epsilon^* = K_{at} \epsilon \quad (5.30)$$

where  $\epsilon$  = momentum diffusivity in a pure fluid ( $m^2/s$ )

$\epsilon^*$  = momentum diffusivity in a concentrated suspension ( $m^2/s$ )

$K_{at}$  = concentration attenuation factor ( $< 1$ )

Pechenkin (1972), from experiments at relatively low concentrations, proposed that :

$$K_{at} = 1 - \frac{C}{C_{max}} \quad (5.31)$$

where  $C$  = solids concentration (volume fraction)

$C_{max}$  = maximum packing density of the solids (volume fraction)

Equation 5.31 has been applied by Roco and Balakrishnam (1985), assuming it to be valid for all concentrations. Hsu et al. (1989) however have expressed the view that the solids dampening effect is greater than that indicated by equation 5.31.

The dampening of turbulence by the presence of solids has not been sufficiently investigated to enable quantification of  $K_{at}$ . The expected boundary conditions for  $K_{at}$  are consistent with equation 5.31 i.e.

$$K_{at} \rightarrow 1 \quad \text{as} \quad C \rightarrow 0$$

$$K_{at} \rightarrow 0 \quad \text{as} \quad C \rightarrow C_{max}$$

In practice, when real suspensions are considered,  $K_{at}$  cannot be solely a function of concentration. In considering 10 % (by volume) concentrations of limestone and bentonite for example, it is found that the former is fairly fluid while the latter is a thick and viscous. It is expected therefore that the dampening effect of a bentonite suspension will be substantially greater than that of limestone, at the same concentrations. It should also be noted that for most real suspensions,  $C_{max}$  is difficult to define. For uniformly sized spheres, the delimitation between cake and suspension is relatively clear (about 0,6 volume fraction). For bentonite however, this delimitation is difficult to define, the packing density being a strong function of compressive pressure.

Noting the limits for  $K_{\alpha t}$ , and in the light of the points raised in the above paragraph, it is proposed that :

$$K_{\alpha t} = \left( 1 - \frac{C}{C_{\max}} \right)^n \quad (5.32)$$

where  $n > 1$  and is a property of the suspension, and  $C_{\max}$  is evaluated at a compressive pressure of 0 Pa (gauge). Equation 5.32 is depicted in Figure 5.5, for various values of  $n$ . The proposed functional form should be applicable to most suspensions. For example  $K_{\alpha t}$  for a suspension where significant dampening is expected at low concentrations could be represented by  $n = 5$ , while  $K_{\alpha t}$  for a suspension where less dampening is expected could be represented by  $n = 2$ .

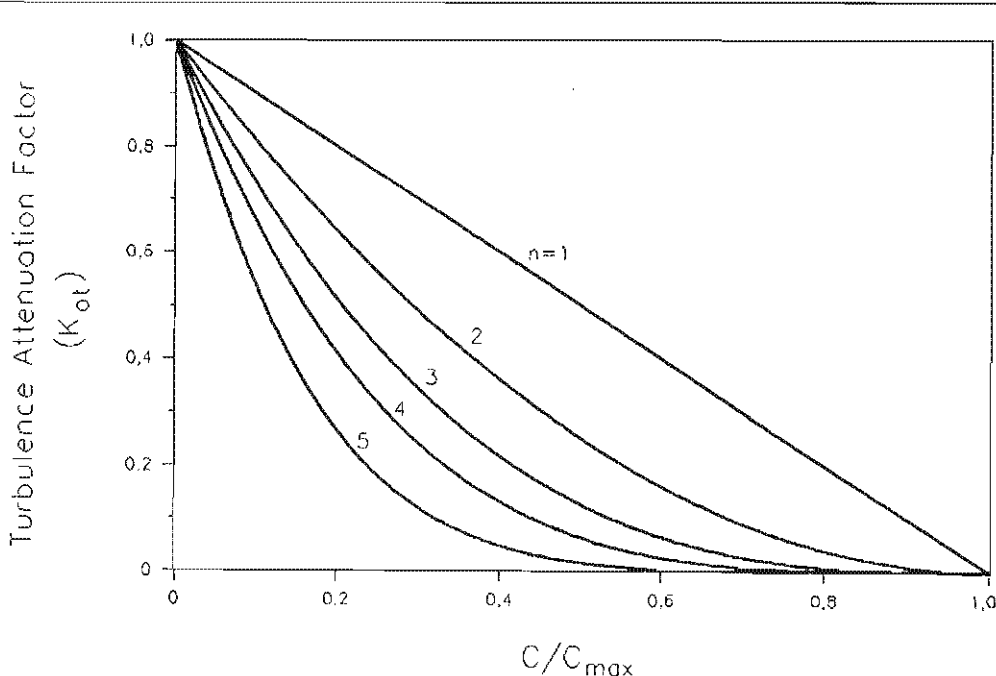


**FIGURE 5.5** Effect of Turbulence Attenuation Parameter on Turbulence Attenuation Function

The attenuation parameter,  $n$ , is an adjustable model parameter.

(d) Summary Of Particle Diffusivity due to Turbulence Effects

The particle diffusivity due to bursts and eddies is given by :

$$D_{pt} = S_c \left( 1 - \frac{C}{C_{max}} \right)^n \epsilon \quad (5.33)$$

where  $S_c$  = inverse particle Schmidt number (adjustable parameter)

$n$  = turbulence attenuation parameter (adjustable parameter)

$\epsilon$  = momentum diffusivity distribution

(obtained from a suitable "pure fluid" correlation)

$C$  = concentration (volume fraction)

$C_{max}$  = maximum packing density (volume fraction)

5.4.1.2 Shear Induced Hydrodynamic Diffusivity

The only significant studies of shear induced diffusion are those of Ekstein (1977) and Leighton and Acrivos (1987a, 1987b). As noted in Chapter 3, Leighton identified a limitation in the experimental apparatus of Ekstein and hence discussions here will be limited to the works of Leighton and Acrivos.

The correlation of Leighton and Acrivos (presented in Chapter 3, and repeated here for convenience) is :

$$D_{ps} = \hat{D} \gamma r_p^2 \quad (5.34)$$

with

$$\hat{D} = 0,33C^2 \left( 1 + \frac{1}{2}e^{8,8C} \right) \quad (5.35)$$

where  $D_{ps}$  = shear-induced hydrodynamic diffusivity of particles ( $m^2/s$ )

$\hat{D}$  = non-dimensional diffusivity

$\gamma$  = shear rate ( $s^{-1}$ )

$r_p$  = particle radius (m)

$C$  = solids concentration (volume fraction)

The above correlation is a result of two separate studies. In the first [Leighton and Acrivos (1987a)], the diffusivity of particles in a shear field, in the presence of a concentration gradient, was measured. Hence the measured diffusivity included the effects of both random and non-random drift components. Volume fractions investigated ranged from 0,4 to 0,5 and particle sizes from  $46 \mu m$  to  $87 \mu m$ . The second study concerned the measurement of particle diffusivity in a uniform concentration field [Leighton and Acrivos (1987b)]. Here the measured diffusivity only reflects the effects of random drift (i.e. *self diffusion*). Two particle sizes were used,  $645 \mu m$  and  $389 \mu m$ , shear rates ranged from  $1,55 s^{-1}$  to  $65 s^{-1}$  and the volume

fraction range investigated was 0 to 0.4. Equation 5.35 is a combination of the shear induced diffusivity measured at the high concentrations and the self diffusivity measured at the low concentrations.

Leighton and Acrivos (1986) note that since the shear induced diffusivity may be up to five times greater than the self diffusivity, equation 5.35 would probably underestimate the shear induced diffusivity at low concentrations. It should also be noted that although equation 5.35 indicates that the non-dimensional diffusivity,  $\hat{D}$ , is independent of  $\gamma$  and  $r_p$ , a significant scatter exists in the data.

Equation 5.35 requires adaptation before it may be applied to the system used in the present study. The particles used in Leighton's studies were spherical and of relatively uniform size, in contrast to the highly irregular, angular limestone particles used in the present study. On the assumption that the shear induced diffusivity of angular particles may differ from that of spherical particles, it is proposed that :

$$\hat{D}^* = K_1 \hat{D} \quad (5.36)$$

where  $\hat{D}$  = non-dimensional diffusivity for spherical particles (equation 5.35)

$\hat{D}^*$  = non-dimensional diffusivity for angular particles

$K_1 < 1$

Evaluation of the diffusivity from equation 5.34 requires the specification of the shear rate,  $\gamma$ . This may of course be obtained by differentiation of the velocity profile in the wall region. As explained in Section 5.3, however, the attenuation of turbulence by the solids will result in the velocity profile in a CFMF system differing from that obtained with a pure fluid. The qualitative effect that turbulence dampening will have on the shear rate may be inferred from Figure 5.6.

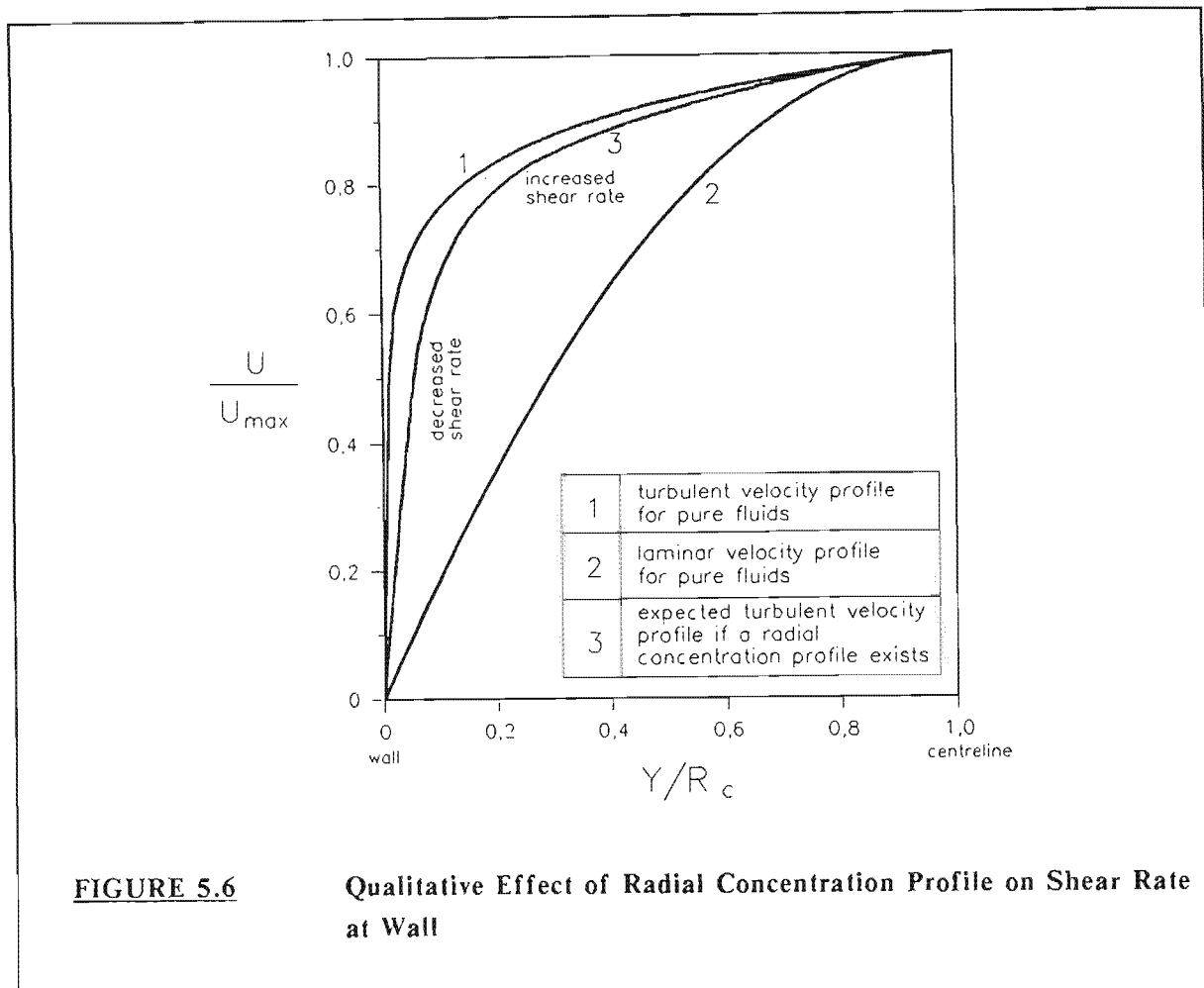
Curve 1 depicts a typical "pure fluid" turbulent velocity profile. Curve 2 is the well known parabolic velocity profile for laminar flow, and thus represents the velocity profile for total dampening of turbulence. The dampening of turbulence due to high concentrations in the near wall region will thus tend to shift the velocity profile from Curve 1 towards Curve 2 e.g. Curve 3. This will result in an increase in the shear rate over most of the core, but in the region of the wall the shear rate must decrease. The shear rate in the wall region may thus be represented by :

$$\gamma^* = K_2 \gamma \quad (5.37)$$

where  $\gamma$  = shear rate calculated from a pure fluid velocity profile

$\gamma^*$  = actual shear rate in a system with a radial concentration profile

$K_2 < 1$



Combining 5.34 to 5.37 yields :

$$D_{ps} = K_{sh} \gamma \hat{D} r_p^2 \quad (5.38)$$

with  $\gamma$  = shear rate calculated for a pure fluid

$K_{sh}$  = shear diffusivity parameter

$$= K_1 K_2$$

$$< 1$$

$\hat{D}$  = non-dimensional diffusivity (equation 5.35)

The shear induced hydrodynamic diffusivity in a CFMF system may thus be modelled as equation 5.38, with  $K_{sh}$  being an adjustable model parameter.

In view of the fact that equation 5.35 underestimates the diffusivity at low concentrations, and noting its exponential form, it is highly feasible that the equation may drastically overestimate the diffusivity at concentrations greater than 0,5. This may have significant implications for the current modelling effort, where concentrations of up to 0,6 will be encountered. It should also be noted that the shear rates encountered in the sub-layer of a turbulent flow (of the order

of  $10\ 000\ s^{-1}$ ) are orders of magnitude greater than the shear rates used in the studies of Leighton and of Ekstein. At present, however, there are no *a priori* indications as to whether equations 5.34 and 5.35 are applicable to the system under study. By default they will be applied and their applicability judged in terms of whether the final solutions seem realistic.

#### 5.4.1.3 Effective Particle Diffusivity

It is expected that the shear induced diffusivity will predominate in the sub-layer while the diffusivity due to eddies will dominate in the outer regions. In the buffer region both diffusivities are expected to be significant.

It is proposed that the diffusivity over the whole flow field will be given by the algebraic sum of the turbulent and shear induced diffusivities i.e. :

$$D_p = D_{pt} + D_{ps} \quad (5.39)$$

with  $D_{pt}$  = particle diffusivity due to turbulence (equation 5.33)

$D_{ps}$  = shear induced hydrodynamic diffusion (equation 5.38)

#### 5.4.2 Radial fluid velocity distribution - $V$

Noting the absence of empirical correlations for the radial velocity profile, the most rigorous option to obtain  $V$  would be the solution of one of the models mentioned in Section 5.3.1 e.g. Kinney and Sparrow (1970). In view of the complexity of those models, however, an alternative approximate method may be employed, based on the evaluation of  $V$  from the fluid continuity equation.

The continuity equation for fluid flow in a porous tube is :-

$$\frac{1}{r} \frac{\partial}{\partial r}(rV) + \frac{\partial U}{\partial z} = 0 \quad (5.40)$$

Rearrangement leads to :-

$$V(r) = \frac{1}{r} \int_0^r \left( r \frac{\partial U}{\partial z} \right) dr \quad (5.41)$$

where  $V(r)$  = radial fluid velocity at radius  $r$ .

Thus, the radial velocity distribution  $V$  may be obtained from equation 5.41 if the radial distribution of the axial velocity gradient ( $\partial U / \partial z$ ) is known.

A global mass balance over a differential length,  $\Delta z$ , of porous tube yields (Figure 5.7) :-

$$\bar{U}_{ci} = \bar{U}_{co} + \frac{2\Delta z}{R_c} V_{cs} \quad (5.42)$$

where  $\bar{U}_{ci}$  = bulk average velocity in core (m/s) ( $i=in, 2=out$ )

$V_{cs}$  = radial velocity at the wall (cake surface) (m/s)

$R_c$  = core radius (m)

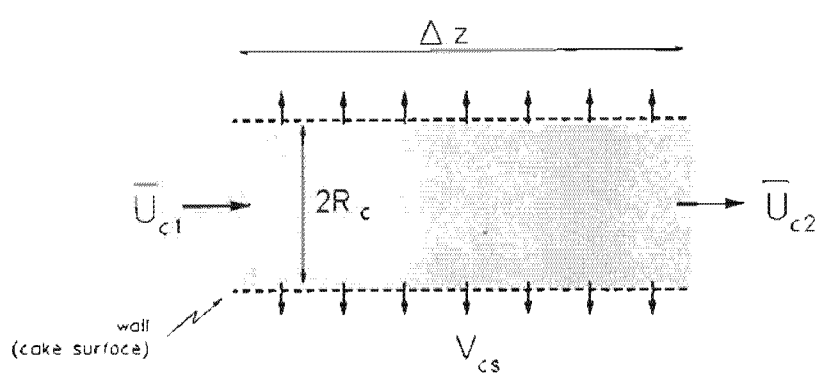


**FIGURE 5.7** Fluid Mass Balance across a Porous Tube

By specifying  $\bar{U}_{ci}$ ,  $R_c$ ,  $V_{cs}$  and  $\Delta z$ ,  $\bar{U}_{co}$  may be obtained from equation 5.42. The axial velocity profiles,  $U_1(r)$  and  $U_2(r)$  may then be calculated from  $\bar{U}_{ci}$ ,  $\bar{U}_{co}$  and a suitable correlation for turbulent flow velocity profiles e.g. the universal velocity profile.

These axial velocity profiles may then be substituted into a finite difference analogue of  $(\partial U / \partial z)$  i.e.

$$\left. \frac{\partial U}{\partial z} \right|_r = \frac{U_1(r) - U_2(r)}{2\Delta z} \quad (5.43)$$

where  $(\partial U / \partial z)|_r$  = axial velocity gradient at radius  $r$

$U_1, U_2$  = inlet and outlet velocities at radius  $r$

yielding the radial distribution of  $(\partial U / \partial z)$ . Equation 5.41 may then be integrated to yield the radial fluid velocity distribution  $V$  as a function of  $\bar{U}_{ci}$ ,  $R_c$ ,  $V_{cs}$  and fluid physical properties.

A typical profile calculated by the above procedure, and using Von Karman's universal velocity profile, is compared to a profile from Kinney and Sparrow (1970) in Figure 5.8.

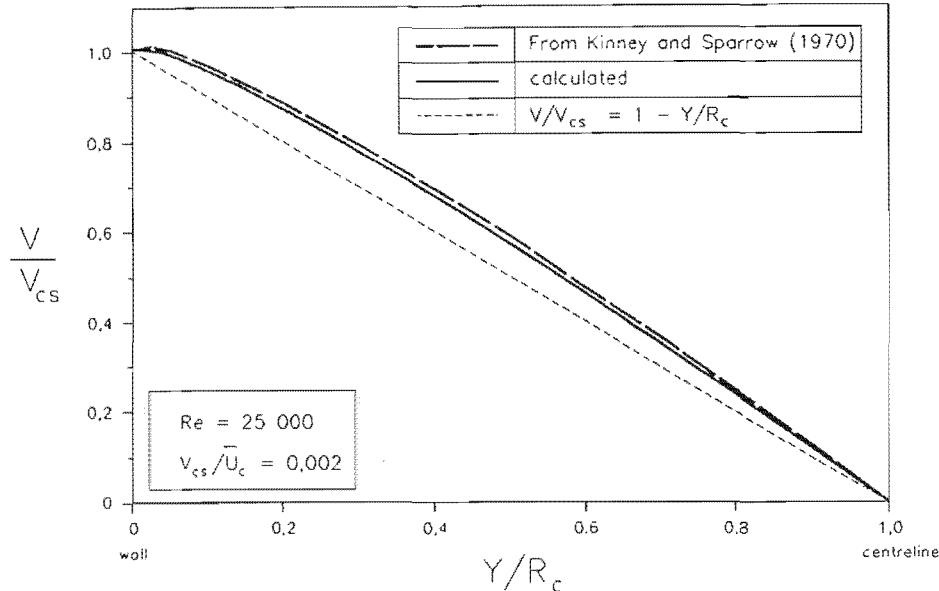


**FIGURE 5.8** Comparison of Calculated Radial Velocity Profile with that of Kinney and Sparrow (1970)

The profiles are substantially similar, validating the above procedure as a method<sup>3</sup> to obtain  $V$ .

Consistent with experimental profiles from Hirata et al. (1982a),  $V$  shows a moderate deviation from the profile that would be obtained for a *plug flow* axial velocity profile i.e.

$$\frac{V}{V_{cs}} = 1 - \frac{Y}{R_c} \quad (5.44)$$

and approaches the expected profile for a *constant radial flowrate* i.e.

$$\frac{V}{V_{cs}} = 1 + \frac{Y}{R_c} \quad (5.45)$$

in the near wall region.

It was found that calculated  $V/V_{cs}$  profiles were insensitive to  $V_{cs}$ , and negligibly sensitive to  $\bar{U}_c$ , at the typical velocities encountered in the present study. Further, the calculated distribution was insensitive to the value chosen for  $\Delta z$ , providing that the value chosen was not too large.

<sup>3</sup> Strictly, the universal velocity profile will only be valid for low wall velocities (see Section 5.3.1).

The  $V$  profiles calculated by the above procedure are "pure fluid" profiles i.e. the effect of the radial concentration profile is not taken into account. The qualitative effect of the radial concentration profile is depicted in Figure 5.9. Curve 1 represents the  $(V/V_{cs})$  profile for a highly turbulent system i.e. where the axial velocity profile approaches plug flow. Curve 2 is the expected profile for a parabolic axial velocity profile (laminar flow). The existence of the radial concentration profile will thus cause curve 1 to shift towards curve 2 i.e. curve 3.

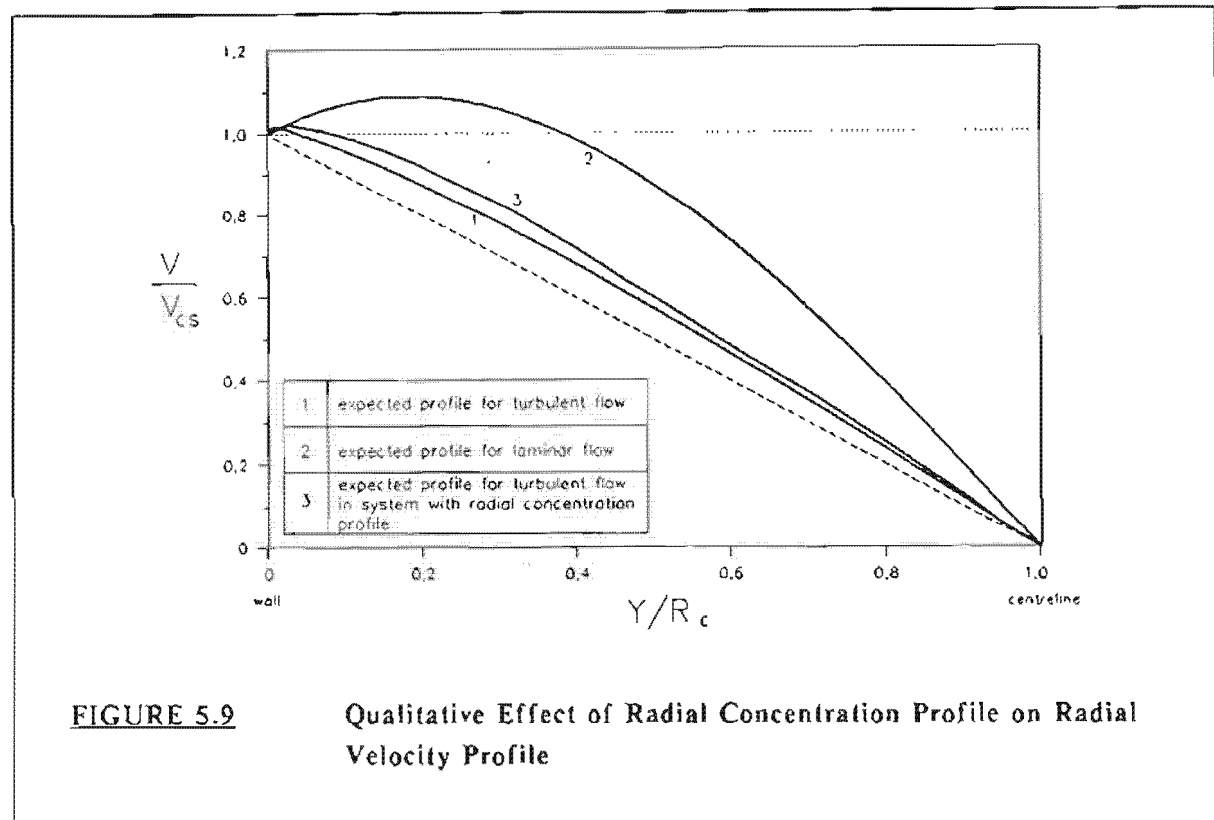


**FIGURE 5.9** Qualitative Effect of Radial Concentration Profile on Radial Velocity Profile

Quantitatively, the effect of the radial concentration profile is not expected to be substantial. Quantities like the shear rate,  $\gamma$ , are functions of the radial gradient of the axial velocity profile i.e.  $(\partial U / \partial r)$ . This radial gradient is substantially affected by the concentration profile in the near wall region, and hence the effects of concentration had to be explicitly taken into account (see equation 5.37).  $V$ , however, is a function of the axial gradient of the axial velocity profile i.e.  $(\partial U / \partial z)$ , which is not expected to be a strong function of the radial concentration profile. The insensitivity of  $V$  to concentration effects may also be inferred from Figure 5.9. Even if curve 1 was substantially shifted towards the laminar flow curve (curve 2) the difference in point values for  $V$  in the near wall region will be small. Accordingly, it will be assumed that the effects of the radial concentration profile may be ignored and the  $V$  profile in CFMF system may reasonably be approximated as a "pure fluid" profile.

Note, once again, that when implementing the above procedures in CFMF systems, velocities based on the core radius, i.e.  $V_{cs}$  and  $\bar{U}_c$ , are used in place of velocities based on the tube radius, i.e.  $V_w$  and  $\bar{U}_w$ .

### 5.4.3 Boundary Concentrations - $C_{crit}$ and $C_{max}$

Following the discussions in Chapter 3,  $C_{max}$  is the limiting cake concentration as the solids compressive pressure,  $P_s$ , approaches 0 Pa. Thus  $C_{max}$  is a property of the suspension and may be evaluated experimentally.

Compression-permeability (CP) cell tests on the limestone used in this study indicated that

$$C_{max} \rightarrow 0.6 \text{ (volume fraction)} \quad \text{as} \quad P_s \rightarrow 0$$

$C_{crit}$  is that concentration at which a suspension ceases flowing and consolidates into cake. This concentration is not necessarily equal to  $C_{max}$ . In considering uniformly sized spheres, for example,  $C_{max}$  would probably correspond to the body-centre-cubic or hexagonal packed state (volume fraction  $\approx 0.74$ ), but the lowest concentration that may be regarded as cake is the cubic packed state (volume fraction  $\approx 0.52$ ). In this instance it is feasible that  $C_{crit}$  will be achieved at a concentration of  $\approx 0.52$ , whereafter the particles will rearrange themselves to achieve a  $C_{max}$  approaching 0.74.

For the present, since information on the packing states of limestone is not available, and noting that the objective is to model the system from experimentally determined quantities and current technology, it will simply be assumed that :-

$$C_{crit} \approx C_{max} = 0.6 \tag{5.46}$$

### 5.4.4 Cake Permeability - $K$

The cake permeability is, fundamentally, a property of the suspension particles and a function of the compressive pressure [Tiller and Yeh (1987)]. Due to preferential deposition effects and the variation of solids compressive pressure through the cake, the permeability is also expected to be a function of cross-flow velocity and distance through the cake. These latter effects were discussed qualitatively in Chapter 4. The study of Baker et al. (1985) provides a quantitative indication of the effect of preferential particle deposition on the permeability (or conversely on the specific cake resistance,  $\alpha$ ). For the mineral suspension used in their experiments, the ratio ( $\alpha_{cross-flow}/\alpha_{dead-end}$ ) ranged from 2 to 3.3 over the pressure range 60 kPa to 160 kPa.

Standard experimental techniques to evaluate  $K$  generally involve some form of dead-ended filtration test e.g. compression-permeability (CP) cell. Baker's results, and the findings in Chapter 4, indicate that dead-end tests are most likely to overestimate the permeability of cakes formed under cross-flow conditions. However, noting that the aim is to evaluate model functions from experimentally measured quantities and current technology, and noting that no simple test exists to evaluate  $K$  under cross-flow conditions, dead-end filtration tests remain the easiest method to obtain an estimate for  $K$ . Note that the results of Baker et al. (1985) indicate, at the very least, that the order of magnitude for  $K$  is the same under dead-end conditions.

Accordingly, it will be assumed that the effects of preferential particle deposition and radial compressive pressure profiles on cake permeability are second order effects and may be neglected. Thus the cake permeability may be represented by an *average* value which is solely a function of the operating pressure and may be estimated from dead-end filtration tests.

CP cell tests on the limestone used in this study indicated that over the range

$$101 \text{ kPa} < P_s < 303 \text{ kPa}$$

the permeability could be represented by :

$$K = 2,6889 \left( \frac{P_s}{101} \right)^{-0.1661} \quad (5.47)$$

where  $P_s$  = compressive pressure (kPa)

The above permeability function will be used in the model. Errors arising from the use of this (most definitely) over-estimated permeability will have to be "absorbed" in the adjustable model parameters.

#### 5.4.5 Concentration Boundary Layer Thickness - ( $\delta$ )

The basic assumption in a *boundary layer approach* is that the concentration field may be roughly divided into two regions - the *core* where concentration gradients are negligible and the concentration is approximately equal to the bulk value, and the *boundary layer* where most of the concentration gradient occurs. Accordingly, analysis of the system is greatly simplified by restricting considerations to this thin boundary layer. Note that in terms of this assumption a system whose concentration profile is as in Curve 1 of Figure 5.10 lends itself to a boundary layer approach while a system with a concentration profile as in Curve 2 does not.

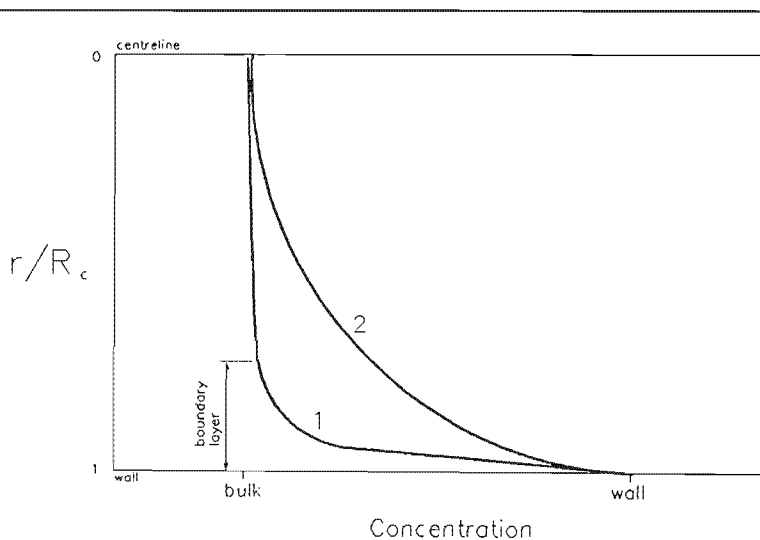


**FIGURE 5.10**

**Concentration Profiles Illustrating Validity of a Boundary Layer Analysis**

One approach to the concentration boundary layer thickness, ( $\delta$ ) , is to relate  $\delta$  to the momentum boundary layer thickness  $\delta_v$  [Bird et al. 1960)] i.e.

$$\frac{\delta}{\delta_v} = (S_c)^{-\frac{1}{3}} \quad (5.48)$$

where  $\delta$  = concentration boundary layer thickness (m)

$\delta_v$  = momentum boundary layer thickness (m)

$S_c$  = Molecular Schmidt number

This approach cannot, unfortunately, be directly applied to CFMF. Firstly, in fully developed pipe flow the momentum boundary layer theoretically extends to the tube centreline. Thus, a boundary layer as defined above no longer exists. Equation 5.48 therefore is strictly applicable to developing or unbounded flows only. It is of course feasible to arbitrarily define  $\delta_v$  as the point where  $U \approx 0.99 U_{max}$  (for example). This approach could yield success in highly turbulent systems, where the velocity profile is flat over most of the tube cross-section. For the typical axial velocities encountered in this study, however, the velocity profiles are similar to curve 1 in Figure 5.6, and  $0.99 U_{max}$  once again approaches the tube centreline.

The second problem concerns the Schmidt number,  $S_c$ . Although the particle diffusivity due to bursts and eddies is related to the momentum diffusivity, the shear induced diffusivity cannot be simply related to the momentum diffusivity. Thus, even if  $\delta_v$  can be evaluated, the specification of  $S_c$  is problematic.

An alternative approach is to formulate an expression for  $\delta$  based on the properties that  $\delta$  is expected to exhibit. These expected properties are :

- (i) as velocity increases,  $\delta$  decreases - (at higher velocities greater mixing in the core results in an increased core region of uniform concentration, and hence a thinner boundary layer).
- (ii) As viscosity increases,  $\delta$  increases - (at higher viscosities, reduced turbulence levels result in a decreased core region of uniform concentration).

These properties will be exhibited if the boundary layer thickness is expressed in terms of the non-dimensional distance co-ordinate in turbulent flows,  $Y^*$  (see equation 3.43). Hence, following Flemmer et al. (1982) and Hunt et al. (1987b), it is proposed that :

$$\delta = K_\delta \left( \frac{v}{U^*} \right) \quad (5.49)$$

where  $K_\delta$  = boundary layer parameter

$K_s$  will be evaluated by computational experiments<sup>4</sup>. The factors that will govern the choice for  $K_s$  are :

- (i) Particle size :-  $\delta$  must be substantially greater than the particle diameter in order to be physically realistic.
- (ii) Calculated concentration profiles :- assume that for some  $K_s$  the calculated concentration profile over the boundary layer is Curve 1 of Figure 5.11. By implication, the profile over the tube will be as in Curve 2 of Figure 5.11. In this instance, the profile is consistent with Curve 1 of Figure 5.10, and hence  $K_s$  is acceptable. Conversely, if the calculated concentration profile over the boundary layer is given by Curve 3 of Figure 5.11, the implied profile over the tube is Curve 4. Curve 4 is not realistic since an obvious discontinuity exists at point A. In this instance, the assumed value for  $K_s$  is too low. Thus the validity of the choice for  $K_s$  may be assessed by observing whether the concentration in the boundary layer smoothly approaches the bulk concentration before the edge of the boundary layer.

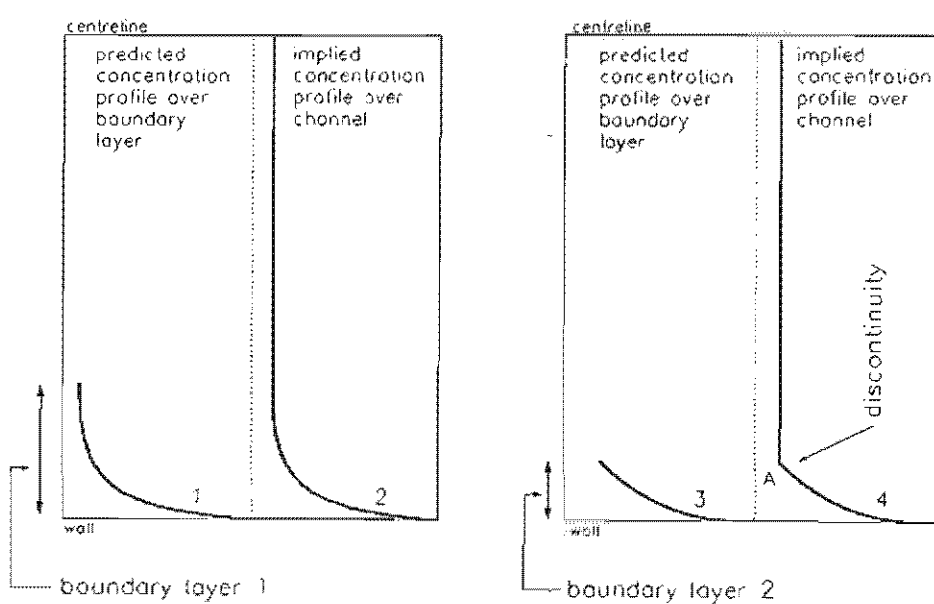


**FIGURE 5.11** Concentration Profiles Illustrating Validity of Assumed Boundary Layer Thickness

<sup>4</sup> This will be elaborated on in Section 5.6.

### 5.4.6 Miscellaneous

The equipment and operating variables that will be specified as inputs to the model are:

- $\bar{U}_s$  - bulk average superficial inlet velocity (m/s)
- $C_B^*$  - bulk concentration (g/l)
- $P$  - operating pressure (Pa)
- $T$  - temperature ( °C)
- $R$  - tube radius (m)

The cake thickness is then iterated until the steady-state equations are solved. For a specified cake thickness,  $t_c$ , the various quantities required for the calculation of model functions are obtained as follows:

#### 5.4.6.1 Core Radius

$$R_c = R - t_c \quad (m)$$

#### 5.4.6.2 Axial Velocity in Core

$$\bar{U}_c = \bar{U}_s \left( \frac{R}{R_c} \right)^2 \quad (m/s)$$

#### 5.4.6.3 Permeate Velocities

$$V_w = \frac{\Delta P}{\mu_l} \frac{K}{R} \frac{1}{\ln\left(\frac{R}{R-t_c}\right)} \quad (m/s) \quad (\text{from 5.11})$$

$$V_{cs} = V_w \left( \frac{R}{R_c} \right) \quad (m/s)$$

#### 5.4.6.4 Fluid Density [from Hunt (1987a)]

$$\begin{aligned} \rho_t &= (999,83952 + 16,945176T - 7,987041 \times 10^{-3}T^2 \\ &\quad - 46,170461 \times 10^{-6}T^3 + 105,563 \times 10^{-9}T^4 \\ &\quad - 280,542 \times 10^{-12}T^5) / (1,0 + 16,879 \times 10^{-3}T) \end{aligned} \quad (5.50)$$

with  $\rho_t$  in kg/m<sup>3</sup>

$T$  in °C

#### 5.4.6.5 Fluid Viscosity [from Hunt (1987a)]

$$\mu_t = \frac{1,002 \times 10^{1.3272(20T) - 0.001053(T-20)^2}}{0.01(T+105.0)} \quad (5.51)$$

with  $\mu$  in Pa.s

$T$  in °C

#### 5.4.6.6 Suspension Concentration (volume fraction)

$$C_B^* = \frac{C_B^*}{\rho_s} \quad (5.52)$$

where  $C_B^*$  = suspension concentration (volume fraction)

$C_B^*$  = suspension concentration (g/l)

$\rho_s$  = particle density

= 2 550 kg/m<sup>3</sup> (from Appendix I)

#### 5.4.6.7 Suspension Concentration (mass fraction)

$$C_B' = \frac{C_B^*}{C_B^*\left(1 - \frac{1000}{\rho_s}\right) + 1000} \quad (5.53)$$

where  $C_B'$  = suspension concentration (mass fraction)

#### 5.4.6.8 Suspension Density

$$\rho = \left( \frac{C_B'}{\rho_s} + \frac{(1 - C_B')}{\rho_l} \right)^{-1} \quad (kg/m^3) \quad (5.54)$$

5.4.6.9 Suspension Viscosity [from Wasp et al. (1977)]

$$\mu = \mu_l ( 1,0 + 2,5 C_B + 10,05 C_B^2 + 0,0027 \exp[16,6 C_B] ) \quad (5.55)$$

5.4.6.10 Suspension Kinematic Viscosity

$$\nu = \frac{\mu}{\rho} \quad (m^2/s)$$

5.4.6.11 Turbulence Variables

$$(i) \quad Re = \frac{2\rho \bar{U}_c R_c}{\mu}$$

$$(ii) \quad f_0 = 0,079(Re)^{1/4}$$

$$f = f_0 \left( 1,0 + 115,8 \frac{V_{cs}}{\bar{U}_c} \right) \quad (5.14)$$

(For the low radial velocities encountered in the present study,  $f \approx f_0$ )

$$(iii) \quad U^* = \sqrt{\tau_w / \rho}$$

$$\tau_w = \frac{1}{2} f \rho \bar{U}_c^2$$

$$\Rightarrow U^* = \bar{U}_c \sqrt{f/2} \quad (m/s) \quad (5.56)$$

### 5.4.7 Summary of Model

#### 5.4.7.1 Steady-State Equations

$$\int_{R_c - \delta}^{R_c} \frac{V}{D_p} dr = \ln \left( \frac{C_{crit}}{C_B} \right) \quad (5.7)$$

$$\Delta P = \frac{\mu_l V_w R}{K} \ln \left( \frac{R}{R - t_c} \right) \quad (5.11)$$

#### 5.4.7.2 Model functions

- (i)  $\delta$  = boundary layer thickness  
=  $K_b (\nu / U^*)$
- (ii)  $C_{crit}$  = critical concentration for consolidation  
= 0,6
- (iii)  $K$  = cake permeability (equation 5.47)
- (iv)  $V$  = radial fluid velocity distribution (equation 5.41)
- (v)  $D_p$  = particle diffusivity distribution (equation 5.39)

#### 5.4.7.3 Model parameters

- (i)  $S_c$  = inverse particle Schmidt number (equation 5.15)
- (ii)  $K_{sh}$  = shear diffusivity parameter (equation 5.38)
- (iii)  $n$  = turbulence attenuation parameter (equation 5.32)
- (iv)  $K_b$  = boundary layer parameter (equation 5.49)

## 5.5 NUMERICAL SOLUTION PROCEDURE

The objective is to determine the steady-state cake thickness ( $t_c$ ), and hence the steady-state flux, for specified superficial inlet velocity ( $\bar{U}_s$ ), operating pressure ( $P$ ) and bulk concentration ( $C_B$ ).

The overall iteration scheme is presented as Algorithm I in Figure 5.12 (highly simplified) :

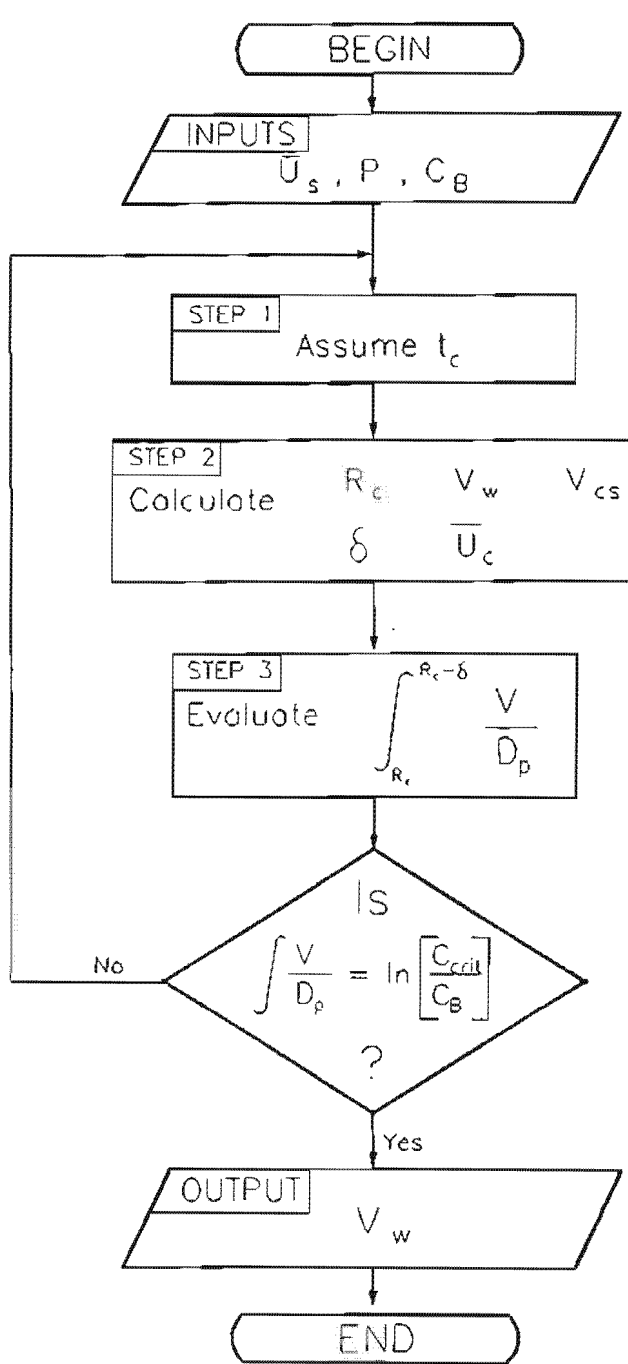


**FIGURE 5.12** Algorithm I - Overall Iteration Scheme (simplified)

The radial velocity distribution,  $V$ , in step 3 may be directly evaluated using the procedure in Section 5.4.2. The diffusivity distribution,  $D_p$ , however is a function of the concentration

profile,  $C$ , in the boundary layer (see equations 5.33 and 5.35). The concentration profile will, in turn, be determined by  $V$  and  $D_p$ . Thus step 3 requires a procedure that will yield simultaneous solutions of the mutually dependent distributions of  $D_p$  and  $C$ .

For this, equation 5.3 (repeated here for convenience) may be employed;

$$\frac{1}{r} \frac{\partial}{\partial r} (rVC) = \frac{1}{r} \frac{\partial}{\partial r} \left( rD_p \frac{\partial C}{\partial r} \right) \quad (5.3)$$

The finite difference analogue of equation 5.3 is:

$$C(i) = \frac{T_1 + T_2 + T_3 - T_4}{T_5} \quad (5.57)$$

where

$$T_1 = \frac{D_p(i)}{B^2} [C(i+1) + C(i-1)]$$

$$T_2 = \frac{1}{4B^2} [D_p(i+1) - D_p(i-1)] [C(i+1) - C(i-1)]$$

$$T_3 = \frac{D_p(i)}{2Br} [C(i+1) - C(i-1)]$$

$$T_4 = \frac{V(i)}{2B} [C(i+1) - C(i-1)]$$

$$T_5 = \frac{V(i+1) - V(i-1)}{2B} + \frac{V(i)}{r} + 2 \frac{D_p(i)}{B^2}$$

with  $i$  = any INTERIOR mesh point

$B$  = mesh spacing

$r$  = radial distance from tube centreline.

The appropriate boundary conditions for equation 5.57 are:

$$r = R_c \quad i = N \quad C(N) = C_{crit}$$

$$r = R_c - \delta \quad i = 1 \quad C(1) = C_B$$

For specified  $V$  and  $D_p$  distributions, therefore, equation 5.57 may be solved by a point relaxation procedure, subject to the specified boundary conditions, to yield the concentration profile in the boundary layer,  $C$ .

In the present instance, however, the diffusivity distribution is not known, since it is a function of the concentration profile. Thus, a nested point relaxation procedure must be employed, to obtain simultaneous solutions for  $D_p$  and  $C$ . The algorithm for this nested procedure is presented in Figure 5.13 (a) and 5.13 (b).

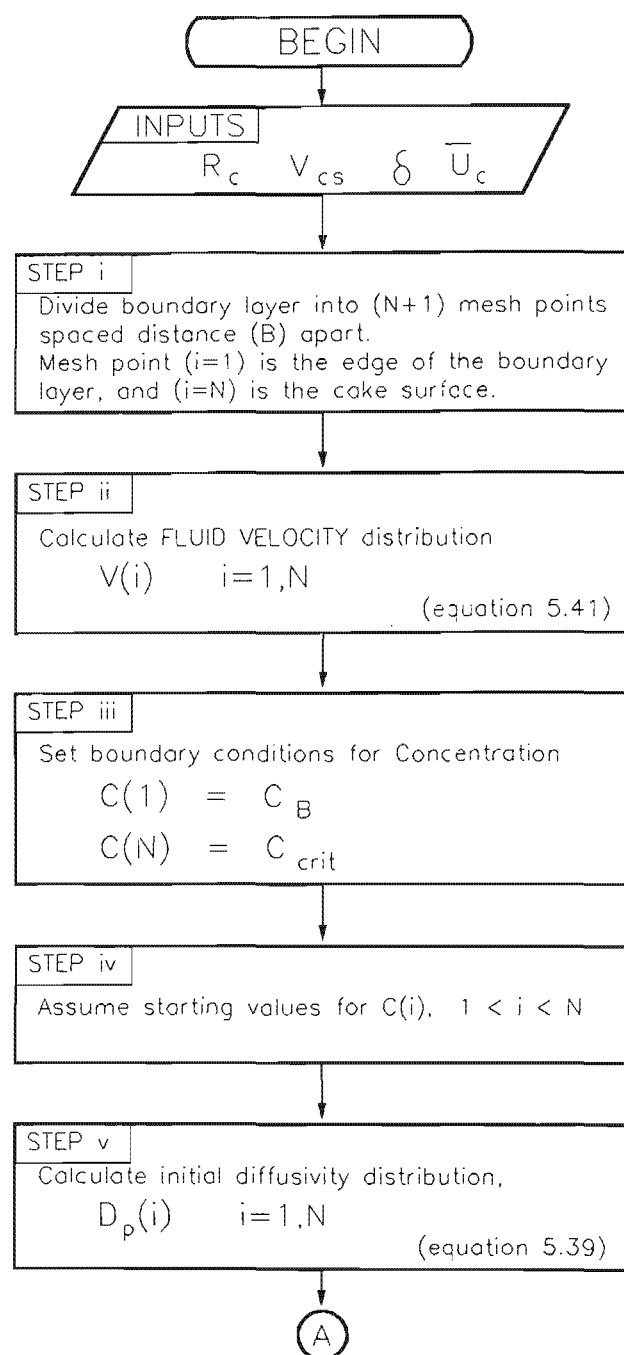


**FIGURE 5.13(a)** Algorithm II - Nested Iteration Procedure to Obtain Simultaneous Solutions for Concentration and Diffusivity (used as Step 3 of Algorithm I)

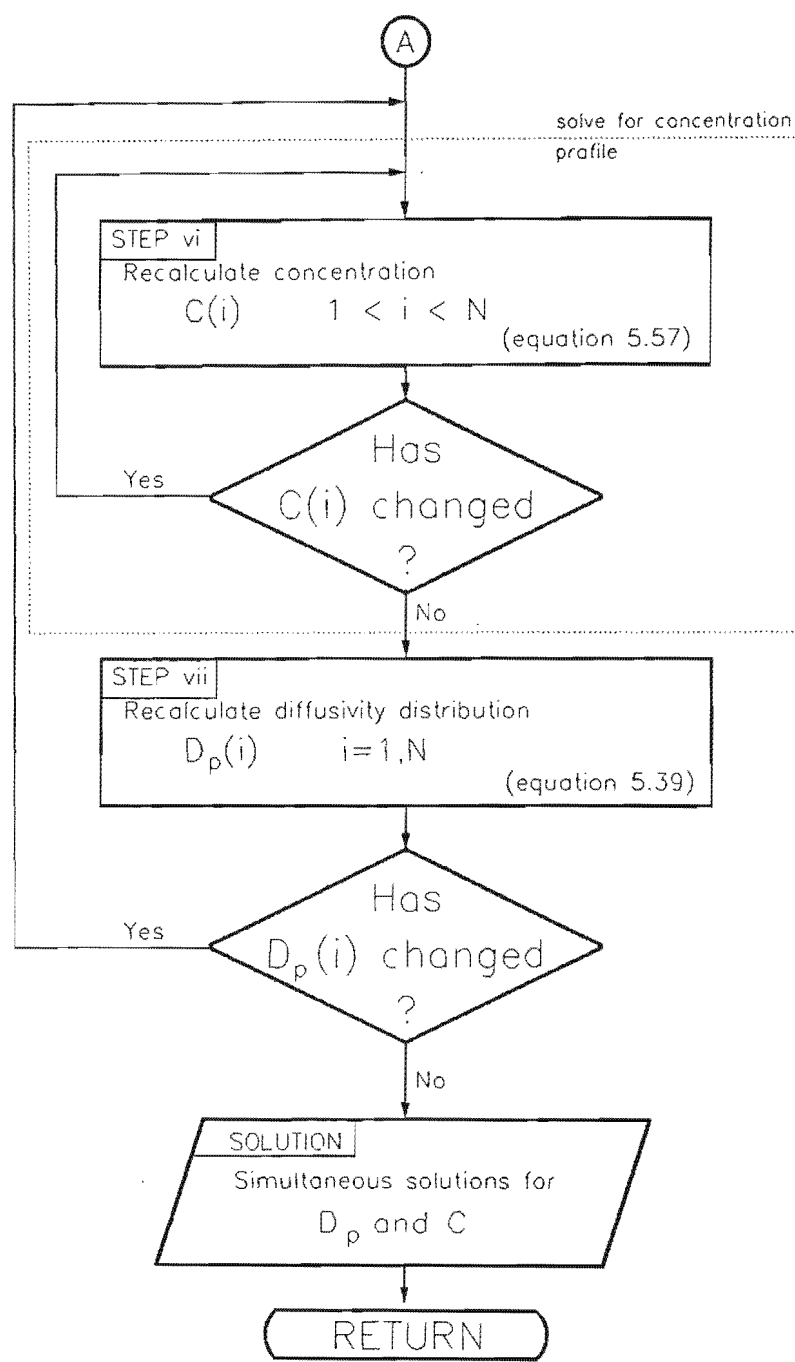


**FIGURE 5.13(b)** Algorithm II (continued)

It will probably be noted that Step (ii) of Algorithm II is seemingly inconsistent with equation 5.3.  $V$  in equation 5.3 refers to the *suspension* velocity distribution whereas  $V$  in Algorithm II has been specified as the *fluid* velocity distribution. The fluid and suspension velocities are only equivalent when the net solids flowrate is zero.

The net solids flowrate may simply be calculated from the output of Algorithm II and equation 5.4 i.e.

$$Q_s = rVC - rD_p \frac{\partial C}{\partial r} \quad (5.4)$$

In general, the output from the Algorithm II will not yield a zero net solids flowrate. In those instances the algorithm is inconsistent with equation 5.3 and the algorithm output is physically meaningless. When Algorithm II is substituted into Step 3 of Algorithm I,  $t_c$  is iterated until  $f(V/D_p) = \ln(C_{crit}/C_B)$ , i.e. until the net solids velocity is zero. At this solution point, therefore, the fluid and suspension velocity distributions are equal, and Algorithm II is consistent with equation 5.3. Thus the *general* solution to Algorithm II may not be consistent with equation 5.3, but the *specific* solution obtained when Algorithm II is coupled with Algorithm I is consistent with equation 5.3.

The above algorithms were coded into Fortran and implemented on the Computing Centre for Water Research (CCWR) mainframe computer. The values used for model parameters will be discussed in the next Section. Computations were initiated by specifying an initial concentration profile (Step iii, Algorithm II) of the form

$$C(r) = \left( \frac{r - R_1}{R_c - R_1} \right)^m (C_{crit} - C_B) + C_B \quad (5.58)$$

where  $C(r)$  = concentration at radius  $r$

$R_1$  =  $R_c - \delta$

$m$  = profile parameter

Note that  $m = 1$  yields a linear initial concentration profile,  $m = 2$  yields a quadratic profile etc. The final solutions were insensitive to the starting profiles used. In general,  $m = 3$ , i.e. a cubic initial profile, seemed to reduce the number of iterations needed for convergence.

Computational stability was controlled by using appropriate relaxation factors e.g. in Steps (vi) and (vii) of Algorithm II,

$$C(i)^{j+1} = C(i)^j + RF_1(C(i)^{j+1} - C(i)^j)$$

$$D_p(i)^{j+1} = D_p(i)^j + RF_2(D_p(i)^{j+1} - D_p(i)^j)$$

where  $RF_1, RF_2$  = relaxation factors

$j$  symbolises the  $j^{\text{th}}$  iteration

In general, computations were still stable if  $C(i)$  was over-relaxed ( $RF_1 = 1, 5$ ). In initial iterations,  $D_p$  needs to be under-relaxed ( $RF_2 = 0, 4$ ), but  $RF_2$  could safely be increased to 0,8 as the solution was approached.

In Algorithm II, convergence was assumed, when at all mesh points,

$$\left( \frac{D_p^{j+1} - D_p^j}{D_p^j} \right) < 1,0E-5$$

$$\left( \frac{C^{j+1} - C^j}{C^j} \right) < 1,0E-5$$

Investigations indicated that decreasing the convergence criterion from the above value produced no change in the final solution.

Algorithm I was assumed to have converged when

$$\left( \frac{\int (V/D_p) - \ln(C_{crit}/C_B)}{\ln(C_{crit}/C_B)} \right) < 0,01$$

The influence of mesh spacing was also tested, by progressively increasing the number of mesh points and comparing the predicted fluxes. Increasing the number of mesh points from 151 to 251 produced negligible change in the predicted flux, and all computations were subsequently performed with 151 mesh points.

## **5.6 QUANTIFICATION OF MODEL PARAMETERS**

### **5.6.1 Introduction**

Computational investigations indicated that the boundary layer constant,  $K_\delta$ , was not significantly dependant on the diffusivity parameters ( $n$ ,  $S_c$  and  $K_{sh}$ ) and vice versa. This enabled  $K_\delta$  and the diffusivity parameters to be quantified independently.

### **5.6.2 Diffusivity Parameters ( $n$ , $S_c$ , $K_{sh}$ )**

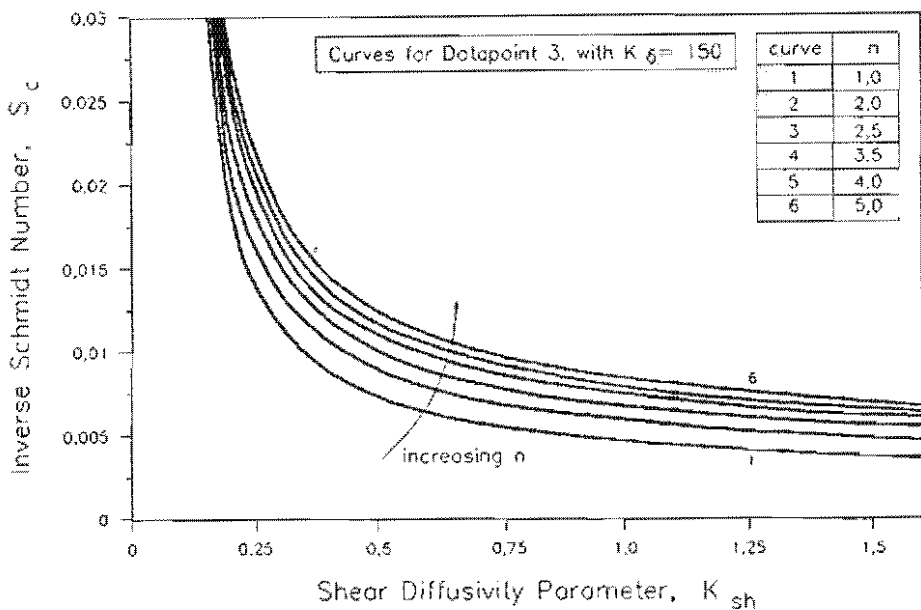
Initially an attempt was made to quantify the optimal  $n$ ,  $S_c$ ,  $K_{sh}$  combination by regression on the entire experimental dataset. It was found that a wide range of  $S_c$ ,  $K_{sh}$  combinations yielded an equivalently good fit between predicted and observed fluxes. This prompted an attempt at "manual" regression in order to better understand the interactions amongst the parameters. This exercise, in turn, indicated the interesting result that  $n$ ,  $S_c$ ,  $K_{sh}$  could reasonably be estimated from a single experimental datapoint (i.e. a single steady-state flux measured at a known velocity, pressure and concentration). The manual regression procedure leading to this surprising observation is detailed below.

The dataset obtained in the experimental study is summarised in Table 5.4. It consists of three subsets, depicting the effects of velocity, concentration and pressure on the steady-state flux. It is seen that datapoint 3 is the central datapoint in all subsets.

**TABLE 5.4** Summary of Experimental Dataset

Datapoint	Run Number	Superficial Inlet Velocity $(\bar{U}_s)$ (m/s)	Concentration $(C_b')$ (g/l)	Pressure (P) (kPa)	Flux $(J_w)$ (l/m <sup>2</sup> h)
<i>(a) Effect of Velocity on Flux</i>					
1	55	0,85	39,4	200	499
2	53	1,13	39,4	200	563
3	48	1,42	39,4	200	638
4	52	1,7	39,4	200	722
5	54	1,98	39,4	200	802
<i>(b) Effect of Concentration on Flux</i>					
6	50	1,42	9,9	200	886
7	47	1,42	19,8	200	749
3	48	1,42	39,4	200	638
8	49	1,42	58,6	200	574
9	51	1,42	77,6	200	530
<i>(c) Effect of Pressure on Flux</i>					
10	59	1,42	39,4	100	502
11	60	1,42	39,4	150	574
3	48	1,42	39,4	200	638
12	61	1,42	39,4	250	672
13	58	1,42	39,4	300	687

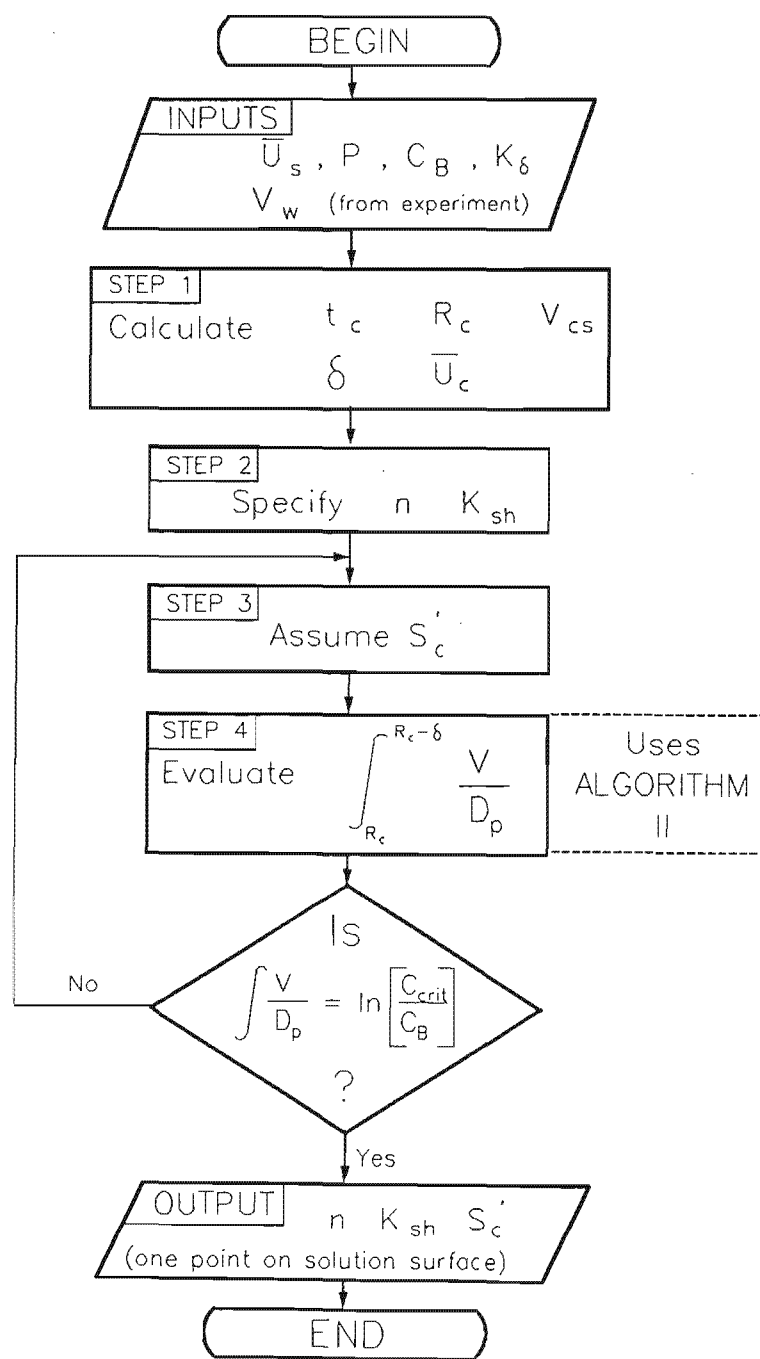
For each datapoint, and for a specified  $K_{sh}$ , there exists innumerable combinations of  $n$ ,  $S_e'$ ,  $K_{sh}$  that will yield an exact match between the predicted and observed flux for that datapoint. These constitute a *parameter solution surface* for that datapoint. A two-dimensional representation of a typical parameter solution surface is shown in Figure 5.14. Every point on every curve represents an  $n, K_{sh}, S_e'$  combination that will result in an exact match between the predicted and observed flux for the particular datapoint. The curves were generated using the algorithm in Figure 5.15 (overleaf).



**FIGURE 5.14** Two-Dimensional Representation of a Typical Solution Surface

It is seen that  $S_e'$  and  $K_{sh}$  are highly correlated at low  $K_{sh}$ , but  $S_e'$  becomes progressively less dependent on  $K_{sh}$  as  $K_{sh}$  increases. It is also clear that the solution curves become less dependant on  $n$  as  $n$  is increased. The significance of this will be addressed shortly.

The parameter solution surface for each datapoint will, in general, be unique and differ markedly from those of the other datapoints. Ideally, the solution surfaces for all datapoints should intersect at a single point, which then defines the optimal  $n, S_e', K_{sh}$  combination. In general, however, the solution surfaces will not intersect at a point. The task then resolves to finding the parameter combination that is "closest" to all surfaces i.e. that which results in the minimum error between predictions and observations.

**FIGURE 5.15****Algorithm III – Algorithm to Generate Solution Surface**

Manipulation of three-dimensional surfaces is not a trivial exercise. However, investigations indicated that the solution surface is not very sensitive to  $n$ . This is typically illustrated in Figure 5.14, where it is seen that the  $S_c, K_{sh}$  solution curve is not very sensitive to  $n$  over the range  $n = 2.5$  to  $n = 5$ . Similar trends were observed for the solution surfaces for other datapoints. This observation enabled  $n$  to be assigned a fixed value, thereby reducing the number of manipulatable parameters to two and hence reducing each solution surface to a parameter solution curve. From Figure 5.14, therefore,

$$n = 3.5 \quad (5.59)$$

It will be shown in Section 5.7.3 that the predicted fluxes are indeed insensitive to  $n$ .

It should be noted that although each point on a given  $S_c, K_{sh}$  solution curve will yield the correct predicted flux for the datapoint, every point does not necessarily yield a realistic concentration profile. This is depicted in Figure 5.16, where concentration profiles predicted at different  $S_c, K_{sh}$  combinations are presented. At low  $K_{sh}$ , all the concentration gradient is confined to an extremely thin region next to the cake. The thickness of this region is the same order of magnitude as the particle diameter. Thus, the solution predicted at low values of  $K_{sh}$  is not physically realistic. At moderate and high  $K_{sh}$  the thickness of the concentrated region is orders of magnitude greater than the particle size, indicating a physically feasible solution.

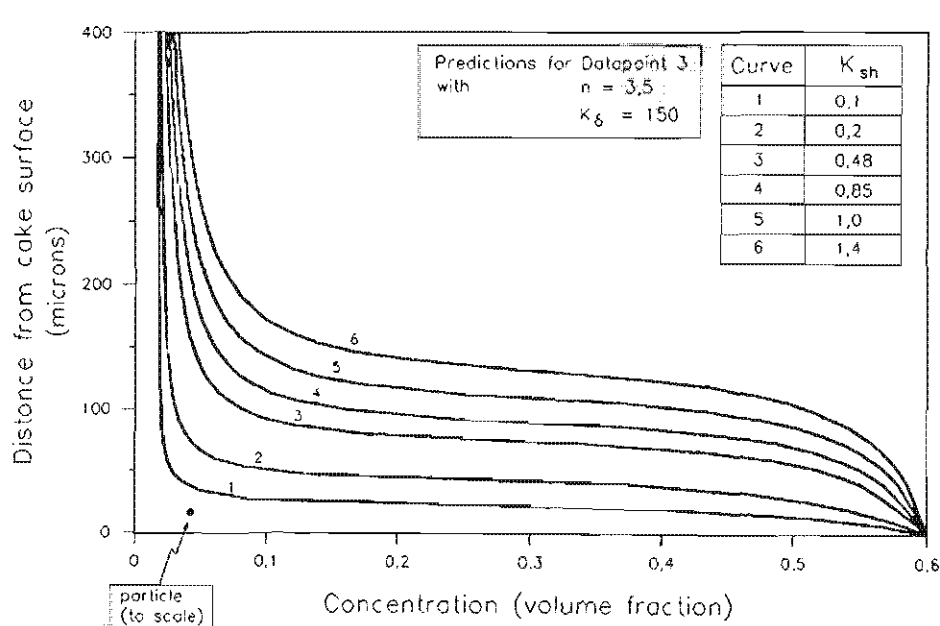


**FIGURE 5.16** Illustration of Realistic and Unrealistic Concentration Profiles

Having fixed  $n$  the task then resolves to graphing the  $S_e, K_{sh}$  solution curves for all datapoints and finding the  $S_e, K_{sh}$  closest to all curves. The solution curves for all datapoints, for  $n = 3, 5$ , are presented in Figure 5.17.

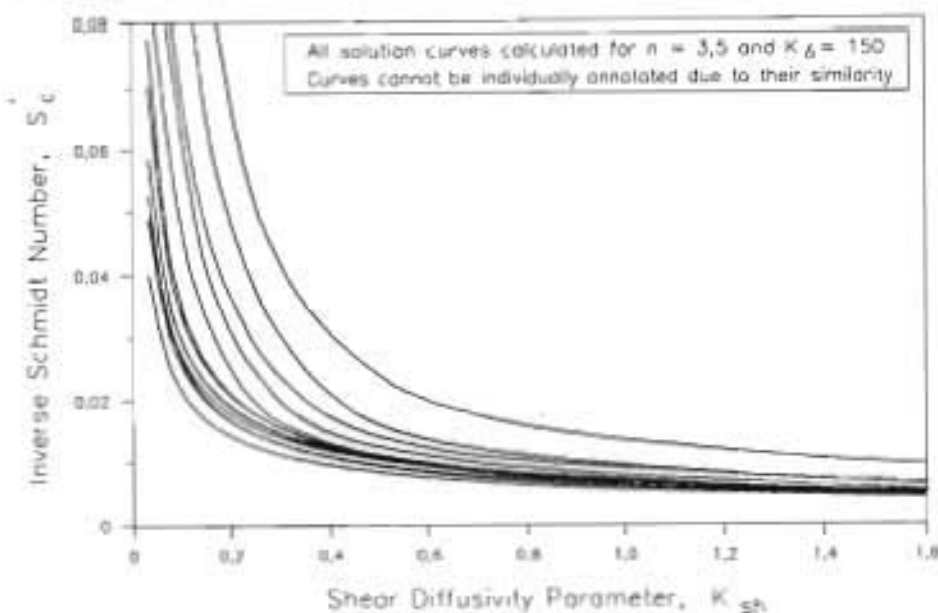


**FIGURE 5.17** Solution Curves for all Datapoints

At low  $K_{sh}$  the curves are substantially dissimilar. As  $K_{sh}$  increases most curves converge and thereafter become similar for  $K_{sh} > 0.6$ . The most significant feature of Figure 5.17 is that the curves do not intersect in a discrete region, but are substantially the same over a wide  $K_{sh}$  range. This indicates that a wide range of optimal  $S_e, K_{sh}$  combinations will exist. The second significance of Figure 5.17 is that, noting the coincidence of the solution curves at moderate to high  $K_{sh}$ , the optimal values for  $S_e, K_{sh}$  may be inferred from any single curve. The curve for datapoint 3 is particularly attractive since datapoint 3 is the central point in each experimental subset (see Table 5.4) and the solution curve for datapoint 3 falls approximately in the middle of the family of solution curves. Using the solution curve for datapoint 3 will also enable a more rigorous evaluation of the model since parameters evaluated for a median velocity, concentration and pressure will then be applied to extreme concentrations, velocities and pressures.

It cannot be determined *a priori* which of the  $S_e, K_{sh}$  combinations from the range  $K_{sh} > 0.6$  should be used. The concentration profiles for all  $S_e, K_{sh}$  combination in this range are expected to be realistic (see e.g. Figure 5.16). Accordingly, the model will be tested at various  $S_e, K_{sh}$  combinations in the range  $K_{sh} > 0.6$ , using parameter combinations obtained from the solution curve for datapoint 3.

### 5.6.3 Boundary Layer Parameter ( $K_b$ )

Computational experiments were performed, involving changing the boundary layer thickness, solving the model and comparing the resultant model outputs. This was done for various "solution combinations" of the other model parameters, as obtained in Section 5.6.2.

These experiments indicated that  $K_b$  was insensitive to the other model parameters and also indicated that the predicted steady-state flux and concentration profile was not very sensitive to the boundary layer thickness, provide that  $\delta$  is greater than some minimum boundary layer thickness. This is typically illustrated in Figures 5.18 and 5.19, where predicted fluxes and concentration profiles for one experimental datapoint are shown as a function of  $K_b$ .

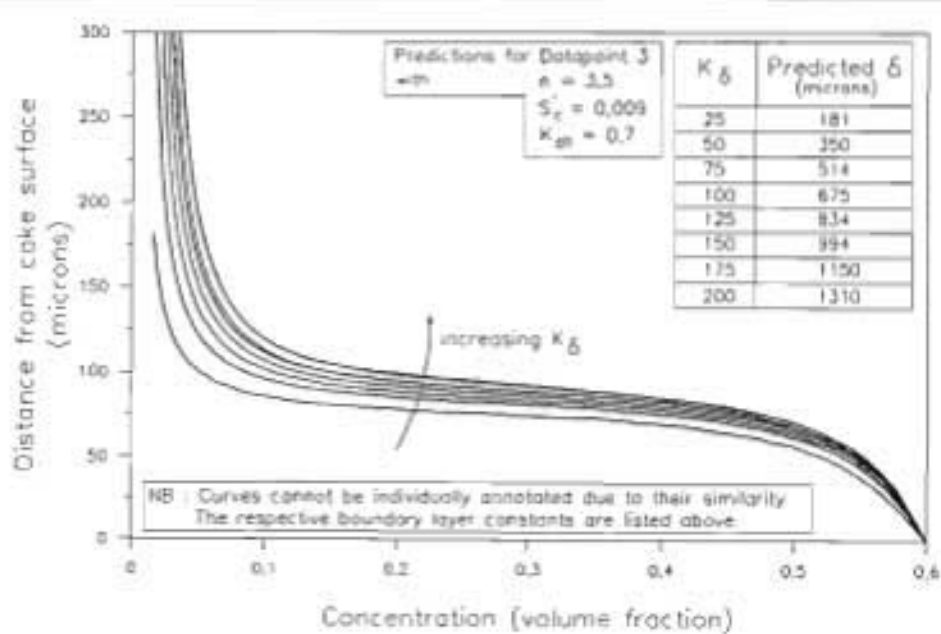


**FIGURE 5.18 Effect of Boundary Layer Parameter on Concentration Profiles**

It is seen that for  $K_b$  greater than some (not very well defined) minimum value, both the predicted flux and the concentration profile are almost independent of  $K_b$ . The insensitivity of the model to  $K_b$  will be explained in Section 5.7.3.

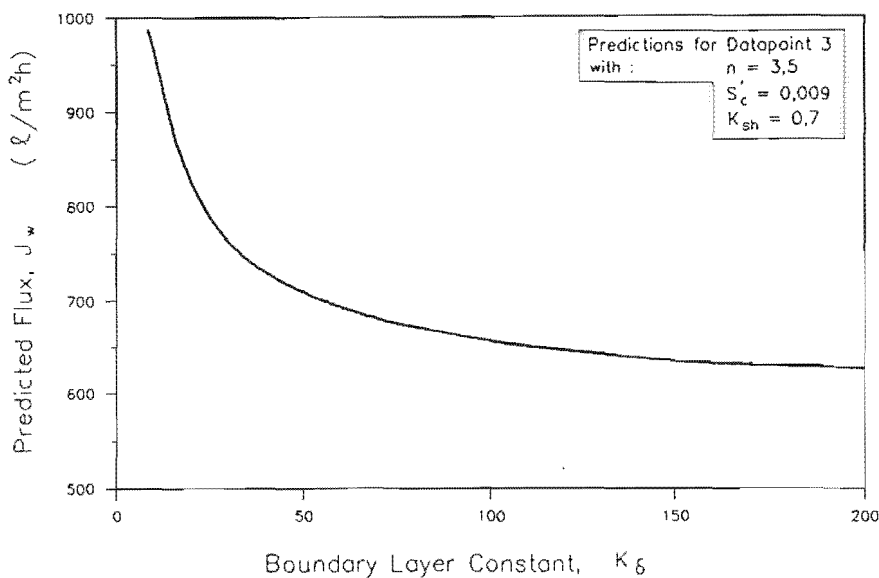


**FIGURE 5.19** Effect of Boundary Layer Parameter on Predicted Flux

For all results presented here, it was found that a boundary layer thickness of 150( $v/U'$ ) was sufficient to fulfil the criteria specified in Section 5.4.5. Hence,

$$K_\delta = 150 \quad (5.60)$$

#### 5.6.4 Summary of Model Parameters

- (a) Examination of the parameter solution surfaces indicates that the solution is not very sensitive to  $n$ , over a reasonable range of  $n$ . Hence, from Figure 5.14,

$$n = 3.5$$

- (b) Examination of the  $S_c', K_{sh}$  solution curves indicate that a wide range of optimal  $S_c', K_{sh}$  combinations possibly exists, and that these could reasonably be quantified from the solution curve for a single datapoint. The  $S_c', K_{sh}$  combinations to be tested will be obtained from the solution curve for datapoint 3, from the range  $K_{sh} > 0.6$ .
- (c) Computational investigations indicate that the model is relatively insensitive to  $K_\delta$ . From computational experiments,

$$K_\delta = 150$$

Note that, in retrospect, the values of all the parameters could have been obtained solely from computational experiments on datapoint 3.

## 5.7 RESULTS AND DISCUSSION

### 5.7.1 Comparison Between Model Prediction and Experimental Observations

Model predictions for steady-state fluxes and cake thicknesses were obtained for the values for  $K_s$  and  $n$  as decided on in Section 5.6, and three  $S_e$ ,  $K_{in}$  solution combinations, as obtained from the solution curve for datapoint 3 from the range  $0.7 < K_{in} < 1.4$ . These parameter combinations are summarised in Table 5.5.

**TABLE 5.5** Parameter Combinations Used in Model Predictions

Set	$K_s$	$n$	$K_{in}$	$S_e$
1	150	3,5	0,7	0,00900
2	150	3,5	1,0	0,00725
3	150	3,5	1,4	0,00609

The predicted effects of inlet velocity, concentration and pressure on the steady-state flux are shown in Figures 5.20, 5.21 and 5.22.

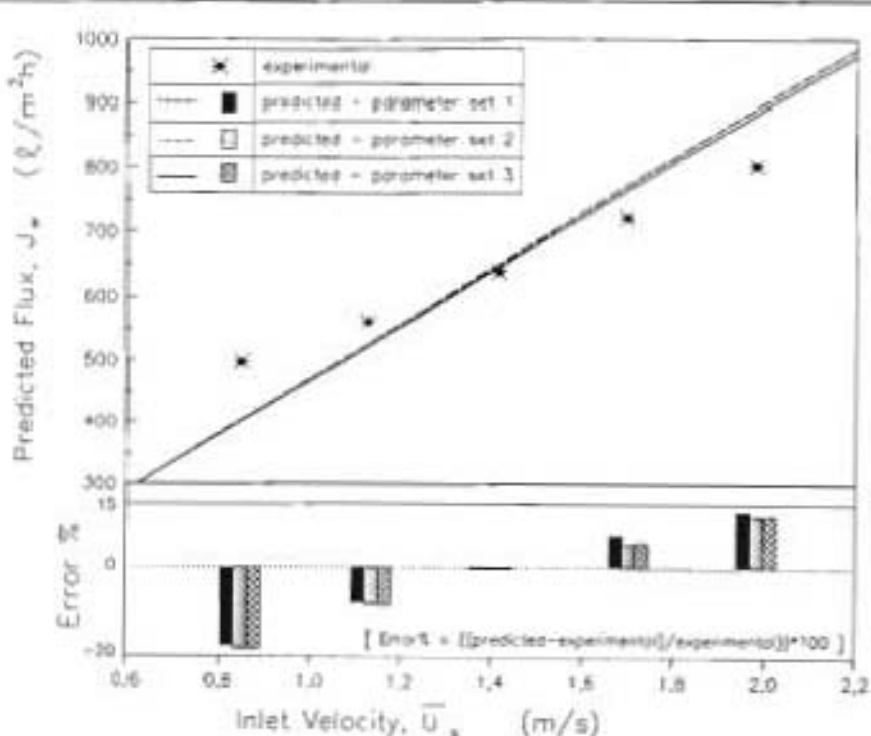


**FIGURE 5.20** Predicted Effect of Velocity on Steady-State Flux

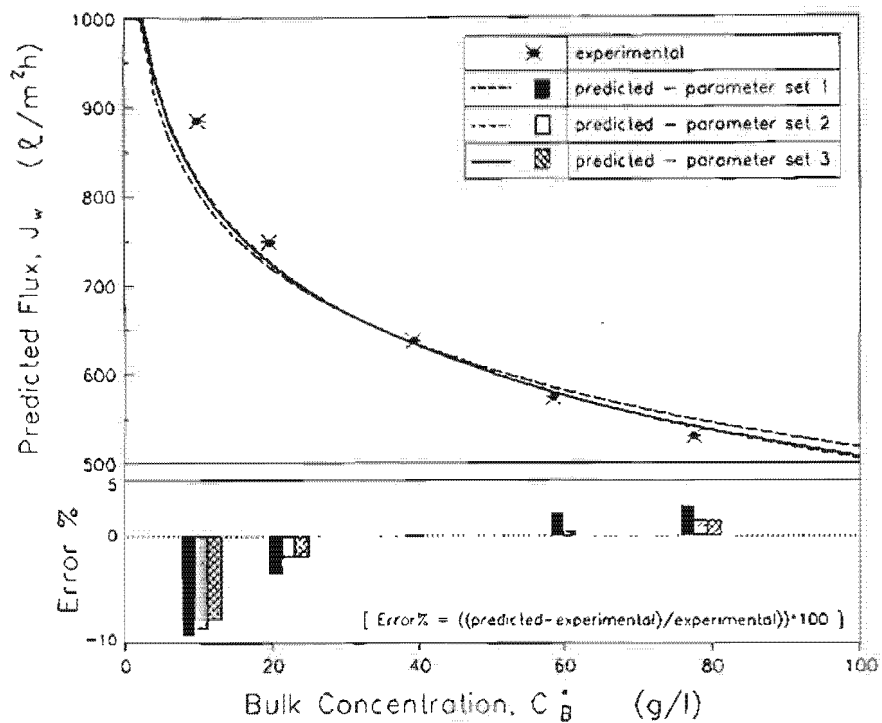


**FIGURE 5.21** Predicted Effect of Concentration on Steady-State Flux

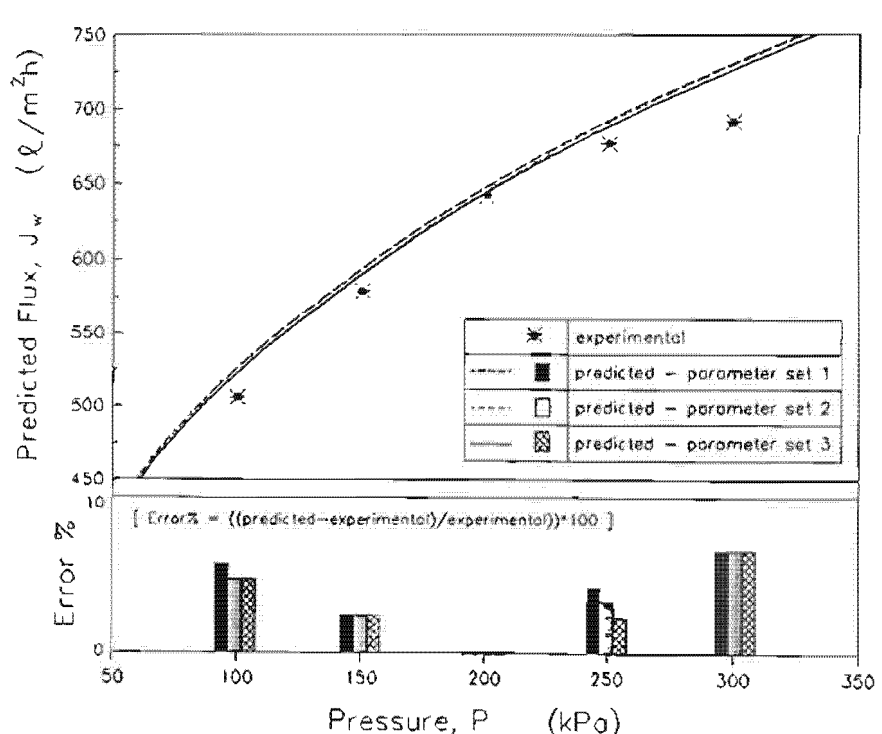


**FIGURE 5.22** Predicted Effect of Pressure on Steady-State Flux

In all instances, the predicted fluxes are insensitive to the  $S_z, K_{st}$  combination used. This confirms that a wide range of parameter combinations will yield equivalently good fits between predictions and observations. The trends predicted with respect to the effects of operating variables on steady-state fluxes are all consistent with experimental observations (see Chapter 2). The largest errors are observed in predictions for the effect of velocity on flux. The predicted curve straddles the experiment curve, under-predicting the flux by  $\approx 20\%$  at low velocity and over-predicting by  $\approx 10\%$  at high velocities. Predictions for the effects of concentration and pressure on flux are quite close to observations, except at high pressures where an over-prediction of  $\approx 5\%$  occurs.

The under-prediction at low velocities and over-prediction at high velocities could possibly be due to the neglect of the effects of preferential particle deposition. If preferential deposition occurs to a significant extent, the cake permeability would decrease as operating velocity is increased (see Chapter 4). Employing a permeability function that is inversely dependent on velocity will result in an increase in predicted fluxes at low velocities and a decrease in predictions at high velocities, leading to a closer match between predictions and observations.

The relatively good predictions with respect to the effect of pressure on flux possibly indicate that compression effects outweigh preferential deposition effects in determining the permeability-pressure relationship.

Predictions for the effect of operating variables on the steady-state cake thickness are shown in Figures 5.23 to 5.25. The cake thicknesses seem somewhat high, and in some instances are up to a third of the tube radius. These high values could possibly be due to the use of the "dead-end" permeability. Without experimental measurements it is impossible to evaluate whether the cake thicknesses are realistic. In all instances, however, the mass of cake as calculated from the predicted cake thickness is substantially less than the mass of feed limestone used in the respective run, indicating that these thicknesses are not impossible from a mass balance point of view.

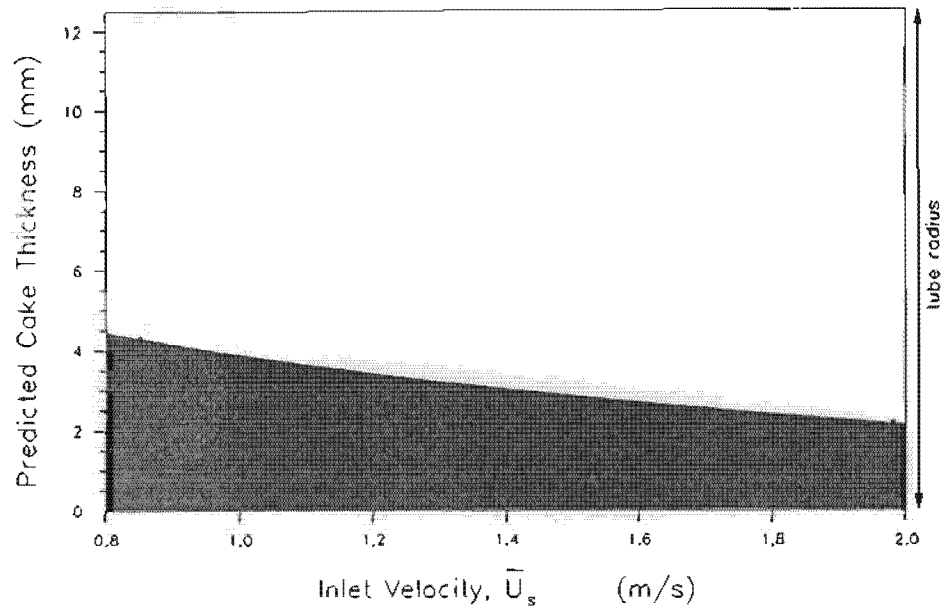


**FIGURE 5.23** Predicted Effect of Velocity on Steady-State Cake Thickness

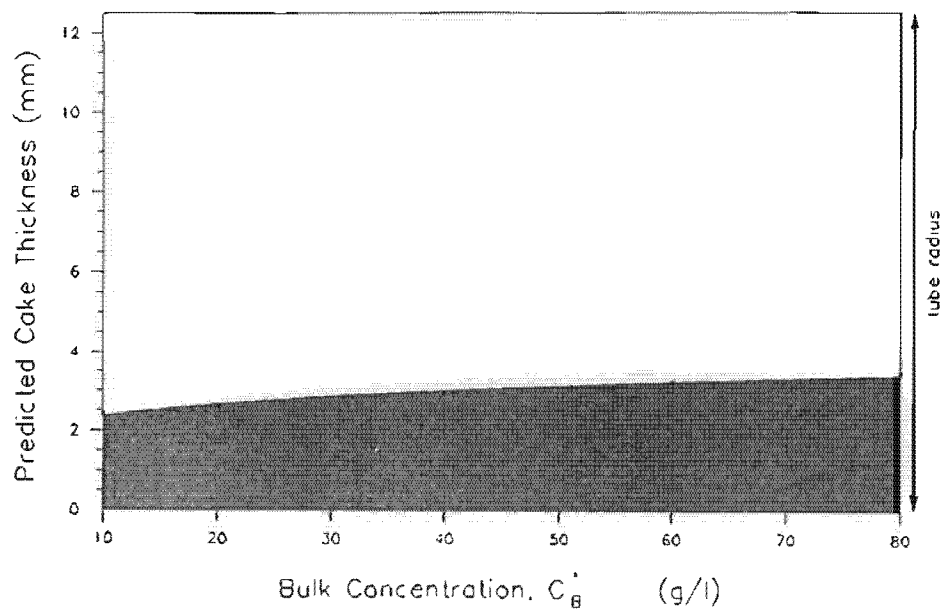


**FIGURE 5.24** Predicted Effect of Concentration on Steady-State Cake Thickness

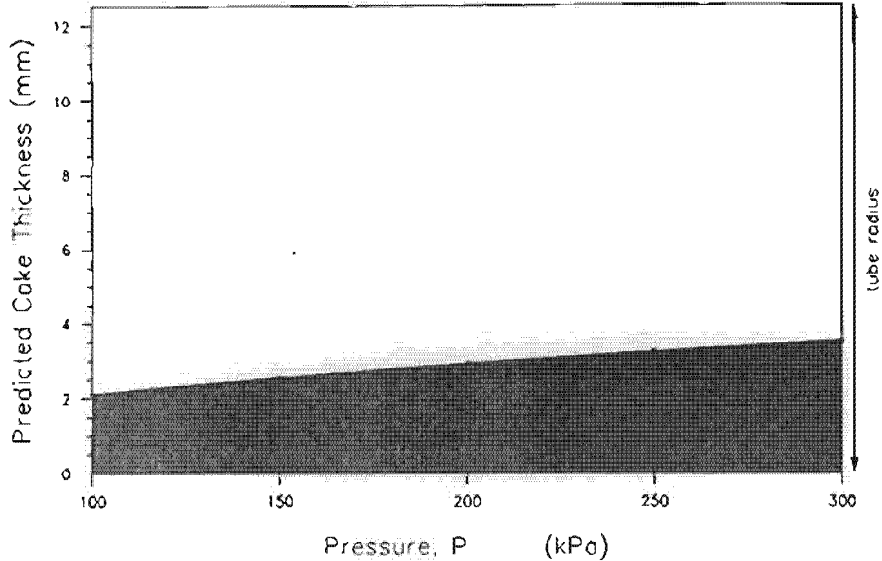


**FIGURE 5.25** Predicted Effect of Pressure on Steady-State Cake Thickness

The overall model performance is shown in Figure 5.26, where predicted fluxes are plotted against experimental fluxes. With the exception of two datapoints, all predictions lie within  $\pm 10\%$  of experimental observations.

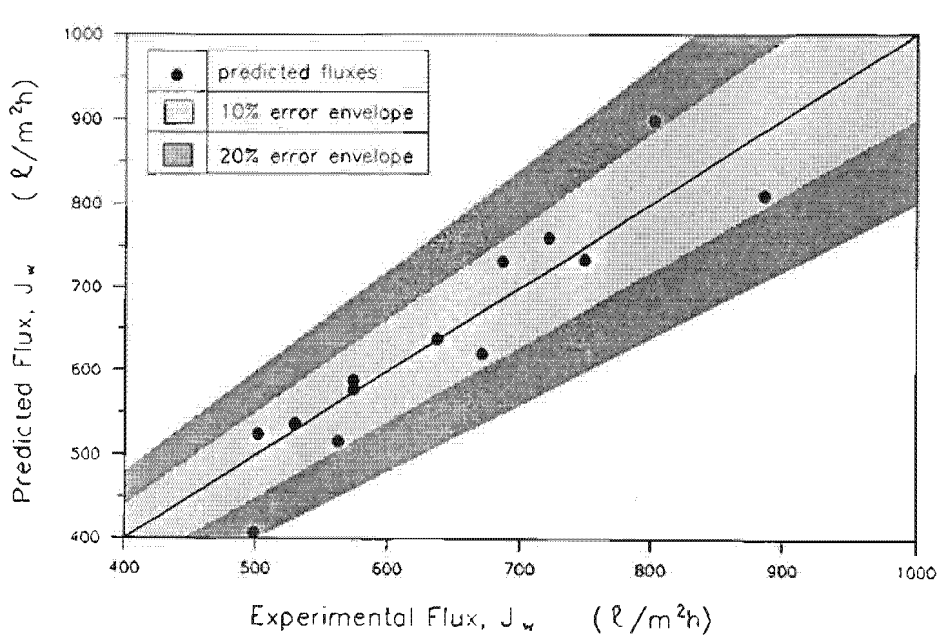


**FIGURE 5.26** Overall Comparison of Predicted and Experimental Steady-State Fluxes

In light of the conservative expectations expressed in the introduction to Chapter 5, the model predictions are surprisingly good. This will be discussed further in Section 5.8.

### 5.7.2 Characteristics of Typical Solutions

A typical steady-state solution is presented in Table 5.6 and Figures 5.27(a) and 5.27(b). Figure 5.27(a) depicts the  $V$ ,  $D_p$ , and  $C$  profiles over the entire boundary layer, while Figure 5.27(b) shows a close up of the near wall region. The general characteristics exhibited by  $D_p$ ,  $V$  and  $C$  were similar for all datapoints and all reasonable parameter combinations.

**TABLE 5.6** Typical Model Predictions

Predictions for Datapoint 3 (Run Number 48)		
<i>Specified Operating Variables:</i>		
Velocity ( $\bar{U}_w$ )	(m/s)	1,42
Concentration ( $C_s^*$ )	(g/l)	39,4
Pressure ( $P$ )	(kPa)	200
Temperature ( $T$ )	(°C)	30
<i>Experimental Observations</i>		
Flux at Tube Wall ( $J_w$ )	( $\ell/m^2h$ )	638
<i>Predictions</i>		
Flux at Tube Wall ( $J_w$ )	( $\ell/m^2h$ )	639
Cake Thickness ( $t_c$ )	(mm)	2,96
Boundary Layer Thickness ( $\delta$ )	(mm)	0,99

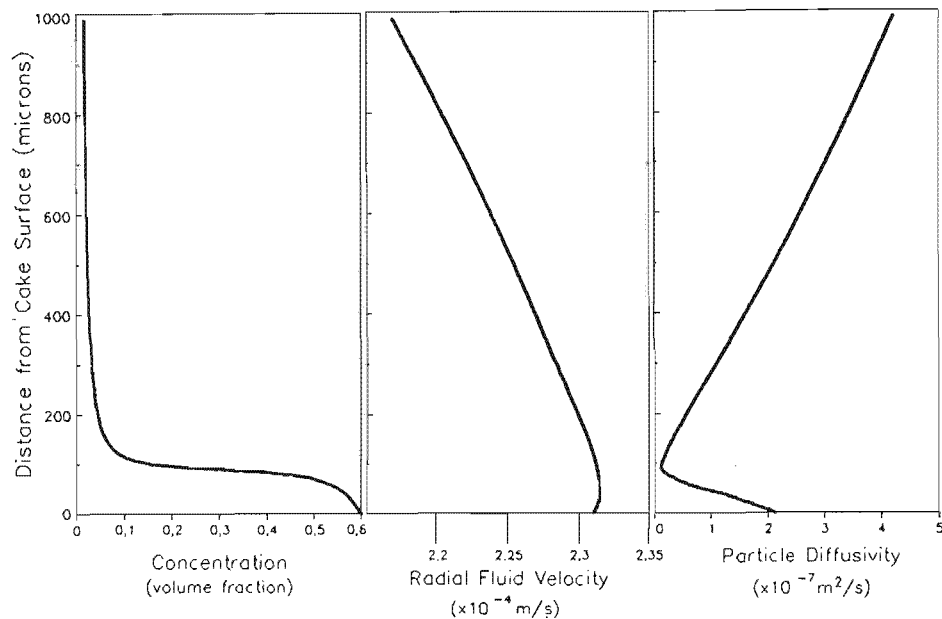


**FIGURE 5.27(a)** Typical Predicted Concentration, Radial Fluid and Diffusivity Profiles (across whole boundary layer)

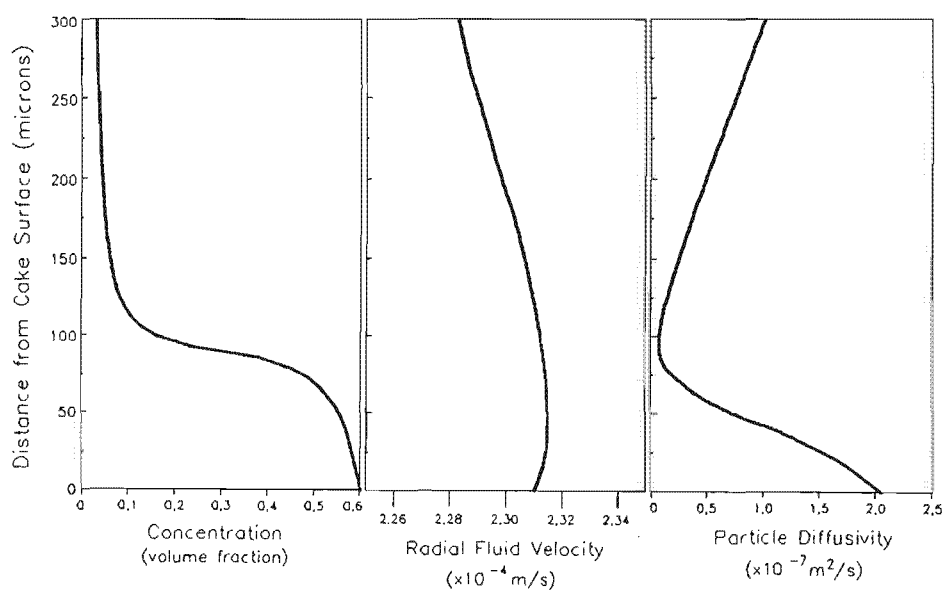


**FIGURE 5.27(b)** Typical Predicted Concentration, Radial Fluid and Diffusivity Profiles (near cake surface)

The radial fluid velocity increases towards the cake, reaches a maximum and then decreases slightly in the near cake region. The net particle diffusivity decreases rapidly, reaches a minimum and subsequently increases rapidly towards the cake surface. The concentration increases very slowly, undergoes an abrupt, step-like increase and thereafter gradually approaches the boundary concentration.

The origin of the rather unexpected trends for  $D_p$  and  $C$  may be ascertained from Figure 5.28. The unattenuated ("pure fluid") momentum diffusivity decreases towards the cake, eventually becoming negligible close to the cake surface (Curve 1). Attenuation due to concentration effects results in a more rapid decline in the near cake region (Curve 2). The low optimal value for  $S_c$  causes the particle diffusivity due to turbulence (Curve 3) to be substantially lower than the attenuated momentum diffusivity. The shear induced diffusivity (Curve 4) is a maximum at the cake surface, where both the shear rate and the concentration are at a maximum. On moving away from the cake the shear induced diffusivity decreases very rapidly, mainly due to the exponential dependence on concentration. The combination of Curves 3 and 4 yields the somewhat unique trend for the net particle diffusivity (Curve 5).

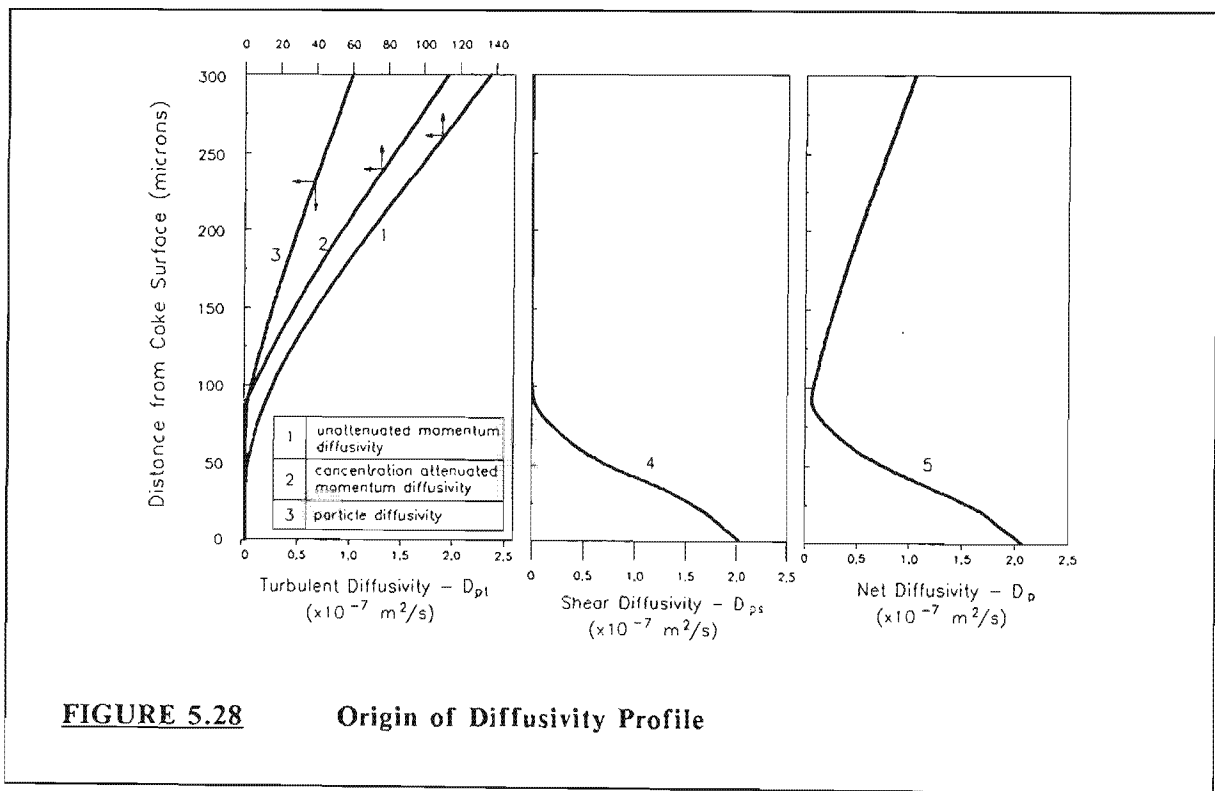


**FIGURE 5.28**      **Origin of Diffusivity Profile**

The system adjusts the concentration profiles so that at all points in the boundary layer the relationship  $VC = D_p \partial C / \partial r$  holds (see equation 5.6). The concentration gradient at any point is thus a function of the  $V/D_p$  ratio at that point. Accordingly a substantial concentration gradient exists at the point of minimum  $D_p$  and the gradient then decreases, as  $V/D_p$  decreases, towards the cake surface.

The question arises as to whether the above solution is realistic and meaningful. As noted previously, the uncommon trends exhibited by  $D_p$  and  $C$  were observed for all solution parameter combinations, and for all data points.

The trend exhibited by  $V$  is consistent with the studies of Kinney and Sparrow (1970) and Hirata et al. (1982). The trends exhibited by  $D_{\mu}$  and  $D_{\rho}$  are consistent with their correlations, and thus by implication are consistent with the studies from which the correlations were obtained. The resultant trend for  $D_p$ , however, cannot be evaluated by comparison with previous studies. To the best of the author's knowledge, the combination of  $D_{\mu}$  and  $D_{\rho}$  is unique to the present study. It was noted in Section 5.4.1.2 that the correlation for  $D_{\mu}$  would probably underestimate the diffusivity at low concentrations and overestimate the same at high concentrations. If so, the gradient of the  $D_{\mu}$  distribution will be less steep than that depicted in Figure 5.28.  $D_p$  however will most probably still pass through a minimum and the concentration profile will still exhibit a sharp increase at the point of minimum diffusivity.

Noting that  $D_p$  cannot be evaluated in terms of previous studies it will, by default, be assumed that since the parts (i.e.  $V$ ,  $D_{\mu}$ , and  $D_{\rho}$ ) are realistic, the sum of the parts (i.e.  $D_p$  and  $C$ ) are also realistic.

One interesting interpretation of the concentration profile is that it indicates the existence of a relatively distinct thickened suspension layer, of sub-critical concentration, next to the cake (Figure 5.29).

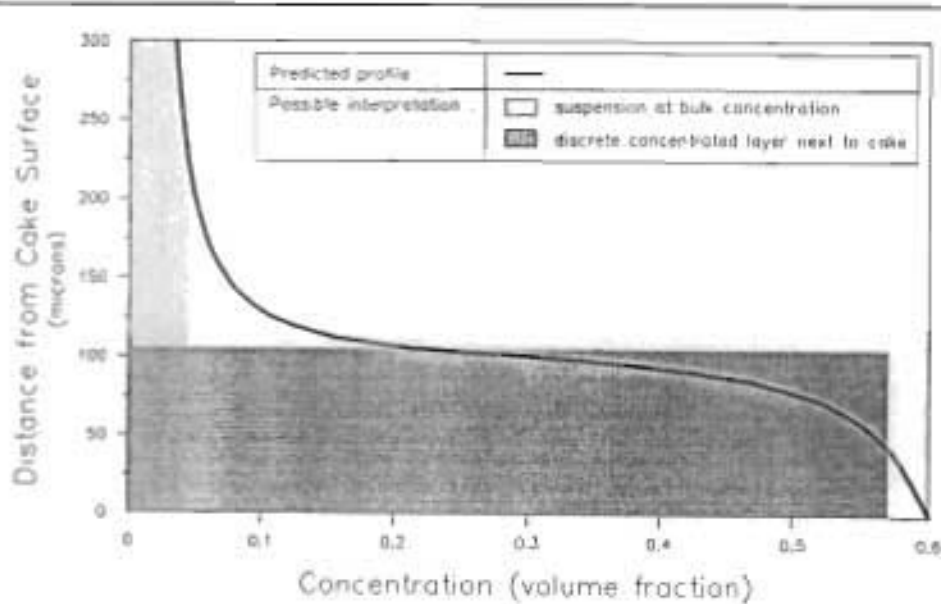


**FIGURE 5.29**

Indication of Distinct Thickened Suspension Layer next to Cake Surface

The existence of such a layer is explicable in terms of the  $V$  and  $D_p$  distributions. The high diffusivity at the cake surface promotes diffusion away from the cake. However, a significant resistance to outward diffusion exists at the point of minimum diffusivity. Particles are thus "trapped" between the cake surface and the point of minimum diffusivity. The radial fluid velocity increases towards the cake surface. This further increases the tendency for particles to accumulate in the near cake region. On moving towards the core, past the point of minimum diffusivity, the diffusivity increases rapidly and the fluid velocity decreases significantly. This results in a substantial increase in particle dispersion, leading to a relatively homogeneous suspension. The overall effect is that particle accumulation is confined to a thin region next to the cake, manifesting as a relatively distinct concentrated suspension layer.

That a distinct concentrated layer has not been observed in other known mass transfer systems, e.g. molecular mass transfer, is explicable. For molecular mass transfer in turbulent flows, the overall diffusivity will be the summation of the molecular diffusivity and the diffusivity due to turbulence, i.e. :

$$D_{net} = D + \epsilon_M$$

where  $D_{net}$  = net diffusivity of mass ( $m^2/s$ )

$D$  = molecular diffusivity ( $m^2/s$ )

$\epsilon_M$  = eddy diffusivity of mass ( $m^2/s$ )

The molecular diffusivity, given by e.g. the Stokes-Einstein equation, will be constant across a flow field. The eddy diffusivity of mass will exhibit a similar radial profile to the "pure fluid" eddy diffusivity of momentum (Curve 1 of Figure 5.28). Thus the net diffusivity will either decrease progressively towards the wall or alternatively decrease towards the wall and then attain a constant value a short distance away from the wall. This will yield a concentration profile that increases smoothly and progressively towards the wall.

Conversely, in particulate CFMF the equivalent of the molecular diffusivity,  $D$ , i.e.  $D_{ps}$ , is not a constant and decreases away from the cake. This, combined with the significant attenuation of turbulent diffusivity in regions of high concentration, leads to the unique distribution for  $D_p$  depicted in Figure 5.27, and hence to a distinct concentrated layer.

For the entire feasible range for  $K_{sh}$ , this concentrated layer is  $100 \mu m$  to  $150 \mu m$ , i.e. 20 to 30 particle diameters, thick (see e.g. Figure 5.16). It is seen that this distinct concentrated layer is similar to the hypothetical *precake* proposed in Chapter 2. The similarity is purely coincidental. The strong probability that this layer exists does however place the proposed mechanism for cake growth and limit (Chapter 3) and the preferential deposition effect (Chapter 4) on a firmer footing. It is of interest to note that the solution of a full convection-diffusion model, as has been attempted in the present study, indicates that the cake growth and limit is most probably controlled by a distinct concentrated layer next to the cake. This indicates that modelling effort could be considerably simplified by restricting analysis to this layer, and lends credence to proposed *moving layer* models for CFMF [e.g. Fane et al. (1990)].

### 5.7.3 Sensitivity to Parameters

In Section 5.6.3 it was shown that the model is relatively insensitive to the boundary layer constant,  $K_b$ . Model sensitivity to the diffusivity parameters, i.e.  $n$ ,  $K_{sh}$  and  $S_c'$ , was tested by choosing a parameter set from Table 5.5, independently changing each parameter by  $\pm 10\%$ , and comparing the predicted steady-state fluxes. Typical sensitivity analyses, for three datapoints, are presented in Table 5.7.

**TABLE 5.7** Typical Sensitivity Analyses

Base Case : Parameter Set 2

$$n = 3,5$$

$$K_{sh} = 1,0$$

$$S_c' = 0,00725$$

Varied Parameter <sup>a</sup>	Change in Predicted Flux (%) <sup>b</sup>		
	Datapoint 3	Datapoint 6	Datapoint 9
<i>n</i>			
0,9 n	1,8	0,9	2,1
1,1 n	2,0	0,9	2,6
<i>S_c'</i>			
0,9 <i>S_c'</i>	4,4	4,4	3,9
1,1 <i>S_c'</i>	5,8	4,7	4,2
<i>K<sub>sh</sub></i>			
0,9 <i>K<sub>sh</sub></i>	2,6	2,2	1,3
1,1 <i>K<sub>sh</sub></i>	1,8	2,8	1,3

<sup>a</sup> all other parameters are as in base case

<sup>b</sup>

$$\% \text{change} = \left( \frac{\text{predicted flux} - \text{predicted flux}_{(\text{base case})}}{\text{predicted flux}_{(\text{base case})}} \right) \times 100$$

The predicted flux is relatively insensitive to  $n$ , confirming the observation that the parameter solution surface is not a strong function of  $n$  (see Section 5.6.2). The model is also relatively insensitive to  $K_{sh}$ , consistent with the observation that the parameter solution curve is not a

strong function of  $K_{sh}$  for  $K_{sh} > 0.6$ . A moderate sensitivity is exhibited with respect to  $S_c^+$ . Note that in many instances, the percentage change obtained by varying the parameters is similar to the convergence criterion used in the outer iteration loop (1%, see Section 5.5), indicating that the change is not significant. Overall, changing the parameter values by 10 % results in a maximum 6% change in predicted fluxes, indicative of a model that is only moderately sensitive to parameter values.

In general, the model exhibits a remarkable insensitivity to parameter values, for values within certain wide ranges. From Figures 5.18 and 5.19, it is seen that predicted concentration profiles and fluxes are not very sensitive to changes in  $K_b$  over the range  $100 < K_b < 200$ . Figure 5.14 indicates that the solution surface is not very sensitive to changes in  $n$  over the range  $2.5 < n < 5.0$ . This is confirmed in Table 5.7. Figure 5.11 illustrates that the solution curve is insensitive to changes in  $K_{sh}$  for  $K_{sh} > 0.6$ .

The insensitivity to  $K_b$  may be explained by noting that the concentration gradients are mostly restricted to the region between the cake surface and the point of minimum diffusivity (see Section 5.7.2). Thus, providing that the boundary layer is significantly greater than the thickness of this region, the concentration profile, and hence model predictions, will be insensitive to  $K_b$ . In effect therefore, the insensitivity to  $K_b$  is due to the unique form of the diffusivity distribution.

Model insensitivity to  $n$  and  $K_{sh}$  is most probably due to the strong mutual dependence between the concentration and diffusivity distributions, and the contrasting effects that concentration has on  $D_{ps}$  and  $D_{pl}$ . (Recall that  $D_{ps}$  increases with concentration while  $D_{pl}$  decreases as concentration is increased).

Consider, for example, system response when  $K_{sh}$  is increased. The increase in  $D_{ps}$  will promote the diffusion of particles away from the cake and hence tend to increase the concentration in regions away from the cake (i.e. increasing  $K_{sh}$  tends to *spread concentration* away from the cake). However, any spread of concentration away from the cake will tend to decrease the local  $D_{pl}$  in those regions away from the cake. This effect will, in turn, restrict the diffusion of particles away from the cake and hence arrest the spread of concentration away from the cake. Effectively a *self-dampening* effect exists, within the system. Any tendency to spread concentration away from the cake is attenuated by a simultaneous decrease in  $D_{pl}$ . Conversely, any tendency to pull the concentration profile towards the cake will be attenuated by a simultaneous increase in  $D_{pl}$ .

At low  $K_{sh}$  the concentrated layer is well within the sublayer and the local  $D_{pl}$  is low. Hence the self-dampening effect is not significant, and the parameter solution curve is sensitive to  $K_{sh}$ . As  $K_{sh}$  is increased, the thickness of the concentrated layer extends to the buffer zone, where  $D_{pl}$  is significant. Here, seemingly, changes in  $K_{sh}$  and  $n$  are completely offset by the self-dampening effect, resulting in model predictions being relatively insensitive to changes in  $K_{sh}$  and  $n$  over a wide range thereof. The greater sensitivity with respect to  $S_c^+$  may be explained by noting that any change in  $S_c^+$  results in a direct linear change in  $D_{pl}$ , in contrast to changes

in  $n$  which affect  $D_{pt}$  indirectly, through the concentration profile (see equations 5.33). Thus the self-dampening effect is less noticeable with respect to changes in  $S_c$ , manifesting as a greater sensitivity to that parameter.

Note that, similar to the uncommon concentration profile, the model insensitivity to parameters is mainly due to the unique diffusivity distribution obtained by the combination of  $D_{pt}$  and  $D_{ps}$ .

#### **5.7.4 Are the Parameter Values Realistic ?**

##### **5.7.4.1 Boundary Layer Constant - $K_b$**

Concentration boundary layer thicknesses for all datapoints, and for  $K_b = 150$ , are shown Figure 5.30.  $\delta$  ranges from 0,8 mm to 1,5 mm, consistent with the boundary layer assumption that concentration gradients are confined to a narrow region next to the cake. Further, in all instances the concentration smoothly approaches the bulk concentration well before the edge of the boundary layer (see e.g. Figure 5.21). Thus,  $K_b$  is seemingly realistic.

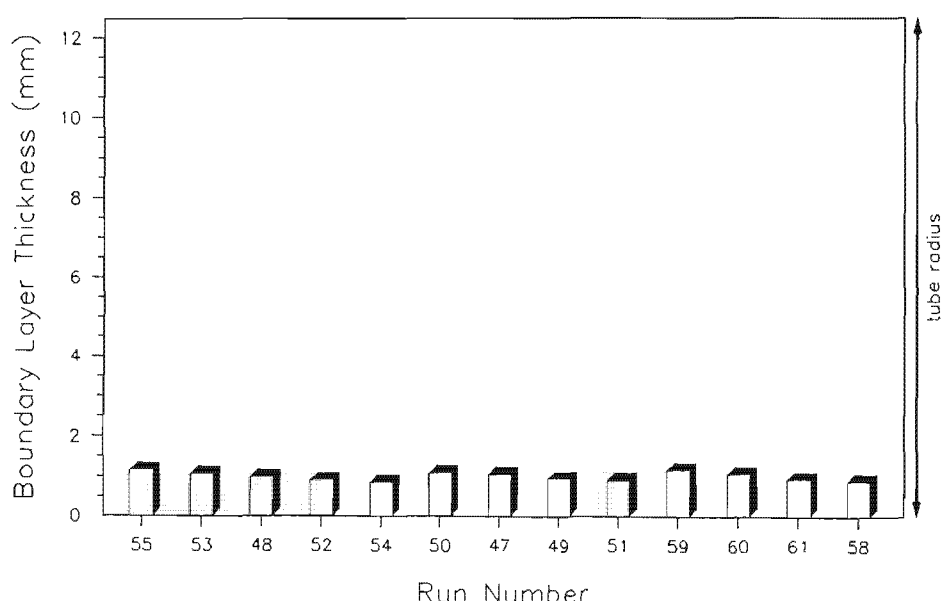


**FIGURE 5.30 Predicted Concentration Boundary Layer Thicknesses**

##### **5.7.4.2 Turbulence Attenuation Parameter - $n$**

The turbulence attenuation function corresponding to  $n = 3,5$  can be inferred from Figure 5.5. At the current state of knowledge it is not possible to ascertain whether this attenuation function is realistic for limestone.

#### 5.7.4.3 Shear Diffusivity Parameter - $K_{sh}$

Following the argument in Section 5.4.1.2, it is expected that  $K_{sh}$  should be less than 1. As noted in Section 5.7.1, it is impossible to ascertain an optimal  $K_{sh}$  since all  $S_c$ ,  $K_{sh}$  combinations tested in the range  $0.7 < K_{sh} < 1.4$  yielded equivalently good fits between predictions and experimental observations. It may be concluded that  $K_{sh}$  values in the range  $0.7 < K_{sh} < 1$  are realistic and consistent with expectations.

$K_{sh}$  values  $> 1$  are only feasible if the following apply :

- (i) the diffusivity of angular particles is substantially greater than that of spherical particles
- (ii) Leighton's correlation (equations 5.34 and 5.35) drastically underestimates the shear induced diffusivity of small particles

At the present state of knowledge, the validity of the above cannot be ascertained.

#### 5.7.4.4 Inverse Particle Schmidt Number - $S_c^{-1}$

For the entire feasible range for  $K_{sh}$  the corresponding solution values for  $S_c^{-1}$  are at least one order of magnitude below that reported in previous studies (see Figure 5.17 and Section 5.4.1.1). Possible reasons for this discrepancy are :

- (i) The particle Schmidt number in concentrated suspensions may be significantly lower than that in dilute suspensions. All the studies reported in Section 5.4.1.1 concerned systems where the particle concentrations were well below that encountered in the concentration boundary layers here. Soo (1987) has stated that the particle diffusivity seems to decrease as concentration increases.
- (ii) The underlying turbulence levels in systems having a significant radial concentration (and hence viscosity) gradient may be substantially below that obtained with pure fluids. Studies on turbulence have shown that the region of maximum turbulence intensity lies within the buffer zone [Hinze (1975)]. From the model solutions obtained here it is seen that regions of very high concentration extend well into the buffer zone. Noting the significant attenuation of turbulence that will result in regions of high concentration, it is therefore likely that the overall turbulence levels in CFMF could be well below those reported for pure fluids, leading to the extremely low values for  $S_c^{-1}$ .

If indeed the turbulence structure in systems that have a significant radial viscosity profile is substantially different from that of pure fluids then the modelling approach adopted in this study, i.e. using a diffusivity correlation developed for pure fluids with some correction factor to account for concentration effects, is invalid. However, the alternative would be to employ a turbulence model that correctly predicts turbulence diffusivities as a function of local fluid properties and global flow characteristics. To the best of the author's knowledge, such a model is well beyond the scope of current technology in turbulence modelling.

## 5.8 EVALUATION OF MODEL

Predicted steady-state fluxes show a good correspondence with experimental observations, especially with regard to the effects of concentration and pressure on steady-state flux. This good correspondence is notable, in view of the fact that solution parameter combinations evaluated for a single datapoint were subsequently used to obtain predictions for the whole dataset. The model also exhibits a remarkable insensitivity to parameter values, within certain wide ranges thereof. The values for  $n$ ,  $K_{sh}$  and  $K_t$  are seemingly realistic, but the values for  $S_c$  are at least one order of magnitude below values reported in previous studies. The predicted concentration profiles indicate that the concentration does not increase smoothly from bulk to cake. Instead, a distinct thickened suspension layer, of sub-critical concentration, seems to exist next to the cake. Seemingly, cake growth and limit is controlled by this 20 to 30 particle diameter thick layer, consistent with the qualitative model presented in Chapter 3.

The good predictions obtained from parameters evaluated for a single datapoint are most probably just another manifestation of the model insensitivity to parameter values. This insensitivity, in turn, is almost wholly due to the unique form of the diffusivity distribution, obtained by the combination of shear induced hydrodynamic diffusion and a concentration-attenuated turbulent diffusion.

The good model predictions are notable, in light of the reservations expressed in Section 5.1. However, there are various potential discrepancies which should be stated. The correlations used to formulate the turbulent diffusivity function were developed for pure fluids. There are no indications in the literature as to whether they can be confidently applied to systems having significant radial concentration variations, as in the present study. The correlations for shear induced hydrodynamic diffusivity were developed for relatively uniformly sized spherical particles, of large particle diameter, sheared at low shear rates. In the system under study, the shear rates are orders of magnitude greater, and the particles are considerably smaller. Further for the limestone suspension used in the present study, charge effects etc. are likely to affect inter-particle interaction at high concentrations. It is not known what effects this would have on the shear diffusivity of the particles. Once again, there are no clear indications in the literature as to whether the shear induced diffusivity correlations are in fact applicable to the system under study.

It is thus feasible that the unique form of the diffusivity distribution, and hence the model insensitivity to parameters, may be an artefact introduced by the application of fluid and particle dynamics technology to a system vastly different from those for which the technology was developed. From that point of view, the fundamental basis of the model is not beyond question.

Despite the reservations noted above, the good model predictions are indeed encouraging, indicating that at the very least a reasonable correlative model may be developed from current technology. The model would have to be tested on other systems to assess its general validity and predictive ability.

The predictive ability of the model is currently restricted by the fact that most model parameters cannot be specified *a priori* from suspension properties and flow conditions. This is mainly due to the lack of definitive knowledge on turbulence in concentrated suspensions. In the present instance, the parameters could have been obtained from a single datapoint. If this is the general case, then the model could prove to be a useful *order of magnitude* predictive tool. Once again, the validity of this approach can only be assessed if the model is tested on other systems.

If, in general, model parameters cannot be estimated from a single datapoint, a set of *best fit* parameters may be estimated from a regression on the entire experimental dataset. However, due to the nested iteration loops, a regression on the whole dataset could prove to be extremely demanding and expensive in terms of computing time. Thus if a model is required solely for correlation of experimental results, and mechanistic inconsistencies are to be ignored, the simpler models discussed in Chapter 3 may exhibit distinct advantages over the model proposed in this study.

In applying the model to other systems the limits to its applicability should be taken into cognisance. The model would only be applicable to systems where the limiting cake thickness is controlled by convection-diffusion processes. It is entirely feasible that in some systems the differentiation between stagnant cake and flowing suspension may be primarily determined by the suspension rheology and flow conditions, and not by some critical concentration. In those instances, it is most likely that the limiting cake thickness will be determined by a shear mechanism, and not by the convection diffusion processes. Clearly, the model will be inapplicable in such circumstances. Chapter 3 indicates some methods by which the controlling process may be inferred from the flux-time curves obtained at different operating velocities.

The utilisation of a shear induced hydrodynamic diffusivity limits the model's applicability to particulate suspensions, where fluid induced forces on particles are substantially greater than physico-chemical interactions between particles. This would preclude the application of the model to suspensions which exhibit significant non-Newtonian characteristics.

## *Chapter 6*

### **CONCLUSION** **AND** **RECOMMENDATIONS**

---

This study has concerned investigations into, and the modelling of, the cross-flow microfiltration of particulate suspensions under turbulent flow conditions. The characteristic flux-time behaviour, effects of operating variables on flux, and system responses to perturbations in operating variables were experimentally obtained for a limestone suspension cross-flow filtered in a 25 mm woven hose tube. A qualitative model of the steady-state condition was then developed, based on an analysis of the likely particle dynamics in the system. The qualitative model was subsequently formulated into a mathematical model of the steady-state, with a strong emphasis being placed on formulating model functions from current fluid and particle dynamics technology. The study also entailed qualitative investigations into the effects of cake characteristics on system behaviour.

The shape of the characteristic flux-time curve may be attributed to two phenomena. On start-up, the flux decreases rapidly, due to a rapid increase in cake thickness. Thereafter, the cake becomes limited to some steady-state thickness, but changes in the cake characteristics lead to a slow, long-term decline in flux. It was inferred that, for the limestone system studied, this change in characteristics is most probably due to the infiltration of finer particles (*fines*) into the cake, leading to a cake of progressively decreasing permeability. It has also been inferred that fines infiltration is most likely to be a *surface effect*, i.e. fines infiltrate, and progressively saturate, only the surface layers of the cake, and not the entire cake volume.

The flux-time curve is a function of the operating variables studied here, viz. inlet velocity, bulk concentration and pressure. However, the flux may not be a unique function of the operating point but may also be dependent on the operating path taken to reach the operating point. This was explained in terms of an apparent irreversibility of the cake, due to irreversible hydraulic compression, and the fines infiltration effect. The path dependence of the flux-time curve has significant implications for operation of CFMF systems. In practise, various strategies may exist to start-up a plant, or to change an operating point during operation. In light of the

experimental findings in this study, some strategies could result in a considerably lower flux than is expected at the final operating point. This necessitates a careful evaluation of possible operational strategies. The general guide-lines in this regard are that operational changes that require a decrease in cake thickness in order to be effective should definitely be avoided, and changes that tend to increase the cake thickness should preferably not be implemented during the slow decline in flux period.

Although the fines infiltration effect is likely to occur only in cakes formed from particulate suspensions, irreversible hydraulic compression would most probably also occur in non-particulate fouling layers e.g. colloidal gels formed in ultra-filtration systems. It is thus highly feasible that ultra-filtration and non-particulate CFMF systems may also exhibit the path dependence of flux observed in the present study. The extension of the present experimental study to non-particulate systems could prove to be of practical significance.

The dependence of flux on the operating path, as well as the long-term flux decline, indicate that system behaviour is determined not only by internal hydrodynamics but is also significantly affected by the behaviour of the cake.

A qualitative model of the mechanisms that determine cake growth and limit was developed from an analysis of the likely particle transport processes in the system, utilising the observations from the experimental study to infer the controlling processes. In essence, there are three significant particle transport processes - convection of particles towards the cake, shearing of particles off the cake into the adjacent suspension layer (the *precake*), and diffusion of particles from the precake back to the bulk suspension. This back-diffusion is effected by three mechanisms, viz. shear induced hydrodynamic diffusion, entrainment by turbulent bursts and entrainment by turbulent eddies. The convection - diffusion processes determine the concentration of the precake, and hence whether the precake would reach some critical concentration and consolidate into cake. The limiting, or steady-state cake thickness is thus determined by the convection - back-diffusion processes, although the shearing mechanism is an integral part of the back transport process. It was shown that this qualitative model explains phenomena that are indicative of a shear controlled system (i.e. the preferential deposition effect and the irreversibility of the cake formation), as well as phenomena associated with convection-diffusion controlled systems (i.e. the effect of inlet velocity on flux-time behaviour, and the semi-log relationship between the steady-state flux and bulk concentration).

The qualitative model was subsequently formulated into a mathematical model of the steady-state. The appropriate steady-state equations were identified. Model functions required for the solution of the equations were formulated from either laboratory scale experiments, or from fluid and particle dynamics correlations from the literature. Four model parameters resulted which could not be quantified in terms of current technology. These were subsequently evaluated by computational experiments and a manual regression technique, and were in effect evaluated

from a single experimental datapoint. A numerical solution procedure was developed, which enables the prediction of the steady-state cake thickness, flux and concentration profile for specified operating and system variables.

The predicted steady-state fluxes show notably good correspondence with experimental observations. Predictions are relatively insensitive to parameter values over wide ranges thereof. The model also predicts unique concentration profiles, indicating that cake growth and limit are most probably determined by thin, distinct, concentrated suspension layers next to the cake.

There are however notable limitations in the model. Firstly, the model is only applicable to the cross-flow microfiltration of particulate suspensions that do not exhibit significant non-Newtonian characteristics, and where the limiting cake thickness is convection-diffusion controlled. This may preclude the application of the model to many suspensions encountered in practice. Secondly, the model parameters cannot be quantified *a priori* from suspension properties and flow conditions, or simple laboratory experiments. This may change as further research is performed into turbulence in concentrated suspensions. For the present however, model parameters must be quantified from regressive techniques, thereby limiting the predictive ability of the model. In the present study, model parameters quantified from computational experiments on a single datapoint yielded good predictions for the rest of the experimental dataset. The model needs to be tested on other suspension systems in order to assess whether this would be the general case.

Despite the reservations noted above, the good predictions of the model are indeed encouraging. This indicates that, at the very least, a reasonable correlative model may be developed from current fluid and particle dynamics technology and correlations. It is difficult to criticise the model in terms of previous studies, noting that the model is strongly based on current knowledge of fluid and particle dynamics. Some of the predictions of the model however, e.g. the unique concentration and diffusivity profiles, depart radically from other known systems. Unequivocal evaluation of the validity of the model may resolve to experimentally monitoring *internal* quantities, e.g. the concentration profile, and comparing this to model predictions.

Modelling effort in this study has been restricted to the development of a steady-state model. In practise, the long-term flux decline, albeit a slow process, may result in a significant reduction in flux over a period of time. Confident design and optimisation of CFMF system would thus also require some model of the slow flux decline. The steady-state model would be utilised to determine the optimum operating and system variables for a specified application. Thereafter the model of the long-term decline would be utilised to predict the true permeate production rate, as well as to optimise operation-cleaning cycle times.

Rigorous modelling of the long term decline is likely to be complex, and would necessitate a knowledge of, *inter alia*, the size distribution of the suspension, the depth to which fines would penetrate the cake and the combined effects of hydraulic compression and radial size distribution variations on the permeability of the cake. In the present instance, it was observed that the gradients of the flux-time curves during the slow decline in flux period were substantially

similar, and relatively independent of operating conditions. In such instances, the long-term flux decline may be modelled in a wholly empirical form, with time as the only independent variable. This should prove adequate for design purposes.

## References

---

- AGGARWAL, J.K., HOLLINGSWORTH, M.A. and MAYHEW, Y.R. (1972), Experimental Friction Factors for Turbulent Flow with Suction in a Porous Tube, *International Journal of Heat and Mass Transfer*, 15, pp. 1585-1602.
- ALTENA, F.W. and BELFORT, G. (1984), Lateral Migration of Spherical Particles in Porous Flow Channels : Application to Membrane Filtration, *Chem. Eng. Science*, 39(2), pp. 343-355
- BAKER, R.J., FANE, A.G., FELL, C.J.D., and YOO, B.H. (1985), Factors Affecting Flux in Crossflow Filtration, *Desalination*, 53, pp. 81-93
- BEAVERS, G.S. and JOSEPH, D.D. (1967), Boundary Conditions at a Naturally Permeable Wall, *Journal of Fluid Mechanics*, 30, p. 197
- BELFORT, G. and NAGATA, N. (1985), Fluid Mechanics and Cross-flow Filtration : Some Thoughts, *Desalination*, 53, pp. 57-79
- BERTERA, R., STEVEN, H. and METCALFE, M. (1984), Development Studies of Cross-flow Microfiltration, *The Chemical Engineer*, pp. 10-14, June
- BIRD, R.B., STEWART, W.E. and LIGHTFOOT, E.N. (1960), *Transport Phenomena*, John Wiley and Sons
- BLATT, W.F., DRAVID, A., MICHAELS, A.S. and NELSEN, L. (1970), Solute Polarisation and Cake Formation in Membrane Ultrafiltration : Causes, Consequences and Control Techniques, in *MEMBRANE SCIENCE AND TECHNOLOGY*, pp. 47-97
- BRODKEY, R.S. (1967), *The Phenomena of Fluid Motions*, Addison-Wesley Publishing Co.
- CALABRESE, R.V. and MIDDLEMAN, S. (1979), The Dispersion of Discrete Particles in a Turbulent Fluid Field, *AIChE*, 25(6), pp. 1025-1035
- CLEAVER, J.W. and YATES, B. (1973), Mechanism of Detachment of Colloidal Particles from a Flat Substrate in Turbulent Flow, *Journal of Colloid and Interface Science*, 44(3), pp. 464-474.

- CLEAVER, J.W. and YATES, B. (1975), A Sublayer Model for the Deposition of Particles from a Turbulent Flow, *Chem. Eng. Science*, 30, pp. 983-992
- CLEAVER, J.W. and YATES, B. (1976), The Effect of Re-entrainment on Particle Deposition, *Chem. Eng. Science*, 31, pp. 147-151
- CORINO, E.R. and BRODKEY, R.S. (1969), A Visual Investigation of the Wall Region in Turbulent Flow, *Journal of Fluid Mechanics*, 37, pp. 1-30
- DAHLHEIMER, J.A., THOMAS, D.G. and KRAUS, K.A. (1970), Hyperfiltration - Application of Woven Fibre Hoses to Hyperfiltration of Salts and Crossflow Filtration of Suspended Solids, *Ind. Eng. Chem. Process. Des. Develop.*, 9(4), pp. 566-569
- DAVIES, J.T. (1975), Local Eddy Diffusivities Related to "Bursts" of Fluid Near Solid Walls, *Chem. Eng. Science*, 30, pp. 996-997
- DAVIES, J.T. (1972), *Turbulence Phenomena*, Academic Press, New York
- DAVIS, R.H. and LEIGHTON D.T. (1987), Shear-induced Transport of a Particle Layer Along a Porous Wall, *Chem. Eng. Science*, 42(2), pp. 275-281
- DAVIS, R.J. and BIRDSELL, S.A. (1987), Hydrodynamic Model and Experiments for Crossflow Microfiltration, *Chem. Eng. Communications*, 49, pp. 217-234
- DE PINHO, M. and FAHIEN R.W. (1981), Correlation of Eddy Diffusivities for Pipe Flow, *AICHE*, 27(1), pp. 170-172
- ECKSTEIN, E.C., BAILEY, D.G. and SHAPIRO, A.H. (1977), Self-Diffusion of Particles in Shear Flow of a Suspension, *Journal of Fluid Mechanics*, 79, p. 191
- FANE, A.G., FELL, C.J.D. and NOR, M.T. (1982), Ultrafiltration in the Presence of Suspended Matter, I. *Chem. E. Symposium Series*, (73), C1.
- FANE, A.G. (1984), Ultrafiltration of Suspensions, *Journal of Membrane Science*, 20, pp. 249-259
- FOUST, A.G., WENZEL, A.L., CLUMP, C.W. and MANS, L. (1980), *Principles of Unit Operations*, 2nd ed., Wiley, New York
- FISCHER, E. and RAASCH, J. (1986), Model Tests of the Particle Deposition at the Filter Medium in Cross-flow Filtration, Proceedings of the 4th World Filtration Congress, Ostend, Part III, 11.11.

FLEMMER, R.L.C., BUCKLEY C.A. and GROVES, G.R. (1982), An Analysis of the Performance of a Spiral-Wound Ultrafiltration Membrane with a Turbulence-Promoting Net, *Desalination*, 41, pp. 25-32

FORDHAM, E.J. and LADVA, H.K.J. (1990), Cross-flow Filtration of Bentonite Suspensions, PCH PhysioChemical Hydrodynamics (in press).

GRASS, A.J. (1974), Transport of Fine Sand on a Flat Bed : Turbulence and Suspension Mechanics, EUROMECH 48, pp. 33-34.

GREEN, G. and BELFORT, G. (1980), Fouling of Ultrafiltration Membranes : Lateral Migration and the Particle Trajectory Model, *Desalination*, 35, pp. 129-147

HARRISON, C., CARTER, A.J. and SCARLETT, B. (1981), *Cross Flow Filtration*, Filtech Conference, Uplands Press, Croyden, England

HENRY, J.D. (1972), *Cross Flow Filtration, Recent Developments in Separation Science*, 2, pp. 205-225

HINZE, J.O. (1975), *Turbulence*, 2nd ed., McGraw Hill

HIRATA, Y., KOMATSU, S. and ITO, R. (1982a), Experimental Study of Flow Development in a Porous Tube with Injection or Suction, *Journal of Chemical Engineering of Japan*, 15(6), pp. 445-451

HIRATA, Y and ITO, R. (1982b), Extension of the Mixing Length Theory to a Porous Tube Flow With Injection or Suction, *Journal of Chemical Engineering of Japan*, 15(6), pp. 452-458

HOOGLAND, M.R., FANE, A.G. and FELL, C.J.D. (1988), Crossflow Filtration of Mineral Slurries With Ceramic Membranes, Paper G25, International Membrane Technology Conference, Sydney, Australia

HOOGLAND, M.R., FELL, J.D., FANE, A.G. and JONES, D.A.R. (1990), *The Optimum Design of Crossflow Filtration Elements for Mineral Slurry Processing*, Proceedings - Vth World Filtration Congress, Nice, France

HSU, F., TURIAN, R.M. and MA, T. (1989), Flow of Noncolloidal Slurries in Pipelines, *AIChE*, 35(3), pp. 429-442, March

HUGHMARK, G.A. (1968), Eddy Diffusivity Close to a Wall, *AIChE*, March, pp. 352

- HUGHMARK, G.A. (1971), Heat and Mass Transfer for Turbulent Pipe Flow, *AIChE*, 17(4), pp. 902-909
- HUGHMARK, G.A. (1973), Additional Notes on Transfer in Turbulent Pipe Flow, *AIChE*, 19(5), pp. 1054-1055
- HUNT, J.W. (1987a), Mathematical Modelling of Cross-flow Microfiltration, MSc Thesis, University of Natal
- HUNT, J.W., TREFFRY-GOATLEY, K., FLEMMER, R.L.C., RAAL, J.D. and BUCKLEY, C.A. (1987b), A Mathematical Model for Steady-State Cross-flow Microfiltration in a Woven Hose Support, *Desalination*, 61, pp.187-200
- HUNT, J.W., BROUCKAERT, C.J., RAAL, J.D., TREFFRY-GOATLEY, K. and BUCKLEY, C.A. (1987c), The Unsteady-State Modelling of Cross-flow Microfiltration, Proceedings - 3rd World Congress on Desalination and Water Reuse, Cannes, France
- IM, K.H. and CHUNG, P.M. (1983), Particle Deposition from Turbulent Parallel Streams, *AIChE*, 29(3), p. 498
- KINNEY, R.B. and SPARROW, E.M. (1970), Turbulent Flow, Heat Transfer and Mass Transfer in a Tube with Surface Suction, *Journal of Heat Transfer*, February, pp. 117-125
- KNIBBS, R.H. (1981), The Development of a High Flux Microfilter with a Wide Range of Applications, Filtech Conference, pp. 56-68
- KRAUS, K.A. (1974), Cross-flow Filtration and Axial Filtration, *Purdue University Engineering Bulletin*, 145(2), pp. 1059-1075
- LE, M.S. (1987), Recovery of Beer from Tank Bottoms with Membranes, *J. Chem. Tech. Biotechnol.*, 37, pp. 59-66
- LEGER, J.-P. (1985), Dynamic Membranes from Surface Water Impurities - A Study of Membrane Fouling by Rand Water Board Water, MSc Thesis, University of Natal
- LEIGHTON, D. and ACRIVOS, A. (1986), Viscous Resuspension, *Chem. Eng. Science*, 41(6), pp. 1377-1384
- LEIGHTON, D. and ACRIVOS, A. (1987a), The Shear-induced Migration of Particles in Concentrated Suspensions, *Journal of Fluid Mechanics*, 181, pp. 415-439
- LEIGHTON D. and ACRIVOS, A. (1987b), Measurement of Shear-induced Self-diffusion in Concentrated Suspensions of Spheres, *Journal of Fluid Mechanics*, 177, pp. 109-131

- LEONARD and VASSILIEFF, (1984), The Deposition of Rejected Matter in Membrane Separation Processes, *Chem. Eng. Communications*, 30, pp. 209-217
- MERKINE, L., SOLAN, A. and WINOGRAD, Y. (1971), Turbulent Flow in a Tube with Wall Suction, pp. 242-244, May
- MIZUSHINA, T., TAKESHITA, S., YOSHIZAWA, J. and NAKAMAE, I. (1972), Study of Turbulent Flow in a Porous Tube with High Mass Flux To and From the Wall, *Journal of Chemical Engineering of Japan*, 5(4), pp. 361-364
- MURKES, J. and CARLSSON, C.G. (1988), *Crossflow Filtration - Theory and Practise*, 1st ed., John Wiley and Co. Ltd.
- NA, T.Y. (1972), Analysis of Turbulent Pipe Flow with Mass Transfer, *Journal of Basic Engineering*, September, p. 701
- NEDDERMAN, R.M. (1961), The Measurement of Velocities in the Wall Region of Turbulent Liquid Pipe Flow, *Chem. Eng. Science*, 16, pp. 120-126
- NI, S. (1986), Particle Diffusivity in Fully Developed Turbulent Pipe Flow of Dilute Suspensions, PhD Thesis, University of Illinois, USA
- NOTTER, R.H. and SLEICHER, C.A. (1971), The Eddy Diffusivity in the Turbulent Boundary Layer Near a Wall, *Chem Eng. Science*, 26, pp. 161-171
- PECHENKIN, M.V. (1972), Experimental Study of Flows with High Solid Particle Concentration, Proceedings - Congress A.I.R.H., Tokyo
- PHILLIPS, M. (1980), A Force Balance Model for Particle Entrainment into a Fluid Stream, *Journal of Physics D : Applied Physics*, 13, pp. 221-223
- PILLAY, V.L., RAAL, J.D. and BUCKLEY, C.A. (1988a), Analysis of Viscous Flow in a Pipe with Suction through a Porous Wall, Proceedings - 5th National Meeting of SAICHE, Pretoria, South Africa, August
- PILLAY, V.L., RAAL, J.D. and BUCKLEY, C.A. (1988b), Theoretical Approaches to the Modelling of Cross-Flow Microfiltration, Proceedings - International Membrane Technology Conference, Sydney, Australia, November
- PILLAY, V.L., BROUCKAERT, C.J., RAAL, J.D. and BUCKLEY, C.A. (1989), Predicted Performance Profiles Along a Long Tube Cross-Flow Microfiltration System, *Desalination*, 71(3)

- PINCZEWSKI, W.V. and SIDEMAN, S. (1974), A Model for Mass (Heat) Transfer in Turbulent Tube Flow. Moderate and High Schmidt (Prandtl) Numbers, *Chem. Eng. Science*, 29, pp. 1969-1976
- PORTR, M.C. (1972), Ultrafiltration of Colloidal Suspensions, AIChE Symposium Series 68(20)
- RAUDKIVI, A.J. (1967), *Loose Boundary Hydraulics*, 1st ed., Pergamon Press Ltd., Great Britain
- RAUTENBACH, R. and SCHOCK, G. (1988), Ultrafiltration of Macromolecular Solutions and Cross-flow Microfiltration of Colloidal Suspensions. A Contribution to Permeate Flux Calculations, *Journal of Membrane Science*, 30, pp. 231-242
- REED, R.H., GREEN, G. and BELFORT, G. (1980), Characterisation of Fouling Potential for Pressure Driven Membrane Process, Presented at 5th Membrane Seminar, Clemson University (reference 26 in Green and Belfort (1980))
- REED, R.H. and BELFORT, G. (1982), Characterisation of Fouling Potential for Pressure Driven Membrane Process : A New Simulated Flow Cell, *Water Science Technology*, 14, pp. 499-522
- ROCO, M.C. and BALAKRISHNAN, N. (1985), Multi-Dimensional Flow Analysis of Solid-Liquid Mixtures, *Journal of Rheology*, 29
- ROCO, M.C. and SHOOK, C.A. (1985), Critical Deposit Velocity in Slurry Flow, *AIChE*, 31(8), pp. 1401-1404
- ROMERO, C.A. and DAVIS, R.H. (1988), Global Model of Crossflow Microfiltration Based on Hydrodynamic Particle Diffusion, *Journal of Membrane Science*, 39, pp. 157-185
- RUSHTON, A., HOSSEINI, M. and RUSHTON, A. (1979), Shear Effects in Cake Formation Mechanism, *Filtration and Separation*, p. 456, September
- SAW, C.B., ANDERSON, G.K., JAMES, A. and LE, M.S., (1985), A Membrane Technique for Biomass Retention in Anaerobic Waste Treatment Processes, Proceedings of the 40th Industrial Waste Conference, Lafayette, Indiana
- SCARLETT, B. and TREASURE, G. (1974), Evaluation of Crossflow Filtration, Private Communication to Murkes (1988)
- SCHLICHTING, H. (1968), *Boundary layer Theory*, 6th ed., McGraw Hill

- SCHNEIDER, K. and KLEIN, W. (1982), The Concentration of Suspensions by Means of Crossflow Microfiltration, *Desalination*, 41, pp. 263-275
- SCHULZ, G. and RIPPERGER, S. (1989), Concentration Polarisation in Crossflow Microfiltration, *Journal of Membrane Science*, 40, pp. 173-187
- SIMONS, D.B. and SENTURK, F. (1976), *Sediment Transport Technology*, Water Resources Publications, Colorado, USA
- SMITH, G.N. (1982), *Elements of Soil Mechanics for Civil and Mining Engineers*, 5th ed., Granada, London
- SNYDER, W.H. and LUMLEY, J.L. (1971), Some Measurements of Particle Velocity Autocorrelation Functions in a Turbulent Flow, *Journal of Fluid Mechanics*, 48, p. 41
- SON, J.S. and HANRATTY, T.J. (1967), Limiting Relation for the Eddy Diffusivity Close to a Wall, *AIChE*, 13(4), pp. 689-696
- SOO, S.L. (1967), *Fluid Dynamics of Multiphase Systems*, Blaisdell Publishing Co., US
- SOO, S.L. (1987), Pipe Flow of a Dense Suspension, *Journal of Pipelines*, 6, p. 193.
- SOO, S.L. and TUNG, S.K. (1972), Deposition and Entrainment in Pipe Flow of a Suspension, *Powder Technology*, 6, pp. 283-294
- SUTHERLAND, A.J. (1967), Proposed Mechanism for Sediment Entrainment by Turbulent Flows, *Journal of Geophysical Research*, 72(24), pp. 6183-6194
- THOMAS, D.G., GALLAGHER, R.B. and JOHNSON, J.S. (1973), Hydrodynamic Flux Control for Waste Water Application of Hyperfiltration Systems, EPA-R2-73-228, EPA, Washington DC (reference 15 in Green and Belfort, (1980))
- TILLER, F.M. and YEH, C.S. (1985), The Role of Porosity in Filtration - Part X : Deposition of Compressible Cakes on External Radial Surfaces, *AIChE*, 31(8), pp. 1241-1248
- TILLER, F.M. and YEH, C.S. (1987), Compressibility of Particulate Structures in Relation to Thickening, Filtration and Expression - A Review, *Separation Science and Technology*, 22, pp. 1037-1063
- TURIAN, R.M., HSU, F. and MA, T. (1987), Estimation of the Critical Velocity in Pipeline Flow of Slurries, *Powder Technology*, 51, pp. 35-47

- WASP, E.J., KENNY, J.P. and GANDHI, R.L. (1977), *Solid-Liquid Flow - Slurry Pipeline Transportation*, 1st ed., Trans. Tech. Publications
- WEISSBERG, H.L. (1955), Velocity and Pressure Distributions in Turbulent Pipe Flow with Uniform Wall Suction, Report No. K-1187, Union Carbide Nuclear Company, Tennessee, USA
- WEISSBERG, H.L. (1956), Velocity Profiles and Friction Factors for Turbulent Pipe Flow with Uniform Wall Suction, Report No. K-1264, Union Carbide Nuclear Company, Tennessee, USA
- WELTY, J.R., WICKS, R.E. and WILSON, R.E. (1976), *Fundamentals of Momentum, Heat and Mass Transfer*, 2nd ed., John Wiley and Sons Ltd.
- YALIN, M.S. (1972), *Mechanics of Sediment Transport*, Pergamon Press
- YUAN, S.W. and FINKELSTEIN, A.B. (1956), Laminar Pipe Flow with Injection and Suction Through a Porous Wall, *Transactions of ASME*, p. 719
- YUNG, B.P.K., MERRY, H. and BOTT, T.R. (1989), The Role of Turbulent Bursts in Particle Re-entrainment in Aqueous Systems, *Chem. Eng. Science*, 44(4), pp. 873-882
- ZYDNEY, A.L. and COLTON, C.K. (1986), A Concentration Polarisation Model for the Filtrate Flux in Cross-flow Microfiltration of Particulate Suspensions, *Chem. Eng. Communications*, 47, pp. 1-21

## *Appendix 1*

### **SUSPENSION PROPERTIES**

### A1.1 Particle Size Distribution

The particle size distribution was measured on a Malvern E3600 Type E Particle Sizer. The cumulative size distribution is shown in Figure A1.1. The mean particle size ( $\bar{d}_\rho$ ) was taken to be the  $d_{50}$  size, i.e.  $4.99 \mu\text{m}$ .

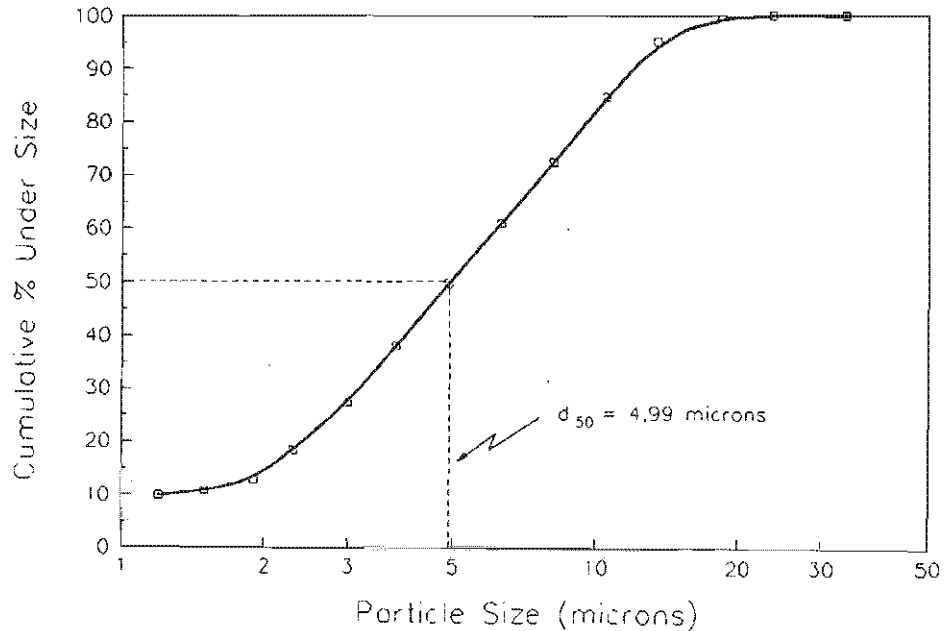


FIGURE A1.1      Cumulative Particle Size Distribution

### A1.2 Particle Density

The particle density was measured by liquid pycnometry, yielding

$$\rho_s = 2550 \text{ kg/m}^3$$

## *Appendix 2*

**RESULTS**  
**OF**  
**EXPERIMENTAL STUDY**

<u>SUMMARY OF EXPERIMENTAL RUNS</u>		
TABLE	RUN NUMBER	RUN DESCRIPTION
A2-1	47	Effect of bulk concentration on flux :- $C_B^* = 19,8 \text{ g/l}$ , $\bar{U}_s = 1,42 \text{ m/s}$ , $P = 200 \text{ kPa}$
A2-2	48	Effect of bulk concentration on flux (also central datapoint for effect of velocity and pressure on flux) :- $C_B^* = 39,4 \text{ g/l}$ , $\bar{U}_s = 1,42 \text{ m/s}$ , $P = 200 \text{ kPa}$
A2-3	48R	Repeat of Run 48
A2-4	49	Effect of bulk concentration on flux :- $C_B^* = 58,6 \text{ g/l}$ , $\bar{U}_s = 1,42 \text{ m/s}$ , $P = 200 \text{ kPa}$
A2-5	50	Effect of bulk concentration on flux :- $C_B^* = 10,0 \text{ g/l}$ , $\bar{U}_s = 1,42 \text{ m/s}$ , $P = 200 \text{ kPa}$
A2-6	51	Effect of bulk concentration on flux :- $C_B^* = 77,6 \text{ g/l}$ , $\bar{U}_s = 1,42 \text{ m/s}$ , $P = 200 \text{ kPa}$
A2-7	52	Effect of inlet velocity on flux :- $\bar{U}_s = 1,7 \text{ m/s}$ , $C_B^* = 39,4 \text{ g/l}$ , $P = 200 \text{ kPa}$
A2-8	53	Effect of inlet velocity on flux :- $\bar{U}_s = 1,13 \text{ m/s}$ , $C_B^* = 39,4 \text{ g/l}$ , $P = 200 \text{ kPa}$
A2-9	54	Effect of inlet velocity on flux :- $\bar{U}_s = 1,98 \text{ m/s}$ , $C_B^* = 39,4 \text{ g/l}$ , $P = 200 \text{ kPa}$
A2-10	55	Effect of inlet velocity on flux :- $\bar{U}_s = 0,85 \text{ m/s}$ , $C_B^* = 39,4 \text{ g/l}$ , $P = 200 \text{ kPa}$
A2-11	58	Effect of pressure on flux :- $P = 300 \text{ kPa}$ , $\bar{U}_s = 1,42 \text{ m/s}$ , $C_B^* = 39,4 \text{ g/l}$
A2-12	59	Effect of pressure on flux :- $P = 100 \text{ kPa}$ , $\bar{U}_s = 1,42 \text{ m/s}$ , $C_B^* = 39,4 \text{ g/l}$
A2-13	60	Effect of pressure on flux :- $P = 150 \text{ kPa}$ , $\bar{U}_s = 1,42 \text{ m/s}$ , $C_B^* = 39,4 \text{ g/l}$
A2-14	61	Effect of pressure on flux :- $P = 250 \text{ kPa}$ , $\bar{U}_s = 1,42 \text{ m/s}$ , $C_B^* = 39,4 \text{ g/l}$
NB All steady-state fluxes chosen at 30 minutes after start-up		

<u>SUMMARY OF EXPERIMENT RUNS (continued)</u>		
TABLE	RUN NUMBER	RUN DESCRIPTION
A2-15	67	System response to step-increase in concentration :- start-up at $C_a = 19,8 \text{ g/l}$ , then increase concentration to $77,6 \text{ g/l}$ after 10 minutes
A2-16	68	System response to step-increase in concentration :- start-up at $C_a = 19,8 \text{ g/l}$ , then increase concentration to $77,6 \text{ g/l}$ after 60 minutes
A2-17	70	System response to step-decrease in concentration :- start-up at $C_a = 77,6 \text{ g/l}$ , then switch to water after 10 minutes
A2-18	71	System response to step-decrease in concentration :- start-up at $C_a = 77,6 \text{ g/l}$ , then switch to water after 60 minutes
A2-19	72	System response to step-increase in velocity :- start-up at $\bar{U}_s = 1,13 \text{ m/s}$ , then increase velocity to $1,7 \text{ m/s}$ after 10 minutes
A2-20	74	System response to step-increase in velocity :- start-up at $\bar{U}_s = 1,13 \text{ m/s}$ , then increase velocity to $1,7 \text{ m/s}$ after 60 minutes
A2-21	75	System response to step-decrease in velocity :- start-up at $\bar{U}_s = 1,7 \text{ m/s}$ , then decrease velocity to $1,13 \text{ m/s}$ after 10 minutes
A2-22	76	System response to step-decrease in velocity :- start-up at $\bar{U}_s = 1,7 \text{ m/s}$ , then decrease velocity to $1,13 \text{ m/s}$ after 60 minutes
A2-23	77	System response to step-decrease in pressure :- start-up at $P = 200 \text{ kPa}$ , then decrease pressure to $100 \text{ kPa}$ after 10 minutes
A2-24	78	System response to step-decrease in pressure :- start-up at $P = 200 \text{ kPa}$ , then decrease pressure to $100 \text{ kPa}$ after 60 minutes
A2-25	80	System response to step-increase in pressure :- start-up at $P = 100 \text{ kPa}$ , then increase pressure to $200 \text{ kPa}$ after 10 minutes
A2-26	81	System response to step-increase in pressure :- start-up at $P = 100 \text{ kPa}$ , then increase pressure to $200 \text{ kPa}$ after 60 minutes

TABLE A2-1 Flux Measurements - RUN 47

Start-up Conditions :			
Bulk Concentration ( $C_B$ )		(g/l)	19,8
Superficial Inlet Velocity ( $\bar{U}_s$ )		(m/s)	1,42
Pressure (P)		(kPa)	200
Temperature		(°C)	30
Time from Start-up (minutes)		Permeate Flux ( $J_w$ ) (l/m <sup>2</sup> h)	
0			
5		1376,5	
7,5		1144,5	
10		1039,4	
12,5		985,7	
15		885,7	
20		825,9	
25		775,6	
30		749,0	
35		717,3	
40		700,9	
45		682,1	
50		676,1	
55		658,6	
60		646,0	
65		637,9	
70		631,4	
75		618,6	
80		616,1	
85		601,5	
90		592,2	
95		589,9	
100		588,8	
105		576,6	
110		576,6	
115		569,0	
120		561,7	

TABLE A2-2 Flux Measurements - RUN 48

Start-up Conditions :			
Bulk Concentration ( $C_B$ )		(g/l)	39,4
Superficial Inlet Velocity ( $\bar{U}_s$ )		(m/s)	1,42
Pressure ( $P$ )		(kPa)	200
Temperature		(°C)	30
Time from Start-up (minutes)		Permeate Flux ( $J_w$ )	
			(l/m <sup>2</sup> h)
0			
5		1079,8	
7,5		904,1	
10		823,7	
12,5		767,8	
15		738,1	
20		700,9	
25		664,3	
30		637,9	
35		623,6	
40		608,7	
45		599,2	
50		589,9	
55		579,8	
60		571,2	
65		563,8	
70		557,6	
75		554,6	
80		544,7	
85		544,7	
90		538,9	
95		531,4	
100		529,6	
105		523,2	
110		517,9	
115		516,2	
120		513,6	

TABLE A2-3 Flux Measurements - RUN 48R

Start-up Conditions :			
Bulk Concentration ( $C_B$ )		(g/l)	39,4
Superficial Inlet Velocity ( $\bar{U}_s$ )		(m/s)	1,42
Pressure ( $P$ )		(kPa)	200
Temperature		(°C)	30
Time from Start-up (minutes)		Permeate Flux ( $J_w$ )	
		(l/m <sup>2</sup> h)	
0			
5		1057,4	
10		812,7	
15		732,8	
20		700,9	
25		665,7	
30		647,4	
35		628,8	
40		611,2	
45		602,7	
50		595,7	
55		586,5	
60		579,8	
65		571,2	
70		566,9	
75		562,8	
80		557,6	
85		553,6	
90		549,6	
95		543,7	
100		537,0	
105		534,2	
110		529,6	
115		526,0	
120		522,4	

**TABLE A2-4 Flux Measurements - RUN 49**

Start-up Conditions :		(g/l)	58,6
Bulk Concentration ( $C_B$ )		(m/s)	1,42
Superficial Inlet Velocity ( $\bar{U}_s$ )		(kPa)	200
Pressure ( $P$ )		(°C)	30
Temperature			
Time from Start-up (minutes)		Permeate Flux ( $J_w$ ) (l/m <sup>2</sup> h)	
0			
5		878,1	
7,5		763,9	
10		714,0	
12,5		673,1	
15		655,7	
20		613,6	
25		594,5	
30		574,4	
35		562,8	
40		559,7	
45		547,6	
50		536,1	
55		532,4	
60		528,7	
65		523,2	
70		517,9	
75		511,0	
80		501,8	
85		496,1	
90		492,9	
95		483,5	
100		486,6	
105		477,5	
110		477,5	
115		471,6	
120		465,8	

TABLE A2-5 Flux Measurements - RUN 50

Start-up Conditions :			
Bulk Concentration ( $C_B$ )		(g/l)	10,0
Superficial Inlet Velocity ( $\bar{U}_s$ )		(m/s)	1,42
Pressure ( $P$ )		(kPa)	200
Temperature		(°C)	30
Time from Start-up (minutes)		Permeate Flux ( $J_w$ )	
		(l/m <sup>2</sup> h)	
0			
5		1909,9	
7,5		1575,1	
10		1346,2	
15		1131,8	
20		1025,4	
25		934,5	
30		885,7	
35		856,0	
40		830,4	
45		802,0	
50		787,6	
55		771,7	
60		745,3	
65		745,3	
70		734,6	
75		719,0	
80		714,0	
85		699,3	
90		692,9	
95		689,8	
100		686,7	
105		676,1	
110		664,3	
115		662,9	
120		657,2	

TABLE A2-6 Flux Measurements - RUN 51			
Start-up Conditions :			
Bulk Concentration ( $C_B$ )		(g/l)	77,6
Superficial Inlet Velocity ( $\bar{U}_s$ )		(m/s)	1,42
Pressure ( $P$ )		(kPa)	200
Temperature		( °C)	30
Time from Start-up (minutes)		Permeate Flux ( $J_w$ ) (l/m <sup>2</sup> h)	
0			
5			763,9
7,5			679,1
10			630,1
12,5			609,9
15			591,1
20			565,9
25			540,8
30			529,6
35			517,9
40			508,4
45			506,8
50			499,3
55			496,9
60			488,9
65			483,5
70			478,2
75			476,0
80			469,4
85			468,7
90			463,0
95			461,6
100			456,8
105			454,7
110			452,0
115			448,7
120			443,5

TABLE A2-7 Flux Measurements - RUN 52

Start-up Conditions :			
Bulk Concentration ( $C_B$ )		(g/l)	39,4
Superficial Inlet Velocity ( $\bar{U}_s$ )		(m/s)	1,7
Pressure ( $P$ )		(kPa)	200
Temperature		(°C)	30
Time from Start-up (minutes)		Permeate Flux ( $J_w$ )	
		(l/m <sup>2</sup> h)	
0			
5		1153,1	
7,5		1018,6	
10		912,2	
12,5		873,1	
15		828,1	
20		773,6	
25		736,3	
30		722,4	
35		694,5	
40		679,1	
45		668,7	
50		660,0	
55		652,9	
60		644,7	
65		636,6	
70		628,8	
75		621,1	
80		612,4	
85		602,7	
90		599,2	
95		593,2	
100		585,4	
105		582,1	
110		576,6	
115		569,0	
120		563,8	

TABLE A2-8 Flux Measurements - RUN 53

Start-up Conditions :			
Bulk Concentration ( $C_s$ )		(g/l)	39,4
Superficial Inlet Velocity ( $\bar{U}_s$ )		(m/s)	1,13
Pressure ( $P$ )		(kPa)	200
Temperature		(°C)	30
Time from Start-up (minutes)		Permeate Flux ( $J_w$ )	
		(l/m <sup>2</sup> h)	
0			
5		1042,9	
7,5		856,0	
10		782,0	
12,5		709,0	
15		662,9	
20		617,3	
25		591,1	
30		562,8	
35		545,7	
40		528,7	
45		521,5	
50		512,7	
55		511,0	
60		493,7	
65		485,8	
70		485,0	
75		481,2	
80		476,7	
85		471,6	
90		468,0	
95		463,0	
100		459,5	
105		454,7	
110		454,1	
115		450,0	
120		448,1	

TABLE A2-9 Flux Measurements - RUN 54

Start-up Conditions :			
Bulk Concentration ( $C_B$ )		(g/l)	39,4
Superficial Inlet Velocity ( $\bar{U}_s$ )		(m/s)	1,98
Pressure ( $P$ )		(kPa)	200
Temperature		(°C)	30
Time from Start-up (minutes)		Permeate Flux ( $J_w$ ) (l/m <sup>2</sup> h)	
0			
5		1189,0	
7,5		1064,7	
10		979,4	
12,5		914,9	
15		888,3	
20		851,2	
25		830,4	
30		802,0	
35		777,6	
40		762,0	
45		756,4	
50		739,9	
55		725,8	
60		715,6	
65		712,3	
70		694,5	
75		683,6	
80		677,6	
85		674,6	
90		665,7	
95		652,9	
100		648,8	
105		644,7	
110		640,6	
115		635,3	
120		628,8	

TABLE A2-10 Flux Measurements - RUN 55

Start-up Conditions :			
Bulk Concentration ( $C_s$ )		(g/l)	39,4
Superficial Inlet Velocity ( $\bar{U}_s$ )		(m/s)	0,85
Pressure ( $P$ )		(kPa)	200
Temperature		(°C)	30
Time from Start-up (minutes)		Permeate Flux ( $J_w$ ) (l/m <sup>2</sup> h)	
0			
5		1022,0	
7,5		819,2	
10		707,4	
12,5		646,0	
15		600,3	
20		547,6	
25		511,0	
30		498,5	
35		484,3	
40		474,5	
45		460,2	
50		454,1	
55		450,0	
60		446,1	
65		434,7	
70		432,2	
75		426,2	
80		425,0	
85		422,1	
90		420,3	
95		418,6	
100		416,3	
105		414,1	
110		410,2	
115		408,0	
120		404,7	

TABLE A2-11 Flux Measurements - RUN 58

Start-up Conditions :			
Bulk Concentration ( $C_b$ )	(g/l)		39,4
Superficial Inlet Velocity ( $\bar{U}_s$ )	(m/s)		1,42
Pressure ( $P$ )	(kPa)		300
Temperature	(°C)		30
Time from Start-up (minutes)		Permeate Flux ( $J_w$ )	
0			
5		1193,7	
10		909,5	
15		789,6	
20		762,0	
25		704,1	
30		686,7	
35		679,1	
40		661,4	
45		654,3	
50		640,6	
55		628,8	
60		622,4	
65		607,5	
70		600,3	
75		601,5	
80		587,6	
85		589,9	
90		584,3	
95		576,6	
100		570,1	
105		561,7	
110		558,6	
115		556,6	
120		553,6	

TABLE A2-12 Flux Measurements - RUN 59

Start-up Conditions :			
Bulk Concentration ( $C_b$ )		(g/l)	39,4
Superficial Inlet Velocity ( $\bar{U}_s$ )		(m/s)	1,42
Pressure ( $P$ )		(kPa)	100
Temperature		(°C)	30
Time from Start-up (minutes)		Permeate Flux ( $J_w$ )	
0			
5		719,0	
10		612,4	
15		560,7	
20		536,1	
25		517,9	
30		501,8	
35		496,1	
40		485,0	
45		477,5	
50		468,0	
55		459,5	
60		457,5	
65		452,0	
70		448,7	
75		447,4	
80		440,3	
85		439,0	
90		432,2	
95		426,8	
100		423,8	
105		418,6	
110		414,1	
115		416,9	
120		413,5	

TABLE A2-13 Flux Measurements - RUN 60

Start-up Conditions :			
Bulk Concentration ( $C_B$ )		(g/l)	39,4
Superficial Inlet Velocity ( $\bar{U}_s$ )		(m/s)	1,42
Pressure ( $P$ )		(kPa)	150
Temperature		( °C)	30
Time from Start-up (minutes)		Permeate Flux ( $J_w$ )	
			(l/m <sup>2</sup> h)
0			
5		870,6	
10		707,4	
15		650,2	
20		613,6	
25		589,9	
30		574,4	
35		558,6	
40		555,6	
45		550,6	
50		533,3	
55		524,1	
60		517,9	
65		506,8	
70		505,9	
75		504,3	
80		493,7	
85		495,3	
90		488,9	
95		477,5	
100		476,0	
105		474,5	
110		468,7	
115		467,2	
120		465,1	

TABLE A2-14 Flux Measurements - RUN 61

Start-up Conditions :		(g/l)	39,4
Bulk Concentration ( $C_B$ )	(m/s)	1,42	
Superficial Inlet Velocity ( $\bar{U}_s$ )	(kPa)	250	
Pressure ( $P$ )	( °C)	30	
Temperature			
Time from Start-up (minutes)		Permeate Flux ( $J_w$ )	( $\ell/m^2h$ )
0			
5		1161,9	
10		880,6	
15		771,7	
20		734,6	
25		686,7	
30		671,6	
35		652,9	
40		643,3	
45		632,7	
50		623,6	
55		611,2	
60		603,9	
65		584,3	
70		586,5	
75		580,9	
80		573,3	
85		566,9	
90		564,8	
95		558,6	
100		553,6	
105		549,6	
110		540,8	
115		541,8	
120		539,9	

TABLE A2-15 Flux Measurements - RUN 67

Start-up Conditions :			
Bulk Concentration ( $C_B$ )		(g/l)	19,8
Superficial Inlet Velocity ( $\bar{U}_s$ )		(m/s)	1,42
Pressure ( $P$ )		(kPa)	200
Temperature		(°C)	30
Time from Start-up (minutes)		Permeate Flux ( $J_w$ ) (l/m <sup>2</sup> h)	
0			
5		1358,1	
10		985,7	
Increase concentration to 77,6 g/l			
15		765,9	
20		677,6	
25		619,8	
30		587,6	
35		554,6	
40		531,4	
45		516,2	
50		503,4	
55		492,1	
60		484,3	
65		478,2	
70		473,8	
75		466,5	
80		461,6	
85		455,4	
90		452,7	
95		449,4	
100		446,1	
105		442,9	
110		442,9	
115		436,5	
120		433,4	

TABLE A2-16 Flux Measurements - RUN 68

Start-up Conditions :			
Bulk Concentration ( $C_B$ )	(g/l)	19,8	
Superficial Inlet Velocity ( $\bar{U}_s$ )	(m/s)	1,42	
Pressure ( $P$ )	(kPa)	200	
Temperature	(°C)	30	
Time from Start-up (minutes)		Permeate Flux ( $J_w$ ) (l/m <sup>2</sup> h)	
0			
5		1455,1	
10		1131,8	
15		952,0	
20		865,7	
25		814,9	
30		781,5	
35		745,3	
40		717,3	
45		696,1	
50		677,6	
55		654,3	
60		630,1	
Increase concentration to 77,6 g/l			
65		579,8	
70		541,8	
75		515,3	
80		488,9	
85		473,8	
90		460,9	
95		449,4	
100		441,6	
105		435,3	
110		429,8	
115		418,0	
120		412,9	
125		408,5	
130		406,4	

TABLE A2-17 Flux Measurements - RUN 70

Start-up Conditions :			
Bulk Concentration ( $C_B$ )		(g/l)	77,6
Superficial Inlet Velocity ( $\bar{U}_s$ )		(m/s)	1,42
Pressure ( $P$ )		(kPa)	200
Temperature		( °C)	30
Time from Start-up (minutes)		Permeate Flux ( $J_w$ )	
0			
5			770,6
10			637,6
Decrease concentration to 0 g/l (switch to water)			
15			635,9
20			635,4
25			636,5
30			636,5
35			633,7
40			635,4
45			634,8
50			632,6
55			630,9
60			633,7
65			633,1
70			633,1
75			633,1
80			633,1
85			633,4
90			633,1

TABLE A2-18 Flux Measurements - RUN 71

Start-up Conditions :		(g/l)	77,6
Bulk Concentration ( $C_b$ )	(m/s)		1,42
Superficial Inlet Velocity ( $\bar{U}_s$ )	(kPa)		200
Pressure ( $P$ )	(°C)		30
Temperature			
Time from Start-up (minutes)		Permeate Flux ( $J_w$ ) ( $\ell/m^2h$ )	
0			
5		760,4	
10		630,9	
15		590,5	
20		561,4	
25		543,1	
30		524,7	
35		515,1	
40		509,9	
45		505,3	
50		499,6	
55		494,6	
60		489,9	
Decrease concentration to 0 g/l (switch to water)			
65		489,3	
70		489,3	
75		489,9	
80		489,9	
85		492,2	
90		492,7	
95		487,9	
100		489,6	
105		484,8	
110		487,7	
115		490,7	
120		490,4	

TABLE A2-19 Flux Measurements - RUN 72

Start-up Conditions :			
Bulk Concentration ( $C_s^*$ )		(g/l)	39,4
Superficial Inlet Velocity ( $\bar{U}_s$ )		(m/s)	1,13
Pressure ( $P$ )		(kPa)	200
Temperature		(°C)	30
Time from Start-up (minutes)		Permeate Flux ( $J_w$ )	
0			
5		1015,2	
10		754,5	
Increase velocity to 1,7 m/s			
15		732,8	
20		719,0	
25		704,1	
30		688,2	
35		682,1	
40		665,7	
45		662,9	
50		654,3	
55		643,3	
60		636,6	
65		626,2	
70		622,4	
75		611,2	
80		607,5	
85		599,2	
90		593,4	
95		586,5	
100		577,7	

TABLE A2-20 Flux Measurements - RUN 74

Start-up Conditions :			
Bulk Concentration ( $C_s^*$ )		(g/l)	39,4
Superficial Inlet Velocity ( $\bar{U}_s$ )		(m/s)	1,13
Pressure (P)		(kPa)	200
Temperature		(°C)	30
Time from Start-up (minutes)		Permeate Flux ( $J_w$ )	
			(l/m <sup>2</sup> h)
0			
5			1053,7
10			756,4
15			662,9
20			611,2
25			685,4
30			555,6
35			544,7
40			528,7
45			517,9
50			509,3
55			503,4
60			492,9
Increase velocity to 1,7 m/s			
65			492,9
70			488,1
75			484,3
80			477,5
85			473,8
90			470,8
95			468,7
100			462,3
105			453,4
110			449,4
115			446,1

TABLE A2-21 Flux Measurements - RUN 75

Start-up Conditions :			
Bulk Concentration ( $C_B$ )		(g/l)	39,4
Superficial Inlet Velocity ( $\bar{U}_s$ )		(m/s)	1,7
Pressure ( $P$ )		(kPa)	200
Temperature		(°C)	30
Time from Start-up (minutes)		Permeate Flux ( $J_w$ )	
0			
5			1222,3
10			898,8
Decrease velocity to 1,13 m/s			
15			709,0
20			636,6
25			583,2
30			555,6
35			543,7
40			522,4
45			510,1
50			500,9
55			492,9
60			488,9
65			485,0
70			481,2
75			477,5
80			476,0
85			471,6
90			470,1
95			468,0
100			464,4
105			461,6
110			457,5
115			454,7
120			452,7

TABLE A2-22 Flux Measurements - RUN 76

Start-up Conditions :			
Bulk Concentration ( $C_B$ )		(g/l)	39,4
Superficial Inlet Velocity ( $\bar{U}_s$ )		(m/s)	1,7
Pressure ( $P$ )		(kPa)	200
Temperature		(°C)	30
Time from Start-up (minutes)		Permeate Flux ( $J_w$ )	
		(l/m <sup>2</sup> h)	
0			
5			1198,3
10			954,9
15			863,2
20			793,7
25			756,4
30			727,6
35			709,0
40			692,9
45			679,1
50			664,3
55			647,4
60			636,6
Decrease velocity to 1,13 m/s			
65			544,7
70			516,2
75			496,9
80			483,5
85			470,1
90			460,9
95			452,7
100			442,9
105			436,5
110			431,0
115			426,8
120			424,4
125			419,7

**TABLE A2-22      Flux Measurements - RUN 76**  
**(continued)**

Start-up Conditions :			
Bulk Concentration ( $C_s$ )		(g/l)	39,4
Superficial Inlet Velocity ( $\bar{U}_s$ )		(m/s)	1,7
Pressure ( $P$ )		(kPa)	200
Temperature		(°C)	30
Time from Start-up (minutes)		Permeate Flux ( $J_w$ ) (l/m²h)	
(velocity was decreased to 1,13 m/s, 60 minutes after start-up)			
130		415,8	
135		411,8	
140		408,5	
145		405,8	
150		403,7	

TABLE A2-23 Flux Measurements - RUN 77

Start-up Conditions :			
Bulk Concentration ( $C_b$ )		(g/l)	39,4
Superficial Inlet Velocity ( $\bar{U}_s$ )		(m/s)	1,42
Pressure ( $P$ )		(kPa)	200
Temperature		(°C)	
Time from Start-up (minutes)		Permeate Flux ( $J_w$ )	
0			
5			1053,7
10			814,9
Decrease pressure to 100 kPa			
15			434,1
20			431,0
25			428,6
30			425,6
35			423,2
40			423,2
45			419,2
50			416,9
55			414,1
60			411,3

TABLE A2-24 Flux Measurements - RUN 78

Start-up Conditions :			
Bulk Concentration ( $C_s$ )		(g/l)	39,4
Superficial Inlet Velocity ( $\bar{U}_s$ )		(m/s)	1,42
Pressure ( $P$ )		(kPa)	200
Temperature		( °C)	30
Time from Start-up (minutes)		Permeate Flux ( $J_w$ )	
0			
5		1091,3	
10		837,2	
15		760,1	
20		719,0	
25		671,6	
30		650,2	
35		630,1	
40		621,1	
45		609,9	
50		600,3	
55		594,5	
60		585,4	
Decrease pressure to 100 kPa			
65		315,0	
70		314,7	
75		315,0	
80		314,1	
85		313,4	
90		313,4	
95		313,1	
100		312,1	
105		311,8	
110		312,5	
115		312,5	
120		311,8	

**TABLE A2-25 Flux Measurements - RUN 80**

Start-up Conditions :		(g/l)	39,4
Bulk Concentration ( $C_b$ )		(m/s)	1,42
Superficial Inlet Velocity ( $\bar{U}_s$ )		(kPa)	100
Pressure ( $P$ )		( °C)	30
Temperature			
Time from Start-up (minutes)		Permeate Flux ( $J_w$ )	
0			
5		762,0	
10		608,7	
Increase pressure to 200 kPa			
15		954,9	
20		802,0	
25		712,3	
30		662,9	
35		626,2	
40		605,1	
45		592,2	
50		576,6	
55		566,9	
60		557,6	
65		550,6	
70		543,7	
75		526,9	
80		530,5	
85		526,9	
90		523,2	
95		517,1	
100		510,1	
105		509,3	
110		500,1	
115		495,3	
120		488,9	

TABLE A2-26 Flux Measurements - RUN 81

Start-up Conditions :			
Bulk Concentration ( $C_s^*$ )		(g/l)	39,4
Superficial Inlet Velocity ( $\bar{U}_s$ )		(m/s)	1,42
Pressure ( $P$ )		(kPa)	100
Temperature		( °C)	30
Time from Start-up (minutes)		Permeate Flux ( $J_w$ )	
			(l/m <sup>2</sup> h)
0			
5		773,6	
10		676,1	
15		587,6	
20		550,6	
25		526,0	
30		509,3	
35		496,9	
40		484,8	
45		471,6	
50		463,7	
55		456,1	
60		450,7	
Increase pressure to 200 kPa			
65		692,9	
70		608,7	
75		564,8	
80		526,9	
85		513,6	
90		498,5	
95		483,5	
100		470,1	
105		461,6	
110		452,7	
115		446,1	
120		439,7	